UCLA
UCLA Electronic Theses and Dissertations

Title
Hydrodynamic models for multicomponent plasmas with collisional-radiative kinetics

Permalink
https://escholarship.org/uc/item/8kv306qn

Author
Le, Hai

Publication Date
2014

Peer reviewed|Thesis/dissertation

eScholarship.org Powered by the California Digital Library
University of California

University of California

Los Angeles

Hydrodynamic models for multicomponent plasmas with collisional-radiative kinetics

A dissertation submitted in partial satisfaction

of the requirements for the degree

Doctor of Philosophy in Mechanical Engineering

by

Hai Phuoc Le

2014

© Copyright by
Hai Phuoc Le
2014

Abstract of the Dissertation

Hydrodynamic models for multicomponent plasmas with collisional-radiative kinetics

by

Hai Phuoc Le

Doctor of Philosophy in Mechanical Engineering

University of California, Los Angeles, 2014

Professor Ann R. Karagozian, Chair

Energy and space propulsion are two of the largest applied research areas requiring contributions from fundamental physical sciences, due to the growing world-wide demand in energy and continuing interests in expanding the frontier of deep space exploration. One of the common thrust areas in these two disciplines is plasma physics, the study of the motion of charged particles and their interaction with the electromagnetic field. The characterization of these plasma systems requires a comprehensive understanding of the physics of charged particles, collisional and radiative interactions among these particles, and how they interact with the electromagnetic field.

This dissertation presents some advances in the development of hydrodynamic models for plasma modeling and simulations in highly non-equilibrium conditions. Expressed in the form of conversation laws, these governing equations are solved by a finite volume discretization with a high-order reconstruction procedure and a multi-stage time integration method. High-fidelity collisional-radiative (CR) models are constructed by taking into account various elementary processes responsible for the excitation and ionization kinetics. The accuracy of the CR model

Distribution A: Approved for public release; distribution is unlimited.

is benchmarked against different experimental shock tube data, and yields satisfactory agreement for a wide range of flow conditions. A mechanism reduction scheme, based on a level grouping approach, is derived to lower the complexity of the CR kinetics while maintaining sufficient accuracy to capture the non-equilibrium dynamics of the plasma kinetics. The method is shown to be more accurate and efficient than standard level grouping approach, and is suitable for multidimensional flow calculations.

Although the hydrodynamic or fluid approach offers a convenient way to model the system, it requires some assumptions on the time and length scales, which in some case might be violated. Fortunately, small deviations from these assumptions can still be captured by extending the fluid equations to multi-fluid equations, which characterize the plasma species (ions and electrons) via their own set of conservation laws. The extension of the CR model to the multi-fluid regime requires a new derivation for exchange source terms. A model for excitation and deexcitation collisions within the multi-fluid framework is derived, starting from kinetic theory, where the model obeys the principle of detailed balance. The multi-fluid equations developed in the current work are used to study ion acceleration in laser-plasma interaction. The role of the laser parameters and the mechanism of the acceleration are examined in detail, demonstrating the capabilities of this computational framework.

The dissertation of Hai Phuoc Le is approved.

Jean-Luc Cambier

Russel Caflisch

George Morales

Xiaolin Zhong

Ann R. Karagozian, Committee Chair

University of California, Los Angeles

2014

This dissertation is lovingly dedicated to my mother, Mai Hoang, for everything she has given to me and her unconditional love.

Table of Contents

1 Introduction **1**

1.1 Background 1

1.1.1 Plasma-assisted combustion 2

1.1.2 Re-entry physics 4

1.1.3 Laser-plasma interactions 6

1.2 Overview of plasma physics 9

1.2.1 Plasma kinetic equations 9

1.2.2 Modeling and simulations 12

1.3 Scope of present work 15

2 Hydrodynamic Equations **17**

2.1 Introduction 17

2.2 Multi-fluid equations 19

2.2.1 Euler-Maxwell and Euler-Poisson systems 19

2.2.2 Time and length scales of multi-fluid equations 21

2.2.3 Generalized Ohm's law 23

2.3 Magnetohydrodynamics 25

2.4 Multi-temperature and chemically reactive hydrodynamics 29

3 Numerical Formulation **34**

3.1 Introduction 34

3.2 Numerical methods 34

3.2.1 Finite volume methods 34

3.2.2 Hyperbolic solvers - Approximated Riemann solvers 36
3.2.3 High-order reconstruction 39
3.2.4 Hyperbolic solvers - Implicit time marching 42
3.2.5 Source term treatment 44
3.2.6 Diffusive transport 45
3.3 Benchmark problems 47
3.3.1 Euler equations 48
3.3.2 Multi-fluid equations 55
3.3.3 Diffusion processes 65

4 Collisional-Radiative Models for Atoms 73
4.1 Introduction 73
4.2 Thermal equilibrium 74
4.2.1 Maxwell distribution 75
4.2.2 Boltzmann distribution 76
4.2.3 Saha distribution 77
4.2.4 Planck distribution 78
4.3 Elementary processes and detailed balance 79
4.3.1 Collisional excitation/deexcitation 81
4.3.2 Collisional ionization/recombination 82
4.3.3 Radiative processes 83
4.3.4 Elastic processes 85
4.4 Rate equations 86
4.5 Physical models 87
4.5.1 Argon 87

4.5.2 Krypton . . . 93
4.5.3 Xenon . . . 96
4.5.4 Electron-neutral elastic collisions . . . 98
4.6 Benchmark studies . . . 102
4.6.1 Steady-state flows . . . 102
4.6.2 Unsteady flows . . . 115

5 Complexity Reduction of Collisional-Radiative Kinetics . . . 119
5.1 Introduction . . . 119
5.2 Collisional-Radiative model . . . 122
5.2.1 Definitions and rates . . . 122
5.2.2 Master equations . . . 124
5.3 Level grouping strategies . . . 126
5.3.1 Uniform grouping . . . 126
5.3.2 Boltzmann grouping - number and energy . . . 128
5.3.3 Boltzmann grouping - partitioning . . . 131
5.3.4 Boltzmann grouping - effective rates . . . 135
5.4 Accuracy of uniform and Boltzmann methods . . . 138
5.4.1 Isothermal ionization test case . . . 138
5.4.2 Isothermal recombination test case . . . 146
5.5 Energy conservation . . . 150
5.5.1 Isochoric ionization test case . . . 153
5.5.2 Corrected energy rates . . . 156

6 Modeling of Collisions in Multifluid Plasmas . . . 162

6.1 Introduction 162
6.2 Transfer integral 163
6.3 Excitation/Deexcitation collisions 168
6.3.1 Zeroth-order moment: number density 169
6.3.2 First-order moment: momentum density 171
6.3.3 Second-order moment: total energy density 174
6.4 Summary of results 177

7 Simulations of Laser-Plasma Interactions 178
7.1 Introduction 178
7.2 Electromagnetic wave propagation in plasmas 179
7.2.1 Electrodynamic equations 179
7.2.2 WKB approximation 183
7.2.3 Collisional absorption 184
7.2.4 Ponderomotive forces 186
7.3 Multi-fluid model for laser plasma interactions 188
7.4 Numerical solutions of the wave equations 192
7.4.1 Finite difference method 192
7.4.2 Transfer-matrix method 193
7.4.3 Benchmark problems 194
7.5 Ion acceleration via Ponderomotive forces 198

8 Conclusions and Future Directions 208
8.1 Achievements and contributions 208
8.2 Future directions 211

A Eigensystems **213**

A.1 2T Model 213

A.2 Maxwell's equations 216

B Steady-state Flow Equations **218**

C Collision kinematics **220**

C.1 Two-body processes 220

C.2 Three-body processes 224

D Microscopic Detailed Balance **230**

D.1 Collisional excitation and deexcitation 230

D.2 Collisional ionization and recombination 232

D.3 Line emission and absorption 234

D.4 Photoionization and radiative recombination 234

E Derivation of the Ponderomotive Force for a Single Particle . . **236**

References **238**

List of Figures

1.1 Flame stabilization by plasma enhancement [15]. 3

1.2 PDRIME concept: a) Overpressure at the nozzle exit launch a shock to enter the bypass tube, which slows and raises the temperature of the air stream inside the tube. Energy is extract from the flow (MHD power generation). b) During the blowdown, the nozzle pressure drops, and power is applied to accelerate compressed air in the bypass channel (MHD acceleration). [18, 19] 4

1.3 Physical phenomena occurred during planetary entry (courtesy of NASA). 6

1.4 Physical processes in typical laser-plasma interaction: (1) collisional absorption, instabilities, magnetic field generation; (2) resonance absorption, profile steepening, hot electrons generation; (3) heat transport, soft x-rays generation; (4) hard x-rays generation. Figure adapted from [38]. 8

3.1 Schematic of computational stencil for MP5 and WENO schemes with left and right states of an interface. 41

3.2 Solution of the Woodward-Colella blast wave problem with 600 cells. Only part of the simulated domain is shown to illustrate the difference of two schemes. 49

3.3 Solution of the Shu-Osher problem with 300 cells. Only part of the simulated domain is shown to illustrate the difference of two schemes. 50

3.4 Solution of the forward step problem using MP5 scheme with 600,000 cells. 52

3.5 Diffraction of a Mach 2.4 shock wave down a step using MP5 scheme with 27,000 cells. Comparison between numerical schlieren (left) and experimental image (right). 53

3.6 Rayleigh-Taylor instability computed with the MP5 scheme using 640,000 cells. 54

3.7 Evolution of pressure and temperature in a 2D detonation simulation. 56

3.8 Numerical soot film produced by recording the maximum density at each grid cell over the entire simulation for a 2D detonation corresponding to figure 3.7. 57

3.9 Number density of the ions at the electron at different time and comparison of the time evolution of the ion current at the electrode with analytical solution of Lieberman [78]. Time is normalized by the ion plasma frequency, and velocity is normalized by the Bohm velocity $u_B = \sqrt{\frac{kT_e}{m_i}}$. 58

3.10 Number density and velocity profile of the ions and the electric potential at steady-state condition. Velocity is normalized by the Bohm velocity $u_B = \sqrt{\frac{kT_e}{m_i}}$. 60

3.11 Electric potential and velocity profile of the ions at steady-state condition with and without collisional drag. Velocity is normalized by the Bohm velocity $u_B = \sqrt{\frac{kT_e}{m_i}}$ and $\alpha = \frac{\lambda_D}{\lambda_i}$. 61

3.12 Ion density of the ideal two-fluid Riemann problem 64

3.13 Transverse magnetic field of the ideal two-fluid Riemann problem 64

3.14 Numerical solution and error of the heat conduction problem with 100 cells using both explicit and implicit schemes. The explicit scheme is stable for $\Delta t \leq 10^{-6}$ while the implicit scheme is stable up to $\Delta t = 10^{-3}$. 66

3.15 Temperature profile at $t = 100\tau_e$ for the hot spot relaxation by electron heat conduction. The solid line indicated the initial temperature. 68

3.16 Temperature profile for the hot spot simulation with and without laser heating. 70

3.17 Heat flux for the hot spot simulation with and without laser heating. The value of the heat flux is normalized by the freestream limit given by $q_f = p_e(kT_e/m_e)^{1/2}$. 71

3.18 Steady profile of a shock propagation into a cold Nitrogen plasma (N^+, e) with (bottom) and without (top) electron heat conduction. Free stream conditions are $u_\infty = 7000$ m/s, $T_\infty = 273$ K, $n_\infty = 2.14 \times 10^{14}$ cm^{-3}. Solid lines are ion (black) and electron (red) temperatures. The dashed line is the number density. The x axis is adjusted so the shock starts at $x = 0$. 72

4.1 Excitation cross sections from ground state to the $4s$ manifold due to electron-impact for Ar I taken from [102]. 91

4.2 Ionization cross sections due to electron-impact for Ar I as computed by the Deutsch-Märk formalism 92

4.3 Excitation cross sections from ground state to the $5s$ manifold due to electron-impact for Kr I taken from [105]. 96

4.4 Ionization cross sections due to electron-impact for Kr I as computed by the Deutsch-Märk formalism 97

4.5 Excitation cross sections from ground state to the $6s$ manifold due to electron-impact for Xe I taken from [105]. 98

4.6 Ionization cross sections due to electron-impact for Xe I as computed from the work of Erwin and Kunc [108]. 100

4.7 Momentum transfer cross sections for Argon, Krypton and Xenon. Solid lines are the results of McEachran *et al.* [104, 107]. Dashed lines are the results of Zatsarinny *et al.* [109]. 101

4.8 Computed and experimental results of ionizing shock in Argon for case 1: $p_\infty = 5.14$ Torr, $T_\infty = 293.6$ K, $Ma = 15.9$. The values of the electron number density and the total mass density are normalized by the equilibrium values: $n_e^* = 1.69 \times 10^{17}$ cm^{-3}, $\rho^* = 8.4 \times 10^{-3}$ g/cm^3. Symbols represent experimental data for n_e and ρ from Glass and Liu [110]. 104

4.9 Temperature profile of the electrons and heavy particles for case 1 from table 4.13. 105

4.10 The atomic state distribution function (ASDF) plotted at different locations of starting from the shock front utilizing the experimental condition from case 1 of table 4.13. 106

4.11 Electron number density and total density for $M_\infty = 16.1$ Ar shock corresponded to case 2 in table 4.13. The freestream conditions are: $p_\infty = 5.15$ Torr, $T_\infty = 295.9$ K. The values of the electron number density and the total mass density are normalized by the equilibrium values: $n_e^* = 1.83 \times 10^{17}$ cm^{-3}, $\rho^* = 0.87 \times 10^{-4}$ g/cm^3. Symbols represent experimental data for n_e and ρ from Glass and Liu [110]. 107

4.12 Electron number density and total density for $M_\infty = 16.5$ Ar shock corresponded to case 3 in table 4.13. The freestream conditions are: $p_\infty = 5.12$ Torr, $T_\infty = 296.6$ K. The values of the electron number density and the total mass density are normalized by the equilibrium values: $n_e^* = 2.1 \times 10^{17}$ cm^{-3}, $\rho^* = 0.88 \times 10^{-4}$ g/cm^3. Symbols represent experimental data for n_e and ρ from Glass and Liu [110]. 108

4.13 Electron number density and total density for $M_\infty = 13.0$ Ar shock corresponded to case 4 in table 4.13. The freestream conditions are: $p_\infty = 5.00$ Torr, $T_\infty = 296.6$ K. The values of the electron number density and the total mass density are normalized by the equilibrium values: $n_e^* = 5.62 \times 10^{16}$ cm^{-3}, $\rho^* = 0.62 \times 10^{-4}$ g/cm^3. Symbols represent experimental data for n_e and ρ from Glass and Liu [110]. 109

4.14 Electron number density and total density for $M_\infty = 15.05$ Kr shock corresponded to case 1 in table 4.14. The freestream conditions are: $p_\infty = 5.15$ Torr, $T_\infty = 296.2$ K. The values of the electron number density and the total mass density are normalized by the equilibrium values: $n_e^* = 1.677 \times 10^{17}$ cm^{-3}, $\rho^* = 1.712 \times 10^{-4}$ g/cm^3. Symbols represent experimental data for n_e and ρ from Glass *et al.* [111]. 111

4.15 Temperature profile of the electrons and heavy particles for case 1 from table 4.14. 112

4.16 The ASDF plotted at different locations of starting from the shock front utilizing the experimental conditions from case 1 of table 4.14. 112

4.17 Computed and experimental results of ionizing shock in Krypton for case 2: $p_\infty = 5.07$ Torr, $T_\infty = 295.4$ K, $Ma = 15.17$. The values of the electron number density and the total mass density are normalized by the equilibrium values: $n_e^* = 1.712 \times 10^{17}$ cm^{-3}, $\rho^* = 1.708 \times 10^{-4}$ g/cm^3. Symbols represent experimental data for n_e and ρ from Glass *et al.* [111]. 113

4.18 Electron number density and heavy particle number density for $M_\infty = 13.1$ Xe shock. Symbols represent experimental data for n_e and n_h from Ezumi *et al.* [112]. The freestream conditions are: $p_\infty = 2.00$ Torr, $T_\infty = 300$ K. 114

4.19 Total mass density of ionizing shock in Argon for case 1 of table 4.13. Different lines correspond to the solutions at the different times, and the arrow indicates flow solutions as time increases. The symbols are the experimental data from the UTIAS experiment [110].117

4.20 Electron number density of ionizing shock in Argon for case 1 of table 4.13. Different lines correspond to the solutions at different times. The symbols are the experimental data from the UTIAS experiment [110]. 118

5.1 Time evolution of the electron number density using different total number of atomic levels. The electron temperature is set at 3.0 eV. 129

5.2 Comparison of the time evolution of the excited states during the isothermal heating test case ($T_e = 3$ eV). From top to bottom: (a) full solution with 20 levels; (b) solution with 5 levels and 2 Uniform groups; (c) solution with 5 levels and 2 Boltzmann groups. The first excited state - H(2) - is the top curve, followed by the next higher level, etc. 141

5.3 Comparison between the solution obtained using both level grouping approaches. The solid line represents the full solution. 142

5.4 The internal states population during the heating process at various times. The solid symbols are the full solution; the solid lines are the level grouping with Boltzmann distribution; the doted lines are for level grouping with uniform distribution; dashed lines are for a simplified model with $T_b \equiv T_e$. 143

5.5 Boltzmann temperature of the upper states 143

5.6 Radiative loss due to bound-bound radiation from the upper states to the first 3 atomic states. The lines indicate the solution obtained from the full CR kinetics. The dots represent solution obtained with level grouping (5 levels + 1 group). 145

5.7 Comparison of the time evolution of the ground state and the free electrons during the isothermal cooling process (3 eV $\rightarrow$ 1 eV) using level grouping with Uniform and Boltzmann distribution (3 levels + 1 group). 147

5.8 Comparison of the time evolution of the excited states during the isothermal cooling test case (T_e = 1 eV). From top to bottom: (a) full solution with 20 levels; (b) solution with 3 levels and 1 Uniform group; (c) solution with 3 levels and 1 Boltzmann group. H(3) - is the bottom curve, followed by the next higher level, etc.; the non-conforming red curve is H(2). 148

5.9 Comparison of the time evolution of the excited states number densities during the isothermal cooling process (3 levels + 1 B group). 150

5.10 Snapshots of the ASDF at several times during the cooling process. The dots represent the full solution. The solid lines are the solution obtained using the level grouping with Boltzmann distribution. The broken lines are the solution obtained using the level grouping with uniform distribution. 151

5.11 N_e, T_e evolution in constant-volume case. 154

5.12 Cumulative and instantaneous relative errors in energy conservation - test case 3. 155

5.13 Cumulative and instantaneous relative errors in energy conservation - test case 3 - with revised formulation 161

5.14 Cumulative relative errors in energy conservation as function of group sizes; revised formulation. 161

6.1 Frame rotation and relative orientation of (a) $\mathbf{w}$ and $\mathbf{g}$ and (b) $\mathbf{g}$ and $\mathbf{g}'$. The rotation operator matrix $R(\varphi, \theta)$ (or $R(\rho, \chi)$) is defined such that $\hat{\mathbf{g}} = R(\varphi, \theta) \cdot \hat{\mathbf{w}}$ and $\hat{\mathbf{g}}' = R(\rho, \chi) \cdot \hat{\mathbf{g}}$. 167

7.1 Coordinate system of a one dimensional electromagnetic wave propagation where x is the direction of propagation: $\mathbf{E} = E(x)\hat{\mathbf{e}}_y$, $\mathbf{B} = B(x)\hat{\mathbf{e}}_z$, and $\mathbf{k} = k\hat{\mathbf{e}}_x$. 182

7.2 Solution of the electric field for a linear density profile (shown by the black dotted line) computed using both TMM and FD methods. The solid black line is the exact solution given by the Airy function. The length is normalized by the laser wavelength 196

7.3 Ponderomotive force for a linear density profile. The numerical solution is obtained using the electric field computed in figure 7.2. The solution of Lindl and Kaw [136] is reproduced by omitting the term containing the magnetic field in the expression of the Maxwell stress tensor. The broken line is the solution obtained from the WKB approximation, i.e., equation (7.44). 197

7.4 Spatial profile of the electromagnetic wave intensity as it propagates into the plasma. The wave energy is completely absorbed near the critical surface. 198

7.5 Gaussian laser pulse with a maximum intensity of $10^{16}\ W/cm^2$ . . 200

7.6 Ion number density (solid line) and the ponderomotive potential (dashed line) at four different times during the laser pulse. The ponderomotive potential is defined as $\epsilon_0(E^2 + c^2B^2)$. The ion number density is normalized by the laser critical number density, and the potential is normalized by its value at the vacuum region. . . 202

7.7 Electrostatic field generated in the plasmas due to charge separation. 203

7.8 Ion velocity at various times after the laser pulse initiation. 204

7.9 Ion number density at (a) 20 ps, (b) 50 ps, and (c) 90 ps for both cases of negatively chirped and unchirped laser pulse. For the negatively chirped laser, the frequency is linearly decreased 25 % over the entire pulse duration. 205

7.10 Comparison of the ponderomotive pontential for (a) negatively chirped and (b) unchirped laser. The ponderomotive potential is defined as $\epsilon_0(E^2 + c^2B^2)$. The values of the potential are normalized by its value in the vacuum region. 207

List of Tables

4.1 Rate coefficients for collisional-radiative model 80

4.2 Lowest 31 levels of Ar I by energy. 88

4.3 Atom impact excitation parameters for allowed transitions for Argon. χ^*_{nm} for allowed transitions from ground state of neutral Ar has been tuned to match the experimental induction length. . . . 89

4.4 Electron-impact ionization parameters as taken from [103]. 90

4.5 Radii of Ar valence electron and reduced weighting factors for $\xi = 1$ as taken from [103]. 91

4.6 Summary of the elementary cross sections used in the CR model for Argon 93

4.7 Lowest 31 levels of Kr I by energy. 94

4.8 Atom impact excitation parameters for allowed transitions for Krypton. 95

4.9 Summary of the elementary cross sections used in the CR model for Krypton 97

4.10 Lowest 31 levels of Xe I by energy 99

4.11 Atom impact excitation parameters for allowed transitions for Xenon. 100

4.12 Summary of the elementary cross sections used in the CR model for Xenon 102

4.13 Summary of test conditions of the UTIAS experiments for ionizing shock in Argon with the predicted thermal equilibrium flow properties. Data are taken from Glass and Liu [110]. 103

4.14 Summary of test conditions of the UTIAS experiments for ionizing shocks in Krypton with the predicted thermal equilibrium flow properties. Data are taken from Glass *et al.* [111]. 110

5.1 Summary of level-grouping models investigated. 138

5.2 Initial conditions of test cases. For all cases, the total atomic density N_H is 10^{21} m^{-3}. 139

5.3 Relative error on electron density at peak rate of growth (approx. 33 μsec). 140

Nomenclature

Roman Characters

$\mathbf{B}$	magnetic field
$\mathbf{E}$	electric field
E_s	total energy (thermal + kinetic)
f_s	distribution function
I	radiative intensity
$\mathbf{j}_s$	charge current density
k	Boltzmann constant
Kn	Knudsen number
Ma	Mach number
n_s, N_s	number density
p_s	thermodynamic pressure
$\mathbb{P}$	pressure tensor
$\mathbf{q}_e$	electron heat flux
q_s	electric charge of specie s
$\mathbf{S}$	Poynting vector
$\mathbb{T}$	electromagnetic pressure tensor
$\mathbf{u}_s$	hydrodynamic velocity
v_{Ts}	thermal velocity

Z_s charge number of specie s

$\mathcal{Z}$ partition function

Greek Characters

$\overline{\sigma}$ electric conductivity

β_e Hall parameter

ϵ_0 permittivity of free space

η refractive index

κ_e electron thermal heat conductivity

μ_0 permeability of free space

ν_{st}^{ε} thermal relaxation frequency between s and t

ν_{st} collisional frequency between s and t

ρ_s mass density

ε_s thermal energy

Acronyms

ASDF atomic state distribution function.

CFD computational fluid dynamics.

CFL Courant-Friedrichs-Lewy.

COM center of mass.

CPA chirped pulse amplification.

CR collisional-radiative.

DB detailed balance.

DM Deutsch-Märk.

DNS direct numerical solution.

EEDF electron energy distribution function.

ENO essentially non-oscillatory.

FRC field-reversed configuration.

HLLE Harten, Lax, vanLeer and Einfeldt.

ISP specific impulse.

LHS left hand side.

LPI laser-plasma interaction.

LPP laser produced plasmas.

MHD magnetohydrodynamic.

MP monotonicity-preserving.

MR microscopic reversibility.

ODEs ordinary differential equations.

PAC plasma assisted combustion.

PAI plasma assisted ignition.

PDEs partial differential equations.

PDRE pulse detonation rocket engines.

PDRIME pulse detonation rocket-induced magnetohydrodynamic ejectors.

PIC particle-in-cell.

RHS right hand side.

RK Runge-Kutta.

SH Spitzer-Harm.

TVD total variation diminishing.

UTIAS University of Toronto's Institute of Aerospace Studies.

VDF velocity distribution function.

WENO weighted essentially non-oscillatory.

Acknowledgments

This dissertation would have not been possible without the continuous support and encouragement from many individuals. I would like to thank my advisor, Prof. Ann Karagozian, for her guidance, support, and inspiration throughout my graduate study. I am grateful for her flexibility in allowing me to tackle many problems of interests. She has always been responsive when I have questions. Her encouragement and great insights to the academia has helped guide me towards a career in teaching and research.

I am very fortunate to have met and worked with my AFRL mentor, Dr. Jean-Luc Cambier. I thank him for being very patient with me from the beginning, answering my never-ending questions, giving me countless opportunities to excel in my research, and sharing his knowledge in a wide range of topics. His passion for science has influenced me positively, and shaped me into who I am today. His attention to detail has had a significant impact on the quality of my research.

I would also like to acknowledge other members of my committee, who have contributed in one way or another to my research. In particular, I thank Prof. Morales for offering a solid foundation in plasma physics, Prof. Zhong for fundamental courses in gas dynamics and CFD, Prof. Smith for sharing his elegant course notes in chemical kinetics, and Prof. Caflisch for many positive comments about my research. I would also like to acknowledge Prof. Periklis Papadopoulos from SJSU for inspiring me to pursue graduate study, and giving me advices on choosing the topic of my research.

During the course of my graduate study, I have been privileged to work with an excellent team of researchers from AFRL. I thank Dr. Michael Kapper for his brief but valuable assistance in the start. His initial work on collisional-radiative cross section database has allowed me to immediately be proficient in doing CR modeling. I also thank Dr. Lord Cole for sharing his passion in coding and CFD.

Dr. David Bilyeu is gratefully acknowledged for scaring me away from the CESE method, hence keeping my focus on finite-volume method. I would also like to thank Drs. Rob Martin and Carl Lederman for many stimulating discussions on physics and math, and Dr. Justin Koo for making my time in the desert and at the lab much easier and enjoyable. Despite being the only one in the group without a PhD (according to Dr. Bilyeu's record as of June 2014), I am glad that I still have much fun working with all of you.

I would also like to thank various friends and classmates at UCLA: Ali, Ayaboe, Clifton, Dung, Giang, Kyle, Lauren, Levon, Patrick, San and many more. Thank you all for the fun times during group study, conferences, and get-together after school. A large portion of my weekends in the bay area was filled with joy in the company of friends: Chau, Dante, Freddy, Luong, Oanh and many others. I am grateful for the support and love of my companion and best friend, Diem. Thank you for being understanding and putting up with me through my bad times.

My accomplishment today would not have been successful without the support of my family. I thank my stepfather, Chuong Nguyen, for always being there when I needed. Most importantly, I thank my mother, Mai Hoang, for her sacrifice throughout the years to get me to where I am today. Her love is the main driver to get me through difficult times, and her support is the key foundation for my accomplishment.

This research was supported by the Air Force Office of Scientific Research (AFOSR) laboratory task 12RZ06COR (PM: Dr. Fariba Fahroo), ERC, Inc. under subcontracts RS111738 and RS131109, and the UCLA MAE Department graduate fellowship program.

Vita

2009	B.S. (Aerospace Engineering) San José State University, San José, CA
2009–2010	Research Assistant, ELORET Corp. NASA Ames Research Center, Moffett Field, CA
2011	M.S. (Aerospace Engineering) San José State University, San José, CA
2012	M.S. (Mechanical Engineering) University of California, Los Angeles, CA
2010–Present	Research Engineer, ERC Inc. Air Force Research Laboratory, Edwards AFB, CA

Publications

H.P. Le, A. Karagozian, J.-L. Cambier, Complexity Reduction of Collisional-Radiative Kinetics for Atomic Plasma, *Phys. Plasmas* 20, 123304 (2013).

H.P. Le, J.-L. Cambier, L. Cole, GPU-based Flow Simulation with Detailed Chemical Kinetics, *Computer Physics Communication* 184, 596-606 (2013).

H.P. Le, J.-L. Cambier. Development of a Flow Solver with Complex Kinetics on the Graphic Processing Units. AIAA paper 2012-721, 2012.

B. Cruden, **H.P. Le**, R. Martinez. Electron Density Measurement in Re-Entry Shocks for Lunar Return. AIAA paper 2011-3628, 2011.

B. Cruden, D. Prabhu, R. Martinez, **H.P. Le**, D. Bose, J. Grinstead. Absolute

Radiation Measurement in Venus and Mars Entry Conditions. AIAA paper 2010-4508, 2010.

CHAPTER 1

Introduction

1.1 Background

Plasma science is a multidisciplinary topic, with a wide spectrum of applications such as thermonuclear fusion [1], astrophysical plasmas [2], solar physics [3], electric propulsion thrusters [4], material processing [5], and many others. High temperature and collisionless plasmas have been studied extensively by Vlasov theory [6, 7]; these studies laid a foundation on the understanding of linear and quasi-linear phenomena occurred in a plasma, e.g., Landau damping, plasma instabilities, and collisonless shock [8, 9]. These phenomena are pertinent to the study of plasma waves in fusion devices or astrophysical phenomena, e.g., supernova, active galactic nucleus jets, etc.

Low temperature and partially ionized plasmas, on the other hand, have tremendous technological applications in manufacturing and material processing, miniaturized ion propulsion device [4], novel combustion devices [10], and re-entry physics [11]. These plasmas often exhibit strong deviation from thermal and chemical equilibrium, thus collisional and radiative kinetics play an important role in characterizing their dynamic behavior. For example, the interaction of the plasma with the radiation field is directly applicable to predicting and analysing thrusters' plume signature, radiative heat in hypersonic shock layer, and X-ray generation in laser-plasma interaction (LPI).

The challenges in exploring non-linear phenomena and the transport of par-

ticles and energy still remain, both of which would require theoretical, computational and experimental efforts. In the non-linear regime, one has to solve the full set of governing equations; this task is quite challenging, and can only be done by numerical calculations. Even so, the numerical methods themselves have limitations[1], and often cannot be used in a general scenario. In such cases, theoretical knowledge is required to give insights to the design of the numerical methods, and experimental verification (or code validation) is very essential to completely understand the physics of the problem. The abundance and complexity of plasma science can be seen in three representative technical application areas: plasma-assisted combustion, re-entry physics, and laser-plasma interactions.

1.1.1 Plasma-assisted combustion

Plasmas have long been of interest as a propellant candidate for spacecraft due to the ability to generate very high exhaust velocities, and thus very high specific impulse (ISP) as a consequence of electromagnetic and/or electrostatic acceleration [4]. Besides electric propulsion, plasma physics also finds use in chemical propulsion applications due to the unique advantage coming from the participation of the plasma species in the combustion processes and their interactions with the electromagnetic field. The existence of a plasma inside a combustion chamber can potentially be utilized for different purposes, whether to enhance the reaction kinetics or to be used for flow control [12, 13].

Recently, the concepts of plasma assisted combustion (PAC) and plasma assisted ignition (PAI) have drawn a lot of attention due to their potential for improving ignition reliability, enhancing flame stabilization and reducing pollutant emission [14, 15, 13]. These concepts have been proposed in a variety of combus-

[1]This comes from both from a numerical and physical points of view. The numerical limitation lies in the deterministic or stochastic nature of the methods when dealing with high dimensional problems. The physical limitation simply comes from the fact that it is impossible to include physics at all scales so one must be aware of which physics can be included and/or missing from the model.

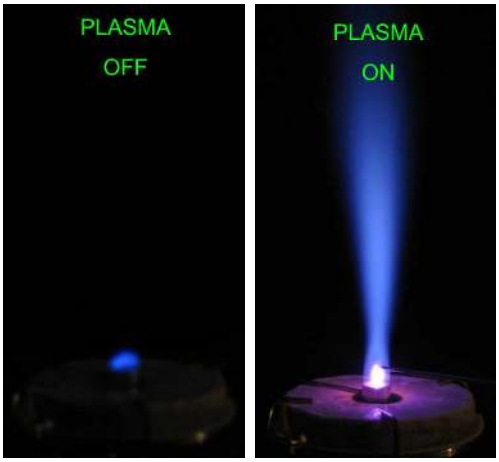

Figure 1.1: Flame stabilization by plasma enhancement [15].

tion devices including scramjets and gas turbine engines [16, 17]. The plasma, typically created by electric discharges, can deposit heat locally in the vicinity the flame, which quickly raises the gas temperature, and creates reactive radicals and excited species, which initiate chain reactions, therefore stabilizing the flame. Figure 1.1 illustrates the flame stabilization effects that can be seen by application of a nanosecond repetitively pulsed plasma [15].

Several concepts of propulsion systems have been proposed to take advantage of magnetohydrodynamic (MHD) phenomena. One example is the pulse detonation rocket-induced magnetohydrodynamic ejectors (PDRIME) concept, proposed by Cambier [18], from which MHD power is extracted from the unsteady nozzle flows within a pulse detonation rocket engines (PDRE) and applied in a bypass air stream to provide additional thrust. The schematic concept of PDRIME is illustrated in figure 1.2 showing the flow patterns for different stages of the cycle. Numerical simulations of the PDRIME, as well as other MHD-based cycle modification, were carried out by Zeineh *et al.* [19] showing potential increases in performance for many operating conditions. Technical challenges associated with the requirement for PDRIME operation were also revealed, which suggests further analysis and optimization study. The numerical simulations have proven

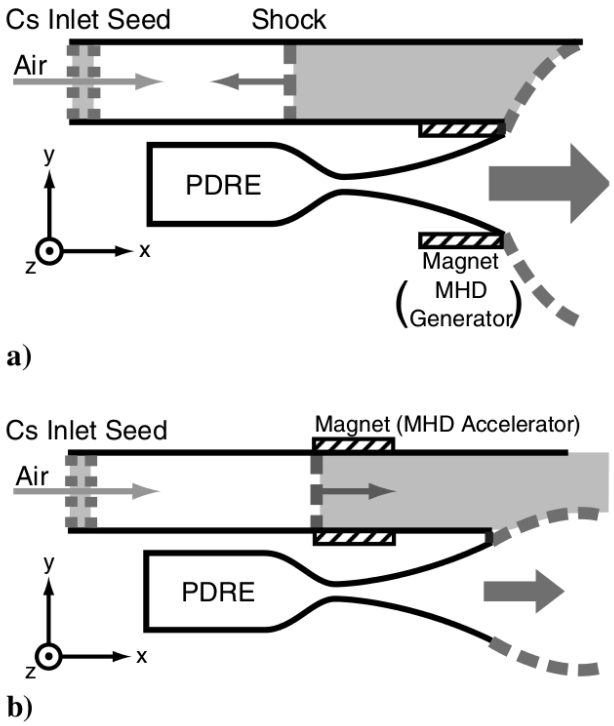

Figure 1.2: PDRIME concept: a) Overpressure at the nozzle exit launch a shock to enter the bypass tube, which slows and raises the temperature of the air stream inside the tube. Energy is extract from the flow (MHD power generation). b) During the blowdown, the nozzle pressure drops, and power is applied to accelerate compressed air in the bypass channel (MHD acceleration). [18, 19]

to be very useful in the preliminary evaluation of the PDRIME concept and its variants.

1.1.2 Re-entry physics

Re-entry plasmas are typically created due to a strong bow shock that forms in front of a vehicle such as the space shuttle when it enters the atmosphere. As the air passes through the shock, the kinetic energy is quickly converted to thermal energy, which for high re-entry Mach number, is sufficient to ionize the gas. Nonequilibrium phenomena such as chemical reactions and energy relaxation

processes are particularly relevant and extremely important (see figure 1.3), owing to the fact that the success of the flight mission depends on how accurately the flow field can be predicted in order to design adequate thermal protection system [20].

In high speed re-entry conditions, the convective time scales of the fluid can be of the same order of magnitude as the chemical and energy relaxation time scales. The processes of translational, rotational and vibrational relaxation as well as ionization of the gas thus must be taken into account for an accurate prediction of the flow field [21, 11]. In addition, at very high velocity and low density regime, the radiation from the gas becomes significant and can in turn interact with the plasma; one must then take in account radiation transport and kinetic processes involving the radiation field such as photo-excitation and photo-ionization must be included[2]. In that case, the problem quickly becomes intractable and one must rely mostly on empirical flight data or simplified models. These simplified models are sometimes questionable and can not be used in a wide range of conditions.

In the past decade, experimental data from ground facilities for radiative heat spectra relevant to re-entry conditions for different atmospheric gas composition have become available, providing a useful set of validation data for physical models and chemical reaction rates used in current state-of-the-art computational fluid dynamics (CFD) tools [22, 23, 24, 25, 26]. These data have motivated a number of studies using high-fidelity collisional-radiative (CR) models [27, 28, 29] to benchmark against experimental data, e.g., radiative spectrum of shock-heated gas. The results from these studies are mixed: good agreement is obtained in some regions of the spectrum but poor agreement is reported in other regions. Moreover, the experimental spectrum also reveals additional features, e.g., contaminated species,

[2]In that case, one must solve the radiation transport equation in addition to the fluid equations. The radiation transport is a challenging problem in itself due to the hyper-dimensionality aspect of the governing equation. Typically, radiation transport is decoupled from the flow field and only used as a post-processing step [21]. In simple flow geometry, one can rely on approximation such as the tangent slab method to reduce the dimensionality of the problem.

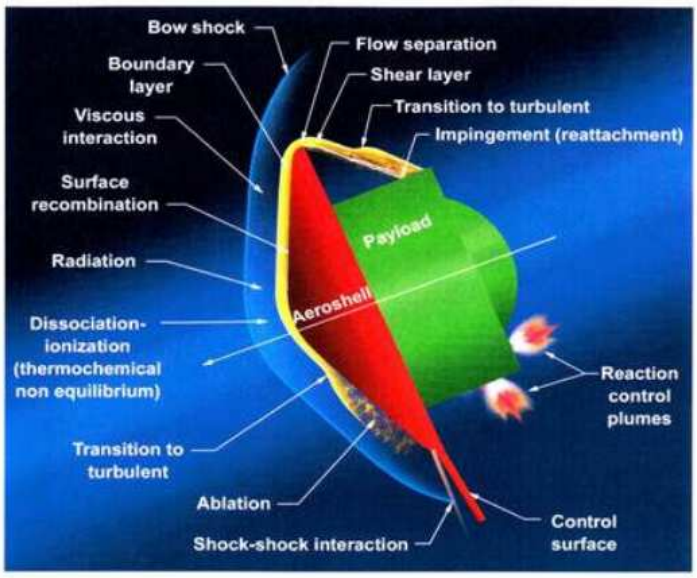

Figure 1.3: Physical phenomena occurred during planetary entry (courtesy of NASA).

continuum radiation, and high-lying transitions, all of which appear to be missing or inadequately understood from the numerical model. There are several reasons for the discrepancies: incomplete thermochemical rates, unsteady phenomena, and possibly experimental artifact. These problems are current being tackled with a better *ab inito* chemical database [30, 31], improved high-order and more efficient transport schemes[32, 33, 34, 35], as well as mechanism reduction [36, 37] for unsteady and multidimensional simulations.

1.1.3 Laser-plasma interactions

Lasers, among the greatest inventions of mankind, are devices which can produce electromagnetic radiation at a range of wavelengths at very high intensity. Due to their ability to deliver a large amount of energy at short duration, lasers have been used widely in a wide numbers of applications [38]. As a consequence, the physics of LPI has quickly become one of the fastest growing fields of research.

LPI has direct applications in inertial confinement fusion, particle accelerators, and medical imaging [39].

The physics of LPI can be quite complex, depending on both the laser configuration and the plasma condition. For example, while long-pulse lasers (nanosecond) have long been used for target heating in inertial fusion [40], ultra-short-pulse lasers (femtosecond), following the invention of chirped pulse amplification (CPA) in 1985, created an immense range of exotic phenomena (some of which are still not well understood), including particle acceleration, x-rays generation, and atomic physics [41]. Furthermore, while the interaction of a laser with an under-dense plasma results in different types of instabilities and particle acceleration, its interaction with an over-dense plasma can be utilized to create soft and hard x-rays (see figure 1.4 for an illustration).

It is worthwhile to highlight several aspects of the fundamental plasma physics, which contribute to the understanding of LPI. Firstly, the propagation of electromagnetic wave propagation in plasma directly relates to various instabilities as well as absorption mechanisms occurring in the corona layer of laser produced plasmas (LPP). Secondly, the self-consistent coupling of the plasma with the field gives rise to particle acceleration; this is a direct result of the Coulomb force from the electrostatic field induced in the plasma. Lastly, X-ray generation can be explained by collisions induced by the superthermal electrons generated in short-pulse LPI.

In the three research areas described above, several key processes can be identified to better model the plasma therein. The first one is based on a complete understanding of the CR processes and their coupling with the flow dynamics. The challenges associated with these studies are twofold. In the case of PAC, the combustion kinetics itself is a very complicated process, which comprises very detailed reaction mechanisms. Moreover, the existence of a plasma in a flame results in the generation of highly energetic excited species and reaction radicals;

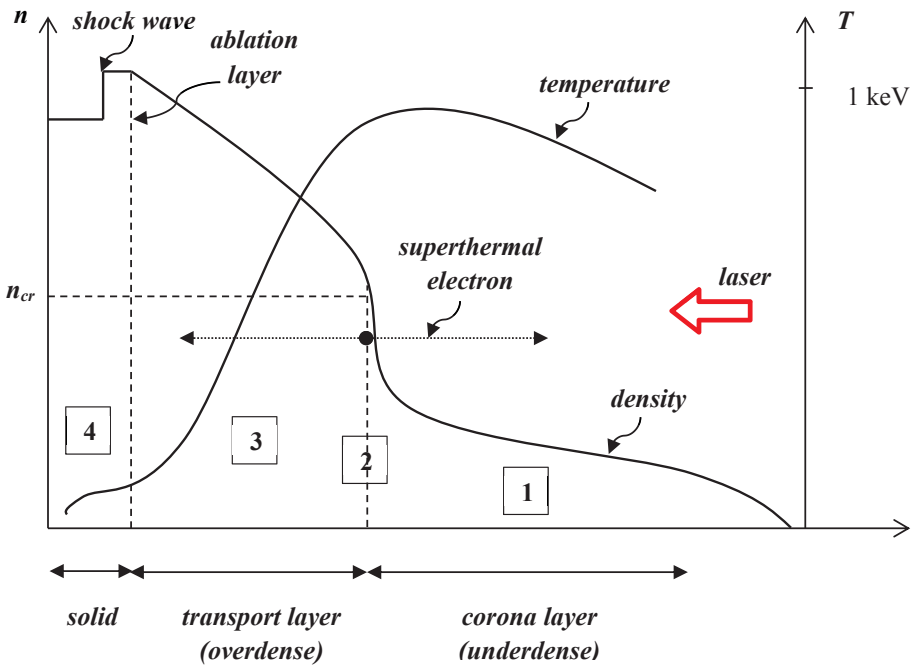

Figure 1.4: Physical processes in typical laser-plasma interaction: (1) collisional absorption, instabilities, magnetic field generation; (2) resonance absorption, profile steepening, hot electrons generation; (3) heat transport, soft x-rays generation; (4) hard x-rays generation. Figure adapted from [38].

these processes add more complexity to the overall kinetics of the system. In addition, the effects of species and thermal transport from both convection and diffusion processes, also introduce more couplings to the system. These effects are also relevant for applications in re-entry physics. Therefore, in order to accurately model such a complex system, one needs to understand different aspects of the plasmadynamics, the plasma chemical kinetics, and, more importantly, the coupling of the two.

On the other hand, typical plasma conditions found in LPI exhibit a high degree of translational non-equilibrium and charge separation between different species. These effects are most severe for ultra high intensity laser since relativistic electrons can be generated, which significantly alters the dynamics of the system. Moreover, the plasma evolution in these applications might span several physical regimes, from which multi-scale phenomena quickly arise. One must then be able to obtain a multi-scale description of the plasma; from a numerical modeling point of view, this is most computationally efficient with a hybrid model, i.e., combination of different numerical models at different regimes of interests. Some of these issues are addressed in this dissertation, specifically on the modeling of CR processes and non-equilibrium plasmas.

1.2 Overview of plasma physics

1.2.1 Plasma kinetic equations

Plasma flow can be modelled accurately at the microscopic level by the kinetic equation, which describes the evolution of the plasma *distribution function* in phase-space and Maxwell's equations, which describe the evolution of the electromagnetic field. In the simplest case of a single plasma component, the kinetic

equation for the distribution function takes the form:

$$\frac{\partial f}{\partial t} + \mathbf{v} \cdot \nabla_{\mathbf{x}} f + \mathbf{a} \cdot \nabla_{\mathbf{v}} f = \left(\frac{\partial f}{\partial t} \right)_{\mathrm{CR}} \tag{1.1}$$

where $f \equiv f(\mathbf{x}, \mathbf{v}, t)$ is the distribution function in phase-space, and $\mathbf{a}$ is the acceleration due to external force.

The terms on the left hand side (LHS) of the kinetic equation is denoted the streaming operator, and the term on the right hand side (RHS) is the collision operator responsible for all the exchange processes, including elastic (Coulomb) and inelastic collisions (i.e., CR kinetics). Without the RHS, equation (1.1) represent an advection equation in six-dimension so-called Vlasov equation. While the advection in configuration space is linear in nature, the advection in velocity space, as in the case of a plasma, can be non-linear due to the acceleration term $\mathbf{a}$. In the case of a plasma, $\mathbf{a}$ represents the coupling terms between the plasma and the electromagnetic field, i.e., via the Coulomb and Lorentz forces $\mathbf{a} = \frac{q}{m} (\mathbf{E} + \mathbf{v} \times \mathbf{B})$. The electromagnetic field is governed by Maxwell's equations:

$$\nabla \times \mathbf{B} = \mu_0 \mathbf{j} + \mu_0 \epsilon_0 \frac{\partial \mathbf{E}}{\partial t} \tag{1.2}$$

$$\nabla \times \mathbf{E} = \frac{\partial \mathbf{B}}{\partial t} \tag{1.3}$$

$$\nabla \cdot \mathbf{E} = \frac{\rho_q}{\epsilon_0} \tag{1.4}$$

$$\nabla \cdot \mathbf{B} = 0 \tag{1.5}$$

The non-linearity in the acceleration comes from the fact that an electric field can be induced from the plasma current, as can be seen in equation (1.2), and this field in turn acts on the plasma. Indeed, this closed loop system with constant feedback is the essential ingredient for particle-wave coupling, which in many cases results in instabilities or damping mechanisms [6].

The RHS of the kinetic equation (1.1) is quite complex, since it comprises of all the exchange processes due to collisional and radiative interactions. It is

well known that Coulomb collisions are generally the most important process in plasma; however, when the plasma is partially ionized or the energy transfer between the components is large enough to activate the large number of atomic transitions, inelastic collisions become significant and must be included. For example, inelastic collisions play an important role in the formation of field-reversed configuration (FRC) plasma [42], and internal energy excitation process in hypersonic shock layer.

One can see from equation (1.1) that a direct numerical solution (DNS) of the kinetic equation in 6-dimensional space with a complete detailed model of all the exchange processes is unrealistic and would require enormous computational resources. In addition, the plasma's chemical composition can add complexity to the system due to non-equilibrium effects between the components. In such cases, one needs to model each component separately (i.e., having one kinetic equation for each component).

Besides having to deal with the *curse of dimensionality* when directly solving the kinetic equation, the time scales associated with each component might be orders of magnitude different from the others, making the system extremely stiff. For example, electrons are much lighter than the heavy particles and therefore their transport occurs at a much shorter characteristic time scales. The interaction of the electrons with other species also gives rise to both the elastic and inelastic exchange processes, e.g., electron-impact excitation and ionization. The numerical solution of CR kinetics presents a huge challenge for traditional multi-scale methods due to the non-separation of time scales characteristics of the master equations; some of the issues and novel techniques devised to deal with these problems will be shown in this dissertation for the case of CR kinetics.

1.2.2 Modeling and simulations

Various methods had been derived in order to solve the kinetic equations, whether in simplified or the original form. The choice of the methods depends on the plasma collisionality and the ratios of length and time scales. These methods can be categorized as two main group of approaches: fluid based methods and kinetic methods.

The plasma fluid equations can be derived by taking a finite number of moments of the kinetic equation[43], and therefore obtaining a set of conservation laws for these moment variables. The most common model is the five-moment model, which results in the classical hydrodynamic equations, e.g., the Euler or Navier-Stokes equations. The fundamental issue with the moment approach is the closure problem, that is, each moment equation is always coupled to the next higher order moment variable, and the system cannot be completely closed without knowing the form of the distribution function. For example, in the energy equation, the coupling effect introduces the heat flux term, which is a high-order term; this term cannot be determined without the distribution function.

Two limiting cases can be identified where the fluid equations are valid. Theses are referred to as the *isothermal* and *inertial* (or *adiabatic*) regime. These regimes can be defined by comparing the characteristic velocity v_{char} to the thermal velocity of the plasma $v_T = \sqrt{\frac{kT}{m}}$. In the isothermal regime ($v_{\text{char}} << v_T$), the heat flux term in the energy equation dominates the inertial and collision terms, and temperature becomes spatially uniform. In the inertial regime ($v_{\text{char}} >> v_T$), the heat flux terms can be neglected and the system can be closed at the energy equation.

Besides the two limiting cases where the fluid equations can be closed exactly, one can also perform an asymptotic expansion of the distribution function with a small parameter, i.e., $f = f^{(0)} + \epsilon f^{(1)} + \epsilon^2 f^{(2)} + \ldots$, and deriving the fluid

equations by keeping only low-order terms of the distribution function. The most well-known closure scheme is the Chapman-Enskog method [44], first introduced for neutral gases, in which the distribution function is expanded with the small parameter being the ratio of the mean-free-path between collisions to the macroscopic length-scale so-called Knudsen number ($\epsilon = Kn$). Therefore, the scheme is only valid when the plasma is dominated by collisions (i.e., very similar to neutral gas), making the distribution function very close to a Maxwellian distribution function. For zeroth and first order Chapman-Enskog expansion, the resultant set of fluid equations are the Euler and Navier-Stokes equations. For second order expansion, the resultant system is the Burnett equations [45]. In 1965, Braginskii [46] derived the plasma fluid equations for electrons and ions with the Chapman-Enskog closure, the result of which, led to the well-known Braginskii equations for a two-fluid fully ionized plasma.

Another classical closure scheme is Grad's moment method [47]. Grad's method originally attempted to extend the validity of the fluid equations into the rarefied regime by conserving higher order moments (e.g., individual component of the full stress tensor) of the distribution function. Grad's closure is done based on the Hilbert expansion of the distribution function in Hermite polynomials. The resultant systems from this family of closure are the Grad 13-moment and 26-moment equations. One of the challenges associated with Grad's type equations is the lack of physical intuition of the moment variables, which imposes difficulties on boundary conditions.

Since moment equations can always be represented as a set of conservation laws, they can be solved by various efficient finite difference, finite volume, or finite element methods. In both closure approaches described above, the complication of modeling the exchange processes still remains, some of which are present in the current research, but the computational resource required for solving these equations are much more affordable. For example, in chemically reacting flow, the

exchange source terms (mass production/consumption) are often computed from a zeroth-order (Maxwellian) distribution, which is inconsistent with the Chapman-Enskog closure. A rigorous treatment of the exchange terms requires including high-order correction to the both chemical rates and the transport coefficient [48, 49].

The second approach, kinetic methods, aim at solving the distribution function f in equation (1.1) by means of either a deterministic or stochastic method. There have been various attempts in solving the kinetic equation directly in phase-space, but most of the simulations is only limited to 2D-2V (that is, two-dimensional in both physical and velocity space).

The most widely used plasma simulation method, introduced in the late 1950s, is the particle-in-cell (PIC) method [50], the most favorite choice for simulating collisionless plasma (i.e., solving the Vlasov equation). In PIC codes, the distribution function f is represented as a collection of pseudo-particles, i.e., the distribution function is discretized into Lagrangian points in phase-space. In that case, the distribution function is given by the superposition of these computational particles.

$$f(\mathbf{x}, \mathbf{v}, t) = \sum_p w_p \delta(\mathbf{v} - \mathbf{v}_p) S(\mathbf{x} - \mathbf{x}_p) \tag{1.6}$$

where w_p is the statistical weight[3] and $S(\mathbf{x} - \mathbf{x}_p)$ is the shape function of the computational particle p.

The evolution of the distribution function is modelled by solving the equations of motion for these particles under the influence of the electromagnetic fields. These equations can be derived by introducing the expression (1.6) into the kinetic equation, and then taking the moment of the kinetic equations. A complete derivation is given by Lapenta [51] and will not be repeated here.

Neglecting relativistic effects, the resultant equations of motion for these pseudo

[3]the number of real particle each pseudo particle represents.

particles read:

$$\frac{d\mathbf{x}_p}{dt} = \mathbf{v}_p \tag{1.7}$$

$$\frac{d\mathbf{v}_p}{dt} = \frac{q}{m}\left(\mathbf{E} + \mathbf{v}_p \times \mathbf{B}\right) \tag{1.8}$$

These are the characteristic equations of the Vlasov system. Furthermore, these equations are coupled with Maxwell's equations for the evaluation of the electric and magnetic fields. The advantage of PIC method is that instead of solving the distribution function, one only needs to keep track of these computational particles and the complete distribution function can always be reassembled. However, similar to other particle-based methods for neutral gas, the PIC method has difficulties modeling dense and highly collisional plasmas due to statistical noise.

1.3 Scope of present work

In the previous sections, multiple approaches in the numerical modeling of non-equilibrium plasma were described, which revealed significant challenges in constructing a unified model for non-equilibrium plasma simulation. These challenges are associated with the hyper-dimensionality aspect, and the complexity and abundance of the physical processes embedded in the collisional operators.

In the current research, special attention is paid to the dynamics of collisional and radiative interactions in a plasma, and more importantly, the coupling between collisions and transport. The current work focuses on studying this coupling in plasma regimes, for which the dimensionality of the problem can be reduced. In particular, the research presented here is restricted to the hydrodynamic framework. The validity and variation of these hydrodynamic models will be discussed, and a self-consistent treatment of CR kinetics will be presented.

To summarize, the overall objective of this dissertation is to construct hydrodynamic models for non-equilibrium plasma flows with self-consistent treatment of

the exchange terms due to CR kinetics, and present a numerical model for solving these coupled sets of equations. The dissertation can be divided into three parts. In the first part, different hydrodynamic models for plasma flows are presented with emphasis on clarifying the assumptions of each model and their relation to one another. The multi-fluid equations, which constitutes by far the most general treatment of plasmadynamics within the hydrodynamic framework, will also be introduced. The high-order numerical methods used to solve these equations are also presented.

In the second part, the description of the CR model is introduced. The coupling of CR kinetics with fluid equations will be detailed for the case of an atomic plasma. The constructed CR model will be used to study in detail the dynamic of excitation and ionization, as well as their coupling with convection. A novel technique is derived to lower the complexity of CR kinetics while maintaining high accuracy; this technique can help making multidimensional calculation with CR kinetics feasible. In the last part, a self-consistent treatment of elastic and inelastic collisions in multi-fluid equations will be presented. The multi-fluid model is then used to study laser-plasma interaction phenomena.

CHAPTER 2

Hydrodynamic Equations

2.1 Introduction

In this chapter, the hydrodynamic equations for plasma flow in thermal non-equilibrium conditions are presented. It is worthwhile to go over the fundamental assumptions which suggest to the domain of validity of these models. We emphasize that here, the fluid is assumed to be sufficiently collisional that the *continuum hypothesis*[1] is satisfied. In the picture of neutral gas flow, this is characterized by a single unit-less parameter known as the Knudsen number Kn, defined as the ratio of collision mean free path to the characteristic length scale. In the limit of $Kn \ll 1$, the flow is said to be strongly collisional such that the translational degrees of freedom are in equilibrium, that is, they can be represented by a classical Maxwellian distribution function. Small perturbations from Maxwellian equilibrium of order Kn can be incorporated into the kinetic equations, which result in various transport phenomena, commonly seen in the Navier-Stokes equations [52, 44, 53].

While justification of the continuum hypothesis is fairly straight-forward in neutral gas flow, the situation gets quite complicated in plasma flows, mainly due to the stiff time scales introduced by the electrons and the coupling of the plasma to electrodynamic forces, e.g., electron-ion collision time, plasma frequency, gyrofrequency, etc. The implied consequence is that the system's degree of stiffness

[1] This term is commonly used in fluid dynamics literature.

can no longer be characterized by a single parameter, and the hydrodynamic regime cannot be distinguished without further assumptions. Moreover, these fundamental time scales can also be evolved dynamically with the system, which allows the plasma to go from one regime to another. For examples, in ultra-high intensity LPI, while the plasma formation and interaction with a femtoseconnd laser pulse are commonly simulated with a kinetic code, the slower plasma expansion, on the other hand, can be simulated with a fluid code or a hybrid kinetic-fluid code. This dynamical stiffness creates significant challenges for numerical modeling and simulations.

It is therefore more convenient to define the assumptions of a particular hydrodynamic model in each section rather than listing all the assumptions at once. However, since we are working in the hydrodynamic framework, it is sufficient to say that at all time the velocity distribution function (VDF) of *each* plasma component can be characterized by a Maxwellian VDF. This is indeed a very crude approximation and needs further elaboration.

It must be assumed that the electromagnetic field is not strong enough to distort the distribution function. For the electrons, this assumption is quite hard to satisfy due to their high mobility. Fortunately enough, in a lot of cases, deviation from Maxwellian equilibrium can be localized in both physical and velocity space, that is to say, the electron VDF can be efficiently decomposed into an equilibrium and a non-equilibrium parts. This is typically done in laser fusion, where the electrons are divided into two populations: cold and hot (superthermal) electrons [40]. The "hot" electrons, typically represented by a fast tail in the VDF, can be extracted from a bulk Maxwellian VDF and treated using a kinetic method, while the "cold" population can be well characterized by a fluid approximation.

Therefore, the models presented in this work, despite being unable to capture kinetic effects, are still useful for a hybrid description of the plasma. It must be noted that, for a typical Chapman-Enskog expansion of the plasma VDF,

the electric and magnetic fields can affect the plasma transport properties, i.e., the transport coefficient is dependent of the field strength. These results can be found from classical transport theory, and will not be described here [46, 54, 55]. In this chapter, all the transport terms are omitted in the presentation of the fluid equations, except for electron heat conduction, since it is one of the main mechanisms for thermal transport in LPI applications [38]. This term is introduced in the multi-temperature model presented in section 2.4.

2.2 Multi-fluid equations

2.2.1 Euler-Maxwell and Euler-Poisson systems

Let us now consider the multi-fluid equation for a multicomponent plasma. The plasma described here can be partially ionized, so there is a neutral population among the charged species. In this section, s and t are defined to be a general species index, while n, i, and e are the used to refer to the neutral, ion, and electron populations, respectively, i.e., $s, t \in \{n, i, e\}$. For clarity in the presentation of the hydrodynamic framework, detailed treatment of the collision terms is omitted here, and their description is deferred for chapter 6. The elastic collision terms appearing in the momentum and energy equations are kept in general form. The inelastic terms are omitted in the current discussion.

The continuity equation for each plasma species follows conservation law:

$$\partial_t \rho_s + \nabla \cdot (\rho_s \mathbf{u}_s) = 0 \tag{2.1}$$

where the subscript s is used to distinguish between the given species properties from the total plasma properties. For example, $\mathbf{u}_s$ is the average velocity of the species s, which is different from the mass averaged velocity, denoted as $\overline{\mathbf{u}}$. In the absence of chemical reactions, the RHS of equation (2.1) is zero. Since each species can have its own hydrodynamic velocity, its momentum can be separately

conserved. The conservation equation of the momentum can be written as:

$$\partial_t \left(\rho_s \mathbf{u}_s\right) + \nabla \cdot \left(\rho_s \mathbf{u}_s \mathbf{u}_s\right) + \nabla p_s = n_s q_s \left(\mathbf{E} + \mathbf{u}_s \times \mathbf{B}\right) + \sum_t \mathbf{R}_{st} \tag{2.2}$$

The first term on the RHS of equation (2.2) represents the electrodynamic forces acting on the plasma. This term is zero for the neutral population ($q_n = 0$). The second term comprises of momentum exchange due to collision with other populations. For example, the conservation equation for the electron momentum includes two terms representing collisions with neutral and ion populations: $\mathbf{R}_{ei}$ and $\mathbf{R}_{en}$. In addition, momentum conservation implies:

$$\mathbf{R}_{st} + \mathbf{R}_{ts} = 0 \tag{2.3}$$

The conservation of thermal energy of each species can be written as:

$$\partial_t \varepsilon_s + \nabla \cdot \left(\varepsilon_s \mathbf{u}_s\right) + p_s \nabla \cdot \mathbf{u}_s = \sum_t Q_{st} \tag{2.4}$$

The RHS of equation (2.4) represents thermal relaxation effects due to elastic collisions (inelastic collisions are neglected here). Equation (2.4) can be combined with (2.2) to yield the conservation equation for the total energy of each species:

$$\partial_t E_s + \nabla \cdot \left[\left(E_s + p_s\right) \mathbf{u}_s\right] = \mathbf{j}_s \cdot \mathbf{E} + \sum_t \left(Q_{st} + \mathbf{R}_{st} \cdot \mathbf{u}_s\right) \tag{2.5}$$

where $E_s = \varepsilon_s + \frac{1}{2}\rho_s \mathbf{u}_s \cdot \mathbf{u}_s$. Similarly, conservation of energy implies the following relation to hold:

$$Q_{st} + \mathbf{R}_{st} \cdot \mathbf{u}_s + Q_{ts} + \mathbf{R}_{ts} \cdot \mathbf{u}_t = 0 \tag{2.6}$$

The fluid equations can be closed by specifying an equation of state, similar to that of an ideal gas:

$$p_s = n_s k T_s \tag{2.7}$$

where $n_s = \rho_s / m_s$. For an atomic plasma, the thermal energy is simply $\varepsilon_s = p_s/(\gamma_s - 1)$, where γ_s is the ratio of specific heat for the plasma.

The evolution of the electric and magnetic fields are governed by Maxwell's equations and will not be repeated here. In the case where the field is electrostatic, the electric field can be solved from Gauss's law, equation (1.4). It is more convenient to express the electric field in term of the electric potential, i.e., $\mathbf{E} = -\nabla\phi$, such that Gauss's law can be transformed to Poisson's equation:

$$\nabla^2\phi = \frac{e}{\epsilon_0}(n_e - Z_i n_i) \tag{2.8}$$

The Euler-Maxwell (or Euler-Poisson) system, equations (1.2)-(1.5) and (2.1)-(2.8) form a complete self-consistent model for a multicomponent plasma. These equations are referred to as comprising the multi-fluid plasma model.

2.2.2 Time and length scales of multi-fluid equations

Several fundamental time scales associated with the multi-fluid equations can be identified. These time scales are crucial in the design of the numerical methods for solving hyperbolic partial differential equations (PDEs) with source terms. Firstly, a thermal velocity for each species can be defined from the translational temperature, leading to a resultant time scale:

$$\tau_s = \frac{L}{v_{Ts}} \tag{2.9}$$

where v_{Ts} is the thermal speed of species s, i.e., $v_{Ts} = \sqrt{\frac{kT_s}{m_s}}$ and L is a characteristic length scale. The time scales associated with the electromagnetic forces are given in terms of the plasma frequency (inverse of time scale):

$$\omega_{ps} = \sqrt{\frac{n_s q_s^2}{\epsilon_0 m_s}} \tag{2.10}$$

and the gyrofrequency:

$$\omega_{cs} = \frac{q_s \left|\mathbf{B}\right|}{m_s} \tag{2.11}$$

In addition, when electromagnetic wave propagation must be considered, the light transit time becomes relevant:

$$\tau_c = \frac{L}{c} \tag{2.12}$$

where $c = 3 \times 10^8$ m/s is the speed of light. Lastly, the momentum and energy exchange processes between the species introduce relaxation time scales to the system. In a typical fully-ionized plasma, the scaling of these collisional frequencies is as follows [55]:

$$\nu_{ee} \sim T_e^{-3/2} \tag{2.13}$$

$$\nu_{ei} \sim Z_i \nu_{ee} \tag{2.14}$$

$$\nu_{ii} \sim Z_i^3 \sqrt{\frac{m_e}{m_i}} \nu_{ee} \tag{2.15}$$

$$\nu_{ei}^{\varepsilon} \sim Z_i \frac{m_e}{m_i} \nu_{ee} \tag{2.16}$$

where ν_{ei}^{ε} is the energy relaxation frequency between the ion and electron. This term scales as the mass ratio m_e/m_i and is much smaller compared to the momentum relaxation frequency ν_{ei}. In a typical plasma system, the electron plasma frequency ω_{pe} is the largest frequency in the system with the possible exception of low density and strongly magnetized plasma, where ω_{ce} can also become quite large.

Several length scales associated with the plasmadynamics characterized by the multi-fluid equations can be identified. The characteristic length scale corresponding to the plasma frequency is the Debye length, defined as follows:

$$\lambda_D = \sqrt{\frac{\epsilon_0 kT}{e^2 n_e}} \tag{2.17}$$

If the characteristic length scale of the system is much larger compared to the Debye length, the plasma can be approximated to be quasi-neutral. Similarly, the characteristic length scale corresponding to the gyro-motion of the particle due to

the magnetic field can be defined as:

$$r_{Ls} = \frac{v_{Ts}}{\omega_{cs}} \tag{2.18}$$

where r_{Ls} is known as the gyro-radius (or Larmor radius). If the plasma is collisional, one can also define a collision mean free path λ_s as follows:

$$\lambda_s = \frac{v_{Ts}}{\nu_s} \tag{2.19}$$

where ν_s is the collisional frequency of species s. Typically, it is more convenient to define the collision mean free path for each collision type, since the collision dynamics can be quite different from each other.

An important observation to be made about the multi-fluid equations, is that there is a large disparity in the time scales. The electrons, being very mobile and responsive to the electromagnetic fields, might be approximated in a quasi steady-state condition. Using this approximation, the electron momentum equation is reduced to the so-called generalized Ohm's law, which is derived in the next section.

2.2.3 Generalized Ohm's law

In order to simplify the derivation, let us consider for now a two-component fully ionized plasma consisting of ions and electrons with Coulomb interaction. The generalization to include an additional neutral population can be done, but with a more lengthy derivation since more collision terms need to be involved.

Starting from the electron momentum equation:

$$\partial_t \left(\rho_e \mathbf{u}_e\right) + \nabla \cdot \left(\rho_e \mathbf{u}_e \mathbf{u}_e\right) + \nabla p_e = -e n_e \left(\mathbf{E} + \mathbf{u}_e \times \mathbf{B}\right) + \mathbf{R}_{ei} \tag{2.20}$$

the so-called *massless electron* assumption is utilized, i.e., the two inertial terms on the LHS of equation (2.20) are negligible compared to the other terms. Note that the collision term $\mathbf{R}_{ei}$ can be expressed in terms of the collisional frequency,

i.e., $\mathbf{R}_{ei} = m_e n_e \nu_{ei}(\mathbf{u}_i - \mathbf{u}_e)$ [46]. Hence, equation (2.20) is reduced to:

$$\nabla p_e = -en_e\left(\mathbf{E} + \mathbf{u}_e \times \mathbf{B}\right) + m_e n_e \nu_{ei}(\mathbf{u}_i - \mathbf{u}_e) \tag{2.21}$$

In this case, the electron dynamics are given by a steady-state condition given by equation (2.21). In the limit of $m_e \to 0$, one also obtains:

$$\overline{\mathbf{u}} = \frac{\rho_i \mathbf{u}_i + \rho_e \mathbf{u}_e}{\rho_i + \rho_e} \simeq \mathbf{u}_i + o\left(\frac{m_e}{m_i}\right) \tag{2.22}$$

where $\overline{\mathbf{u}}$ is the mass averaged velocity of the plasma. From the definition of the total current density, one also obtains:

$$\mathbf{j} = Z_i e n_i \mathbf{u}_i - e n_e \mathbf{u}_e = e n_e(\overline{\mathbf{u}} - \mathbf{u}_e) + e(Z_i n_i - n_e)\overline{\mathbf{u}} \tag{2.23}$$

Let us now assume that the system is *close* to charge neutrality ($Z_i n_i - n_e \simeq 0$), such that the second term on the RHS of equation (2.23) is smaller compared to the first one, which leads to the following expression for the electron velocity:

$$\mathbf{u}_e \simeq \overline{\mathbf{u}} - \frac{\mathbf{j}}{e n_e} \tag{2.24}$$

Using expression (2.24), equation (2.21) can be brought into the form:

$$\mathbf{j} = \overline{\sigma}(\mathbf{E} + \overline{\mathbf{u}} \times \mathbf{B}) + \frac{\overline{\sigma}}{n_e e}\nabla p_e - \beta_e \mathbf{j} \times \hat{\mathbf{b}} \tag{2.25}$$

where

$$\overline{\sigma} = \frac{n_e e^2}{m_e \nu_{ei}} \tag{2.26}$$

$$\beta_e = \frac{\omega_{ce}}{\nu_{ei}} \tag{2.27}$$

$$\hat{\mathbf{b}} = \frac{\mathbf{B}}{|\mathbf{B}|} \tag{2.28}$$

Equation (2.25) is known as the generalized Ohm's Law. $\overline{\sigma}$ and β_e are the plasma conductivity and Hall parameter, respectively. The first term on the RHS of equation (2.25) is the conduction term, the second term is the electron diffusion, and the last term is the Hall term. Various MHD models can be derived starting from Ohm's law.

2.3 Magnetohydrodynamics

In this section, Ohm's law is utilized to derive the MHD equations. It is worthwhile to clarify that the MHD approximation corresponds to the assumption of a steady-state current given by Ohm's law, i.e., using equation (2.25) in place of the electron momentum equation. One can easily retain all the other equations in the multi-fluid systems and solve the system self-consistently. Those equations are commonly referred to as the multi-fluid MHD equations. In this study, the term multi-fluid is strictly reserved for the case where each plasma component including the electrons are conserved as a separate fluid, as previously shown in section 2.2.

Let us now look at the MHD equations in the single fluid limit, which implies that the momentum exchange is sufficiently fast such that one only needs to keep track of the total momentum of the bulk plasma[2]. This needs not be the case for the energy equation, since the energy transfer rate is rather slow, e.g., see equation (2.16); this suggests a multi-temperature approach, which will be described in the next section. For simplicity, consider Ohm's law in the following form:

$$\mathbf{j} = \overline{\sigma}(\mathbf{E} + \mathbf{u} \times \mathbf{B}) \tag{2.29}$$

where the electron diffusion and the Hall terms were neglected. Also for clarity, we drop the bar in the expression of the plasma average velocity, i.e., $\overline{\mathbf{u}} \rightarrow \mathbf{u}$.

The continuity equation for the plasma is in its typical form of conservation law:

$$\partial_t \rho + \nabla \cdot (\rho \mathbf{u}) = 0 \tag{2.30}$$

where the convective speed is now $\mathbf{u}$, and ρ is the plasma total density. If chemical reactions and transport phenomena between the species (such as diffusion) are

[2]This condition is required for the single fluid approximation, i.e., all species have the same averaged velocity. In general, one only needs $\rho_e \mathbf{u}_e \ll \rho_i \mathbf{u}_i$; if the plasma mixture contains several ion species with different averaged velocity, a multi-fluid MHD description can be used.

important, equation (2.30) is replaced by a set of conservation equations for each species, convected at the same velocity. The chemical reactions are represented by a source term for each species equation, representing the rate of consumption or formation of the species. The difference between each species velocity and the bulk is given by the given species diffusion velocity. For brevity, only the total plasma density here is considered. The extension to multi-species for a chemically reactive plasma is given in the next section.

The total plasma momentum equation can be written as:

$$\partial_t (\rho \mathbf{u}) + \nabla \cdot (\rho \mathbf{u}\mathbf{u}) + \nabla p = \epsilon_0 \mathbf{E} (\nabla \cdot \mathbf{E}) + \mathbf{j} \times \mathbf{B} \tag{2.31}$$

where all the quantities now denote the properties of the bulk plasma instead of individual species.

Let us now introduce two further approximations. The first approximation corresponds to *charge neutrality* condition[3], from which the first term on the RHS of (2.31) vanishes ($\nabla \cdot \mathbf{E} = 0$). This assumption is valid when the characteristic length of the domain is much larger than the Debye length, or equivalently, when the characteristic time is much slower than the plasma oscillation time. The second one is the *infinite speed of light* approximation. In this limit, the displacement current is negligible compared to the electric current and Ampere's law yields:

$$\nabla \times \mathbf{B} = \mu_0 \mathbf{j} \tag{2.32}$$

Inserting the expression above for $\mathbf{j}$ into the total plasma momentum equation and with some vector calculus identities, one can obtain:

$$\partial_t (\rho \mathbf{u}) + \nabla \cdot (\rho \mathbf{u}\mathbf{u} + \mathbb{P}_B) + \nabla p = 0 \tag{2.33}$$

where $\mathbb{P}_B = \frac{1}{\mu_0} \left(\frac{1}{2} \mathbf{B} \cdot \mathbf{B} - \mathbf{B}\mathbf{B} \right)$ is known as the Maxwell stress tensor[4]. It is shown

[3]This approximation is now consistent with the assumption first made in arriving at equation (2.24).

[4]Here charge neutrality was assumed, so the effect of electric field does not show up in the expression of Maxwell stress tensor.

that the effect of the Lorentz force is now replaced by an equivalent magnetic pressure [56].

The conservation equation of the plasma total energy can be written as:

$$\partial_t E + \nabla \cdot [(E + p)\,\mathbf{u}] = \mathbf{j} \cdot \mathbf{E} \tag{2.34}$$

where Joule heating is the only coupling term remaining on the RHS. The conservation equation for the magnetic energy density [56] can be written as:

$$\partial_t \left(\frac{\mathbf{B} \cdot \mathbf{B}}{2\mu_0} \right) + \nabla \cdot \left(\frac{\mathbf{E} \times \mathbf{B}}{\mu_0} \right) = -\mathbf{j} \cdot \mathbf{E} \tag{2.35}$$

Taking a cross product of Ohm's law (2.29) with $\mathbf{B}$ and substituting the expression of $\mathbf{E} \times \mathbf{B}$ back into equation (2.35), one obtains:

$$\partial_t \left(\frac{\mathbf{B} \cdot \mathbf{B}}{2\mu_0} \right) + \nabla \cdot \left(\frac{\mathbf{B} \cdot \mathbf{B}}{2\mu_0} \mathbf{u} \right) + \nabla \cdot (\mathbb{P}_B \cdot \mathbf{u}) - \nabla \cdot \left(\frac{1}{\mu_0 \overline{\sigma}} \nabla \cdot \mathbb{P}_B \right) = -\mathbf{j} \cdot \mathbf{E} \tag{2.36}$$

Combining equation (2.36) and (2.34) yields the conservation for the total plasma energy density including the magnetic field energy:

$$\partial_t E^\star + \nabla \cdot [(E^\star + p)\,\mathbf{u}] + \nabla \cdot (\mathbb{P}_B \cdot \mathbf{u}) = \nabla \cdot \left(\frac{1}{\mu_0 \overline{\sigma}} \nabla \cdot \mathbb{P}_B \right) \tag{2.37}$$

where $E^\star = E + \frac{\mathbf{B} \cdot \mathbf{B}}{2\mu_0}$. The term on the RHS of equation (2.37) corresponds to the resistive diffusion of the magnetic field energy. The equation of state to is that of ideal gas similar to equation (2.7):

$$p = nkT = (\gamma - 1)E \tag{2.38}$$

where $n = \rho/m$ is the number density of the gas.

Similarly, an equation for the evolution of the magnetic field can also be derived. Starting with Faraday's law of induction (1.3), Ohm's law can be used to express $\nabla \times \mathbf{E}$ in terms the current density and the magnetic field, which leads to:

$$\partial_t \mathbf{B} - \nabla \times (\mathbf{u} \times \mathbf{B}) = -\nabla \times \frac{1}{\overline{\sigma}} \mathbf{j} \tag{2.39}$$

Using Ampere's law (2.32) to relate the current density to the magnetic field and utilizing some vector calculus identities, one obtain an equation for the evolution of the magnetic field:

$$\partial_t \mathbf{B} - \nabla \times (\mathbf{u} \times \mathbf{B}) = -\nabla \times \left(\frac{1}{\mu \overline{\sigma}} \nabla \times \mathbf{B} \right) \tag{2.40}$$

Equations (2.30), (2.33), (2.37), (2.38) and (2.40) constitute a complete set for a standard resistive MHD model. In the limit of infinitely conducting plasma, i.e., $\overline{\sigma} \to \infty$, all the diffusion terms associated with the magnetic field vanish, and the ideal MHD equation is recovered. This point will be revisited in section 3.3.2.3 when we make comparison between the solution of the multi-fluid system and the MHD equation.

It must be noted that the effect of electron diffusion and Hall current has been left out in the expression of Ohm's law. In the first case, one can introduce an effective electric field $\hat{\mathbf{E}} = \mathbf{E} + \frac{\nabla p_e}{e n_e}$ such that Ohm's law can be put in the form of (2.29). In the case when the Hall term is also included, Ohm's law can still be written in the same form where the scalar conductivity $\overline{\sigma}$ now becomes a conductivity tensor [57]. Introducing the expression of the effective electric field into generalized Ohm's law equation (2.25), one obtains:

$$\mathbf{j} + \beta_e \mathbf{j} \times \hat{\mathbf{b}} = \overline{\sigma} \hat{\hat{\mathbf{E}}} \tag{2.41}$$

where $\hat{\hat{\mathbf{E}}} = \hat{\mathbf{E}} + \mathbf{u} \times \mathbf{B}$. Let us introduce a coordinate such that the magnetic field is aligned with the z-direction, i.e., $\mathbf{B} = |\mathbf{B}| \hat{\mathbf{e}}_z$. Ohm's law can be brought into the following form:

$$\begin{bmatrix} j_x \\ j_y \\ j_z \end{bmatrix} = \frac{\overline{\sigma}}{1 + \beta_e^2} \begin{bmatrix} 1 & -\beta_e & 0 \\ \beta_e & 1 & 0 \\ 0 & 0 & 1 + \beta_e^2 \end{bmatrix} \begin{bmatrix} \cdot \hat{\hat{E}}_x \\ \hat{\hat{E}}_y \\ \hat{\hat{E}}_z \end{bmatrix} \tag{2.42}$$

One can see from equation (2.42) that in the limit of strongly magnetized plasma, the current parallel to the magnetic field is much stronger than the transverse currents.

2.4 Multi-temperature and chemically reactive hydrodynamics

When the chemical reaction time scale is of the same order of magnitude as the hydrodynamic time scale, one must take in account the species mass production/consumption and energy exchanges between different modes. The resultant set of equations is referred to as the multi-species multi-temperature model. These models are widely used in numerical simulations due to their high efficiency in multi-dimensional calculations [21].

The number of "temperature" variables included in the model is dictated by the underlying assumption of the energy transfer rate between different energy modes. For example, in an atomic plasma, due to the slow energy exchange rates between the heavy species and the electrons, an additional conservation equation for the electron energy is usually required, resulting in the so-called two-temperature (2T) plasma model.

In the case of a molecular plasma, due to additional degrees of freedom such as rotational and vibrational modes, one can write separate conservation equation for rotational and vibrational energies, leading to various multi-temperature models. The choice of partition between these energy modes is not trivial, and is highly condition dependent. In hypersonic plasma, a typical assumption is that the rotational modes is in equilibrium with the translational mode, and vibrational energy can be considered separately. High-fidelity kinetic models indicate that this assumption is questionable and indeed for high temperature and low pressure conditions, rotational and vibrational exchange can proceed at the same rate [58].

In this section, a 2T model for atomic plasma is presented, where the electron thermal energy is separated conserved from the total energy. In addition, chemical reactions are taken into account by extending the Euler equation to multiple species. For simplicity, only the single-fluid approximation is considered, and the

effects of the electromagnetic fields is omitted. The resultant system of equations is similar to the Euler equations for reactive neutral gas flow:

$$\partial_t \rho_s + \nabla \cdot (\rho_s \mathbf{u}) = m_s \dot{\omega}_s \tag{2.43}$$

$$\partial_t (\rho \mathbf{u}) + \nabla \cdot (\rho \mathbf{u}\mathbf{u}) + \nabla p = 0 \tag{2.44}$$

$$\partial_t E + \nabla \left[(E + p) \mathbf{u} \right] + \nabla \cdot \mathbf{q}_e = \dot{\omega}_{\varepsilon_e} + \dot{\omega}_{\varepsilon_h} \tag{2.45}$$

$$\partial_t \varepsilon_e + \nabla (\varepsilon_e \mathbf{u}) + p_e \nabla \cdot \mathbf{u} + \nabla \cdot \mathbf{q}_e = \dot{\omega}_{\varepsilon_e} \tag{2.46}$$

where the total energy of the plasma is this case is defined as:

$$E = \varepsilon_h + \varepsilon_e + \frac{1}{2} \rho \mathbf{u} \cdot \mathbf{u} \tag{2.47}$$

and

$$\varepsilon_h = \frac{p_h}{\gamma - 1} \tag{2.48}$$

$$\varepsilon_e = \frac{p_e}{\gamma_e - 1} \tag{2.49}$$

For the case of an atomic plasma, one simply takes $\gamma = \gamma_e = \frac{5}{3}$. The equation of state for a 2T plasma can be written as:

$$p = \sum_{s \neq e} n_s k T_h + n_e k T_e \tag{2.50}$$

$$p_e = n_e k T_e \tag{2.51}$$

The electron translational energy equation written in (2.46) is non-conservative due to the adiabatic heating term $p_e \nabla \cdot \mathbf{u}_e$. A conservative form of the equation can be obtained by defining an entropy-like variable $S_e \equiv \rho \hat{s}_e = \rho \frac{p_e}{\rho^{\gamma_e}}$ and rewriting the equation accordingly[5]:

$$\partial_t \left(\frac{p_e}{\rho^{\gamma_e - 1}} \right) + \nabla \cdot \left(\frac{p_e \mathbf{u}}{\rho^{\gamma_e - 1}} \right) = \frac{\gamma_e - 1}{\rho^{\gamma_e - 1}} \left[\frac{\partial \varepsilon_e}{\partial t} + \nabla \cdot (\mathbf{u} \varepsilon_e) \right] + \frac{\gamma_e - 1}{\rho^{\gamma_e - 1}} (p_e \nabla \cdot \mathbf{u}) \tag{2.52}$$

[5]This is similar to the approach taken in [59] but the electron entropy is defined in term of ρ instead of ρ_e. The advantage is that the entropy remains finite when the ionization fraction goes to zero ($\rho_e \to 0$) [60].

Using equation (2.46), we can obtain a conservation equation for the electron entropy:

$$\frac{\partial S_e}{\partial t} + \nabla \cdot (S_e \mathbf{u}) + \left(\frac{\gamma_e - 1}{\rho^{\gamma_e - 1}} \right) \nabla \cdot \mathbf{q}_e = \frac{\gamma_e - 1}{\rho^{\gamma_e - 1}} \dot{\omega}_{\varepsilon_e} \tag{2.53}$$

Note that the source term must be modified based on the definition of the new variable. The equation of state can be expressed in term of the electron entropy:

$$p = p_h + p_e = \rho^{\gamma_e - 1} S_e + \sum_{s \neq e} n_s k T_h \tag{2.54}$$

Similarly, we can rewrite the expression for the total energy in term of the electron entropy:

$$E = \frac{S_e \rho^{\gamma_e - 1}}{\gamma_e - 1} + \sum_{s \neq e} \rho_s \varepsilon_s + \frac{1}{2} \rho \mathbf{u} \cdot \mathbf{u} \tag{2.55}$$

It is important to mention that the source term on the RHS of the total energy equation (2.45) is non-zero, which, however, does not violate energy conservation. The reason for this is that the species heat of formation is not included in the definition of the total energy E. Therefore, the change of the energy when a new species is produced or destroyed has to be accounted for properly[6]. The choice of such a definition of the total energy is purely due to numerics. It was observed that for the simulation of flow containing species of high chemical energy, the linearization of the energy (or enthalpy), an important step in the finite volume method for solving non-linear PDEs, can introduce some error at the composition discontinuity if the heat of formation is included in the definition of E [61].

The term on the RHS of (2.43) corresponds the rate of change of each species due to chemical reaction. Consider a general reaction of the following type:

$$s + t \Leftrightarrow s' + t' \tag{2.56}$$

[6]One must take in account the rate of change of energy for the heavy particle and electron accordingly depending on a specific chemical process. For example, heavy-particle impact and electron impact excitations must be considered as two separate processes, since the energy exchange is taken from different conserved quantities.

the corresponding source term for species s due to this reaction can be written as:

$$\dot{\omega}_s = -k_f n_s n_t + k_b n_{s'} n_{t'} \tag{2.57}$$

where k_f denote the forward rate and k_b denote the backward rate of reaction (2.57). The most commonly used expression for the chemical reaction rate is the modified Arrhenius form:

$$k_f = A_f T^{\beta_f} \exp\left(-\frac{\delta E_f}{kT}\right) \tag{2.58}$$

where A, β, and δE are the three main parameters controlling the rate. It is important to note that the forward and the backward rates can always be related by the principle of detailed balance. In the single-fluid approximation, these two rates can be related by the so-called equilibrium constant:

$$k_{eq} = \frac{k_f}{k_b} \tag{2.59}$$

The principle of detailed balance for atomic collisional and radiative processes, resulting in a particular form of the equilibrium constant k_{eq}, will be described in detailed in chapter 4. In addition, it will also be shown in chapter 6 that expressions of the same type as equation (2.59) no longer hold for multi-fluid equations. A detail treatment of these terms will be described in chapter 4.

The electron heat conduction process is also included in both conservation equations for the total energy and electron entropy. This term is expressed as a divergence of the electron heat flux $\mathbf{q}_e$. The electron heat flux is usually expressed by Fourier's law of heat conduction:

$$\mathbf{q}_e = -\kappa_e \nabla T_e \tag{2.60}$$

where κ_e is the electron heat conductivity.

The most commonly used expression for the electron heat flux in fully ionized plasma is due to Spitzer-Harm (SH) [54], from which κ_e is determined from

Coulomb interaction. The SH expression yields $\mathbf{q}_e \sim \kappa_0 \nabla(T_e^{7/2})$ where κ_0 is a constant. This expression is used, for example, in calculation of target heating in inertial fusion. However, cautions must be exercised when using this formula, especially in the region where the temperature gradient is large. This issue is discussed in detailed in chapter 7 for a numerical study of LPI using hydrodynamic equations.

CHAPTER 3

Numerical Formulation

3.1 Introduction

The numerical methods for solving the governing equations described in chapter 2 are presented in this chapter. Although the numerical methods are applicable for a general set of hyperbolic PDEs with source term, in this research we only focus on the multi-fluid equations and the 2T model for partially and fully ionized plasma describe in sections 2.2 and 2.4, respectively. The procedure for solving the MHD equations in section 2.3 can be performed with the same numerical approach. The relation between the solutions of the multi-fluid and MHD equation will be discussed later in this chapter.

3.2 Numerical methods

3.2.1 Finite volume methods

In the absence of viscous effects, the full set of governing equations can be written in the form of a hyperbolic system of PDEs with a source term vector:

$$\partial_t \mathbf{Q} + \nabla \cdot \overline{\overline{\mathbf{F}}} = \dot{\mathbf{\Omega}} \tag{3.1}$$

where $\mathbf{Q}$ is the vector of conservative variables, $\overline{\overline{\mathbf{F}}}$ is the inviscid flux tensor, and $\dot{\mathbf{\Omega}}$ is the source term vector due to exchange processes and/or coupling forces. The diffusive term, i.e., electron heat conduction, can also be included in equation (3.1) using an expression of a diffusive flux tensor. This term is described separately

in section 3.2.6. For the fluid equations, $\mathbf{Q} = [\rho_s, \rho u_x, \rho u_y, \rho u_z, E, S_e]^T$, and for Maxwell's equations, $\mathbf{Q} = [E_x, E_y, E_z, B_x, B_y, B_z]^T$.

In this research framework, a finite volume method is developed to solve both of these equations, using a similar discretization procedure. For the sake of generality, the numerical methods are presented using the general form of the PDEs. Specific details regarding a particular set of equations will be mentioned where appropriate.

Equation (3.1) is solved using an operator splitting technique, where the changes in the conservative variables for each process are evaluated independently within a time step, and accumulated independently at the end of each time step. For example, at each time step n, the solution of the next time step $n+1$ is computed as follows:

$$\Delta \mathbf{Q}_{\text{conv}} = \mathcal{L}_{\text{conv}}^{\Delta t}(\mathbf{Q}^n) - \mathbf{Q}^n \tag{3.2}$$

$$\Delta \mathbf{Q}_{\text{diff}} = \mathcal{L}_{\text{diff}}^{\Delta t}(\mathbf{Q}^n) - \mathbf{Q}^n \tag{3.3}$$

$$\Delta \mathbf{Q}_{\text{source}} = \mathcal{L}_{\text{source}}^{\Delta t}(\mathbf{Q}^n) - \mathbf{Q}^n \tag{3.4}$$

$$\mathbf{Q}^{n+1} = \mathbf{Q}^n + \Delta \mathbf{Q}_{\text{conv}} + \Delta \mathbf{Q}_{\text{diff}} + \Delta \mathbf{Q}_{\text{source}} \tag{3.5}$$

where $\mathcal{L}_{\text{conv}}$, $\mathcal{L}_{\text{diff}}$, $\mathcal{L}_{\text{source}}$ are the convective, diffusive, and source term operators, respectively, which advance the solution forward in time (so-called "propagators").

The splitting scheme described above is a first order splitting scheme of $\mathcal{O}(\Delta t)$. High-order splitting schemes such as Strang splitting [62] can also be employed. For a convective-diffusive-reactive system, the splitting is as follows:

$$\mathbf{Q}^{n+1} = \mathcal{L}_{\text{source}}^{\Delta t/2} \mathcal{L}_{\text{diff}}^{\Delta t/2} \mathcal{L}_{\text{conv}}^{\Delta t} \mathcal{L}_{\text{diff}}^{\Delta t/2} \mathcal{L}_{\text{source}}^{\Delta t/2}(\mathbf{Q}) \tag{3.6}$$

where the splitting error is $\mathcal{O}(\Delta t^2)$. In the current research, only the first order splitting scheme is employed. The reason is due to its simplicity in implementation. Also, the source terms of these equations are very stiff, e.g.,

CR kinetics, which results in a small time scale restriction[1]. Since local time-stepping is not used, all the operators are marched at the smallest time step introduced by these operators, making the splitting error of $\mathcal{O}(\Delta t_{\min})$ where $\Delta t_{\min} = \min(\Delta t_{\text{conv}}, \Delta t_{\text{diff}}, \Delta t_{\text{source}})$. A detailed analysis of high-order schemes and error estimate for time operator splitting approach can be found in the work of Duarte *et al.* [63].

The integral form of the governing equations suitable for finite-volume formulation can be obtained by integrating equation (3.1) over the control volume and using Gauss's law for the divergence of the flux.

$$\frac{d\mathbf{Q}}{dt} + \frac{1}{V}\sum_{s} \mathbf{F}_s A_s = \dot{\mathbf{\Omega}} \tag{3.7}$$

where $\mathbf{F}_s$ is the numerical flux computed at each face and A_s is its surface area. Note that in equation (3.7), $\mathbf{Q}$ and $\dot{\mathbf{\Omega}}$ denote volume averaged quantities. For the case of the Euler terms, the fluxes are computed by solving a Riemann problem at each face of the control volume.

3.2.2 Hyperbolic solvers - Approximated Riemann solvers

3.2.2.1 Semi-discrete approach

For simplicity, consider now a hyperbolic system of PDEs in one-dimensional of the form:

$$\partial_t \mathbf{Q} + \partial_x \mathbf{F}(\mathbf{Q}) = 0 \tag{3.8}$$

where the domain is discretized into a uniform grid with constant spacing Δx. The system (3.8) is classified as a hyperbolic system if the eigenvalues of the flux Jacobian, $\frac{\partial \mathbf{F}}{\partial \mathbf{Q}}$, are real, which is the case for the Euler equations and Maxwell's equations. Utilizing the standard finite volume approximation similar to equation

[1]Even when implicit time integration is employed, accuracy constraint still introduces time step restriction.

(3.7), the spatial derivative in equation (3.8) is replaced by the expression of a numerical flux, yielding the following expression:

$$\frac{d\mathbf{Q}_i}{dt} = -\frac{1}{\Delta x}\left(\mathbf{F}_{i+1/2} - \mathbf{F}_{i-1/2}\right) \tag{3.9}$$

where $i \pm 1/2$ denote the left and right faces of cell i.

Equation (3.9) is known as the semi-discrete form of (3.8), where only the spatial terms had been discretized [64]. This approach converts the original system of PDEs to a coupled system of ordinary differential equations (ODEs). The advantage of the semi-discrete approach is that any time integration method can be utilized to solve equation (3.9), once the fluxes had been computed. In the current work, a third-order total variation diminishing (TVD) Runge-Kutta (RK) time integration is utilized. The resultant scheme is referred to as RK3:

$$\mathbf{Q}^{n+1/3} = \mathbf{Q}^n + \Delta t \boldsymbol{\mathcal{F}}(\mathbf{Q}^n) \tag{3.10}$$

$$\mathbf{Q}^{n+2/3} = \frac{3}{4}\mathbf{Q}^n + \frac{1}{4}\left(\mathbf{Q}^{n+1/3} + \Delta t \boldsymbol{\mathcal{F}}(\mathbf{Q}^{n+1/3})\right) \tag{3.11}$$

$$\mathbf{Q}^{n+1} = \frac{1}{3}\mathbf{Q}^n + \frac{2}{3}\left(\mathbf{Q}^{n+2/3} + \Delta t \boldsymbol{\mathcal{F}}(\mathbf{Q}^{n+2/3})\right) \tag{3.12}$$

where $\boldsymbol{\mathcal{F}}(\mathbf{Q})$ is now referred to the RHS of equation (3.9). Since RK3 is an explicit method, the time step must satisfy the Courant-Friedrichs-Lewy (CFL) condition:

$$\left[\max_i |\lambda_i^{\max}|\right] \frac{\Delta t}{\Delta x \upsilon} \leq 1 \tag{3.13}$$

where υ is the CFL number, and $\lambda_i^{\max}$ is the maximum eigenvalues of the flux Jacobian. In the case of Euler equations, $\lambda_i^{\max} = [|\mathbf{u}| + a]_i$ where a is the speed of sound. For Maxwell's equations, $\lambda_i^{\max} = c = 3 \times 10^8$.

3.2.2.2 Approximate Riemann solvers

In order to compute the flux term in equation (3.9), a Riemann problem needs to be solved at each face from the given left and right states. The exact solution of the Riemann problem can be computationally expensive and thus is not practical

for numerical calculation. The numerical framework in this research utilizes an approximate Riemann solver for the solution at the faces, that is, instead of solving (3.8), one can solve:

$$\partial_t \mathbf{Q} + \mathbf{A}(\mathbf{Q})\partial_x \mathbf{Q} = 0 \tag{3.14}$$

where the flux Jacobian, $\mathbf{A} = \frac{\partial \mathbf{F}}{\partial \mathbf{Q}}$, is replaced by a constant matrix $\tilde{\mathbf{A}}$, which is determined from the left and right states of each face, i.e., $\tilde{\mathbf{A}} = \tilde{\mathbf{A}}(\mathbf{Q}^L, \mathbf{Q}^R)$.

The validity of the linearization process requires that the Jacobian $\mathbf{A}$ be diagonalizable with real eigenvalues, i.e., $\mathbf{A} = \mathbf{R}\mathbf{\Lambda}\mathbf{L}$. The left and the right eigenvectors can be used to project equation (3.14) from the physical to characteristic space.

$$\frac{\partial(\mathbf{LQ})}{\partial t} + \mathbf{\Lambda}\frac{\partial(\mathbf{LQ})}{\partial x} = 0 \tag{3.15}$$

By introducing the characteristic variable $\mathbf{W} = \mathbf{LQ}$, equation (3.15) now becomes:

$$\frac{\partial \mathbf{W}}{\partial t} + \mathbf{\Lambda}\frac{\partial \mathbf{W}}{\partial x} = 0 \tag{3.16}$$

The original system of PDEs now has been linearized and decoupled from the original system resulting in a linear system of scalar hyperbolic PDEs. For the Euler equations, the linearization is carried out using Roe-averaging procedures:

$$\tilde{\rho} = \sqrt{\rho^L \rho^R} \tag{3.17}$$

$$\tilde{\mathbf{u}} = \frac{\sqrt{\rho^L}\mathbf{u}^L + \sqrt{\rho^R}\mathbf{u}^R}{\sqrt{\rho^L} + \sqrt{\rho^R}} \tag{3.18}$$

$$\tilde{h} = \frac{\sqrt{\rho^L}h^L + \sqrt{\rho^R}h^R}{\sqrt{\rho^L} + \sqrt{\rho^R}} \tag{3.19}$$

$$\tilde{s}_e = \frac{\sqrt{\rho^L}\hat{s}_e^L + \sqrt{\rho^R}\hat{s}_e^R}{\sqrt{\rho^L} + \sqrt{\rho^R}} \tag{3.20}$$

For Maxwell's equations, an arithmetic average of the field values is sufficient:

$$\tilde{\mathbf{E}} = \frac{\mathbf{E}^L + \mathbf{E}^R}{2} \tag{3.21}$$

$$\tilde{\mathbf{B}} = \frac{\mathbf{B}^L + \mathbf{B}^R}{2} \tag{3.22}$$

The eigensystems of both Euler and Maxwell's equations are given in appendix A.

The interface fluxes are solved by employing the Harten, Lax, vanLeer and Einfeldt (HLLE) Riemann solver [65], which is given as

$$\mathbf{f}_{i+1/2}^{\mathrm{HLLE}} = \frac{b^+\mathbf{f}_{i+1/2}^R - b^-\mathbf{f}_{i+1/2}^L}{b^+ - b^-} + \frac{b^+b^-}{b^+ - b^-}\Delta\mathbf{W}_{j+1/2} \tag{3.23}$$

where

$$b^+ = \max(0, \tilde{u}_n + \tilde{a}, u_n^R + a^R) \tag{3.24}$$

$$b^- = \min(0, \tilde{u}_n - \tilde{a}, u_n^L - a^L) \tag{3.25}$$

where u_n denote the velocity normal to the face. It must be noted that the fluxes in equation (3.23) are expressed in characteristic form, i.e., $\mathbf{f}_{i+1/2} = \tilde{\mathbf{L}}\mathbf{F}_{i+1/2}$.

3.2.3 High-order reconstruction

3.2.3.1 Monitonicity-Preserving schemes

In order to achieve high-order spatial accuracy, a fifth-order Monotonicity-Preserving (MP5) scheme [66] is used for the reconstruction of the interface values. For non-linear equations, the reconstruction is performed on characteristic variables with the help of the eigenvectors. For a one dimensional stencil, the reconstructed value of the left and right states of interface $i + \frac{1}{2}$ is given as (see figure 3.1)

$$w_{i+\frac{1}{2}}^L = \frac{1}{60}\left(2w_{i-2} - 13w_{i-1} + 47w_i + 27w_{i+1} - 3w_{i+2}\right) \tag{3.26a}$$

$$w_{i+\frac{1}{2}}^R = \frac{1}{60}\left(2w_{i+3} - 13w_{i+2} + 47w_{i+1} + 27w_i - 3w_{i-1}\right) \tag{3.26b}$$

The reconstructed values are then limited to avoid instability.

$$w_{i+\frac{1}{2}}^L \leftarrow \mathrm{median}\left(w_{i+\frac{1}{2}}^L, w_i, w_{\mathrm{MP}}\right) \tag{3.27}$$

where

$$w_{\mathrm{MP}} = w_i + \mathrm{minmod}\left[w_{i+1} - w_i, \alpha\left(w_i - w_{i-1}\right)\right] \tag{3.28}$$

with $\alpha = 2$. The minmod and median functions are defined as follows:

$$\text{minmod}(x, y) = \begin{cases} \text{sgn}(x) \min(|x|, |y|) & \text{if } xy > 0 \\ 0 & \text{otherwise} \end{cases} \tag{3.29}$$

$$\begin{aligned} \text{median}(x, y, z) &= x + \text{minmod}(y - x, z - x) \\ &= y + \text{minmod}(x - y, z - y) \\ &= x + \frac{1}{2} [\text{sgn}(y - x) + \text{sgn}(z - x)] \min(|y - x|, |z - x|) \end{aligned} \tag{3.30}$$

where $\text{sgn}(z)$ is the sign function.

The CFL condition of MP schemes depends on the value of α. In addition, the original MP5 scheme of Suresh and Huynh [66] also contains an additional accuracy-preserving constraint to avoid the loss of accuracy near the shock. The detail of the constraint procedure is discussed in their paper and will not be repeated here.

Another variant of the original MP5 scheme is a third order monotonicity-preserving (MP) scheme, known as MP3, which utilize a three point stencil [32]. The MP3 reconstruction starts with a parabolic interpolation:

$$w^L_{i+\frac{1}{2}} = \frac{1}{6} (2w_{i-1} + 5w_i - w_{i+1}) \tag{3.31}$$

$$w^R_{i+\frac{1}{2}} = \frac{1}{6} (2w_{i+2} + 5w_{i+1} - w_i) \tag{3.32}$$

The MP limiter in (3.27) and (3.28) is then applied to avoid instability in the solution containing discontinuity. The MP schemes have been determined to hold some CFL restriction based on the value of α. It is recommended to use a CFL number close to $1/(1 + \alpha)$ for a stable solution.

3.2.3.2 Weighted essentially non-oscillatory schemes

Weighted essentially non-oscillatory (WENO) schemes, developed by Liu *et al.* [67] and Jiang and Shu [68] are based on the essentially non-oscillatory (ENO)

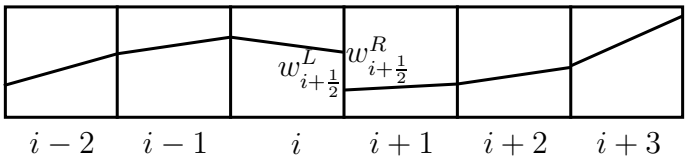

Figure 3.1: Schematic of computational stencil for MP5 and WENO schemes with left and right states of an interface.

schemes developed by Harten *et al.* [69] in the form of cell-averages. In WENO reconstruction, an adaptive-stencil approach is utilized, and the reconstructed values is a convex combination of all the stencils. The WENO schemes preserve the essentially non-oscillatory property of the original ENO scheme, but also improves the order of accuracy in the smooth part of the flow solution. A fifth-order scheme is implemented in the current work. For a one dimensional stencil similar to the one in figure 3.1, the reconstructed value of the left state of interface $i + 1/2$ is written as a weighted summation of three smaller stencils:

$$w^L_{i+1/2} = \omega_1 w^{(1)} + \omega_2 w^{(2)} + \omega_3 w^{(3)} \tag{3.33}$$

The three stencil values are:

$$w^{(1)} = \frac{1}{3}w_{i-2} + \frac{7}{6}w_{i-1} + \frac{11}{6}w_i \tag{3.34}$$

$$w^{(2)} = -\frac{1}{6}w_{i-1} + \frac{5}{6}w_i + \frac{1}{3}w_{i+1} \tag{3.35}$$

$$w^{(3)} = \frac{1}{3}w_i + \frac{5}{6}w_{i+1} - \frac{1}{6}w_{i+2} \tag{3.36}$$

$$\tag{3.37}$$

and the non-linear weight are designed to adapted to the smoothness of the stencil. For a discontinuous stencil, the non-linear weight is reduced to zero:

$$\omega_i = \frac{\chi_i}{\sum_{n=1}^{3} \chi_n} \tag{3.38}$$

$$\chi_i = \frac{C_i^r}{IS_i + \epsilon} \tag{3.39}$$

where $\epsilon = 10^{-7} - 10^{-5}$ is a small number to avoid division by zero. C_i^r is known as the optimal weight, given by:

$$C_1^r = \frac{1}{10} \tag{3.40}$$

$$C_2^r = \frac{6}{10} \tag{3.41}$$

$$C_3^r = \frac{3}{10} \tag{3.42}$$

and the smoothness indicator IS are:

$$IS_1 = \frac{13}{12}\left(w_{i-2} - 2w_{i-1} + w_i\right)^2 + \frac{1}{4}\left(w_{i-2} - 4w_{i-1} + 3w_i\right)^2 \tag{3.43}$$

$$IS_2 = \frac{13}{12}\left(w_{i-1} - 2w_i + w_{i+1}\right)^2 + \frac{1}{4}\left(w_{i-1} - w_{i+1}\right)^2 \tag{3.44}$$

$$IS_3 = \frac{13}{12}\left(w_i - 2w_{i+1} + w_{i+2}\right)^2 + \frac{1}{4}\left(3w_i - 4w_{i+1} + w_{i+2}\right)^2 \tag{3.45}$$

The reconstructed value of the right state can be found easily by symmetry. The stability of both MP and WENO is enhanced by RK3 time integration, yielding a fifth-order spatial accuracy (third order in the case of MP3).

3.2.4 Hyperbolic solvers - Implicit time marching

It was mentioned previously that the solution of the multi-fluid equations contains several time scales, which can be of different orders of magnitude. This is certainly the case for the electron due to the small mass ratio compared to the heavy species. The CFL time step restriction for the electrons is much more severe compared to the heavy species. It is therefore advantageous to be able to solve the electron fluid equation implicitly. A similar argument applies to the case of electromagnetic wave propagation in the Maxwell's equations. In this section, an implicit time stepping scheme is described within the finite volume approximation.

Consider now the discretized equation of (3.8):

$$\frac{\Delta \mathbf{Q}_i^n}{\Delta t} = \frac{1}{\Delta x}\left(\mathbf{F}_{i-1/2} - \mathbf{F}_{i+1/2}\right) \tag{3.46}$$

where $\Delta\mathbf{Q}_i^n = \mathbf{Q}_i^{n+1} - \mathbf{Q}_i^n$. In the explicit scheme, the RHS of equation (3.46) is evaluated at the current time step n. Let us define $\boldsymbol{\mathcal{F}}_i$ to be the explicit flux terms:

$$\boldsymbol{\mathcal{F}}_i = \frac{\Delta t}{\Delta x}\left(\mathbf{F}_{i-1/2}^n - \mathbf{F}_{i+1/2}^n\right) \tag{3.47}$$

In order to facilitate an implicit time-stepping scheme, the numerical fluxes in equation (3.46) need to be evaluated at time level $n+\theta$. This can be done through the linearization approximation:

$$\mathbf{F}_{i\pm1/2}^{n+\theta} = \mathbf{F}_{i\pm1/2}^n + \theta\mathbf{A}(\mathbf{Q})(\Delta\mathbf{Q})_{i\pm1/2} \tag{3.48}$$

The Jacobian can be split based on the sign of the eigenvalues, i.e., $\mathbf{A} = \mathbf{R}(\boldsymbol{\Lambda}^+ + \boldsymbol{\Lambda}^-)\mathbf{L} = \mathbf{A}^+ + \mathbf{A}^-$, where $\boldsymbol{\Lambda}^+$ contains all the positive eigenvalues and $\boldsymbol{\Lambda}^-$ contains all the negative ones. The flux linearization can be written as:

$$\mathbf{F}_{i+1/2}^{n+\theta} = \mathbf{F}_{i+1/2}^n + \theta\mathbf{A}_{i+1/2}^+(\Delta\mathbf{Q})_i + \theta\mathbf{A}_{i+1/2}^-(\Delta\mathbf{Q})_{i+1} \tag{3.49}$$

Similarly,

$$\mathbf{F}_{i-1/2}^{n+\theta} = \mathbf{F}_{i-1/2}^n + \theta\mathbf{A}_{i-1/2}^+(\Delta\mathbf{Q})_{i-1} + \theta\mathbf{A}_{i-1/2}^-(\Delta\mathbf{Q})_i \tag{3.50}$$

The discretized version of equation (3.46) becomes:

$$\left[-\eta\mathbf{A}_{i-1/2}^+\right]\Delta\mathbf{Q}_{i-1} + \left[1 + \eta\mathbf{A}_{i+1/2}^+ - \eta\mathbf{A}_{i-1/2}^-\right]\Delta\mathbf{Q}_i + \left[\eta\mathbf{A}_{i+1/2}^-\right]\Delta\mathbf{Q}_{i+1} = \boldsymbol{\mathcal{F}}_i \tag{3.51}$$

where $\eta = \frac{\theta\Delta t}{\Delta x}$. For stability, the LHS of (3.51) is reverted to first order approximation, the fully implicit system now can be written as:

$$\left[-\eta\mathbf{A}_{i-1}^+\right]\Delta\mathbf{Q}_{i-1} + \left[1 + \eta\mathbf{A}_i^+ - \eta\mathbf{A}_i^-\right]\Delta\mathbf{Q}_i + \left[\eta\mathbf{A}_{i+1}^-\right]\Delta\mathbf{Q}_{i+1} = \boldsymbol{\mathcal{F}}_i \tag{3.52}$$

It must be noted that for $\theta = 1/2$, the resultant scheme is the same as the Crank-Nicolson method. For $\theta = 1$, the scheme is the backward Euler method. System (3.52) is a block tridiagonal system with block size N, where N is the number of

conservative variables. Standard techniques like Gaussian elimination and back substitution can be applied to solve this system of equations. This is referred as the Thomas Block-Tridiagonal algorithm.

A similar approach can be used for 2-D equations, leading to a penta-diagonal system of $N \times N$ block matrices. The cost of inverting the matrix in that case is very large, and for the 3D case, directly inverting a septa-diagonal system is completely prohibitive. Another approach, which consumes less memory, and has a lower number of operations, is via the dimensional splitting technique, that is, a block-tridiagonal system is solved for each direction, and the change in the conservative variables can be successively refined by an iterative procedure. Detail of such an approach is discussed in [70]. It must be pointed out that since most of the problems considered in this work are highly transient, an iterative solution of equation (3.52) does not give any advantage over the Thomas algorithm.

3.2.5 Source term treatment

The source term is solved using a point-implicit solver. In general, we seek the solution of a system of ODEs written in the form:

$$\frac{d\mathbf{Q}}{dt} = \dot{\mathbf{\Omega}} \tag{3.53}$$

where $\mathbf{Q}$ is the state variables, and $\mathbf{S}$ is the source term vectors due to the kinetics or coupling terms with the electromagnetic forces, i.e., Lorentz force and Joule heating terms. For the CR kinetics, the system of ODEs is very stiff due to the multitude of the kinetics time scales involved in the a wide range of physical processes. An implicit time integration method is required to ensure the stability of the solution. The implicit formulation of the system can be obtained by expanding the source term vector via a Taylor series expansion about the current time step n.

$$\frac{d\mathbf{Q}^n}{dt} = \dot{\mathbf{\Omega}}^n + \frac{\partial \dot{\mathbf{\Omega}}^n}{\partial t}\Delta t \tag{3.54}$$

By using the chain rule on the time derivative of the source term vector, one can find

$$\frac{d\mathbf{Q}^n}{dt} = \dot{\mathbf{\Omega}}^n + \mathbf{J}\frac{d\mathbf{Q}^n}{dt}\Delta t \tag{3.55}$$

where $\mathbf{J}$ is the Jacobian matrix written as:

$$\mathbf{J} = \frac{\partial \dot{\mathbf{\Omega}}}{\partial \mathbf{Q}} \tag{3.56}$$

By simple algebraic manipulation, one can obtain:

$$\Delta\mathbf{Q}^n = \Delta t \left(\mathbf{I} - \Delta t\mathbf{J}\right)^{-1} \dot{\mathbf{\Omega}}^n \tag{3.57}$$

The solution of equation (3.57) gives the total change of the conservative variables due to the source term vector. Since the system is integrated implicitly, there is no restriction on the time step. The time step in this case is only restricted for accuracy purpose, i.e., for CR kinetics, the time step is limited by controlling the rate of change in the state population. For the electromagnetic coupling term in the two-fluid equation, the time step is set relative to the electron plasma frequency and the gyro-frequency.

As a linear system of equations, equation (3.57) can be solved using a variety of numerical methods. In the current work, a direct Gaussian elimination procedure is utilized to invert the system. It must be pointed out that the computational cost of the Gaussian elimination procedure scales as N^3 where N is the number of variables. For a large/detailed kinetics mechanism, i.e, many states, solving the system at every cell is clearly a computationally intensive task. For most of the simulations carried out in this dissertation, N is sufficiently small so that Gaussian elimination is the optimal choice.

3.2.6 Diffusive transport

A numerical method for solving the diffusive transport is described in this section. The method is used to solve the electron heat conduction equation. When

the plasma ionization fraction is sufficient, the electron heat conduction process can be very rapid, which suggests an implicit time marching scheme for stability requirement. Let us consider the heat conduction equation in 1d:

$$\begin{aligned} \partial_t E &= -\partial_x q \\ &= \partial_x \left(\kappa \partial_x T \right) \end{aligned} \tag{3.58}$$

where q is the heat flux, E is the energy and κ is the thermal conductivity. Using a finite volume approximation, the discretized form of equation (3.58) can be written as:

$$\Delta E_i^n = \frac{\Delta t}{\Delta x} \left(F_{i+1/2}^{\kappa} - F_{i-1/2}^{\kappa} \right) \tag{3.59}$$

where F^{κ} denotes the diffusive flux ($F^{\kappa} = -q$):

$$F_{i+1/2}^{\kappa} = \kappa_{i+1/2} f_{i+1/2} \tag{3.60}$$

$$f_{i+1/2} = \frac{1}{\Delta x} \left(T_{i+1} - T_i \right) \tag{3.61}$$

For the transport properties at the face, one can use a simple arithmetic average, i.e., $\kappa_{i+1/2} = \frac{\kappa_i + \kappa_{i+1}}{2}$. Let us now define the integrated diffusive flux, i.e., the RHS of equation (3.59) evaluated at the current time n, to be $\mathcal{F}_i^{\kappa}$, such that for an explicit time integration, one simple have $\Delta E_i = \mathcal{F}_i^{\kappa}$. For an implicit scheme, the fluxes can be linearized about the current time step n as follows:

$$F_{i\pm1/2}^{\kappa,n+\theta} = F_{i\pm1/2}^{\kappa,n} + \theta \delta F_{i\pm1/2}^{\kappa} \tag{3.62}$$

where

$$\delta F_{i+1/2}^{\kappa} = \frac{\Delta E_i}{\rho_i c_{v,i}} \frac{\partial F_{i+1/2}^{\kappa}}{\partial T_i} + \frac{\Delta E_{i+1}}{\rho_{i+1} c_{v,i+1}} \frac{\partial F_{i+1/2}^{\kappa}}{\partial T_{i+1}} \tag{3.63}$$

Note that we have used chain rule to relate the energy derivatives to the temperature derivatives. From equation (3.60), one also has:

$$\frac{\partial F_{i+1/2}^{\kappa}}{\partial T_i} = -\frac{\kappa_{i+1/2}}{\Delta x} + \frac{\partial \kappa_i}{\partial T} \frac{f_{i+1/2}}{2} \tag{3.64}$$

$$\frac{\partial F_{i+1/2}^{\kappa}}{\partial T_{i+1}} = \frac{\kappa_{i+1/2}}{\Delta x} + \frac{\partial \kappa_{i+1}}{\partial T} \frac{f_{i+1/2}}{2} \tag{3.65}$$

The expression for $\delta F^{\kappa}_{i-1/2}$ can be found similarly. This leads to:

$$\begin{aligned}\Delta E_i = \mathcal{F}^{\kappa}_i + \frac{\theta\Delta t}{\Delta x}\Bigg\{ & \Delta E_i \frac{1}{\rho_i c_{v,i}}\left[-\frac{\kappa_{i+1/2}}{\Delta x} + \frac{1}{2}\frac{\partial \kappa_i}{\partial T} f_{i+1/2}\right] \\ & + \Delta E_{i+1}\frac{1}{\rho_{i+1} c_{v,i+1}}\left[\frac{\kappa_{i+1/2}}{\Delta x} + \frac{1}{2}\frac{\partial \kappa_{i+1}}{\partial T} f_{i+1/2}\right] \\ & - \Delta E_{i-1}\frac{1}{\rho_{i-1} c_{v,i-1}}\left[-\frac{\kappa_{i-1/2}}{\Delta x} + \frac{1}{2}\frac{\partial \kappa_{i-1}}{\partial T} f_{i-1/2}\right] \\ & - \Delta E_i \frac{1}{\rho_i c_{v,i}}\left[\frac{\kappa_{i-1/2}}{\Delta x} + \frac{1}{2}\frac{\partial \kappa_i}{\partial T} f_{i-1/2}\right]\Bigg\} \end{aligned} \tag{3.66}$$

The resultant system of equation is as follows:

$$A\Delta E_{i-1} + B\Delta E_i + C\Delta E_{i+1} = \mathcal{F}^{\kappa}_i \tag{3.67}$$

where

$$A = \frac{\eta}{\rho_{i-1} c_{v,i-1}}\left[-\frac{\kappa_{i-1/2}}{\Delta x} + \frac{1}{2}\frac{\partial \kappa_{i-1}}{\partial T} f_{i-1/2}\right] \tag{3.68}$$

$$B = 1 + \frac{\eta}{\rho_i c_{v,i}}\left[\frac{\kappa_{i+1/2}}{\Delta x} - \frac{1}{2}\frac{\partial \kappa_i}{\partial T} f_{i+1/2}\right] + \frac{\eta}{\rho_i c_{v,i}}\left[\frac{\kappa_{i-1/2}}{\Delta x} + \frac{1}{2}\frac{\partial \kappa_i}{\partial T} f_{i-1/2}\right] \tag{3.69}$$

$$C = \frac{\eta}{\rho_{i+1} c_{v,i+1}}\left[-\frac{\kappa_{i+1/2}}{\Delta x} - \frac{1}{2}\frac{\partial \kappa_{i+1}}{\partial T} f_{i+1/2}\right] \tag{3.70}$$

and $\eta = \frac{\theta\Delta t}{\Delta x}$. Similarly, $\theta = 1$ corresponds to Backward-Euler and $\theta = 1/2$ corresponds to Crank-Nicolson method. The resulting system of equation to be solved at each time step is a tridiagonal system, which can be solved efficiently with a Thomas algorithm. In the case of multi-dimensional diffusion, one can employ the similar approach of dimensional splitting described in the previous section.

3.3 Benchmark problems

In this section, a series of benchmark test cases is presented to validate the numerical method described in section 3.2. Although most of the simulations are limited to one-dimensional and a few two-dimensional test cases, the numerical method

can be easily generalized to three-dimensional, if the computational resource permits. The reason is because the current research puts emphasis on high-fidelity physical models associated with multiple couplings of the plasma, thus imposing a large requirement on the computer resource. As will be shown later, some of these models are not practical for multidimensional calculation, and a complexity reduction strategy must be formulated.

3.3.1 Euler equations

3.3.1.1 Blastwave problem

The first problem presented for the solution of the Euler equations is the Woodward-Colella blast wave problem [71]. This problem is designed to test the capability of the numerical scheme to handle interaction of strong shock waves. The problem is initialized with two strong shocks travelling past each other and reflected from the wall to expedite multiple interactions. The initial condition of the problem for a domain of $x \in (0, 1)$ is given as:

$$[\rho, u_x, p] = \begin{cases} [1, 0, 10^3] & \text{if } x < 0.1 \\ [1, 0, 10^{-3}] & \text{if } 0.1 \leq x \leq 0.8 \\ [1, 0, 10^2] & \text{if } x > 0.8 \end{cases} \tag{3.71}$$

Figures 3.2 shows the numerical solution of the blast wave problem with 600 cells at $t = 0.038$. The reference solution is computed using MP5 scheme with 5,000 cells. As shown in figure 3.2, the contact discontinuity is well-resolved for both MP5 and WENO scheme. The MP5 scheme performs slightly better in resolving the contact. It must be noted that artificial compression method can be used to enhance resolution in the near the discontinuity. Such a method was not applied here since we want the scheme to be robust and free of numerical parameters which are problem-dependent.

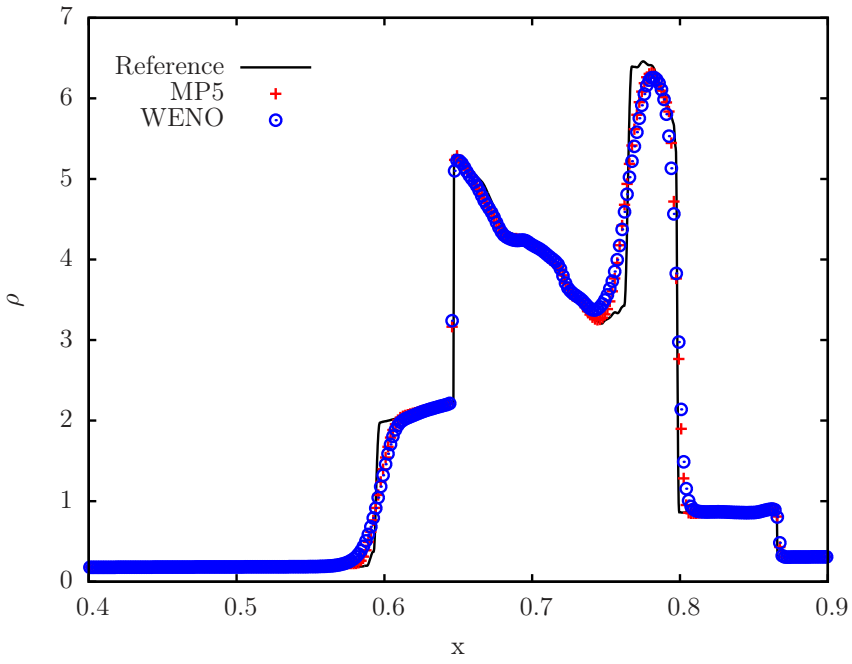

Figure 3.2: Solution of the Woodward-Colella blast wave problem with 600 cells. Only part of the simulated domain is shown to illustrate the difference of two schemes.

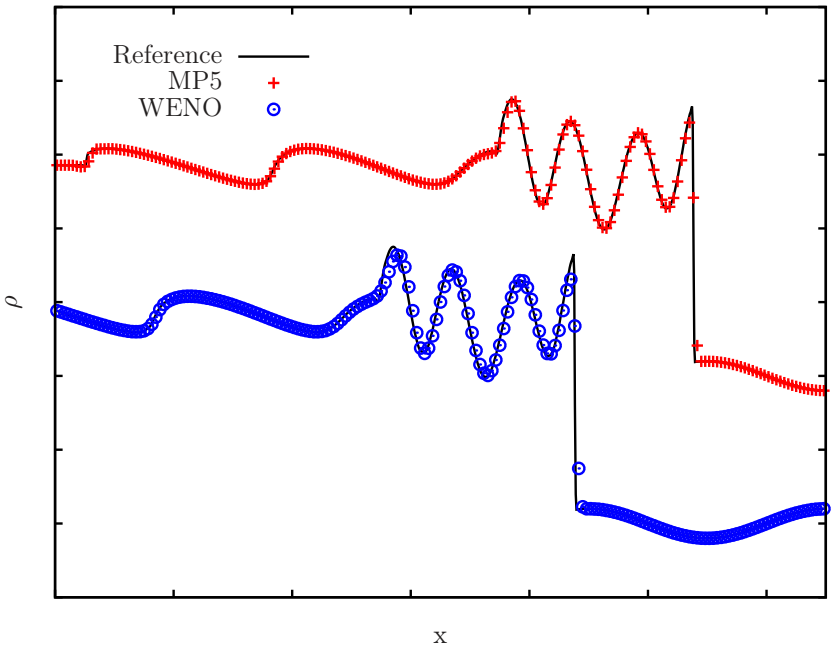

Figure 3.3: Solution of the Shu-Osher problem with 300 cells. Only part of the simulated domain is shown to illustrate the difference of two schemes.

3.3.1.2 Shu-Osher problem

The next test case is the Shu-Osher problem, which models the interaction of a moving shock wave with an entropy disturbance. This problem can be used to test the capability of the scheme to resolve complex flow structure with instability. The initial condition for the problem is given for a domain of $x \in [-1, 1]$ as follows:

$$[\rho, u_x, p] = \begin{cases} [3.857, 2.629, 10.333] & \text{if } x < -0.8 \\ [1 + 0.2\sin(5\pi x), 0, 1] & \text{if } x \geq -0.8 \end{cases} \tag{3.72}$$

Figures 3.3 shows the density plot of the solution using 300 cells at $t = 0.36$. The reference solution is computed using the MP5 scheme with 1600 cells. The solution obtained with both MP5 and WENO schemes shows that complex flow features such as local maximum and minimum density can be efficiently resolved in high-resolution.

3.3.1.3 Forward step problem

Results of two-dimensional test cases are now presented. From the one-dimensional test cases, we learn that MP5 provides slightly better results than WENO in resolving the discontinuity and entropy waves. However, the CFL restriction of the MP5 scheme is more severe than that of the WENO scheme. Therefore, WENO scheme is slightly at more advantage in terms time step requirement, but the MP5 scheme generally yields better solution. For brevity, only the solution computed using the MP5 scheme is presented.

The first two-dimensional test problem is the forward step problem, also known as the Emery problem, or the Mach-3 wind tunnel problem. The problem consists of uniform flow of Mach-3 past a step. The step and upper part boundaries of the domain is set to be reflective. For the left and the right boundaries, simple extrapolation is sufficient. An interesting feature of this problem is located at the corner of the step. Numerical error generated in this region can create a so-called numerical boundary layer which can affect the structure of the flow. A treatment of this problem was given by Woodward and Colella [72], and is not used here.

Figures 3.4 shows the solution of forward step problem with 600,000 computational cells using the MP5 scheme. The WENO solution of this problem, although not shown here, yields similar results but slightly more diffusive notably in the Kelvin-Helmholtz instability occurring near the top of the domain. This is consistent with the observation from the 1D simulations.

3.3.1.4 Backward step problem

The next test involves a similar problem of a diffraction of a shock wave (M = 2.4) down a step [73]. The strong rarefaction at the corner of the step can cause a problem of negative density when performing the reconstruction. The problem is modeled here using 27,000 cells, and the numerical simulation is shown along

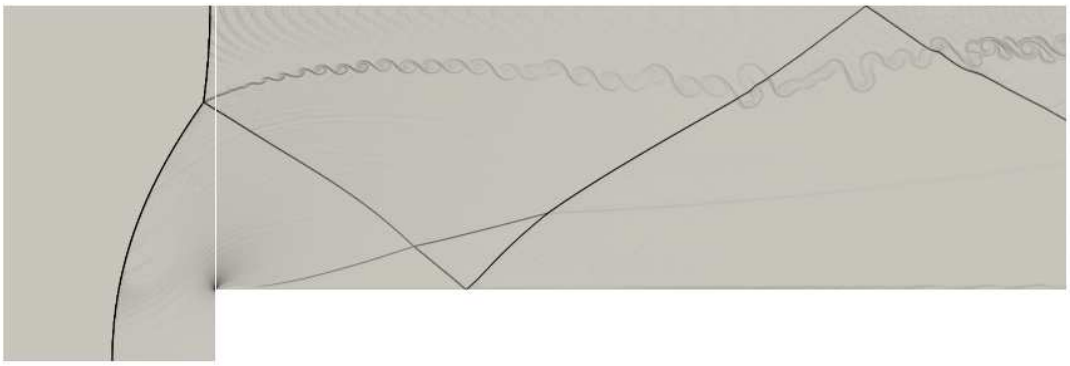

Figure 3.4: Solution of the forward step problem using MP5 scheme with 600,000 cells.

with the experimental images in figure 3.5. The solver was able to reproduce the correct flow features with excellent accuracy.

3.3.1.5 Rayleigh-Taylor instabilities

The Rayleigh-Taylor instability problem [74] is simulated in this section. The problem is described as the acceleration of a heavy fluid into a light fluid driven by gravity. In this test case, the specific heat ratio is set to be a constant ($\gamma = 1.4$). For a rectangular domain of (0.25×1), the initial conditions are given as follows:

$$\rho = 2, u = 0, v = -0.025\cos(8\pi x), p = 2y + 1 \text{ for } 0 \leq y \leq \frac{1}{2} \tag{3.73}$$

$$\rho = 1, u = 0, v = -0.025a\cos(8\pi x), p = y + \frac{3}{2} \text{ for } \frac{1}{2} \leq y \leq 1 \tag{3.74}$$

where a is the speed of sound. The top and bottom boundaries are set as reflecting and the left and right boundaries are periodic. As the flow progresses, the shear layer starts to develop and the Kelvin-Helmholtz instabilities become more evident, as can be seen in figure 3.6. A momentum and energy source terms are added to account for the gravitational effects.

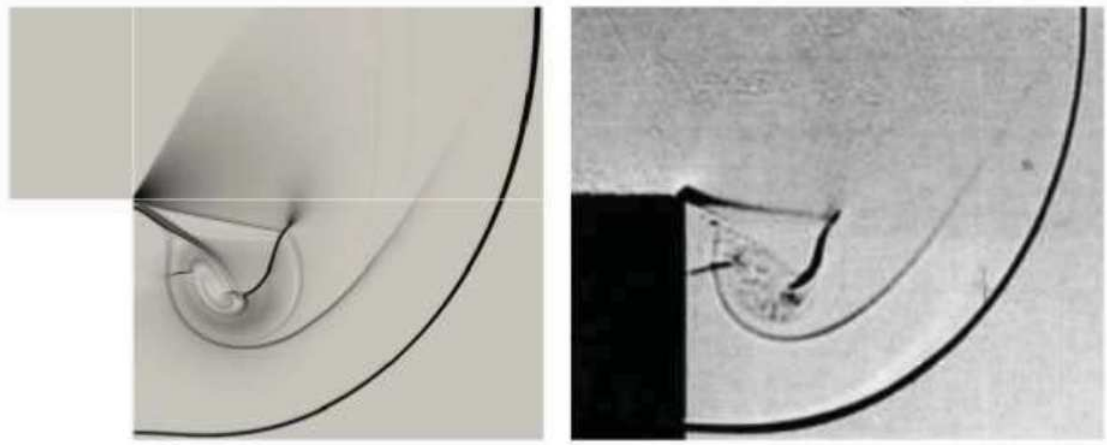

Figure 3.5: Diffraction of a Mach 2.4 shock wave down a step using MP5 scheme with 27,000 cells. Comparison between numerical schlieren (left) and experimental image (right).

3.3.1.6 Two-dimensional detonation

Modeling of a reactive flow field is now considered. A spark-ignited detonation wave both in one- and two-dimension is simulated to demonstrate the capability of the solver. Only the two-dimensional results are shown here. At a well-resolved scale, the detonation wave can be described as a strong shock wave supported by the heat release from a high-temperature flame behind an induction zone. Interesting features have been observed both in the 1-D and 2-D simulations, characterized by the coupling of the fluid dynamics and chemical kinetics. The study of flame-shock coupling dynamics in one-dimension is described in [75].

The evolution of the pressure and temperature of a wall-spark ignited detonation is shown in Figure 3.7. The chemical kinetics is modeled using the reduced H_2-air mechanism which consists of 9 species gas mixture with 38 reactions. The mechanism used for the simulation is taken from the shock tube study by Jachimowski [76]. The computational domain is rectangular with a length of 20 cm and a height of 2 cm. The grid spacing in both directions is 50 μm.

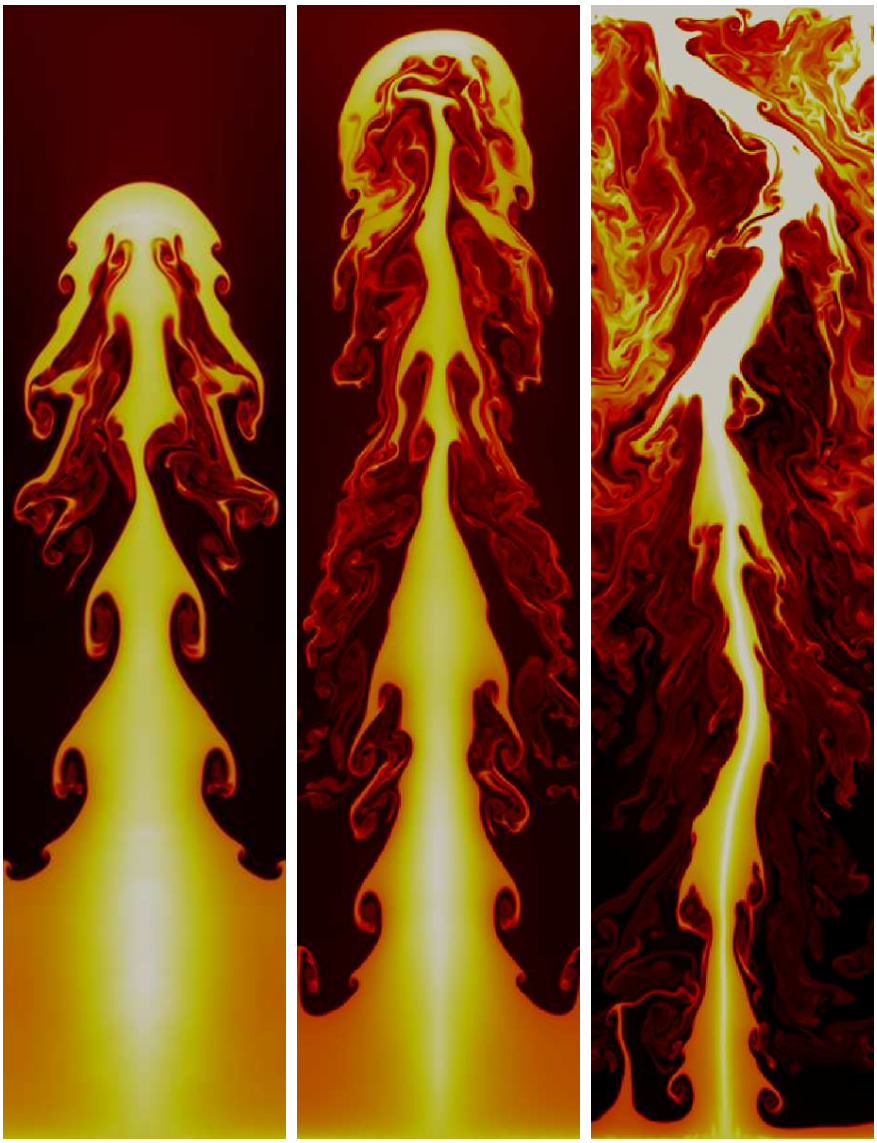

Figure 3.6: Rayleigh-Taylor instability computed with the MP5 scheme using 640,000 cells.

The detonation cells, between the shock and multiple triple points in transverse motion, is clearly seen. Figure 3.8 illustrates the numerical soot film produced by recording the maximum density reached at each computation cell over the entire simulation time which is used to measure the cell structure. This well-known cellular structure has been observed both in experiments and numerical simulations. Various techniques in reproducing these images are discussed by Sharpe and Radulescu [77].

3.3.2 Multi-fluid equations

In this section, several test cases of the multi-fluid equations are described. Before getting into the solution of the full multi-fluid model, the first two test cases model a sheath problem utilizing a simple model for the electron fluids. In these test cases, the electrons are assumed to be in Boltzmann equilibrium with the electrostatic field. At any time, the electron density can be expressed as:

$$n_e = n_0 e^{-(\phi-\phi_0)/kT_e} \tag{3.75}$$

where n_0 is a reference number density value and ϕ_0 is a corresponding reference potential. In this case, we solve a non-linear Poisson equation for the electric field:

$$\nabla^2\phi = -\frac{e}{\epsilon_0} n_i Z_i + \frac{e}{\epsilon_0} n_0 e^{-(\phi-\phi_0)/kT_e} \tag{3.76}$$

This approximation is used to simulate both a transient and steady-state sheath problem.

3.3.2.1 Transient sheath

For the transient sheath problem, the reference plasma condition is $n_0 = 10^{-14} m^{-3}$, $T_i = 0.025$ eV and $T_e = 1$ eV. This corresponds to an ion plasma frequency, $\omega_{pi} = 2.086 \times 10^{-6}$ rad/sec, and a Debye length $\lambda_D = 74.3$ mm as defined in equation (2.17). The transient sheath problem is computed on 1D domain of

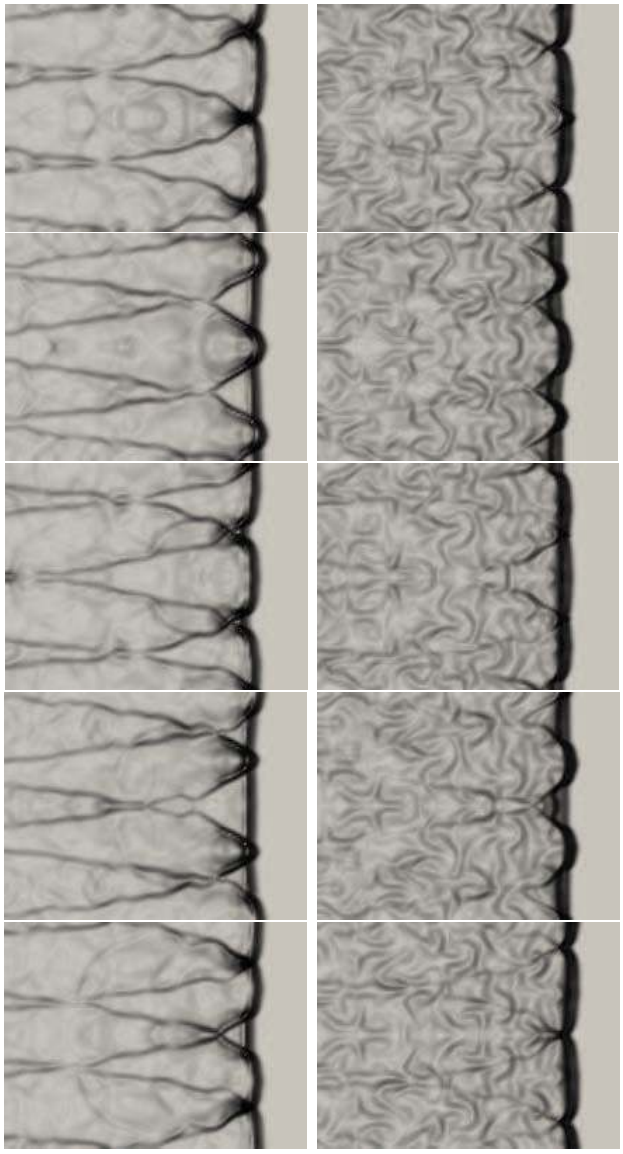

Figure 3.7: Evolution of pressure and temperature in a 2D detonation simulation.

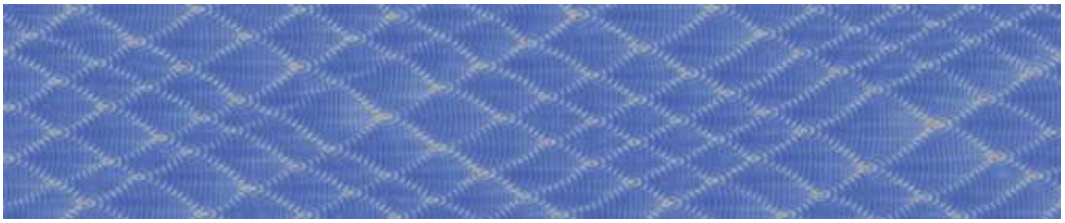

Figure 3.8: Numerical soot film produced by recording the maximum density at each grid cell over the entire simulation for a 2D detonation corresponding to figure 3.7.

$L = 200\lambda_D$. Initially, the domain is filled with ions at rest with number density $n_i = n_0$. At $t = 0$, the electric field is introduced, by setting the electric potential to -50 V at $x = 0$, and 0 V at $x = L$. The electrons are assumed to be in Boltzmann equilibrium. For the ions, the full Euler equations are solved using the WENO scheme. The solution of the electric field is determined from the solution of equation (3.76).

In this simulation, the ion boundary conditions are treated by simple extrapolation. Figure 3.9 shows the profile of the ion and electrons number densities at different instances of time, as well as the time history of the ion current collected at the electrode. The numerical solution of the ion current are compared and in good agreement to the analytical results of Lieberman [78].

3.3.2.2 Steady sheath

The reference plasma condition of the steady sheath is similar to that of the transient sheath simulation. The solution is computed on a 1D domain of $L = 100\lambda_D$. In order to obtain a steady-state sheath, the ion loss to the wall is made up by introducing a ionizing source term $\omega_I = n_e z$ where $z = \frac{n_i u_i|_{x=0}}{\int n_e dx}$. The steady-state is achieved when the ionization rate z has reach a steady value, i.e., the ion loss is exactly balanced by ionizing source and therefore the sheath reaches

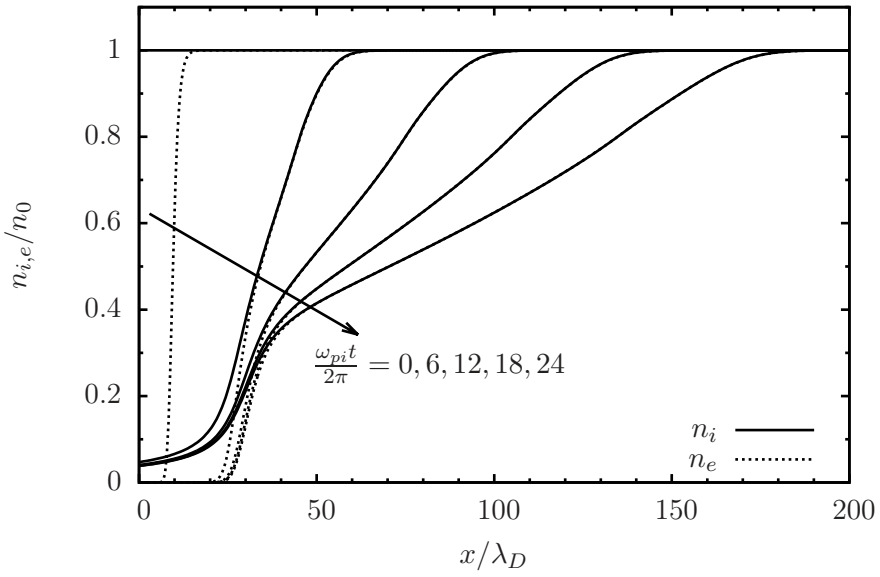

(a) Ion and electron number densities

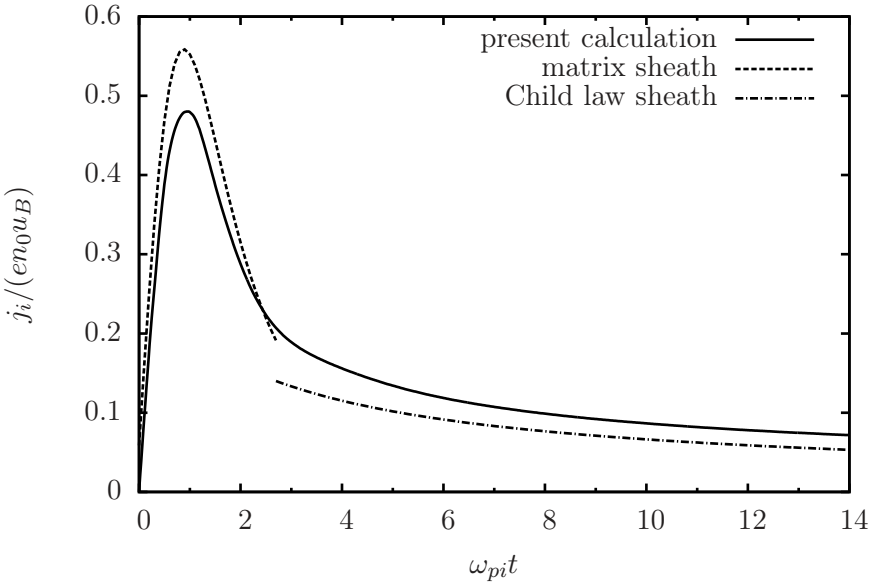

(b) Ion current

Figure 3.9: Number density of the ions at the electron at different time and comparison of the time evolution of the ion current at the electrode with analytical solution of Lieberman [78]. Time is normalized by the ion plasma frequency, and velocity is normalized by the Bohm velocity $u_B = \sqrt{\frac{kT_e}{m_i}}$.

an equilibrium state. In this problem, the electrons are also assumed to be in Boltzmann equilibrium, and the ion fluid equation is solved using WENO scheme. Figure 3.10 shows the spatial profile of the ions number density, velocity and the electric potential at the steady-state condition.

In addition, we also computed a steady-state sheath with a collisional friction force. This acts as a source term on the momentum equation of the ions, which is written as follows:

$$f_i = -\frac{|u_i|}{\lambda_i}\rho_i u_i \tag{3.77}$$

where λ_i is the ion mean-free-path. One also has a corresponding heating term due to the work done by the friction force. Figure 3.11 shows the electric potential as well as the ion velocity with collisional drag term. For the collisional case, the sheath thickness slightly increases, and the ion velocity at the electrode are lower than the collisionless case. This indicates that the ions while moving to the electrode experiences a drag force, resulting in a thicker sheath.

3.3.2.3 Generalized Brio-Wu problem

This is a generalization of the standard Brio-Wu problem often used to benchmark MHD codes. The MHD approximation corresponds to the use of Ohm's law in deriving a steady-state current density, which was derived in section 2.3. In the case of a fully-ionized plasma, Ohn's law can be written as:

$$\mathbf{E} + \mathbf{u} \times \mathbf{B} = \frac{1}{en_e}\left(\mathbf{j} \times \mathbf{B} - \nabla p_e + \mathbf{R}_{ei}\right) \tag{3.78}$$

The ideal MHD limit simply means $\mathbf{E} + \mathbf{u} \times \mathbf{B} \simeq 0$, i.e., all the terms on the RHS are small. One can derive a scaling relation such that ideal MHD condition is satisfied. Following the work of Freidberg [79], the sufficient conditions for ideal MHD are (1) small Larmor radius, and (2) weak collisionality[2]. The Larmor radii

[2]The collisionality should be weak enough for diffusion to be neglected but still strong enough to satisfy hydrodynamic theory.

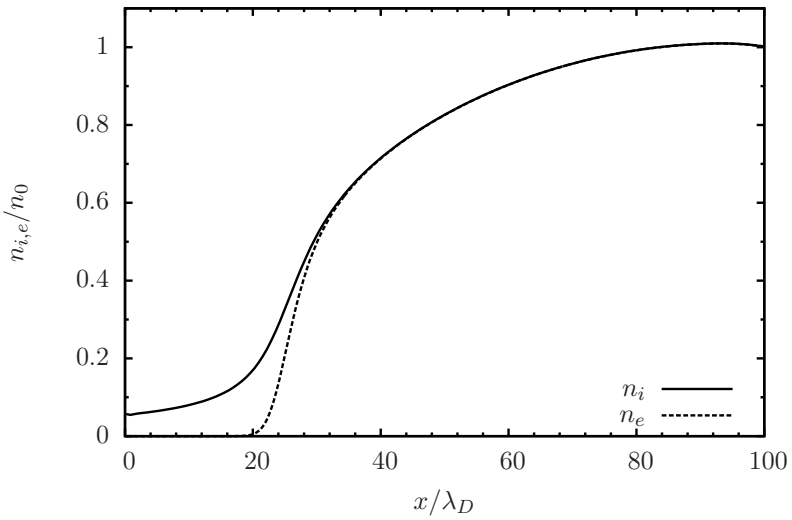

(a) Ion and electron number densities

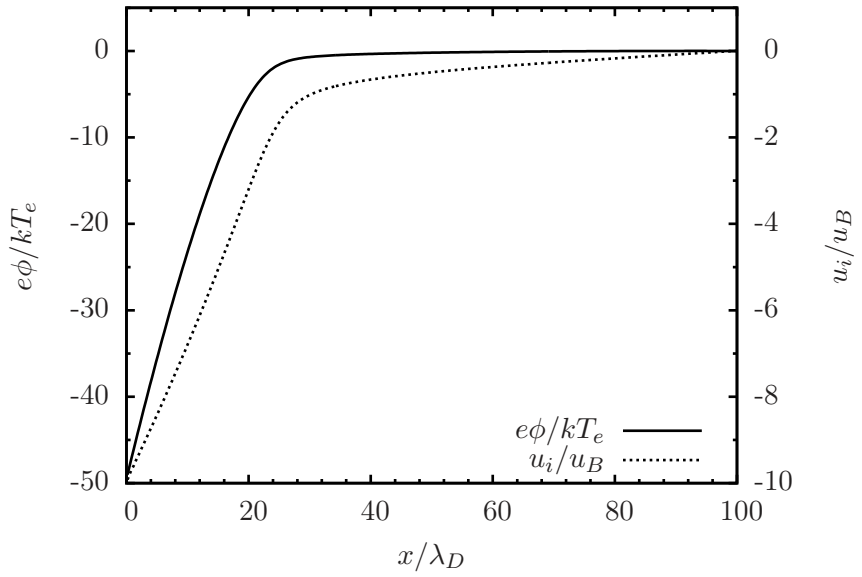

(b) Ion velocity and electric potential

Figure 3.10: Number density and velocity profile of the ions and the electric potential at steady-state condition. Velocity is normalized by the Bohm velocity $u_B = \sqrt{\frac{kT_e}{m_i}}$.

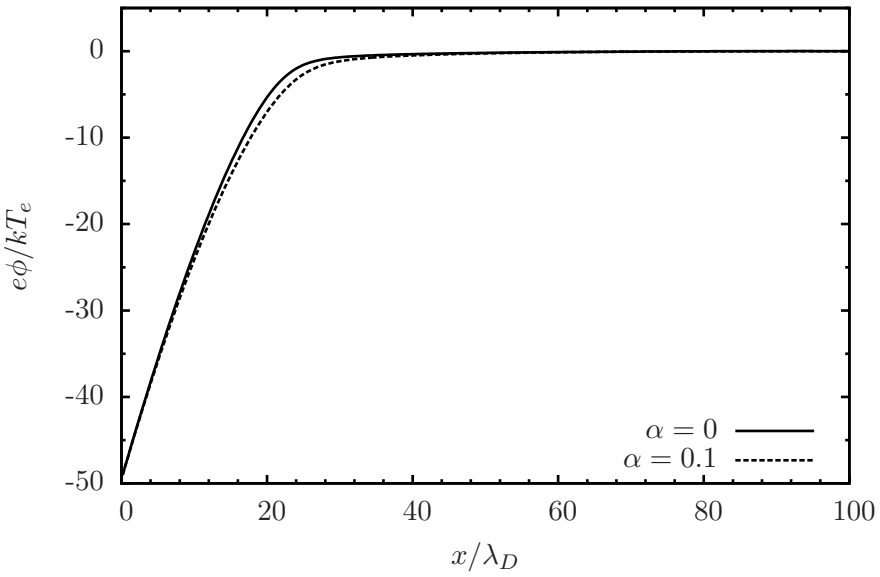

(a) Electric potential

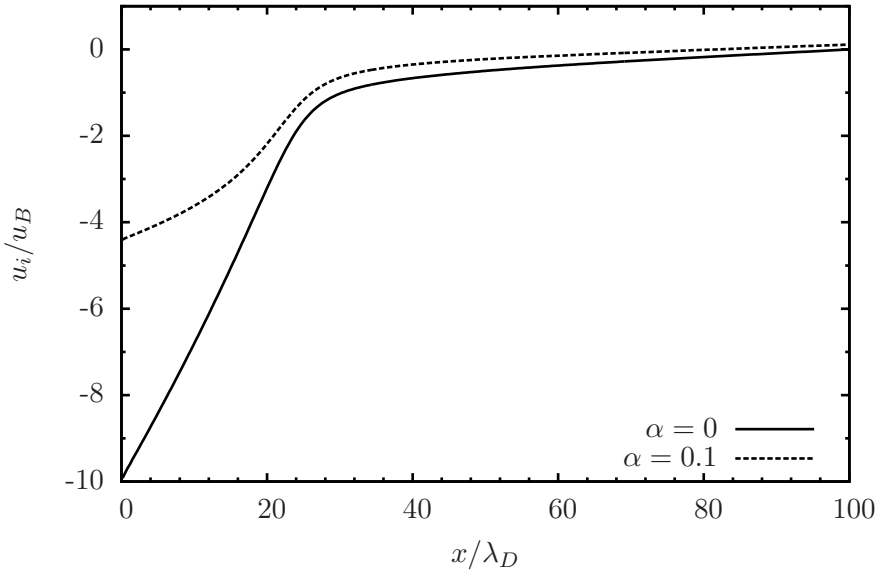

(b) Ion velocity

Figure 3.11: Electric potential and velocity profile of the ions at steady-state condition with and without collisional drag. Velocity is normalized by the Bohm velocity $u_B = \sqrt{\frac{kT_e}{m_i}}$ and $\alpha = \frac{\lambda_D}{\lambda_i}$.

for the ion and electron, defined in equation (2.18), are related as:

$$\frac{r_{Le}}{r_{Li}} \simeq Z_i \sqrt{m_e/m_i} \tag{3.79}$$

where we have assumed $T_i \simeq T_e$. Therefore, we expect that the two-fluid model produces results comparable to the ideal MHD solution at the correct asymptotic limit, that is, in the limit of small electron-ion mass ratio, infinite speed of light, charge neutrality, strongly conducting and large magnetic field. The first three assumptions come from the general MHD approximation.

Strictly speaking, we do not expect an exact agreement between the two-fluid solution and the ideal MHD solution due to the following reasons. Firstly, the two-fluid solution can still capture some electron inertial effects and electromanetic wave propagation; these physics are missing from the ideal MHD model. Secondly, the numerical solution utilizing the MHD model can vary depends on the numerical formulation of the governing equations, and this is purely a numerical artifact. For example, Thompson et al [80] reproduced the solution of the Brio-Wu problem using two different formulations of the magneto-fluid-dynamics (MFD) equations[3] and the results are slightly different from each other.

The initial conditions of the ideal two-fluid electromagnetic shock problem is given by Shumlak and Loverich [81]. In this simulation we assumed a mass ratio $m_i/m_e = 1836$, constant of adiabatic index $\gamma = 5/3$, and set $\epsilon_0, \mu_0, c = 1$. Coulomb collisions are neglected in this simulation such that resistive effects can be neglected. The shock is created by a initial discontinuity in the middle of the

[3]The MFD equations still assume massless electrons but they contain EM wave propagation and charge separation.

domain as follows:

$$\begin{bmatrix} \rho_i \\ u_i^{x,y,z} \\ p_i \\ \rho_e \\ u_e^{x,y,z} \\ p_e \\ B^x \\ B^y \\ B^z \\ E^{x,y,z} \end{bmatrix} = \begin{bmatrix} 1 \\ 0 \\ 5\times10^{-5} \\ m_e/m_i \\ 0 \\ 5\times10^{-5} \\ 0.75\times10^{-2} \\ 1\times10^{-2} \\ 0 \\ 0 \end{bmatrix} \text{ for } x<0; \quad \begin{bmatrix} \rho_i \\ u_i^{x,y,z} \\ p_i \\ \rho_e \\ u_e^{x,y,z} \\ p_e \\ B^x \\ B^y \\ B^z \\ E^{x,y,z} \end{bmatrix} = \begin{bmatrix} 0.125 \\ 0 \\ 5\times10^{-6} \\ 0.125m_e/m_i \\ 0 \\ 5\times10^{-6} \\ 0.75\times10^{-2} \\ -1\times10^{-2} \\ 0 \\ 0 \end{bmatrix} \text{ for } x>0 \tag{3.80}$$

Figure 3.12 shows the ion density for several values of the Larmor radius in addition to the MHD solution of the same problem. WENO schemes are used to solve the fluid and Maxwell's equations for all the test cases here. It was shown that in the limit of $r_{Li} \to 0$ (or r_{Le}), the solution of the two-fluid equation converges to the MHD solution. Same argument can be made about the solution of the transverse magnetic field as shown in figure 3.13.

Two observations were made about the solution of the collisionless two-fluid system. Firstly, it is important that the spatial accuracy of the numerical schemes for solving the fluid and Maxwell's equation is consistent; inconsistency causes the solution to be diffusive. Secondly, since the source term is solved implicitly, a time step restriction is imposed for purposes of accuracy. Typically, in the source term corresponding to the Lorentz force and Joule heating, the time step size is chosen relative to ω_{pe}. All the solutions shown in figure 3.12 correspond to a time step size of $0.1\omega_{pe}$ which is the smallest time step in the system. The solution obtained with a larger time step is more diffusive. These simulations show that the multi-fluid system retains all the correct asymptotic limit of MHD approximation, and

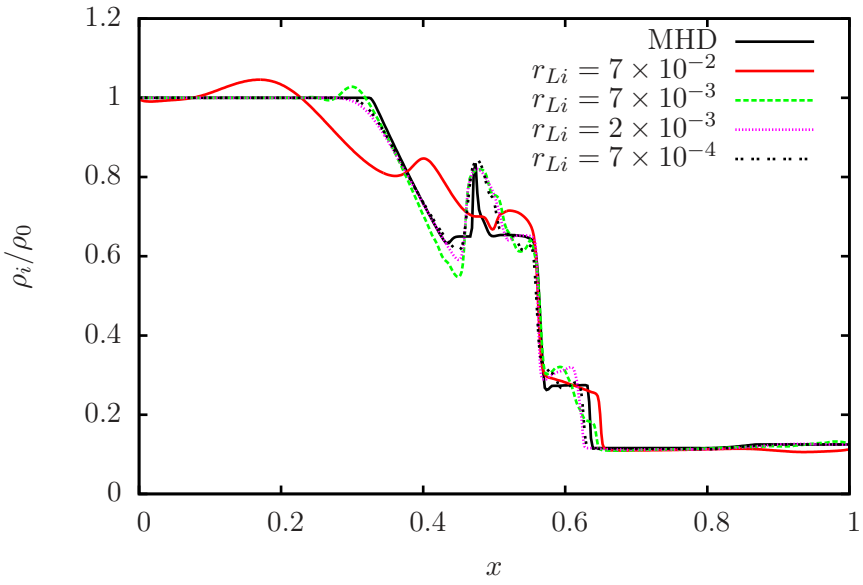

Figure 3.12: Ion density of the ideal two-fluid Riemann problem

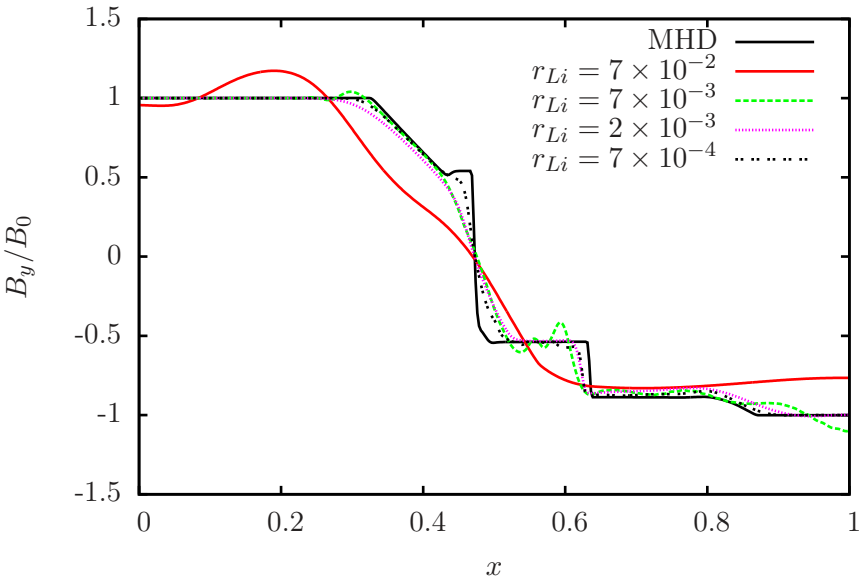

Figure 3.13: Transverse magnetic field of the ideal two-fluid Riemann problem

also includes additional physics of electromagnetic wave propagation and charge separation. However, in the MHD limit, the two-fluid system becomes stiff and the time-step restriction (for accuracy purpose) is quite severe.

3.3.3 Diffusion processes

3.3.3.1 Travelling thermal wave problem

In this section, a one-dimensional travelling heat wave problem is simulated. The problem is representative of the electron thermal transport process in LPI problem. The model equation reads:

$$\partial_t T = \partial_x \left(\lambda_0 T^\alpha \partial_x T \right) \tag{3.81}$$

with the following initial and boundary conditions:

$$T(0,t) = \left[\frac{\alpha D}{\lambda_0} (x_1 + Dt) \right]^{1/\alpha} \tag{3.82}$$

$$T(x,0) = \left[\frac{\alpha D}{\lambda_0} (x_1 - x) \right]^{1/\alpha}; \qquad 0 < x \leq x_1 \tag{3.83}$$

$$T(x,0) = 0 \qquad \text{otherwise} \tag{3.84}$$

The exact solution for this problem reads:

$$T(x,t) = \left[\frac{\alpha D}{\lambda_0} (Dt + x_1 - x) \right]^{1/\alpha}; \qquad x \leq x_1 + Dt \tag{3.85}$$

Figure 3.14 shows the solution of the model problem for $x_1 = 0$, $\lambda_0 = 0.5$, $D = 5$ and $\alpha = 2$ at $t = 0.1$. In this case, the explicit time step corresponds to 10^{-6}. The implicit scheme allows a time step of three orders of magnitude larger than that required for the explicit scheme while the error for the two cases are of the same order of magnitude. This indicates the robustness of the implicit scheme in handling larger time step, which is a desired properties, since transport phenomena can be stiff, e.g., the electron heat conduction process, and the coupling with convection can lift the stiffness ratio of the system.

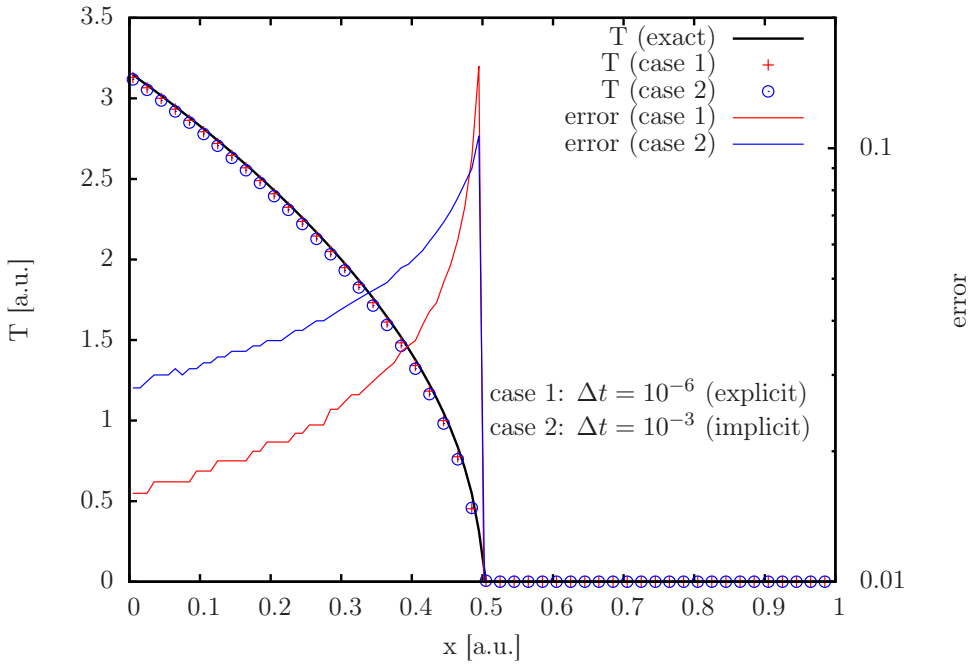

Figure 3.14: Numerical solution and error of the heat conduction problem with 100 cells using both explicit and implicit schemes. The explicit scheme is stable for $\Delta t \leq 10^{-6}$ while the implicit scheme is stable up to $\Delta t = 10^{-3}$.

3.3.3.2 Laser produced plasmas with hot spot

In this section, we simulate the heat transport process of a laser produced plasma hot spot. Convection is neglected here. This problem was simulated using Fokker-Planck and PIC models by Batishchev [82] to study non-local heat transport theory. Generally speaking, non-local effects becomes important when the temperature gradient length scale is of the same order as the collision mean free path. In such case, the electron energy distribution function (EEDF) becomes non-Maxwellian and the classical (local) SH transport [54] breaks down. The current simulation is set up such that classical SH transport remains valid. There are two reference time and length scales, namely the electron collision time τ_e and mean free path λ_e.

$$\tau_e = \frac{3\sqrt{m_e}T_e^{3/2}}{4\sqrt{2\pi}e^4Z^2n_e\ln\Lambda} = 3.5\times10^5\frac{T_e^{3/2}}{Zn_e\ln\Lambda}[sec] \tag{3.86}$$

$$\lambda_e = \frac{3T_e^2}{4\sqrt{2\pi}e^4Z^2n_e\ln\Lambda} = 1.5\times10^{12}\frac{T_e^2}{Zn_e\ln\Lambda}[cm] \tag{3.87}$$

$$\tag{3.88}$$

where T_e is in eV, n_e is in cm^{-3}, and $\ln\Lambda$ is the Coulomb logarithm.

In the first test, we only consider the effect of thermal transport. The problem is initialized with a quasi-neutral plasma containing (Ar^+, e) with an initial electron temperature enhancement near the center. This condition is representative of plasma heating process due to laser absorption. The reference number density are $n_e = n_i = n_0 = 10^{16}\ cm^{-3}$ and $T_0 = 10\ eV$. The domain length, L, is set to span $[-300\lambda_e, 300\lambda_e]$, and the initial electron temperature is assumed to be a spatial Gaussian profile:

$$T_e(x, t=0) = T_0 + T_1e^{-x^2/l^2} \tag{3.89}$$

where $l = 50\lambda_{ei}$ and $T_1 = 0.4T_0$. The electron heat flux from SH theory are

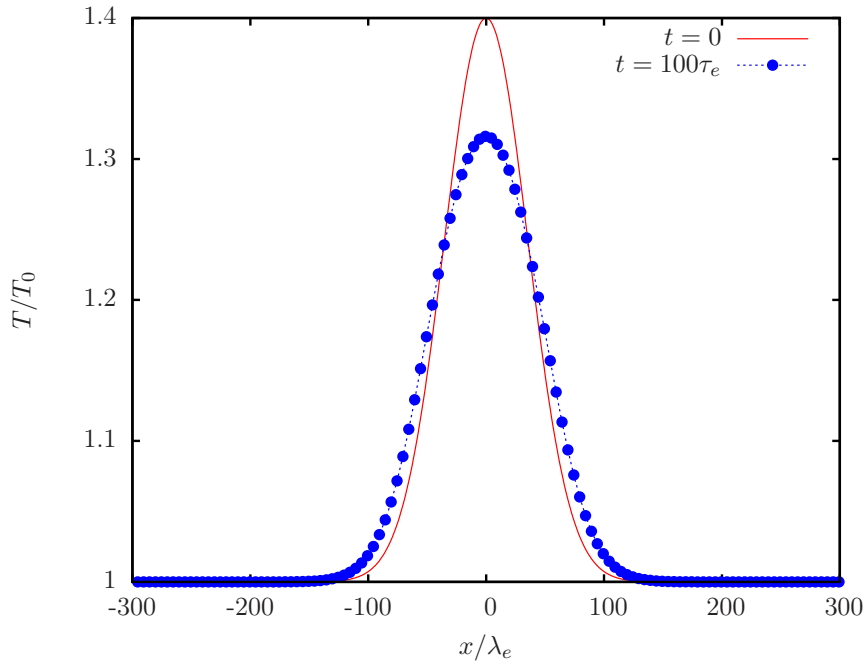

Figure 3.15: Temperature profile at $t = 100\tau_e$ for the hot spot relaxation by electron heat conduction. The solid line indicated the initial temperature.

written as:

$$\mathbf{q}_e = -\kappa_e \nabla T_e \tag{3.90}$$

where $\kappa_e = \gamma_0 n_e k^2 T_e \tau_e / m_e$ and γ_0 is a function depending weakly on ion charge Z. The values of γ_0 for different Z are given in [46, 83, 84]. Here we take $\gamma_0 = 3.16$. This is known as the classical SH transport. This result breaks down when $\frac{\lambda_e}{T/\nabla T}$ exceeds a value of approximately 10^{-2} [85]. Figure 3.15 shows the profile of the electron temperature at time $t = 100\tau_e$, at which the temperature starts diffusing outward. In the simulation, we also include Coulomb thermalization, but the final result shows very little dependence on this term. This is because the energy relaxation time scale between the ions and the electrons is much slower than the diffusive time scales, e.g., $\tau_e \sim (m_e/m_i)\tau_{ei}^{\varepsilon}$.

In the second test, we consider laser absorption due to inverse Bremsstrahlung processes. The electron energy equation now includes an addition term due to the

absorption, and can be written as:

$$\partial_t E_e + \nabla \cdot \mathbf{q}_e = \alpha I \tag{3.91}$$

where α is the absorption coefficient due to collisional process, and I is the laser intensity. Here we assume I is only spatially dependent and takes the form:

$$I(x) = I_0 e^{-x^2/d^2} \tag{3.92}$$

where $I_0 = 10^{12}\ W/cm^2$ and $d = 10\lambda_e$. The absorption coefficient is defined as follows:

$$\alpha = \frac{\nu}{c}\frac{\omega_{pe}^2}{\omega^2}\left(1 - \frac{\omega_{pe}^2}{\omega^2}\right)^{1/2} \tag{3.93}$$

where ν is the collisional frequency, ω is the laser frequency, and c is the speed of light.

Figure 3.16 shows the temperature profile at $t = 100\tau_e$ and a comparison with the former case where IB process was not included. When the laser absorption is taken into account, the electron temperature begins to rise, especially at the center of the hot spot. Figure 3.17 also shows a comparison of the thermal heat flux in both cases. The magnitude of the heat fluxes in both cases remains below 10% of the freestream limit $q_f = p_e(kT_e/m_e)^{1/2}$. SH results tend to break down when the heat-flux exceeds approximately 15% of the free-stream value.

3.3.3.3 Hypersonic shocks

We now simulate a 1D hypersonic plasma shock with electron heat conduction. This test is designed to test the coupling of the transport and convection in addition to thermalization via Coulomb collision. The shock is initiated by imposing a uniform flow with a wall on the right side of the domain. The freestream condition is a fully ionized plasma with (Ar^+, e) where $n_i = n_e = 2.14 \times 10^{14}$ cm^{-3}, $T_\infty = 273$, and $u_\infty = 7000$ m/s. The fluid equations are solved with the MP5 scheme.

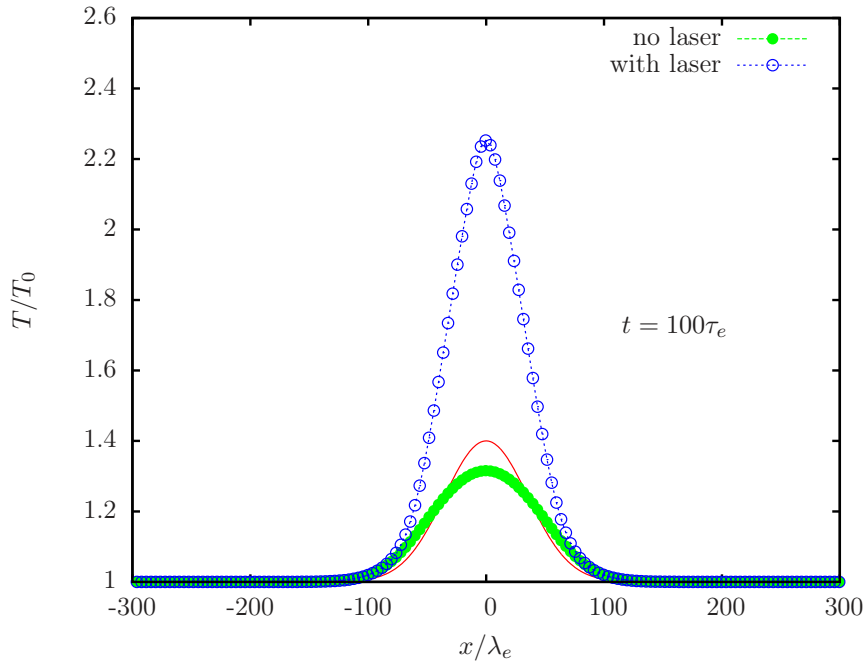

Figure 3.16: Temperature profile for the hot spot simulation with and without laser heating.

Figure 3.18 shows the results for a nitrogen plasma shock computed with and without heat conduction. For the case with heat conduction, the post shock temperature of the heavy particles is lower due to precursor conductive heating of the electron, effectively raising the speed of sound of the plasma ahead of the shock. In case of a partially ionized plasma, this precursor heating can yield interesting dynamics such as precursor excitation and radiation.

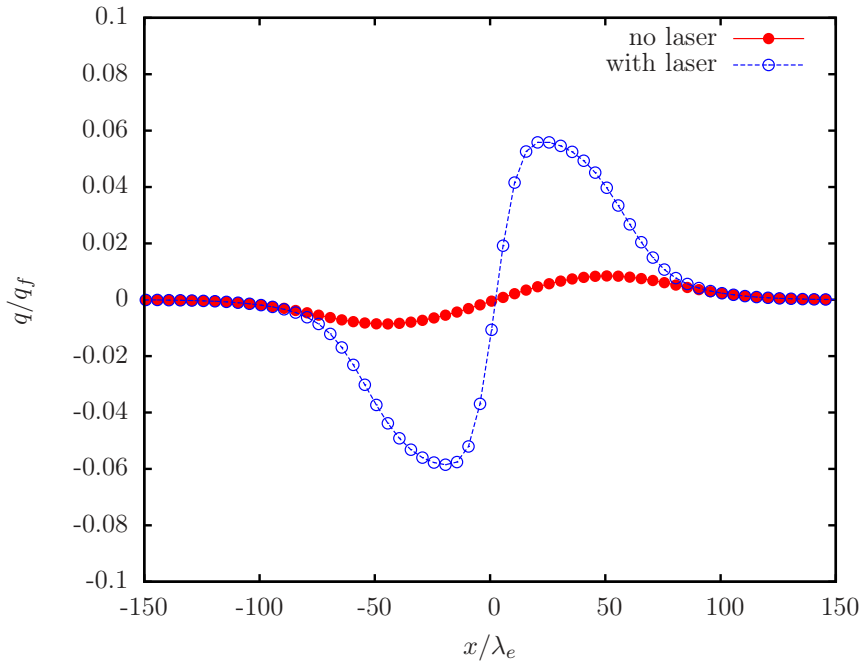

Figure 3.17: Heat flux for the hot spot simulation with and without laser heating. The value of the heat flux is normalized by the freestream limit given by $q_f = p_e(kT_e/m_e)^{1/2}$.

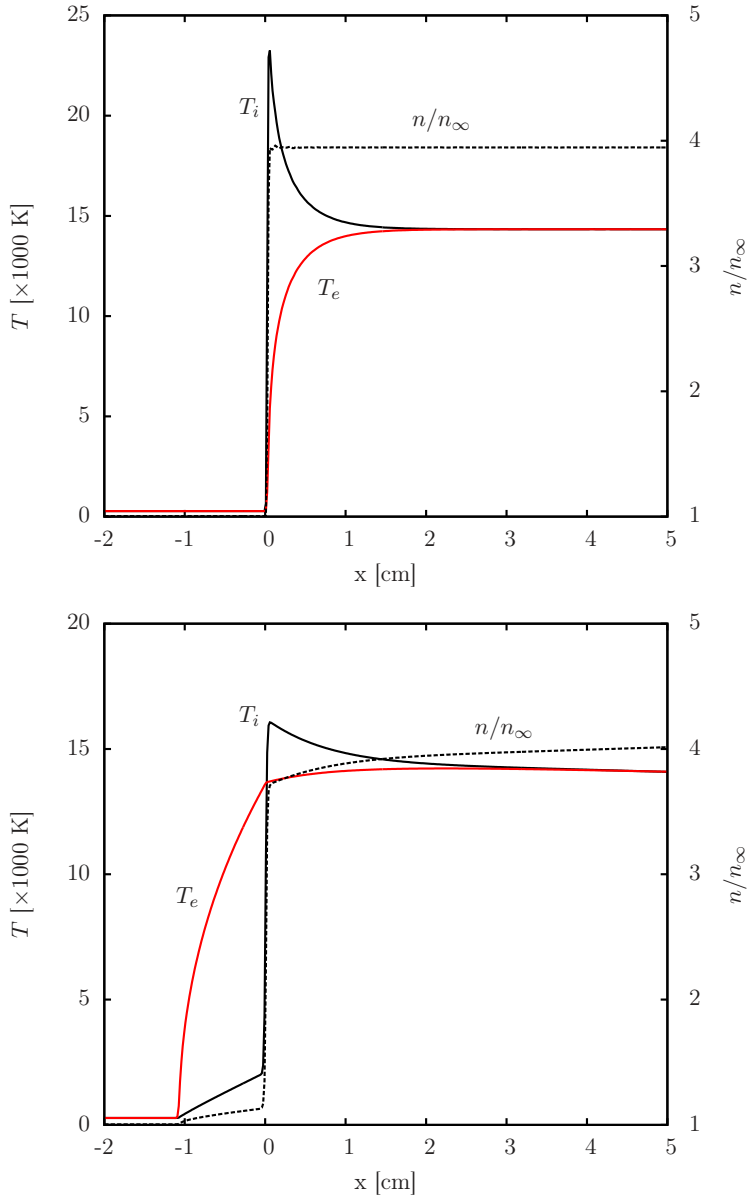

Figure 3.18: Steady profile of a shock propagation into a cold Nitrogen plasma (N^+, e) with (bottom) and without (top) electron heat conduction. Free stream conditions are $u_\infty = 7000$ m/s, $T_\infty = 273$ K, $n_\infty = 2.14 \times 10^{14}$ cm^{-3}. Solid lines are ion (black) and electron (red) temperatures. The dashed line is the number density. The x axis is adjusted so the shock starts at $x = 0$.

CHAPTER 4

Collisional-Radiative Models for Atoms

4.1 Introduction

This chapter goes over a detailed description of the CR models for an atomic plasma. Firstly, different thermal equilibrium distributions are derived, and the principle of detailed balance is discussed for various elementary processes implemented in the CR model. Due to the great complexity in the collection of inelastic processes which could occur in a plasma, we limit ourselves to discussing only several important inelastic processes occurring in an atomic plasma: collisional and radiative excitations/deexcitation, and ionization/recombination. A more complete description of these processes can be found in [86, 87, 88, 89, 83].

Secondly, we describe in detail the cross section models for Argon, Krypton, and Xenon for all the CR transitions. The model for Argon was previously developed by Kapper and Cambier [90] based on prior work of Vlček [91] and Bultel *et al.* [92] with mostly *ab initio* cross sections for electron-impact processes and semi-empirical model for atom-impact processes. Preliminary extensions to Krypton and Xenon were carried out by Magin and Kapper [93] with a software framework named Colorado. We extend their work by adding more *ab initio* cross sections for electron-impact processes, updating some of the old cross sections, and validating the models with available shock tube experimental data.

4.2 Thermal equilibrium

This section goes over various thermodynamic equilibrium distribution of gases and plasmas. Thermodynamic equilibrium of radiation field is also discussed, since it can play an important role in the inelastic exchange processes especially for very high temperature plasmas. It must be noted that thermodynamic equilibrium distributions can be determined from statistical thermodynamics and the principle of maximum entropy. In this section, we derive thermal equilibrium distributions using a different approach, that is, by considering the equilibrium reaction balance of different processes.

We start with the *principle of microscopic reversibility (MR)* which states that in thermal equilibrium, any reaction from a quantum state to another state is exactly counterbalanced by the reverse reaction. In the classical limit, i.e., the case from which the number of quantum states is much larger than number of particles, this leads to the following expression:

$$\begin{aligned} &\mathrm{w}(s,t \rightarrow s',t')N(s)N(t)G(s')G(t') \\ &= \mathrm{w}(s',t' \rightarrow s,t)N(s')N(t')G(s)G(t) \end{aligned} \tag{4.1}$$

where $\mathrm{w}(s,t \rightarrow s',t')$ is the transition probability from states (s,t) to (s',t'), $N(s)$ is the number of particle of type s, and $G(s)$ is the total degeneracy. By introducing the elementary occupation number, $\eta(s) \equiv N(s)/G(s)$, and utilizing the quantum mechanical reciprocity relation, $\mathrm{w}(s,t \rightarrow s',t') = \mathrm{w}(s',t' \rightarrow s,t)$, one arrives at the following expression:

$$\eta(s)\eta(t) = \eta(s')\eta(t') \tag{4.2}$$

The validity of equation (4.2) depends solely on the validity of the quantum mechanical reciprocity relation, which is discussed in more detail by Oxenius [87] from a quantum mechanics point of view. In the scope of the current study, we assume that equation (4.2) is physically acceptable from which thermal equilibrium distribution can be derived. For simplicity, we assume that the system is

isotropic so all the angular variables do not appear in the formula of the distribution function.

4.2.1 Maxwell distribution

Consider an elastic collision between particles X and Y, from which an amount of energy, W, is transferred:

$$X(E) + Y(E') \Leftrightarrow X(E+W) + Y(E'-W) \tag{4.3}$$

where E and E' are the incident energy of particles X and Y, respectively. From the MR relation, equation (4.2), we have:

$$\eta_X(E)\eta_Y(E') = \eta_X(E+W)\eta_Y(E'-W) \tag{4.4}$$

which leads to:

$$\frac{\eta_X(E)}{\eta_X(E+W)} = \frac{\eta_Y(E'-W)}{\eta_Y(E')} = r(W) \tag{4.5}$$

The expression of $r(W)$ is introduced since the first and second terms of equation (4.5) cannot be a function of either E or E'. It can be proved that the solution of equation (4.5) is given by the following (see ref [87]):

$$r(W) = e^{\beta W} \tag{4.6}$$

$$\eta(E) = \zeta e^{-\beta E} \tag{4.7}$$

It is well known from statistical mechanics that $\beta = 1/kT$. The normalization constant ζ is :

$$\zeta = \frac{1}{g} n\lambda^3 \tag{4.8}$$

where g is the statistical weight, $n = N/V$ is the number density, and λ is the thermal de Broglie wavelength of the particle, i.e.:

$$\lambda = \frac{h}{(2\pi mkT)^{1/2}} \tag{4.9}$$

The total degeneracy of the particle $G(E)$ is:

$$G(E)dE = gV\frac{2^{5/2}\pi m^{3/2}}{h^3}E^{1/2}dE \tag{4.10}$$

Using (4.7) and (4.10), we can write the complete form of the Maxwell distribution function $f(E) \equiv N(E)/N$:

$$f(E)dE = \frac{2E^{1/2}}{\pi^{1/2}(kT)^{3/2}}e^{-E/kT}dE \tag{4.11}$$

where $f(E)$ is the normalized distribution function, i.e., $\int_0^\infty f(E)dE = 1$. It must be noted that the Maxwellian distribution function describes the translational states population in the classical limit, i.e., $\eta \ll 1$. When $\eta \to 1$, either Fermi-Dirac or Bose-Einstein statistics should be applied according to the particle type. This condition is relevant, for example, in low temperature and very dense electron gas found in inertial fusion problems where the electrons are characterized by Fermi-Dirac statistics. The case of Bose-Einstein statistics is relevant for the distribution of photons as will be shown later in this chapter.

4.2.2 Boltzmann distribution

The Boltzmann distribution can be derived by considering an inelastic collision where particle X with infinite mass at rest[1] is (de)excited from a bound electronic states by collision with particle M:

$$X(E_1) + M(E) \Leftrightarrow X(E_2) + M(E - \Delta E_{21}) \tag{4.12}$$

where E_1, E_2 are the energy of the electronic bound states and $\Delta E_{21} = E_2 - E_1$ is the energy gap between the lower and upper levels. Utilizing the MR relation, it follows that:

$$\eta_X(E_1)\eta_M(E) = \eta_X(E_2)\eta_M(E - \Delta E_{21}) \tag{4.13}$$

[1]This assumption allows us to neglect the translational degree of freedom of X and M.

Using the same argument as in the previous section, i.e., $\eta_M(E-\Delta E_{21})/\eta_M(E) = e^{\beta\Delta E_{21}}$ we can arrive at the following results:

$$\frac{n_2}{n_1} = \frac{g_2}{g_1} e^{-\Delta E_{21}/kT} \tag{4.14}$$

where g_1 and g_2 is the degeneracy weight of the excited states. This is the Boltzmann distribution for the bound excited states. It can also be written in the following form for any particular state i of particle X:

$$\frac{n_{i\in X}}{n_X} = \frac{g_i}{\mathcal{Z}_X} e^{-E_i/kT} \tag{4.15}$$

where $n_X = \sum_{i\in X} n_i$, and $\mathcal{Z}_X = \sum_{i\in X} g_i e^{-E_i/kT}$ is the electronic partition function of X.

4.2.3 Saha distribution

Let us now consider a collisional ionization and and its reverse process, three-body recombination, as follows:

$$X(E_0) + M(E) \Leftrightarrow X^+(E_+) + M(E - I_0 - E') + e(E') \tag{4.16}$$

where $I_0 = E_+ - E_0$ is the ionization energy. Similarly, the MR relation gives:

$$\eta_X(E_0)\eta_M(E) = \eta_{X^+}(E_+)\eta_M(E - I_0 - E')\eta_e(E') \tag{4.17}$$

Similar to the previous section, this equation can be written in the form:

$$\frac{\eta_X(E_0)}{\eta_{X^+}(E_+)\eta_e(E')} = \frac{\eta_M(E - I_0 - E')}{\eta_M(E)} = r(I_0 + E') = e^{\beta(I_0+E')} \tag{4.18}$$

It can be seen that the mean occupation number of the electron is independent of I_0, i.e., $\eta_e(E') = \frac{1}{2} n_e \lambda_e^3 e^{-\beta E'}$, where λ_e is the thermal de Broglie wavelength of the electron given by equation (4.9). Substituting this expression back to equation (4.18), we obtain the Saha distribution:

$$\frac{n_e n_+}{n_0} = \frac{2g_+}{g_0} \lambda_e^{-3} e^{-I_0/kT} \tag{4.19}$$

Note that the factor of 2 appeared in the Saha distribution is due to the degeneracy weight of the electron spin.

Also, in this process we have also assumed that the atom and ion have infinite mass so that the center of mass (COM) is collocated with the atom and ion. If we were to include the finite electron mass effect, the thermal de Broglie wavelength needs to be computed using the reduced mass of the electron and ion, e.g., $\mu_{+e} = m_+ m_e/(m_+ + m_e)$. If internal degrees of freedom of X and X^+ are taken into account, the Saha relation can be generalized:

$$\frac{n_e n_+}{n_0} = \frac{2\mathcal{Z}_+}{\mathcal{Z}_0}\lambda_e^{-3} e^{-I_0/kT} \tag{4.20}$$

where $\mathcal{Z}_0$ and $\mathcal{Z}_+$ are the partition functions of X and X^+, respectively.

4.2.4 Planck distribution

We now consider an elementary balance of emission and absorption of photons by free particles M:

$$M(E) \Leftrightarrow M(E - h\nu) + p(\nu) \tag{4.21}$$

The MR needs to be modified since quantum effects must be taken into account for photons, which leads to the following relation:

$$\eta_M(E)\,(1 + \eta_p(\nu)) = \eta_M(E - h\nu)\eta_p(\nu) \tag{4.22}$$

Here the photons are treated as bosons, leading to the multiplicative factor of $1 + \eta_p(\nu)$ on the LHS. Hence, we arrive at a slightly different relation:

$$\frac{\eta_M(E - h\nu)}{\eta_M(E)} = \frac{1 + \eta_p(\nu)}{\eta_p(\nu)} = r(h\nu) = e^{\beta h\nu} \tag{4.23}$$

We can then express the mean occupation number of a photon state as follow:

$$\eta_p(\nu) = (e^{\beta h\nu} - 1)^{-1} \tag{4.24}$$

For photons, $G_p(\nu) = V 8\pi\nu^2 c^{-3}$, thus it leads to the expression of photon density per unit volume, aka Planck distribution:

$$n(\nu)d\nu = \frac{8\pi\nu^2}{c^3}(e^{h\nu/kT} - 1)^{-1}d\nu \tag{4.25}$$

By introducing the spectral radiance quantity $I_\nu = n(\nu)h\nu c/4\pi$, we can rewrite Planck's radiation law into its familiar form:

$$I_\nu(T) = \frac{2h\nu^3}{c^2}(e^{h\nu/kT} - 1)^{-1} \tag{4.26}$$

In the low temperature limit ($e^{h\nu/kT} \gg 1$), Planck's distribution is replaced with the so-called Wien approximation:

$$I_\nu^W(T) = \frac{2h\nu^3}{c^2}e^{-h\nu/kT} \tag{4.27}$$

On the other hand, in the high temperature limit ($e^{h\nu/kT} \ll 1$), Planck's distribution reduces to the Rayleigh-Jeans function:

$$I_\nu^{RJ}(T) = \frac{2kT\nu^2}{c^2} \tag{4.28}$$

4.3 Elementary processes and detailed balance

In the CR model, each electronic state of the atom is treated as a separate species. The time evolution of the species' number densities are determined by solving a set of rate equations, which includes all the relevant kinetic processes by means of collisional and radiative interactions. All the macroscopic rates are computed assuming a Maxwellian EEDF of the heavy particles or electrons.

For a given microscopic cross section, $\sigma(E)$, the macroscopic reaction rate is computed as follows:

$$k(T) = \frac{\overline{v}}{(kT)^2}\int_{E_0}^{\infty}\sigma(E)Ee^{-E/kT}dE \tag{4.29}$$

where E_0 is the threshold energy, and $\overline{v} = \left(\frac{8k_BT}{\pi\mu}\right)^{1/2}$ is the mean thermal velocity with μ being the reduced mass. The rates computed in this form are tabulated

Rate Coefficient	Process
$k^{ex}_{(m\|n)}$	collisional excitation by electrons ($n \rightarrow m$)
$k^{hx}_{(m\|n)}$	collisional excitation by ground state atoms ($n \rightarrow m$)
$k^{ed}_{(n\|m)}$	collisional de-excitation by electrons ($m \rightarrow n$)
$k^{hd}_{(n\|m)}$	collisional de-excitation by ground state atoms ($m \rightarrow n$)
k^{ei}_n, k^{hi}_n	collisional ionization
k^{er}_n, k^{hr}_i	three-body recombination
k^{pr}_n	radiative recombination
$A_{(m\|n)}$	transition probability/spontaneous emission (Einstein coefficient)
$\Lambda_{(m\|n)}$	bound-bound optical escape factor
Λ_n	bound-free optical escape factor
$\overline{k}_{ei}$	electron-ion elastic collisions
k_{en}	electron-neutral elastic collisions

Table 4.1: Rate coefficients for collisional-radiative model.

as a function of temperature. It must be noted that for recombination processes, the rates are functions of both the heavy and electron temperatures as will be described later in this chapter.

A summary of all the elementary processes responsible for the excitation and ionization kinetics in a low temperature plasma is presented in this section. The principle of detailed balance is discussed for each type of process, i.e., the relation of the forward and backward rates. In this section, we use Argon as an example, but the same formulation also holds for Krypton and Xenon. A summary of the rates coefficients' definitions is listed in table 4.1. For bound-bound transitions, we use the convention of indexing the rates with the final state on the left, and the initial state on the right, i.e., $(f|i)$.

4.3.1 Collisional excitation/deexcitation

A collisional excitation/deexcitation process of an atom can be due to impact with another atom or the electron. Consider an electron-impact excitation process and its reversed deexcitation process between levels n and m ($n < m$),

$$\mathrm{Ar}(n) + e^- \Leftrightarrow \mathrm{Ar}(m) + e^- \tag{4.30}$$

the rate of change of the population density of state n due to the collisional process is of the form:

$$\frac{dn_n}{dt} = -k^{ex}_{(m|n)} n_n n_e + k^{ed}_{(n|m)} n_m n_e \tag{4.31}$$

The first term on the RHS of equation (4.31) describes the loss due to excitation from level n to m, as a result of collisions of the free electron with the existing state n; the second term describes the gain due to the collisional deexcitation induced by the free electron from state m. The total rate of change of the number density of level n can be determined by summing up the RHS of equation (4.31) for all levels $m \neq n$.

At equilibrium ("Boltzmann"), the ratio of the population densities of the lower and upper states are:

$$\frac{n^\star_m}{n^\star_n} \equiv \mathcal{B}_{nm}(T_e) = \frac{g_m}{g_n} e^{-\Delta E_{nm}/kT_e} \tag{4.32}$$

where $\Delta E_{nm} = E_m - E_n$. The rate of change of the number density at equilibrium is null, i.e., $\frac{dn^\star_n}{dt} \simeq 0$, and therefore we obtain a relation for the forward and the backward rates:

$$\frac{k^{ex}_{(m|n)}}{k^{ed}_{(n|m)}} = \frac{g_m}{g_n} e^{-\Delta E_{nm}/kT_e} \tag{4.33}$$

Similarly for an atom-impact collisional excitation and its reverse process,

$$\mathrm{Ar}(n) + \mathrm{Ar} \Leftrightarrow \mathrm{Ar}(m) + \mathrm{Ar} \tag{4.34}$$

the rate of change of the population is written similar to equation (4.31) with n_e being replaced by n_{Ar} and the expression for the backward rate is the same as

equation (4.33) with T_e being replaced by T_h:

$$\frac{dn_n}{dt} = -k^{hx}_{(m|n)} n_n n_{\mathrm{Ar}} + k^{hd}_{(n|m)} n_m n_{\mathrm{Ar}} \tag{4.35}$$

$$\frac{k^{hx}_{(m|n)}}{k^{hd}_{(n|m)}} = \frac{g_m}{g_n} e^{-\Delta E_{nm}/kT_h} \tag{4.36}$$

4.3.2 Collisional ionization/recombination

Consider an electron-impact ionization and recombination written as:

$$\mathrm{Ar}(n) + e^- \Leftrightarrow \mathrm{Ar}^+ + e^- + e^- \tag{4.37}$$

the rate of change of the number density of level n in this case is:

$$\frac{dn_n}{dt} = -k^{ei}_n n_n n_e + k^{er}_n n_+ n_e^2 \tag{4.38}$$

The first term on the RHS of equation (4.38) describes the loss due to ionization from level n, as a result of collisions of the free electrons with the existing state n; The second term describes the gain due to the three-body recombination process induced by the free electrons from the ion state.

The equilibrium for ionization and recombination ("Saha") involves a different relation:

$$\left(\frac{n_+ n_e}{n_n}\right)^\star \equiv \mathcal{S}_n(T_e) = \frac{2g_+}{g_n}\left(\frac{2\pi m_e k T_e}{h^2}\right)^{3/2} e^{-I_n/kT_e} \tag{4.39}$$

Thus we cannot assume that the equilibrium values are the same for both excitation and ionization. Usually we can have Boltzmann equilibrium without Saha equilibrium, but hardly the reverse, mostly because it takes more energy to ionize than to excite; for the upper states close to the ionization limit ($n \gg 1$), the difference is less significant. Using the principle of detailed balance, the recombination rate is written as:

$$\frac{k^{ei}_n}{k^{er}_n} = \frac{2g_+}{g_n}\left(\frac{2\pi m_e k T_e}{h^2}\right)^{3/2} e^{-I_n/kT_e} \tag{4.40}$$

Similarly for an atom-impact collisional ionization and its reverse process,

$$\mathrm{Ar}(n) + \mathrm{Ar} \Leftrightarrow \mathrm{Ar}^+ + e^- + \mathrm{Ar} \tag{4.41}$$

The rate of change of the state population is written similar to equation (4.38) with n_e being replaced by n_{Ar} and the expression for the backward rate is the same as equation (4.40) with T_h in the exponential term:

$$\frac{dn_n}{dt} = -k_n^{hi} n_n n_{\mathrm{Ar}} + k_n^{hr} n_+ n_e n_{\mathrm{Ar}} \tag{4.42}$$

$$\frac{k_n^{hi}}{k_n^{hr}} = \frac{2g_+}{g_n} \left(\frac{2\pi m_e k T_e}{h^2} \right)^{3/2} e^{-I_n/kT_h} \tag{4.43}$$

where I_n is the ionization potential of the excited state n. Note that the expression for the detailed balance includes the electron translational partition function, which is defined by the electron temperature T_e; therefore, the recombination rate is a function of both T_e and T_h.

4.3.3 Radiative processes

Radiation can also play an important role in the excitation and ionization kinetics. Radiative transition rates between bound states, referred to as bound-bound transition, can be expressed in terms of the Einstein coefficient A. Consider a spontaneous absorption/emission process between level n and m

$$\mathrm{Ar}(n) + h\nu \Leftrightarrow \mathrm{Ar}(m) \tag{4.44}$$

In order to calculate the rate of change in the population due to the forward process, one needs to know the intensity of the radiation field, which is governed by the radiation transport equation. A coupled solution of the CR kinetics with radiation transport, although of great interest, is beyond the scope of the current study. A simplified treatment can be made by using the so-called optical escape factor Λ, which gives a local approximation of the radiative losses. Since the

radiation mean free path can be significantly different for each process, the escape factors are defined for each specific process. The rate of change of the number density of a lower level n due to a bound-bound emission process, or line radiation from an upper level n, can be written as:

$$\frac{dn_n}{dt} = \Lambda_{(n|m)} A_{(n|m)} n_m \tag{4.45}$$

The spontaneous emission rates for this transition, $A_{(n|m)}$, is defined as:

$$A_{(n|m)} = \left(\frac{8\pi^2 e^2}{m_e c^3} \right) \frac{g_n}{g_m} \mathrm{f}_{nm} \tag{4.46}$$

where f_{nm} is the oscillator strength of the transition.

Similarly for the photoionization and radiative recombination process,

$$\mathrm{Ar}(n) + h\nu \Leftrightarrow \mathrm{Ar}^+ + e^- \tag{4.47}$$

the rate of change of the population of level n, using the escape factor, is written as:

$$\frac{dn_n}{dt} = \Lambda_n k_n^{pr} n_+ n_e \tag{4.48}$$

In all the radiative transitions, $\Lambda = 0$ corresponds to the optically thick and $\Lambda = 1$ corresponds to the optically thin approximation. For the radiative recombination case, the electron energy production rate also needs to be computed and tabulated:

$$k'(T) = \frac{\overline{v}}{(kT)^2} \int_{E_0}^{\infty} \sigma(E) E^2 e^{-E/kT} dE \tag{4.49}$$

and the resultant rate of change of the electron thermal energy is as follows:

$$\frac{d\varepsilon_e}{dt} = -\Lambda_n k_n^{pr\prime} n_+ n_e \tag{4.50}$$

The use of the escape factor is convenient and computationally efficient. However, in very high-temperature plasma, the radiation field might have a stronger impact on the inelastic processes, and radiation transport must be taken into account. It is also important, for example, when the radiation mean free path is

comparable to the characteristic length scale of the flow. In such cases, detailed treatment of the radiative terms need to be considered, and the calculation can get very expensive (see [94] and [95]). Moreover, since the escape factor is defined locally, global effects cannot be captured, i.e., precursor effects in plasma shocks [96].

4.3.4 Elastic processes

In addition to the all the excitation and ionization processes, the current model also takes in account the effect of elastic collision between the the heavy particles and the electrons. These collisions are responsible to enforce the equilibrium between the translational energy of the electrons and the heavy particles. The energy transfer between the two components due to the elastic collisions is given as:

$$\frac{d\varepsilon_e}{dt} = -\frac{d\varepsilon_h}{dt} = \frac{2m_e}{m_{\mathrm{Ar}}} n_e n_n \frac{3}{2} k(T_h - T_e) k_{en} + \frac{2m_e}{m_{\mathrm{Ar}}} n_e n_+ \frac{3}{2} k(T_h - T_e) \overline{k}_{ei} \qquad (4.51)$$

where n_n and n_+ are the number densities of the neutral and ion species, respectively.

The first term on the RHS of equation (4.51) describes the energy transfer due to electron-neutral collision, the second term describes the energy transfer due to Coulomb collisions. The Coulomb collision can be computed from the energy-averaged properties [86]:

$$\overline{k}_{ei} = \overline{v}_e \sigma_{ei} \qquad (4.52)$$

$$\sigma_{ei} = 5.58 \times 10^{-10} \frac{\ln \Lambda}{T_e^2} [m^2] \qquad (4.53)$$

Free-free radiation had also been incorporated in the current model via Kramer's formula [83] for Bremsstrahlung emission. The rate of change of the electron energy is as follows:

$$\frac{d\varepsilon_e}{dt} = -\frac{16\pi^2}{3\sqrt{3}} \frac{\overline{v}_e Z_{\mathrm{eff}}^2 e^6 \overline{g}}{m_e h (4\pi E_0 c)^3} n_+ n_e = -1.42 \times 10^{-40} Z_{\mathrm{eff}}^2 T_e^{1/2} n_+ n_e [\mathrm{J \cdot m^{-3} \cdot s^{-1}}] \quad (4.54)$$

where $\overline{g}$ is the gaunt factor taken to be unity and Z_{eff} is the effective charge.

4.4 Rate equations

Once all the macroscopic rates are obtained, one can construct a system of rate equations, which computes the rate of change of the specie's number densities and the energies of the electrons and the heavy particles. These rate equations are summarized below:

Ground state and excited states

$$\begin{aligned}\frac{\partial n_k}{\partial t} &= \sum_{i<k} n_i(n_e k^{ex}_{(k|i)} + n_{\text{Ar}} k^{hx}_{(k|i)}) - \sum_{j<k} n_k(n_e k^{ed}_{(j|k)} + n_{\text{Ar}} k^{hd}_{(j|k)} + \Lambda_{(j|k)} A_{(j|k)}) \\ &\quad - \sum_{j>k} n_k(n_e k^{ex}_{(j|k)} + n_{\text{Ar}} k^{hx}_{(j|k)}) + \sum_{i>k} n_i(n_e k^{ed}_{(k|i)} + n_{\text{Ar}} k^{hd}_{(k|i)} + \Lambda_{(k|i)} A_{(k|i)}) \\ &\quad + n_+ n_e(n_{\text{Ar}} k^{hr}_k + n_e k^{er}_k + \Lambda_k k^{pr}_k) - n_k(n_e k^{ei}_k + n_{\text{Ar}} k^{hi}_k)\end{aligned} \tag{4.55}$$

Ion state

$$\frac{\partial n_+}{\partial t} = \sum_i n_i(n_e k^{ei}_i + n_{\text{Ar}} k^{hi}_i) - n_+ n_e \sum_i (n_{\text{Ar}} k^{hr}_i + n_e k^{er}_i + \Lambda_i k^{pr}_i) \tag{4.56}$$

Heavy particles energy

$$\frac{\partial \varepsilon_h}{\partial t} = n_{\text{Ar}} \sum_i \sum_{j>i} \Delta E_{ij}(n_j k^{hd}_{(i|j)} - n_i k^{hx}_{(j|i)}) + n_{\text{Ar}} \sum_i I_i(n_e n_+ k^{hr}_i - n_i k^{hi}_i) \tag{4.57}$$

$$- 3\rho_e n_n k(T_h - T_e)\frac{k_{en}}{m_{\text{Ar}}} - 3\rho_e n_+ k(T_h - T_e)\frac{\overline{k}_{ei}}{m_{\text{Ar}^+}} \tag{4.58}$$

Electron energy

$$\frac{\partial \varepsilon_e}{\partial t} = n_e \sum_i \sum_{j>i} \Delta E_{ij}(n_j k^{ed}_{(i|j)} - n_i k^{ex}_{(j|i)}) + n_e \sum_i I_i(n_e n_+ k^{er}_i - n_i k^{ei}_i) \tag{4.59}$$

$$- n_e n_+ \sum_i \Lambda_i k^{pr\prime}_i - n_+ n_e \frac{16\pi^2}{3\sqrt{3}} \frac{\overline{v}_e Z^2_{\text{eff}} e^6 \overline{g}}{m_e h (4\pi\epsilon_0 c)^3} \tag{4.60}$$

$$+ 3\rho_e n_n k(T_h - T_e)\frac{k_{en}}{m_{\text{Ar}}} + 3\rho_e n_+ k(T_h - T_e)\frac{\overline{k}_{ei}}{m_{\text{Ar}^+}} \tag{4.61}$$

The electron number density is determined from charge neutrality, i.e., $n_e = \sum_s Z_s n_s$. Also, in the case where the mixture of gas consists of multiple chemical species, one also needs to take in account the collisional processes with all the heavy species. The expression for the atom-impact processes would need to be summed over all the heavy species.

4.5 Physical models

4.5.1 Argon

The CR model for Argon implemented in this study is based on the work of Vlček [91] and Bultel *et al.* [92], both of which, were specifically developed for Argon. Subsequently, Kapper and Cambier [90, 97] extended this model, and obtained a calibrated set of atom-impact excitation rates for Argon. Their CR model takes in account the ground state and the first 30 excited levels of neutral Argon obtained from the NIST database [98]. The electronic levels are split into two configurations based on the core angular momentum numbers, which yield two effective ionization potentials. The energy levels of all the excited states of Argon are listed in table 4.2.

For atom-impact excitation processes, the cross sections are computed form the semi-empirical Drawin's formula [99, 100]. For the low energy range considered in this study, the cross sections can be approximated by a linear function. For excitation from ground state ($1 \rightarrow m$), the cross sections take the form:

$$\sigma^a_{1m} = \chi^*_{1m}(E - \Delta E_{1m}) \tag{4.62}$$

where

$$\chi^*_{nm} = 4\pi a_0^2 \frac{(I_H)^2}{\Delta E^3_{nm}} \xi^2 f_{nm} \frac{2m_e}{m_H} \tag{4.63}$$

and f_{nm} is the oscillator strength of the transition ($n \rightarrow m$). The values of χ^*_{1m} in the current CR model were calibrated to obtain a satisfactory induction length (or

n	$E(n)$ [eV]	g_n	j_c	$n\ell[K]_J$	n	$E(n)$ [eV]	g_n	j_c	$n\ell[K]_J$
1	0	1	1.5	[Mg]$3p^6$	18	13.903	5	1.5	$3d[3/2]_2$
2	11.548	5	1.5	$4s[3/2]_2$	19	13.979	9	1.5	$3d[7/2]_4$
3	11.624	3	1.5	$4s[3/2]_1$	20	14.013	7	1.5	$3d[7/2]_3$
4	11.723	1	0.5	$4s'[1/2]_0$	21	14.063	5	1.5	$3d[5/2]_2$
5	11.828	3	0.5	$4s'[1/2]_1$	22	14.068	5	1.5	$3d[3/2]_1$
6	12.907	3	1.5	$4p[1/2]_1$	23	14.090	3	1.5	$5s[3/2]_2$
7	13.076	7	1.5	$4p[5/2]_3$	24	14.099	7	1.5	$5s[5/2]_3$
8	13.095	5	1.5	$4p[5/2]_2$	25	14.153	3	1.5	$3d[3/2]_1$
9	13.153	3	1.5	$4p[3/2]_1$	26	14.214	5	0.5	$5s'[1/2]_0$
10	13.172	5	1.5	$4p[3/2]_2$	27	14.234	5	0.5	$3d'[5/2]_2$
11	13.273	1	1.5	$4p[1/2]_0$	28	14.236	7	0.5	$5s'[1/2]_1$
12	13.283	3	0.5	$4p'[3/2]_1$	29	14.241	1	0.5	$3d'[3/2]_2$
13	13.302	5	0.5	$4p'[3/2]_2$	30	14.255	3	0.5	$3d'[5/2]_3$
14	13.328	3	0.5	$4p'[1/2]_1$	31	14.304	3	0.5	$3d'[3/2]_1$
15	13.480	1	0.5	$4p'[1/2]_0$	∞	15.760	4	1.5	[Mg]$3p^5$
16	13.845	1	1.5	$3d[1/2]_0$	∞'	15.937	2	0.5	[Mg]$3p^5$
17	13.864	3	1.5	$3d[1/2]_1$					

Table 4.2: Lowest 31 levels of Ar I by energy.

n	m	χ^*_{nm} [m^2/eV]	n	m	χ^*_{nm} [m^2/eV]
1	3	9.35×10^{-25}	2	3	1.79×10^{-24}
1	5	3.36×10^{-24}	2	4	4.80×10^{-26}
1	17	8.14×10^{-27}	2	5	4.80×10^{-26}
1	23	2.64×10^{-25}	3	4	4.80×10^{-26}
1	25	7.27×10^{-25}	3	5	4.80×10^{-26}
1	30	1.35×10^{-25}	4	5	1.79×10^{-24}
1	31	5.88×10^{-25}			

Table 4.3: Atom impact excitation parameters for allowed transitions for Argon. χ^*_{nm} for allowed transitions from ground state of neutral Ar has been tuned to match the experimental induction length.

relaxation length) compared to the experimentally observed values (see Kapper and Cambier[90] for more detail). The inner $3p^5 4s$ maniford transitions take the form:

$$\sigma^a_{nm} = \chi^*_{nm} \frac{E - \Delta E_{nm}}{\Delta E^{2.26}_{nm}} \tag{4.64}$$

where ΔE_{nm} is in eV. The resultant set of values are summarized in table 4.3.

The atom-impact ionization cross sections are less sensitive to the induction length. The ionization cross section from the ground state is taken from the work of Haugsjaa and Amme [101]:

$$\sigma^a_1(E) = 1.8 \times 10^{-25}(E - 15.760)^{1.3} \text{ [m}^2\text{]}, \tag{4.65}$$

where E is in eV. For all other levels, the cross sections are computed from Drawin's formula:

$$\sigma^a_n(E) = 4\pi a_0^2 \left(\frac{I_H}{I_n}\right)^2 \frac{m_{Ar}}{m_H} \xi^2 \frac{2m_e}{m_{Ar} + m_e} \frac{E/I_n - 1}{\left(1 + \frac{2m_e}{m_{Ar}+m_e}(E/I_n - 1)\right)^2}. \tag{4.66}$$

While the atom-impact processes have a significant effect on the overall induction length, the electron-impact processes have a dominated effect on the electron

Parameter for Eq. (4.68)	Valence electron shell			
	s	p	d	f
a	1.06	2	3/2	3/2
b	0.23	1	3	1
c	1	1	2/3	2/3
d	1	1	1	1

Table 4.4: Electron-impact ionization parameters as taken from [103].

avalanche. The cross sections for electron-impact excitation from ground state and $4s$ levels to all the levels below the $5p$ manifold are due to Zatsarinny and Bartschat [102]. Figure 4.1 shows the excitation cross sections due to electron-impact from the ground state to the $4s$ levels. The cross sections of Zatsarinny and Bartschat are obtained from from a semi-relativistic Breit-Pauli B-spline R-matrix calculation of e-Ar collisions. Drawin's formulas have been used for all other transitions.

The electron-impact ionization cross sections have been determined from the Deutsch-Märk (DM) formalism [103].

$$\sigma_i^e(E) = g_{n\ell}\pi r_{n\ell}^2 \xi_{n\ell} f_i(E) \tag{4.67}$$

where $g_{n\ell}$ are the reduced weighting factors, $r_{n\ell}$ are the radii of the valence electron, and

$$f_i(E) \;=\; d\frac{I_i}{E}\left(\frac{E/I_i - 1}{E/I_i + 1}\right)^a \times \left[b + c\left(1 - \frac{I_i}{2E}\right)\ln(2.7 + (E/I_i - 1)^{1/2})\right] \tag{4.68}$$

The necessary parameters for equations (4.67) and (4.68) are given in Tables 4.4 and 4.5. The results of the ionization cross sections due to electron-impact collisions are shown in figure 4.2.

The Einstein coefficients for the all the bound-bound transitions are taken from the NIST database [98]. The radiative capture cross sections are determined

Valence electron shell, $n\ell$	$r_{n\ell}$ [Å]	$g_{n\ell} \times I_{n\ell}$ [eV]
$4s$	2.49	7.40
$5s$	6.35	6.35
$4p$	3.40	31.00
$3d$	4.36	13.60

Table 4.5: Radii of Ar valence electron and reduced weighting factors for $\xi = 1$ as taken from [103].

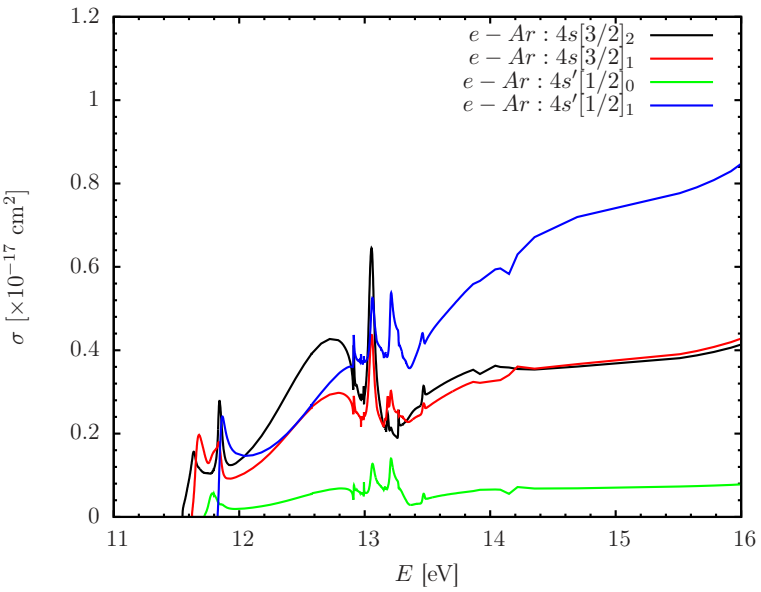

Figure 4.1: Excitation cross sections from ground state to the $4s$ manifold due to electron-impact for Ar I taken from [102].

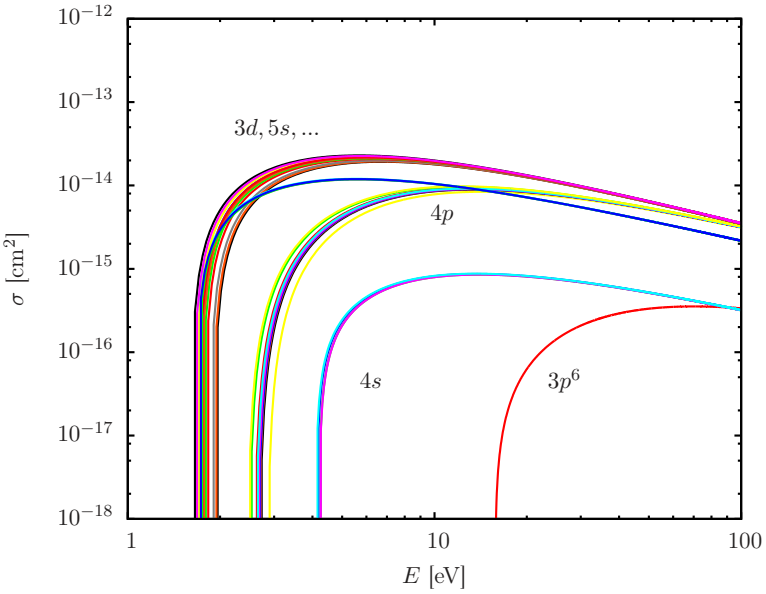

Figure 4.2: Ionization cross sections due to electron-impact for Ar I as computed by the Deutsch-Märk formalism

from detailed balance,

$$\sigma_n^c(\nu) = \frac{g_n}{g_+}\frac{h^2\nu^2}{m_e^2\nu_e^2c^2}\sigma_n^\nu(\nu) \tag{4.69}$$

with the photoionization cross sections given by Vlček [91]. Utilizing the relation $h\nu = E + E_i$, the cross section associated with the ground state is given by

$$\sigma_1^\nu(E) = \frac{g_1}{g_+}\frac{(E+E_1)^2}{2Em_ec^2} \times \begin{cases} 3.5\times10^{-21} & 0 \le E \le 2I_H - E_1 \\ 2.8\times10^{-20}\left(\dfrac{I_H}{E+E_1}\right)^3 & E > 2I_H - E_1 \end{cases} \tag{4.70}$$

while all others are computed using

$$\sigma_i^\nu(E) = \gamma_i\frac{g_i}{g_+}\frac{(E+E_i)^2}{2Em_ec^2}10^{-22} \times \begin{cases} 2 & 0 \le E \le 0.59I_H - E_1 \\ 7.91\left(\dfrac{E_i}{I_H}\right)^{5/2}\left(\dfrac{I_H}{E+E_i}\right)^3 & E > 0.59I_H - E_i \end{cases} \tag{4.71}$$

The parameter γ_i takes the values 0.0763, 0.0458, 0.0305, and 0.0915 for $i = 2$,

Processes	Ref.
Atom-impact exc.	Drawin[99, 100, 92] (allowed trans.)
	Bultel[92] (others)
Atom-impact ion.	Haugsjaa[101] (ground state)
	Drawin[99, 100] (others)
Electron-impact exc.	Zatsarinny[102] (from ground state)
	Drawin[99, 100] (others)
Electron-impact ion.	Deutsch-Märk[103]
Line transition	NIST [98]
Photoionization	Vlček[91]
Bremsstrahlung emission	Kramer's formula[83]
Elastic collisions	McEachran[104]

Table 4.6: Summary of the elementary cross sections used in the CR model for Argon

3, 4, and 5, respectively. The cross sections for all the collisional and radiative transitions of Argon are summarized in table 4.6.

4.5.2 Krypton

In a similar fashion, the CR model for Krypton is constructed starting from the electronic levels taken from NIST database [98]. For brevity, only the first 31 excited states, ordered by increasing energy values, are shown in table 4.7.

Similarly to Argon, the atom-impact excitation cross sections for Krypton are computed from equation (4.62) with the linear dependence on energy. The values of χ^*_{nm} are listed in table 4.8. It must be noted that the excitation cross sections from the ground state were calibrated to obtain a reasonable agreement with the experimental induction length. The heavy particle impact ionization cross sections

n	$E(n)$ [eV]	g_n	j_c	$n\ell[K]_J$	n	$E(n)$ [eV]	g_n	j_c	$n\ell[K]_J$
1	0	1	1.5	[Zn]$4p^6$	18	12.144	5	0.5	$5p'[3/2]_2$
2	9.915	5	1.5	$5s[3/2]_2$	19	12.179	7	1.5	$4d[7/2]_3$
3	10.032	3	1.5	$5s[3/2]_1$	20	12.256	1	0.5	$5p'[1/2]_0$
4	10.562	1	0.5	$5s'[1/2]_0$	21	12.258	5	1.5	$4d[5/2]_2$
5	10.644	3	0.5	$5s'[1/2]_1$	22	12.284	7	1.5	$4d[5/2]_3$
6	11.303	3	1.5	$5p[1/2]_1$	23	12.352	5	1.5	$6s[3/2]_2$
7	11.443	7	1.5	$5p[5/2]_3$	24	12.355	3	1.5	$4d[3/2]_1$
8	11.445	5	1.5	$5p[5/2]_2$	25	12.385	3	1.5	$6s[3/2]_1$
9	11.526	3	1.5	$5p[3/2]_1$	26	12.756	3	1.5	$6p[1/2]_1$
10	11.546	5	1.5	$5p[3/2]_2$	27	12.785	7	1.5	$6p[5/2]_3$
11	11.666	1	1.5	$5p[1/2]_0$	28	12.785	5	1.5	$6p[5/2]_2$
12	11.998	1	1.5	$4d[1/2]_0$	29	12.803	5	0.5	$4d'[3/2]_2$
13	12.037	3	1.5	$4d[1/2]_1$	30	12.809	3	1.5	$6p[3/2]_1$
14	12.100	3	0.5	$5p'[3/2]_1$	31	12.815	5	1.5	$6p[3/2]_2$
15	12.112	5	1.5	$4d[3/2]_2$	∞	14.000	4	1.5	[Zn]$4p^5$
16	12.125	9	1.5	$4d[7/2]_4$	∞'	14.665	2	0.5	[Zn]$4p^5$
17	12.140	3	0.5	$5p'[1/2]_1$					

Table 4.7: Lowest 31 levels of Kr I by energy.

n	m	χ^*_{nm} [m^2/eV]	n	m	χ^*_{nm} [m^2/eV]
1	3	1.11×10^{-23}	3	9	7.01×10^{-22}
1	5	7.93×10^{-24}	3	10	3.68×10^{-22}
2	6	7.15×10^{-22}	3	11	2.44×10^{-22}
2	7	9.93×10^{-22}	3	14	1.20×10^{-23}
2	8	2.57×10^{-22}	4	12	1.09×10^{-21}
2	9	5.05×10^{-23}	4	13	1.15×10^{-21}
2	10	4.41×10^{-22}	5	12	5.96×10^{-22}
2	13	3.79×10^{-24}	5	13	4.22×10^{-22}
2	14	8.32×10^{-25}	5	14	1.26×10^{-21}
3	8	1.31×10^{-21}	5	15	2.36×10^{-22}

Table 4.8: Atom impact excitation parameters for allowed transitions for Krypton.

are computed from the Drawin's formula.

For electron-impact transitions, we have utilized the the cross sections from the work of Zatsarinny and Bartschat [105]. These cross sections are determined from a semi relativistic Breit-Pauli B-spline R-matrix calculation. Figure 4.3 show the cross sections for excitation to the $5s$ manifold. For all other transitions, Drawin's formula has been used systematically. The DM formula has been used for all the ionization cross sections. In particular, we have only considered the $5s$ sub-shell for computing ionization from the core. For the excited states, we have considered the electron in the valence shell. The results of the ionization cross sections due to electron-impact collisions computed with the DM formalism are shown in figure 4.4.

For the radiative combination rates, we have used the same form of the cross sections given by Vlček [91] for Argon where the coefficients are tuned to match with the radiative cooling slope from experimental data. The cross sections for all

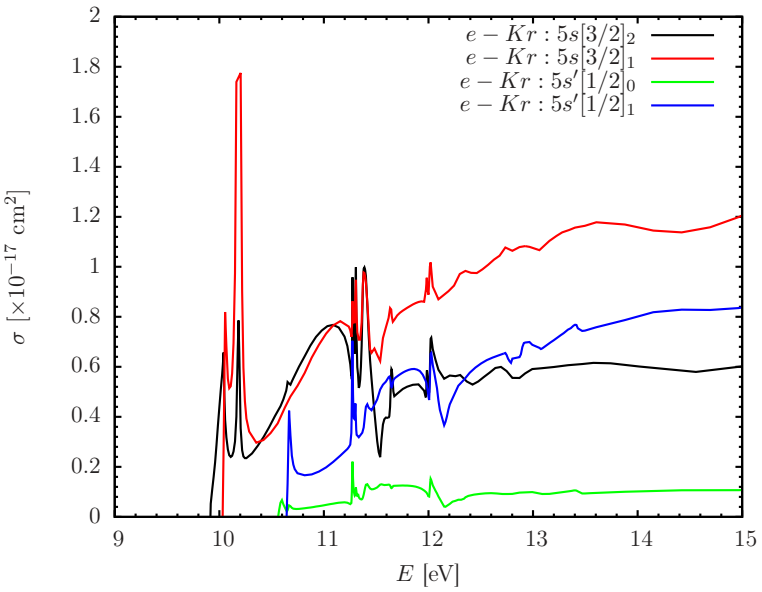

Figure 4.3: Excitation cross sections from ground state to the $5s$ manifold due to electron-impact for Kr I taken from [105].

the collisional and radiative transitions of Krypton are summarized in table 4.9.

4.5.3 Xenon

The CR model for Xenon is constructed similarly to Argon and Krypton. Table 4.10 lists the first 31 excited levels of Xenon ordered by increasing energy values. All the electronic energy of the excited states as well as the oscillator strength of the allowed transition are taken from the NIST database [98]. The effect of spin-orbit splitting of the ion due to different core angular momentum j_c is similar to those of Argon and Krypton.

The atom-impact processes including excitation and ionization have been computed from Drawin's formula. The values of χ^*_{nm} are provided in table 4.11. The electron-impact excitation cross sections from the ground state are computed by Zatsarinnny and Bartschat using R-matrix calculation [105]. The excitation cross sections from the ground state to all the $6s$ levels are plotted in figure 4.5.

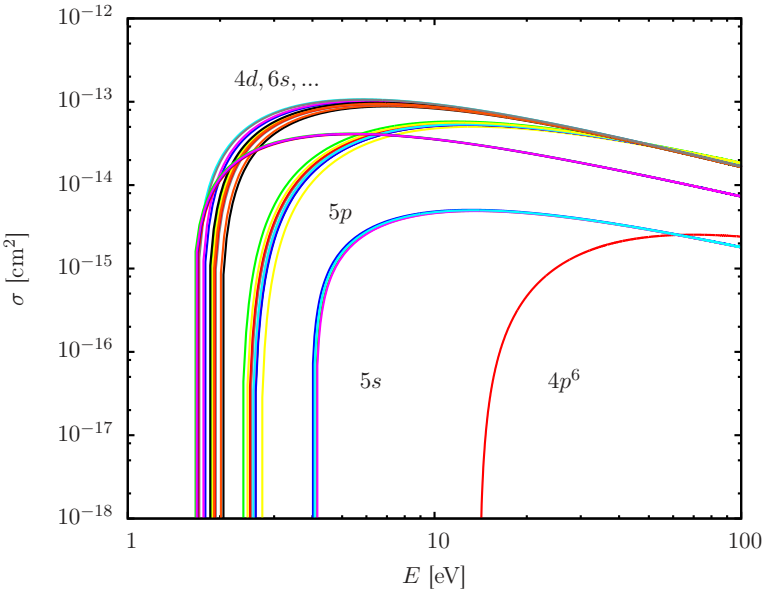

Figure 4.4: Ionization cross sections due to electron-impact for Kr I as computed by the Deutsch-Märk formalism

Processes	Ref.
Atom-impact exc.	Drawin[99, 100]
Atom-impact ion.	Drawin[99, 100]
Electron-impact exc.	Zatsarinny[105] (from ground state)
	Drawin[99, 100] (others)
Electron-impact ion.	Deutsch-Märk[103]
Line transition	NIST [98]
Photoionization	Modified Vlcěk[91]
Bremsstrahlung emission	Kramer's formula[83]
Elastic collisions	Mitroy[106] & McEachran[107]

Table 4.9: Summary of the elementary cross sections used in the CR model for Krypton

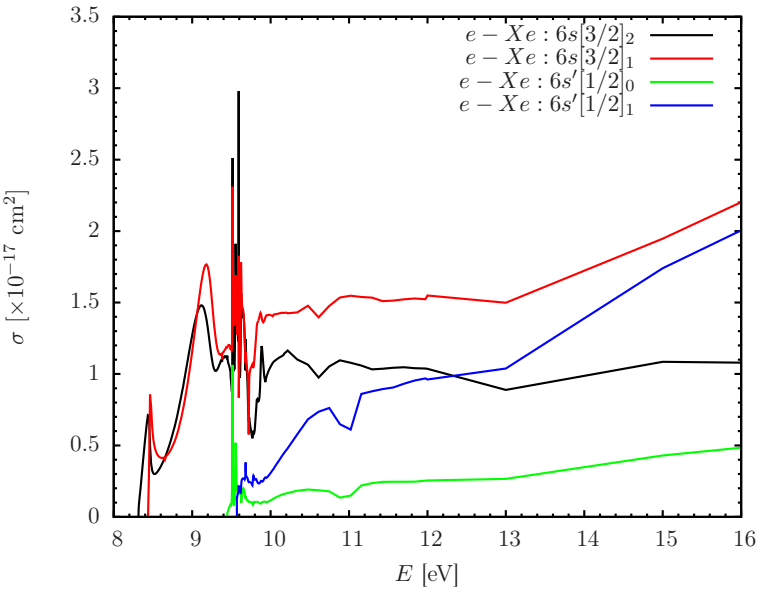

Figure 4.5: Excitation cross sections from ground state to the $6s$ manifold due to electron-impact for Xe I taken from [105].

For electron-impact ionization of the ground state, $6s$ and $6p$ levels, we used the cross sections of Erwin and Kunc [108], which are plotted in figure 4.6. For ionization from higher levels, DM formalism is used. Due to the lack of available cross sections for radiative combination, we have utilized the formula given by Vlček [91]. The cross sections for all the collisional and radiative transitions of Xenon are summarized in table 4.12.

4.5.4 Electron-neutral elastic collisions

The momentum transfer cross sections of elastic collisions with electrons for Argon, Krypton, and Xenon are taken from the works of McEachran [104, 107] and Mitroy [106]. The results of these cross sections are shown in figure 4.7. The comparison with the results of Zatsarinny *et al.* [109] are excellent for all cases.

n	$E(n)$ [eV]	g_n	j_c	$n\ell[K]_J$	n	$E(n)$ [eV]	g_n	j_c	$n\ell[K]_J$
1	0	1	1.5	[Cd]$5p^6$	18	10.220	7	1.5	$5d[5/2]_3$
2	8.315	5	1.5	$6s[3/2]_2$	19	10.401	3	1.5	$5d[3/2]_1$
3	8.437	3	1.5	$6s[3/2]_1$	20	10.562	5	1.5	$7s[3/2]_2$
4	9.447	1	0.5	$6s'[1/2]_0$	21	10.593	3	1.5	$7s[3/2]_1$
5	9.570	3	0.5	$6s'[1/2]_1$	22	10.902	3	1.5	$7p[1/2]_1$
6	9.580	3	1.5	$6p[1/2]_1$	23	10.954	5	1.5	$7p[5/2]_2$
7	9.686	5	1.5	$6p[5/2]_2$	24	10.958	3	0.5	$6p'[3/2]_1$
8	9.721	7	1.5	$6p[5/2]_3$	25	10.969	7	1.5	$7p[5/2]_3$
9	9.789	3	1.5	$6p[3/2]_1$	26	10.971	1	1.5	$6d[1/2]_0$
10	9.821	5	1.5	$6p[3/2]_2$	27	10.979	3	1.5	$6d[1/2]_1$
11	9.890	1	1.5	$5d[1/2]_0$	28	10.996	5	1.5	$7p[3/2]_2$
12	9.917	3	1.5	$5d[1/2]_1$	29	10.998	5	1.5	$6d[3/2]_2$
13	9.933	1	1.5	$6p[1/2]_0$	30	11.003	3	1.5	$7p[3/2]_1$
14	9.943	9	1.5	$5d[7/2]_4$	31	11.015	1	1.5	$7p[1/2]_0$
15	9.959	5	1.5	$5d[3/2]_2$	∞	12.130	4	1.5	[Cd]$5p^5$
16	10.039	7	1.5	$5d[7/2]_3$	∞'	13.436	2	0.5	[Cd]$5p^5$
17	10.157	5	1.5	$5d[5/2]_2$					

Table 4.10: Lowest 31 levels of Xe I by energy

n	m	χ^*_{nm} [m^2/eV]	n	m	χ^*_{nm} [m^2/eV]
1	3	1.16×10^{-22}	2	9	1.42×10^{-23}
1	5	5.41×10^{-23}	2	25	1.74×10^{-24}
1	12	2.56×10^{-24}	2	28	8.46×10^{-25}
1	19	9.06×10^{-23}	3	31	1.16×10^{-24}
1	21	2.12×10^{-23}	4	30	1.62×10^{-23}
1	27	4.82×10^{-25}			

Table 4.11: Atom impact excitation parameters for allowed transitions for Xenon.

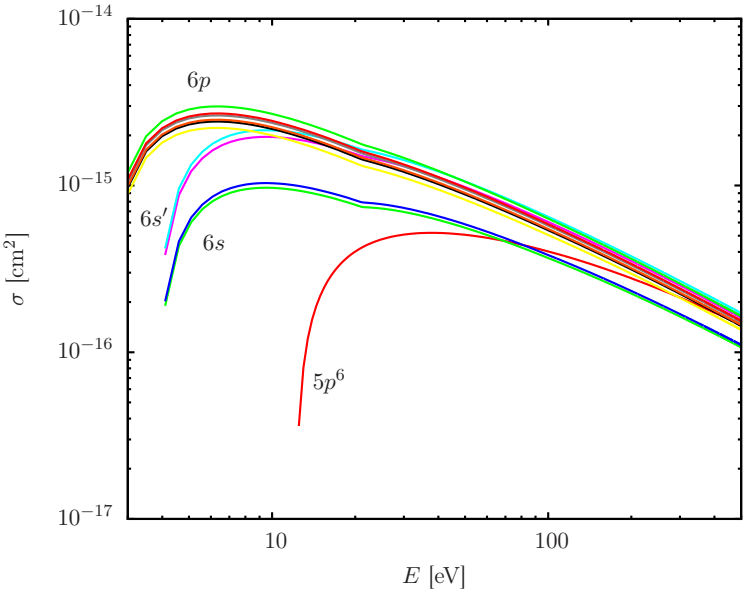

Figure 4.6: Ionization cross sections due to electron-impact for Xe I as computed from the work of Erwin and Kunc [108].

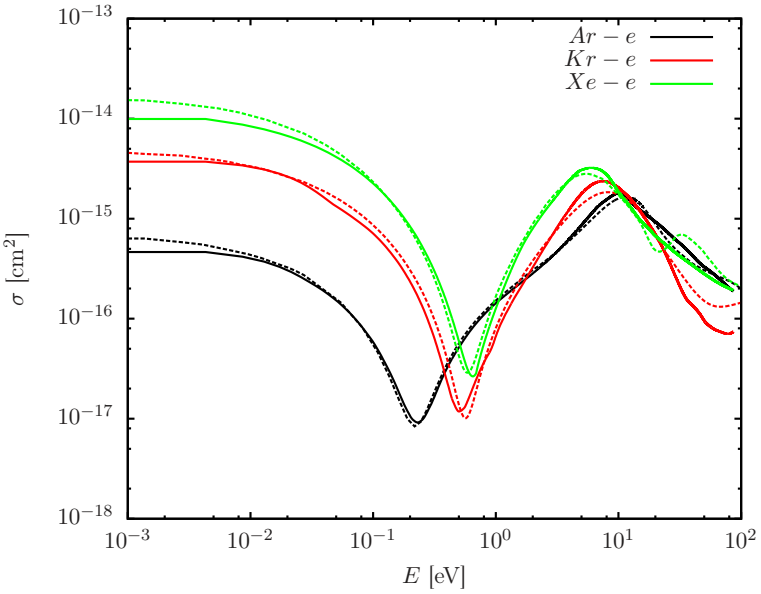

Figure 4.7: Momentum transfer cross sections for Argon, Krypton and Xenon. Solid lines are the results of McEachran *et al.* [104, 107]. Dashed lines are the results of Zatsarinny *et al.* [109].

Processes	Ref.
Atom-impact exc.	Drawin[99, 100]
Atom-impact ion.	Drawin[99, 100]
Electron-impact exc.	Zatsarinny[105] (from ground state)
	Drawin[99, 100] (others)
Electron-impact ion.	Erwin & Kunc[108] ($5p^6$, $6s$, $6p$)
	Deutsch-Märk[103] (others)
Line transition	NIST[98]
Photoionization	Modified Vlček[91]
Bremsstrahlung emission	Kramer's formula[83]
Elastic collisions	Mitroy[106] & McEachran[107]

Table 4.12: Summary of the elementary cross sections used in the CR model for Xenon

4.6 Benchmark studies

4.6.1 Steady-state flows

The CR models described in the previous section for Argon and Krypton are utilized to model the experiments performed at University of Toronto's Institute of Aerospace Studies (UTIAS) in 1977 [110, 111]. Neglecting unsteady effects, the flow properties of an ionizing shock layer can be computed by solving the steady 2T Euler equations with coupling source terms due to kinetics. The procedure for solving this equation is given in appendix B.

The UTIAS experiments provided detailed measurements of the electron number density and the total mass density of the flow behind the shock including the relaxation length as well as the radiative cooling region. The measurement of the induction length is particularly helpful for calibrating the atom-impact excitation

Cases	Ma	p_∞ (Torr)	T_∞ (K)	l^* (cm)
1	15.9	5.14	293.6	2.00
2	16.1	5.15	295.9	1.90
3	16.5	5.12	296.6	1.80
4	13.0	5.00	296.6	8.90

Table 4.13: Summary of test conditions of the UTIAS experiments for ionizing shock in Argon with the predicted thermal equilibrium flow properties. Data are taken from Glass and Liu [110].

rate. For the case of Argon, four different experimental conditions were used to assess the current CR model. The test conditions along with the experimentally measured relaxation lengths [110] are summarized in table 4.13.

Figure 4.8 shows a comparison of the computed electron number density and the total mass density along with the experimental data. It must be noted that acceptable agreement in the relaxation length was obtained by tuning the atom-impact cross sections. The calculation is performed utilizing 31 electronic states of neutral Argon. It has been shown that this level of details is required for an accurate prediction of the radiative cooling region [90]. This is because a major source of radiation is due to line radiation from the upper states. It must be pointed out that since radiation transport is not included, line radiation and radiative recombination are computed with the help of the escape factor. The value of the escape factors (either 1 or 0) is determined by an order of magnitude analysis of the radiation's mean-free-path compared with the shock tube dimension.

The temperature profile of the electrons and the heavy particles for the same test case is shown in figure 4.9, which help identifying severe regimes marking the transition from the atom-impact dominated kinetics to electron-impact dominated kinetics. In addition, figure 4.10 shows the ASDF at several locations behind

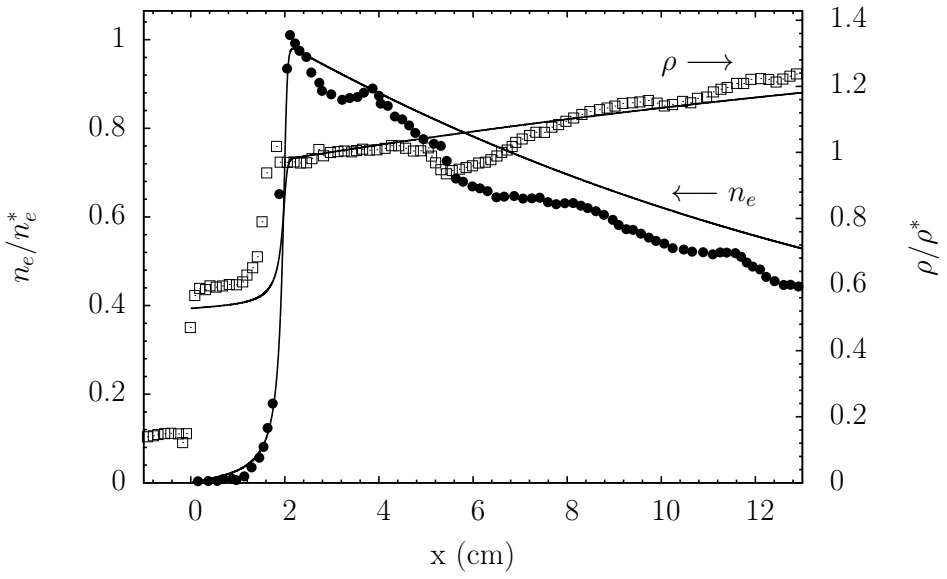

Figure 4.8: Computed and experimental results of ionizing shock in Argon for case 1: $p_\infty = 5.14$ Torr, $T_\infty = 293.6$ K, $Ma = 15.9$. The values of the electron number density and the total mass density are normalized by the equilibrium values: $n_e^* = 1.69 \times 10^{17}$ cm^{-3}, $\rho^* = 8.4 \times 10^{-3}$ g/cm^3. Symbols represent experimental data for n_e and ρ from Glass and Liu [110].

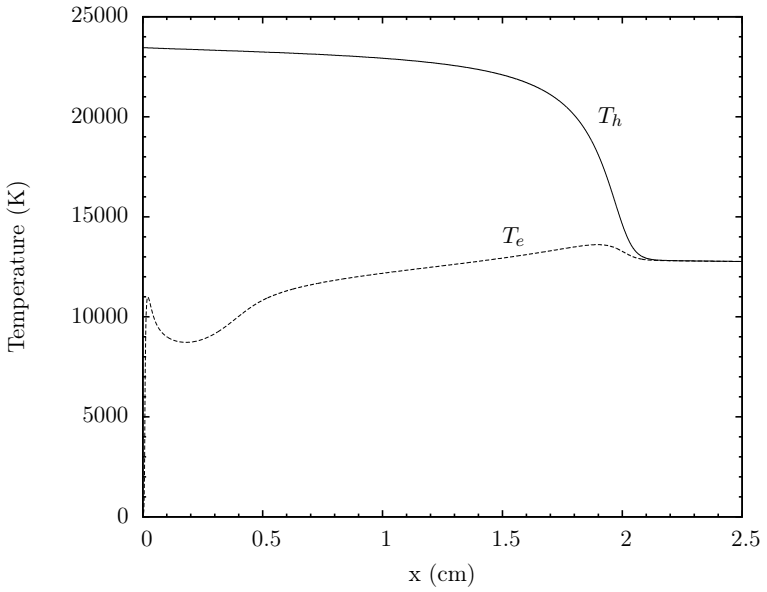

Figure 4.9: Temperature profile of the electrons and heavy particles for case 1 from table 4.13.

the shock. One can see in the region where the priming electrons are produced ($x = 0.01$ cm) and where electron kinetics starts to dominate ($x = 0.1$ cm), the ASDF exhibits a non-Boltzmann behavior, presumably due to a competition between the atom-impact and electron-impact processes. Further downstream from the shock, the ASDF relaxes toward a Boltzmann distribution.

It can be seen that all the upper levels beyond the $4s$ manifold in this test case can be well approximated by a Boltzmann distribution. This small deviation from a Boltzmann distribution (notably only from the $4s$ manifold) indicates that the flow might be approximated by a three-temperature model; however, one still needs to model the losses due to radiation in order to resolve the radiative cooling region behind the avalanche. The results of the steady state calculations for the other three cases are shown in figures 4.11, 4.12 and 4.13. Good agreement is obtained for cases 2 and 3. For case 4, the electron number density and the relaxation length are over-predicted compared to the experimental data. The discrepancies

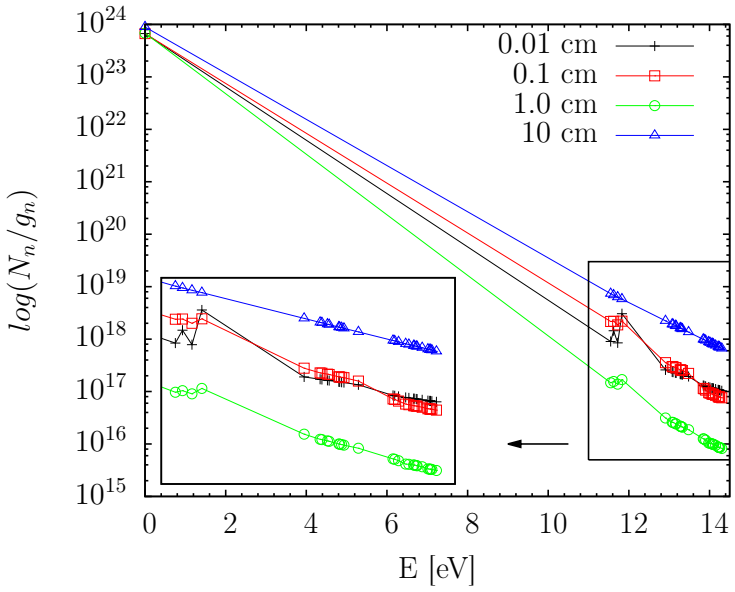

Figure 4.10: The ASDF plotted at different locations of starting from the shock front utilizing the experimental condition from case 1 of table 4.13.

can be attributed to unsteady effects and interaction with the boundary layer, both of which, can be verified by performing unsteady simulations incorporating viscous effects, i.e., solving Navier-Stokes equations.

Similarly, the steady state calculations are performed for the case of Krypton shocks. The flow conditions along with the experimental relaxation length are taken from Glass *et al.* [111] and summarized in table 4.14. The simulation results for case 1 are shown in figures 4.14 and 4.15 for the number densities and temperatures, respectively.

Similar to the Argon shock experiment, with the tuned value of the atom-impact cross section, we were able to obtain good agreement with the experimental relaxation length. For the radiative cooling reason behind the avalanche, the formula of Vlcěk with some modification yields satisfactory results. Non-Boltzmann population of the excited states can be seen most clearly in figure 4.16 at 0.01 and 0.1 cm. The results for case 2 are shown in figure 4.17 with excellent agreement

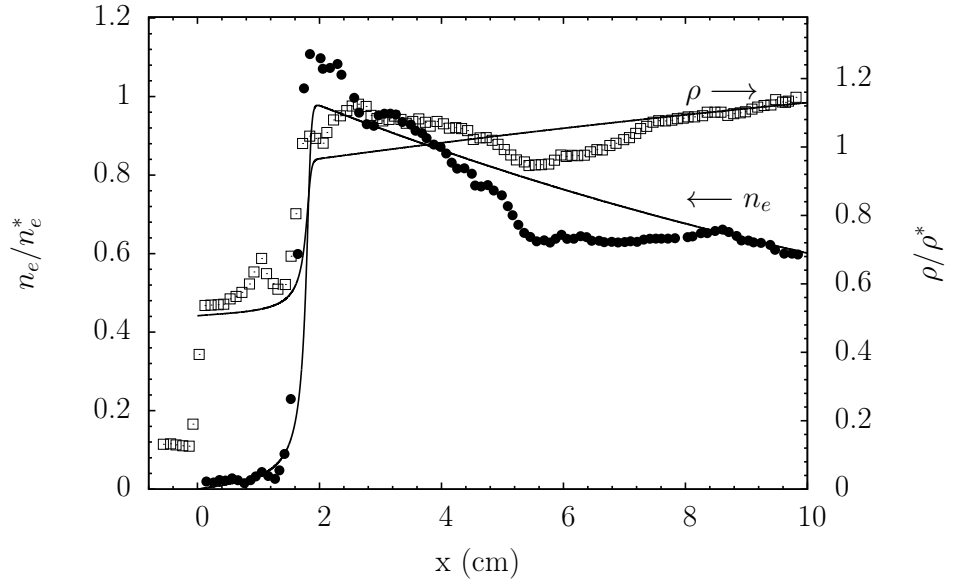

Figure 4.11: Electron number density and total density for $M_\infty = 16.1$ Ar shock corresponded to case 2 in table 4.13. The freestream conditions are: $p_\infty = 5.15$ Torr, $T_\infty = 295.9$ K. The values of the electron number density and the total mass density are normalized by the equilibrium values: $n_e^* = 1.83 \times 10^{17}$ cm^{-3}, $\rho^* = 0.87 \times 10^{-4}$ g/cm^3. Symbols represent experimental data for n_e and ρ from Glass and Liu [110].

.

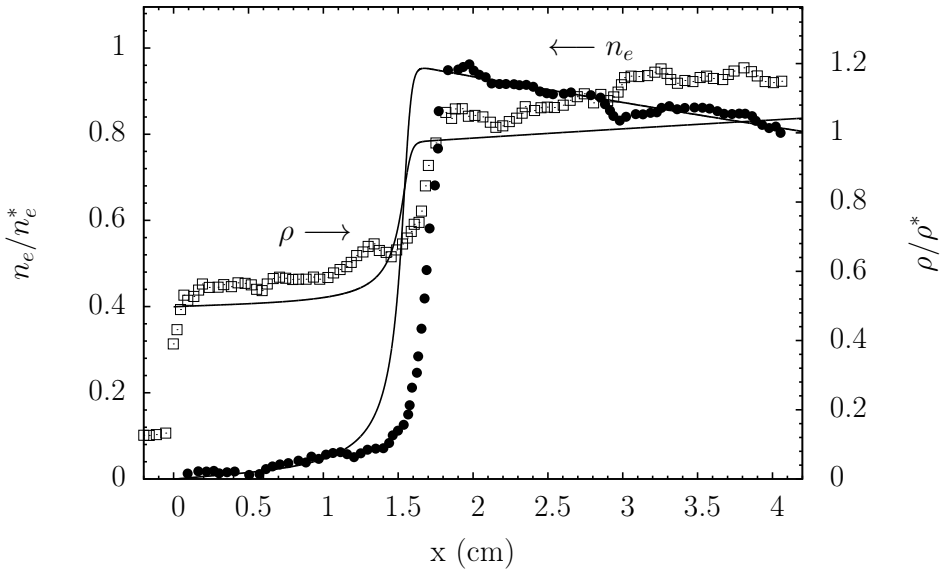

Figure 4.12: Electron number density and total density for $M_\infty = 16.5$ Ar shock corresponded to case 3 in table 4.13. The freestream conditions are: $p_\infty = 5.12$ Torr, $T_\infty = 296.6$ K. The values of the electron number density and the total mass density are normalized by the equilibrium values: $n_e^* = 2.1 \times 10^{17}$ cm^{-3}, $\rho^* = 0.88 \times 10^{-4}$ g/cm^3. Symbols represent experimental data for n_e and ρ from Glass and Liu [110].

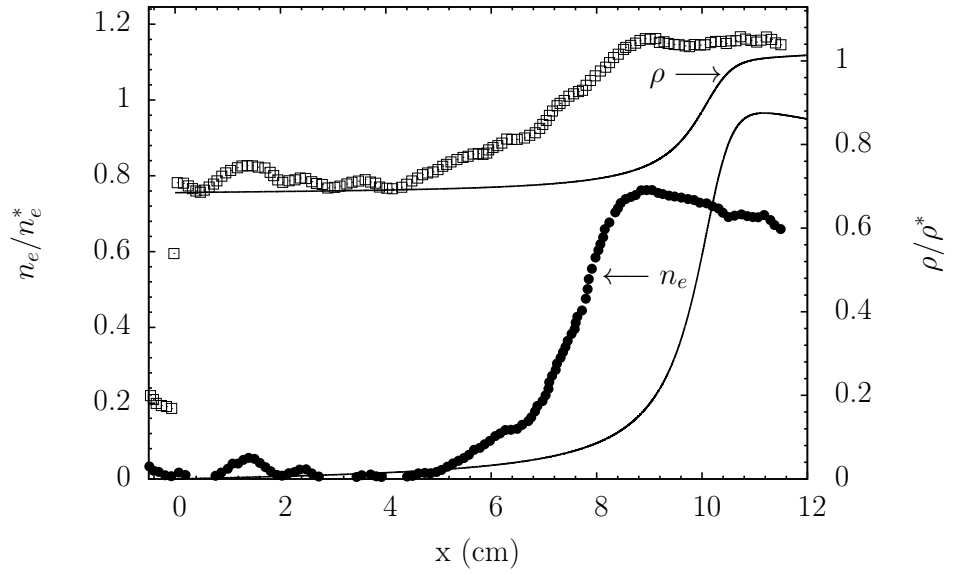

Figure 4.13: Electron number density and total density for $M_\infty = 13.0$ Ar shock corresponded to case 4 in table 4.13. The freestream conditions are: $p_\infty = 5.00$ Torr, $T_\infty = 296.6$ K. The values of the electron number density and the total mass density are normalized by the equilibrium values: $n_e^* = 5.62 \times 10^{16}$ cm^{-3}, $\rho^* = 0.62 \times 10^{-4}$ g/cm^3. Symbols represent experimental data for n_e and ρ from Glass and Liu [110].

Cases	Ma	p_∞ (Torr)	T_∞ (K)	l^* (cm)
1	15.05	5.15	296.2	1.75
2	15.17	5.07	295.4	1.90

Table 4.14: Summary of test conditions of the UTIAS experiments for ionizing shocks in Krypton with the predicted thermal equilibrium flow properties. Data are taken from Glass *et al.* [111].

to the experimental data.

Lastly, the CR model for Xenon is utilized to model the shock tube experiment by Ezumi *et al.* [112]. Similar to the UTIAS experiment, Ezumi *et al.* investigated the ionization relaxation and radiative cooling processes of an ionizing shock flow in Xenon. In their experiment, measurement of the electron number density and the heavy particle number density are carried out using interferometric techniques, and the results are taken at one particular location along the shock tube. The shock Mach number is 13.1 and the freestream pressure is 2.0 Torr. Figure 4.18 shows the steady-state calculation of the shock layer, with satisfactory agreement to experiment.

In this test case, due to the high uncertainty in the use of Drawin's formula for atom-impact rates, these rates are tuned to match the experimental relaxation time. Also, due to the lack of the cross sections data for the radiative cooling process, the values obtained from Vlček's expression [91] also need to be slightly modified. Therefore, the results for Xenon shock presented in this section should be considered as preliminary only. In order to improve the model, radiation transport should be included, and better atom-impact cross sections, those computed from ab initio calculation, should be implemented.

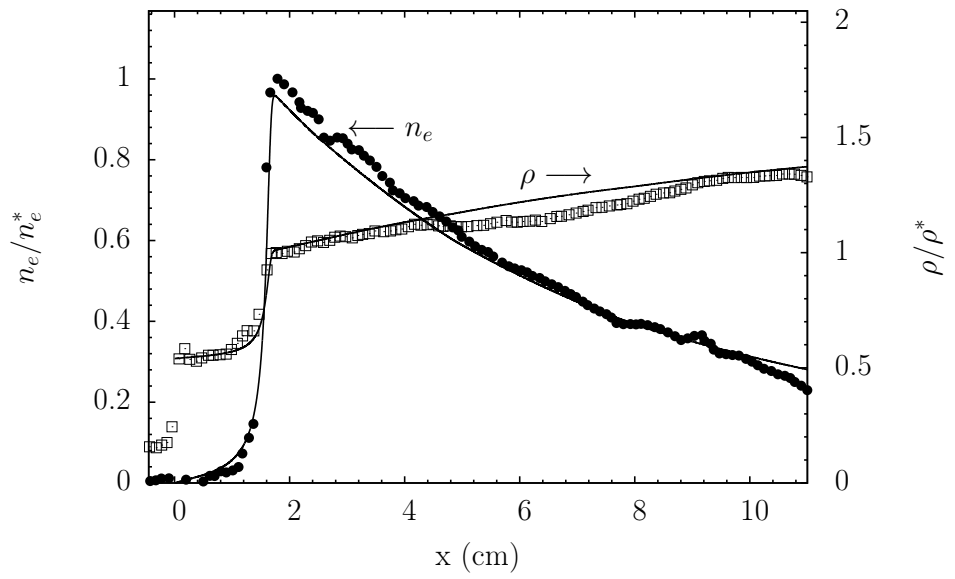

Figure 4.14: Electron number density and total density for $M_\infty = 15.05$ Kr shock corresponded to case 1 in table 4.14. The freestream conditions are: $p_\infty = 5.15$ Torr, $T_\infty = 296.2$ K. The values of the electron number density and the total mass density are normalized by the equilibrium values: $n_e^* = 1.677 \times 10^{17}$ cm^{-3}, $\rho^* = 1.712 \times 10^{-4}$ g/cm^3. Symbols represent experimental data for n_e and ρ from Glass *et al.* [111].

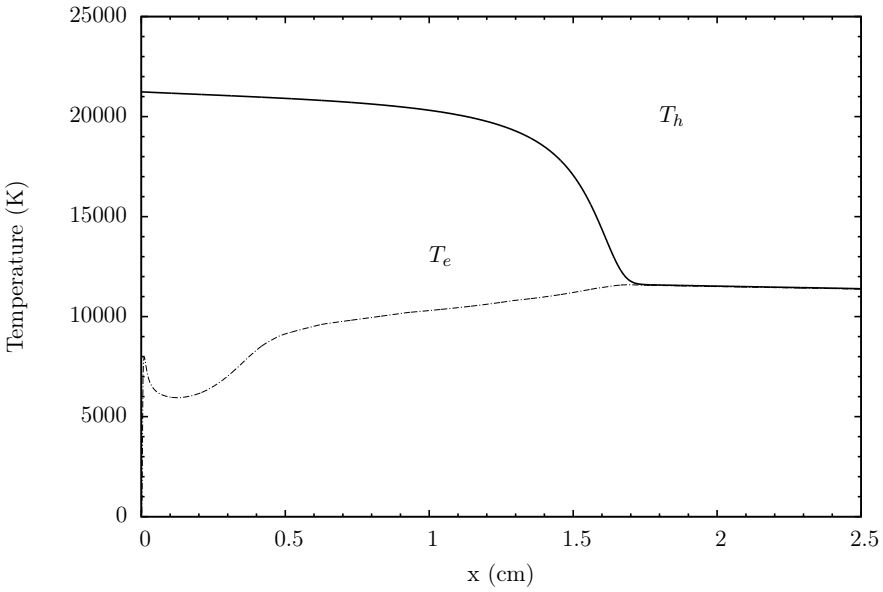

Figure 4.15: Temperature profile of the electrons and heavy particles for case 1 from table 4.14.

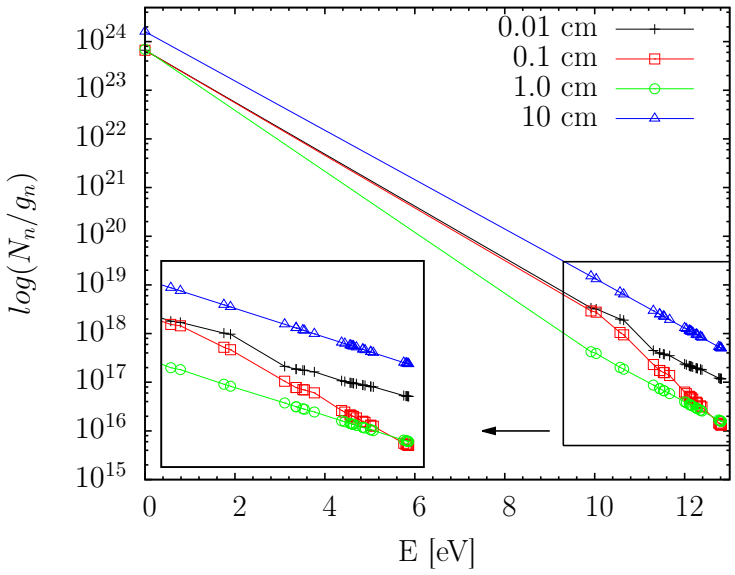

Figure 4.16: The ASDF plotted at different locations of starting from the shock front utilizing the experimental conditions from case 1 of table 4.14.

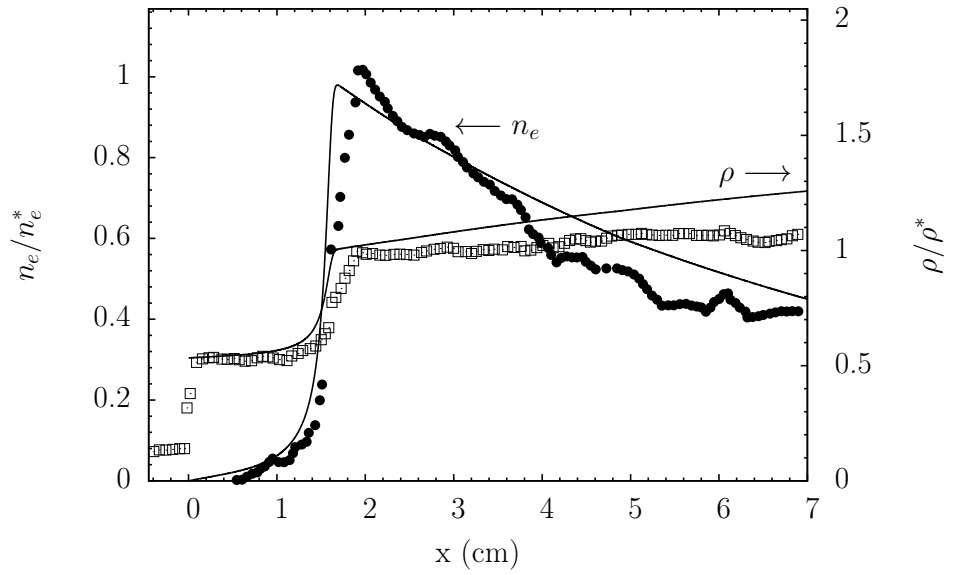

Figure 4.17: Computed and experimental results of ionizing shock in Krypton for case 2: $p_\infty = 5.07$ Torr, $T_\infty = 295.4$ K, $Ma = 15.17$. The values of the electron number density and the total mass density are normalized by the equilibrium values: $n_e^* = 1.712 \times 10^{17}$ cm^{-3}, $\rho^* = 1.708 \times 10^{-4}$ g/cm^3. Symbols represent experimental data for n_e and ρ from Glass *et al.* [111].

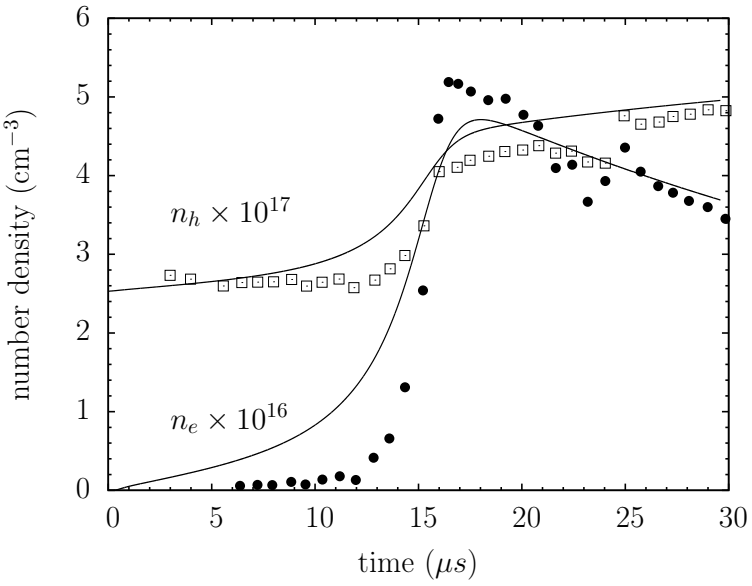

Figure 4.18: Electron number density and heavy particle number density for $M_\infty = 13.1$ Xe shock. Symbols represent experimental data for n_e and n_h from Ezumi *et al.* [112]. The freestream conditions are: $p_\infty = 2.00$ Torr, $T_\infty = 300$ K.

4.6.2 Unsteady flows

In this section, we performed time accurate calculation of the same test cases described in the previous section utilizing the calibrated CR model. The shock is initiated by imposing a uniform flow field on a 1D domain with the right boundary being a reflective wall. The freestream conditions are $T_\infty = 293.6$ K, $p_\infty = 5.14$ Torr, and $u_\infty = 4535$ m/s. The initial condition corresponds to case 1 of table 4.13 for Argon. This test case were studied previously by Kapper and Cambier [97], which reveals complex dynamics of the coupling between convection and chemical kinetics.

In this simulation, the 2T model described in section 2.4 is utilized with detailed kinetic source term as discussed in section 4.4. For the convection term, a third-order MP scheme is used in conjunction with a RK3 scheme for time integration. The reason for using a lower order scheme (as opposed to the 5th order scheme) is due to numerical difficulties encountered in resolving a high density gradient (up to 10 order of magnitude) at the shock.

The origin of such a high density gradient is due to the activation of the CR kinetics right after the shock. In this region, the atom-impact processes start taking place at the rates determined by the post-shock temperature of the heavy species, therefore populating the excited states at a much higher number density compared to the freestream values. In addition, the simplified treatment of the radiative processes also exacerbate the problem. In particular, since the escape factors are pre-determined from an order of magnitude analysis of the radiative mean free path, using the same set of escape factors for all the computational cells causes an artificial radiation in the free steam gas, which effectively lowers the population of the excited states and also raises the electron temperature[2]. These high and low populations of the excited states cause a sharp density gradient

[2]This electron preheating artifact is specifically due to radiative recombination.

which makes high-order reconstruction schemes unstable. The use of an lower order scheme relieve the problem by introducing more numerical diffusion. This problem can be remedied by including the full solution of radiation transport, therefore avoiding the escape factors.

The results of the time accurate solutions are shown in figures 4.19 and 4.20 for the total mass density and electron number density, respectively. The highly unsteady evolution, especially in the induction zone, suggests a non-linear wave coupling mechanism between the shock and the avalanche layer. The coupling cycle, as indicated by Kapper and Cambier [97], starts with an initiation of a pressure wave travelling from the avalanche toward the shock. This pressure wave causes the shock to accelerate, which results in a reflection of a entropy wave. As the entropy wave travels toward the avalanche layer, the sensitivity of the chemical rates to the temperature rise causes an early new avalanche, and the cycle is repeated. The onset of the new avalanche can be seen most clearly from figure 4.20.

The time period of these cycles can be estimated from basic wave theory [113]:

$$\tau = \overline{l}\left(\frac{1}{a_2 - u_2} + \frac{1}{u_2}\right) \tag{4.72}$$

where $\overline{l}$ is the average induction length, and u_2 and a_2 are the post shock velocity and speed of sound. Figure 4.21 shows the density contour on a $x - t$ diagram. One can clearly see the fluctuation in the induction length, and the periodicity of the shock structure. These features are strictly time-dependent, and cannot be revealed in steady-state simulations. The unsteady simulation shows that the sensitivity of the CR cross sections directly translates to the fluctuating mechanism via non-linear coupling with convection process. It must be pointed out that this mechanism possesses similar characteristics to instability in gaseous detonation, which can also be explained by non-linear wave-coupling [75].

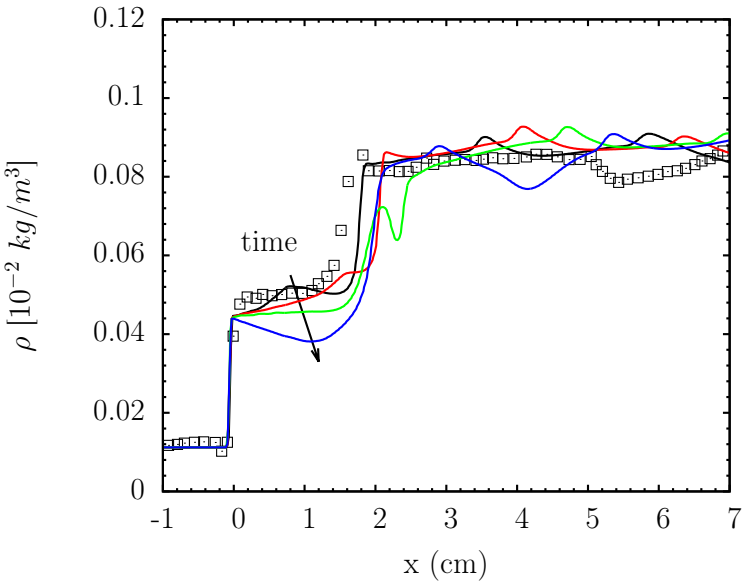

Figure 4.19: Total mass density of ionizing shock in Argon for case 1 of table 4.13. Different lines correspond to the solutions at the different times, and the arrow indicates flow solutions as time increases. The symbols are the experimental data from the UTIAS experiment [110].

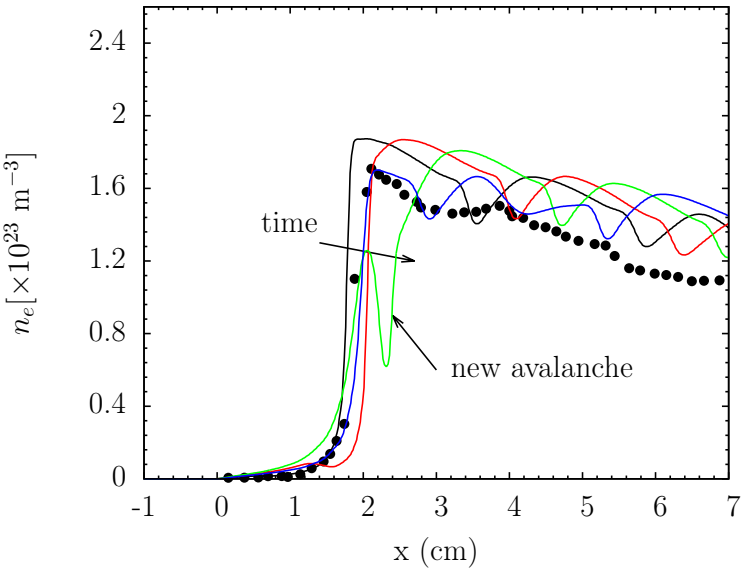

Figure 4.20: Electron number density of ionizing shock in Argon for case 1 of table 4.13. Different lines correspond to the solutions at different times. The symbols are the experimental data from the UTIAS experiment [110].

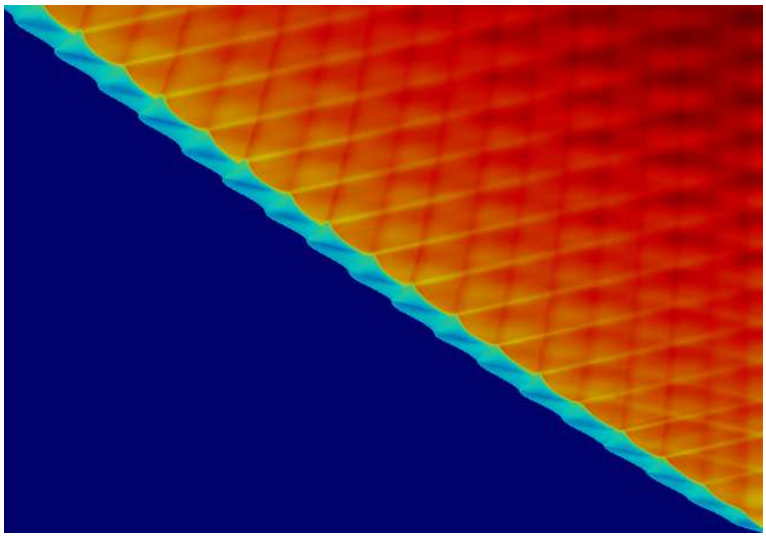

Figure 4.21: $x-t$ diagram of total mass density ρ for a Ma 15.9 ionizing shock in Argon showing complex dynamics of the coupling between convection and kinetics. Colormap: min max

CHAPTER 5

Complexity Reduction of Collisional-Radiative Kinetics

This chapter was taken with slight modification from the article "Complexity reduction of collisional-radiative kinetics for atomic plasma", published in *Physics of Plasmas* [114].

5.1 Introduction

In the previous chapter, we demonstrate the use of the CR model in reproducing the correct structure of an ionizing shock in monatomic gases. This level of detail is needed for an accurate prediction of high-speed plasma flows. In addition, the unsteady coupling of the hydrodynamics and CR kinetics leads to physical phenomena which can, in turn, provide additional information useful for model validation and/or experimental measurement of various parameters. These CR models, although very accurate from a physics point of view, can be computationally very expensive due to the large number of internal states for which the number densities must be computed. For example, in the ionizing shock test case shown in section 4.6.1 for Argon, one needs to include excited states beyond the $4s$ manifold to accurately capture the line radiation responsible for the radiative cooling region behind the shock.

Due to the large computational workload involved in solving the CR master equations, simulations incorporating state-to-state kinetics have only been limited

to zero- or one-dimension with a few exceptions of two-dimensional calculations [115, 116, 90]. For example, the run-time for solving a set of rate equations for the CR kinetics of atomic hydrogen scales as the cubic power of the size of the ASDF when an implicit, backward-Euler method is employed. While better scaling laws could be obtained with iterative and more approximate schemes, their accuracy and stability for extremely stiff problems is still an issue.

The development of very efficient and accurate schemes for CR kinetics is still an ongoing research topic which will be presented elsewhere; here, we discuss a different approach, consisting of lowering the complexity of the calculations by developing a reduced-order kinetic model suitable for multi-dimensional flow calculations while maintaining a sufficient level of detail required to accurately model the plasma.

Several mechanism reduction schemes have been proposed in the literature with applications to various types of kinetics. Colonna *et al.* [117] utilize a two-level distribution model to study nitrogen dissociation rates in recombining flows, in which all the vibrational levels except for the last level are modeled by a single energy equation with an assumption of a Boltzmann distribution, and the last vibrational level is modeled using state-to-state kinetics to take in account the non-equilibrium effects of the upper states. Magin *et al.* [36] have developed a rovibrational collisional coarse-grain model to characterize the internal energy excitation and dissociation processes of nitrogen flow behind a strong shock wave. The coarse-grain model is derived by lumping the rovibrational energy levels into groups, in which the population is described by a uniform distribution. Guy *et al.* [37] proposed a multi-internal-temperatures models for a vibrationally non-equilibrium flow, in which the vibrational distribution is divided into two or three groups, each with its own vibrational temperature. Liu *et al.* [118], on the other hand, proposed a mechanism reduction to CR models based on the multi-group maximum entropy principle with the constraints being the macroscopic parame-

ters.

In this chapter, we examine several different level grouping schemes for the state-to-state kinetics of *atomic* electronic states. The first approach is similar to that of Magin *et al.* [36] for the rovibrational collisional coarse-grain model, and therefore is based on uniform (U) binning of the levels. The second approach here consists of grouping levels into groups with an assumed Boltzmann (B) distribution, allowing a higher-order description of the ASDF. In this case, the effective excitation temperatures are evolved in time by conserving a set of moments of the distribution function; the most obvious solution is to solve for number density and energy, similar to Guys *et al.*'s approach [37]. However, we will show that a different set of moment variables of the same order should be used, due to the specific nature of the ASDF.

The method developed here can be applied to a wide range of state-to-state kinetics models including the rovibrational [36, 58] (RVC) and vibrational [119] (VC) collisional models or the electronic collisional-radiative model [90, 91, 120, 121]. In the interest of simplicity, we consider here the collisional-radiative (CR) model of atomic Hydrogen, using classical models for the level energies and rates; the actual values of these parameters is unimportant here, as long as the structure of the ASDF is representative of the actual species, notably the geometric progression of the level energies of the ASDF and the stiffness ratio. The level grouping techniques are applied to reduce the cost of solving the full master equations and the results are compared with the reference solution computed from the full master equations.

5.2 Collisional-Radiative model

5.2.1 Definitions and rates

As mentioned above, we consider here the ASDF of atomic Hydrogen coupled to electron impact excitation and ionization, and the reverse processes (respectively deexcitation and recombination), as well as the radiative rates for line transitions in an optically-thin approximation. Radiative recombination is neglected and all radiation absorption is ignored, as is free-free (Bremsstrahlung) emission, since this does not directly affect the atomic level populations[1]. The atomic states of the Hydrogen atom are listed as a function of their principal quantum number (n) only, following the Bohr atomic model; the splitting of states with respect to orbital and spin numbers is ignored, and all states have a degeneracy $g_n = 2n^2$. The states number from $n = 1$ to ∞ and we consider a finite number of states $n = 1, \ldots, M < \infty$ before reaching the ionization limit[2]. In this simplified model, the energy of each state is given as $E_n = I_H\,(1-1/n^2)$, as measured from the ground state ($E_1 \equiv 0$), and we will denote by $I_n = I_H\,(1/n^2-1/M^2) \simeq I_H/n^2$ the energy required for ionization of level n.

The classical form of the cross-section for energy exchange between a free electron and the atom [83], leading to an excitation from level n to level $m > n$ is:

$$\sigma^e_{nm} = (4\pi a_0^2)\frac{I_H^2\,(E - \Delta E_{nm})}{E_{nm}E^2} \cdot (3\mathrm{f}_{nm}) \tag{5.1}$$

where a_0 is the Bohr radius, E is the energy of the free electron, $\Delta E_{nm} = E_m - E_n$

[1] Two of the test cases considered here are isothermal, i.e. T_e =constant. The third test case has a variable T_e but is designed only to test energy conservation, and hence radiative energy losses would not serve this purpose.

[2] Strictly speaking, the ionization limit I_H is attained for $n \to \infty$. In reality, the ionization potential is lowered as a result of interaction with the plasma (Debye shielding) and quantum uncertainty. In practice, the truncation is accomplished at a lower limit still; for the current purpose, details of this truncation procedure can be ignored. Suffice to say that the series extends to a number $n = M$, which can be considered large, e.g. $O(100)$.

is the energy gap between n and m and f_{nm} is the oscillator strength:

$$\mathrm{f}_{nm} = \frac{32}{3\pi\sqrt{3}} \frac{1}{n^5} \frac{1}{m^3} \frac{1}{\left(\frac{1}{n^2} - \frac{1}{m^2}\right)^3} \tag{5.2}$$

The free electrons are assumed to follow an isotropic Maxwellian distribution, i.e., equation (4.11). The rate of excitation is obtained by averaging over the distribution function:

$$\alpha^e_{(m|n)} = \frac{\overline{v}_e}{(kT_e)^2} \int_{E_{nm}}^{\infty} \sigma^e_{nm}(E) E f_e(E) dE, \tag{5.3}$$

leading to

$$\alpha^e_{(m|n)} = (4\pi a_0^2)\overline{v}_e \left(\frac{I_H}{kT_e}\right)^2 (3\mathrm{f}_{nm})\psi_{nm} \tag{5.4}$$

where

$$\overline{v}_e = \left(\frac{8kT_e}{\pi m_e}\right)^{\frac{1}{2}}, \quad \psi_{nm} = \frac{e^{-x_{nm}}}{x_{nm}} - E_1(x_{nm}) \qquad \text{and} \qquad E_1(x) = \int_x^{\infty} \frac{e^{-y}}{y} dy \tag{5.5}$$

Here, $\overline{v}_e$ is the mean thermal electron velocity, $x_{nm} = \Delta E_{nm}/kT_e$ and E_1 is the exponential integral. The reverse rate can be found from detailed balance:

$$\beta^e_{(n|m)} = \frac{n^2}{m^2} e^{+x_{nm}} \cdot \alpha_{(m|n)} \tag{5.6}$$

We use the low temperature approximation [83] ($x_{nm} >> 1$)

$$E_1(x) \simeq \frac{e^{-x}}{x}\left(1 - \frac{1}{x}\right), \tag{5.7}$$

in which case:

$$\alpha^e_{(m|n)} \simeq \left[4\pi a_0^2 \cdot \frac{32}{\pi\sqrt{3}} \cdot \overline{v}_e\right] \frac{e^{-x_{nm}}}{n^5 m^3 (n^{-2} - m^{-2})^5} \tag{5.8a}$$

$$\beta^e_{(n|m)} \simeq \left[4\pi a_0^2 \cdot \frac{32}{\pi\sqrt{3}} \cdot \overline{v}_e\right] \frac{1}{n^3 m^5 (n^{-2} - m^{-2})^5} \tag{5.8b}$$

The factor in brackets is an upper bound, which is reached for the upper states when $x_{nm} \to 0$. Another scale is the factor I_H/kT_e in x_{nm}, which is effectively responsible for the stiffness. If that factor is very low (high temperatures), all

rates are of the same order; at low temperatures, the exponential term dominates and the range of time scales is increased.

The cross-section for ionization by electron impact has a form similar to (5.1), i.e.:

$$\sigma_n^e = (4\pi a_0^2)\frac{I_H^2\,(E - I_n)}{I_n E^2} \tag{5.9}$$

This leads to an ionization rate coefficient [83]:

$$\alpha_{(+|n)}^e = (4\pi a_0^2)\overline{v}_e \left(\frac{I_H}{kT_e}\right)^2 \psi(x_n) \tag{5.10}$$

The final state $(+|$ is an ionized state, i.e. where one electron initially bound to the atom has reached the ionization limit ($n = \infty$) and is part of a free continuum of states. Using the principle of detailed balance, the reverse (recombination) rate is:

$$\beta_{(n|+)}^e \simeq \left[\frac{4}{\pi}\frac{a_0^2 h^3}{m_e^2 kT_e}\right]\left(\frac{I_H}{kT_e}\right)^2 n^2 \psi(x_n) e^{x_n} \tag{5.11}$$

Using the same low temperature approximation (5.7), we obtain [83]:

$$\alpha_{(+|n)}^e \simeq (4\pi a_0^2)\left(\frac{8kT_e}{\pi m_e}\right)^{1/2} n^4 e^{-x_n} \tag{5.12a}$$

$$\beta_{(n|+)}^e \simeq \left[\frac{4}{\pi}\frac{a_0^2 h^3}{m_e^2 kT_e}\right] n^6 \tag{5.12b}$$

The rates of radiative transitions between levels can also be obtained classically for the Hydrogen atom [86]. The spontaneous emission rates from an upper level m are:

$$A_{(n|m)} = \left(\frac{8\pi^2 e^2}{m_e c^3}\right)\frac{g_n}{g_m}\mathrm{f}_{nm} = \frac{1.6\times 10^{10}}{m^3 n(m^2 - n^2)}\mathrm{sec}^{-1} \tag{5.13}$$

The expression on the right is for atomic Hydrogen only.

5.2.2 Master equations

Once all the macroscopic rates are obtained, we can construct the master equations describing the collisional-radiative kinetics of all levels. In this study we consider

atomic Hydrogen, which has only one ion state, and only electron collisions, which allows us to remove the super-script e in the rate definition hereafter. The rate of change of the population density of a level n is thus written as:

$$\begin{aligned}\frac{dN_n}{dt} = &- \sum_{m>n} \alpha_{(m|n)} N_e N_n + \sum_{m>n} \beta_{(n|m)} N_e N_m + \sum_{m>n} A_{(n|m)} N_m \\ &+ \sum_{m<n} \alpha_{(n|m)} N_e N_m - \sum_{m<n} \beta_{(m|n)} N_e N_n - \sum_{m<n} A_{(m|n)} N_n \\ &- \alpha_{(+|n)} N_e N_n + \beta_{(n|+)} N_+ N_e^2\end{aligned} \tag{5.14}$$

Similarly, we can write another equation for the rate of change of the population density of the ions according to the rate of ionization or recombination:

$$\frac{dN_+}{dt} = \sum_n \alpha_{(+|n)} N_e N_n - \sum_n \beta_{(n|+)} N_+ N_e^2 \tag{5.15}$$

Finally, the electron density is related to the ion density by the charge neutrality condition:

$$N_e = \sum_q Z_q N_q \tag{5.16}$$

We will compute the time evolution of a uniform plasma; if we assume a constant temperature bath, the conservation equations above constitute a complete set, but for constant-volume conditions – with time variation of the temperature – there is also conservation equation for the electron energy, which will be examined in more detail in section 5.5. The task of deriving a reduced model for the CR kinetics aims at modeling the shape of the atomic state distribution function (ASDF) at a lower computational cost compared to that required to solve the full master equations, while maintaining sufficient accuracy to capture the non-equilibrium effects. The most natural way to accomplish this is to partition the excited states into groups or "bins", therefore reducing the number of variables in the system. Various assumptions can be made about the internal structure of each group, i.e. the distribution of states *within* the groups, and various approaches to solving the group-based variables can be devised.

5.3 Level grouping strategies

5.3.1 Uniform grouping

Consider a group of M individual levels $i = \{n_0, \ldots, n_{M-1}\}$, abbreviated as $i \in n$ and denote the group, or "bin" number by n; hereafter, $n, m, \ldots$ are the group indices and $i, j, \ldots$ are level indices. This first approach to model reduction is essentially a zeroth-order approximation of the internal[3] distribution function, where only one moment variable, either the total number density of the group or the total excitation energy of the group, is required. The traditional choice is to conserve the total number density of the group, i.e., $\mathcal{N}_n = \sum_{i \in n} N_i$. Using (4.32), a Boltzmann approximation of the internal partition function $\mathcal{Z}_n$ is obtained by[4]:

$$\mathcal{N}_n = N_{n_0} \sum_{i \in n} \frac{N_i}{N_{n_0}} \simeq \frac{N_{n_0}}{g_{n_0}} \underbrace{\sum_{i \in n} g_i e^{-\Delta E_i / T_n}}_{\mathcal{Z}_n} \tag{5.17}$$

where $\Delta E_i = E_i - E_{n_0}$ is the difference in energy between the level i and the first level of the group, n_0. The approximation of a group with uniform internal distribution is equivalent to having a characteristic group temperature T_n approaching infinity, compared to the total energy width of the group, i.e.:

$$\mathcal{Z}_n \to g_n = \sum_{i \in n} g_i \tag{5.18}$$

where g_n is the overall group degeneracy. The simplest model therefore consists of assuming all levels within the group to be distributed uniformly, i.e., weighted by the level degeneracy

$$N_i = \frac{g_i}{g_n} \mathcal{N}_n \tag{5.19}$$

[3] That is, within the group.

[4] For further ease of notation, the Boltzmann constant k is not explicitly written.

The rate equation for a group n is obtained by summing the master rate equations (5.14-5.15) for all the levels i within the group, and utilizing relation (5.17):

$$\begin{aligned}\frac{d\mathcal{N}_n}{dt} =& - N_e \mathcal{N}_n \left[\sum_{m>n} \sum_{i\in n} \frac{g_i}{g_n} \sum_{j\in m} \alpha_{(j|i)} + \sum_{m<n} \sum_{i\in n} \frac{g_i}{g_n} \sum_{j\in m} \beta_{(j|i)} \right] \\ &+ N_e \mathcal{N}_m \left[\sum_{m<n} \sum_{i\in n} \sum_{j\in m} \frac{g_j}{g_m} \alpha_{(i|j)} + \sum_{m>n} \sum_{i\in n} \sum_{j\in m} \frac{g_j}{g_m} \beta_{(i|j)} \right] \\ &- \mathcal{N}_n \left[\sum_{m<n} \sum_{i\in n} \frac{g_i}{g_n} \sum_{j\in m} A_{(j|i)} \right] + \mathcal{N}_m \left[\sum_{m>n} \sum_{i\in n} \sum_{j\in m} \frac{g_j}{g_m} A_{(i|j)} \right] \\ &- N_e \mathcal{N}_n \left[\sum_{i\in n} \frac{g_i}{g_n} \alpha_{(+|i)} \right] + N_e^2 N_+ \left[\sum_{i\in n} \beta_{(i|+)} \right]\end{aligned} \tag{5.20}$$

Similarly for the ion state, one obtains:

$$\frac{dN_+}{dt} = N_e \sum_n \mathcal{N}_n \left[\sum_{i\in n} \frac{g_i}{g_n} \alpha_{(+|i)} \right] - N_e^2 N_+ \sum_n \left[\sum_{i\in n} \beta_{(i|+)} \right] \tag{5.21}$$

The terms within brackets in equations (5.20-5.21) contain *effective* rates for the groups, which can be pre-computed. For example, in the first term on the right-hand-side of equation (5.20),

$$\tilde{\alpha}_{(m|n)} = \sum_{i\in n} \frac{g_i}{g_n} \sum_{j\in m} \alpha_{(j|i)}$$

is an effective excitation rate from group n to group m. Note that since this model does not require computing an excitation temperature T_n, all the effective transition rates between the groups can be expressed as a function of the kinetic temperature T_e only. It is important to emphasize that the grouping of levels is applied on the high energy states only; thus in any simulation we must choose a number of low-energy, "resolved" levels, as well as a variable number of groups combining the upper states. The number of discrete states, the number of groups and their widths are variable parameters of the model, whether we use uniform binning as above, or Boltzmann internal distributions, discussed below. In order to bound this parameter space (optimization is beyond the scope of the present work), we need to provide a reference solution, such that the population density

of each level can be compared to the one reconstructed from the assumed internal distribution within each group. Figure 5.1 shows the evolution of the electron density computed from the master equations. This test corresponds to a strong ionization regime and the time evolution of the ASDF shows an increasing population of the higher atomic levels while the electron density grows exponentially. It also demonstrates the effect of the number of levels included in the simulation, i.e. using a fewer number of atomic states has an impact on delaying the onset of the electron avalanche. This indicates that ionization from the high-energy states is an important process, and therefore the evolution of the upper states must be accurately captured. We could always increase the size of the ASDF to obtain higher accuracy, but with diminishing return; ultimately, the time-resolution of interest and the accuracy threshold dictate the number of levels required in a simulation. The mapping between the practical requirements and ASDF size is not a straightforward matter, but is an issue beyond the scope of this work. Convergence studies with respect to the size of the system showed that beyond 20 levels, there were no discernible differences in the results – see Figure 5.1. Thus, we chose our reference solution to be the one obtained for 20 levels, and all level-grouping models investigated here will be based on this extent of the ASDF.

5.3.2 Boltzmann grouping - number and energy

Several assumptions can be made regarding a Boltzmann-like structure within the group. Panesi *et al.* [121] and Munafo *et al.* [122] rely on the the assumption that the population within a group follows a Boltzmann distribution at the kinetic temperature, i.e. in this case, $T_n \equiv T_e$. This approach is only valid if the rates of exchange between the levels within the group are much faster than the exchange rates with levels outside the group; otherwise, one could then assume that the entire ASDF is governed by T_e and is always in Boltzmann equilibrium. The validity of this assumption is highly questionable for atomic state popula-

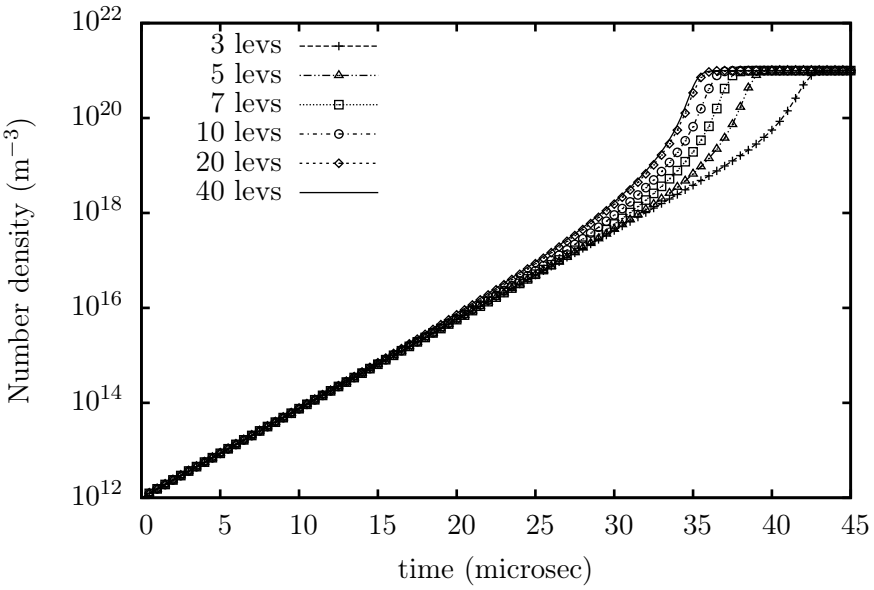

Figure 5.1: Time evolution of the electron number density using different total number of atomic levels. The electron temperature is set at 3.0 eV.

tions[5]. Furthermore, when different collision partners must be considered, the kinetic temperature can be either that of the heavy particles or the electrons (e.g. electron-impact excitation and heavy impact quenching); in this case, choosing either one of the kinetic temperature can impact on the results.

In order to accurately describe the population of a group with a Boltzmann distribution, two moment variables of the ASDF need to be conserved. The selection of these variables, however, can be arbitrary. Guy *et al.* [37] conserved the total number density of the group and the average excitation energy; these respectively correspond to zeroth- and first-order moment variables, and would appear to be a natural choice. Consider the total number of states $\mathcal{N}_n$ - defined in equation (5.17) - and the total energy within the bin $\mathcal{E}_n = \sum_{i \in n} E_i N_i$, for which

[5]In a log-plot, this model assumes that the slope within each "bin" is always the same, and is not related to the average slope determined by the difference between adjacent bins.

we can write conservation equations, derived from (5.14):

$$\frac{d\mathcal{N}_n}{dt} = -N_e \mathcal{N}_n \left[\sum_{m>n} \sum_{i\in n} \frac{g_i e^{-\Delta E_i/T_n}}{\mathcal{Z}_n} \sum_{j\in m} \alpha_{(j|i)} + \sum_{m<n} \sum_{i\in n} \frac{g_i e^{-\Delta E_i/T_n}}{\mathcal{Z}_n} \sum_{j\in m} \beta_{(j|i)} \right] + \dots \tag{5.22a}$$

$$\frac{d\mathcal{E}_n}{dt} = -N_e \mathcal{N}_n \left[\sum_{m>n} \sum_{i\in n} \frac{g_i e^{-\Delta E_i/T_n}}{\mathcal{Z}_n} \sum_{j\in m} E_i \alpha_{(j|i)} + \sum_{m<n} \sum_{i\in n} \frac{g_i e^{-\Delta E_i/T_n}}{Z_n} \sum_{j\in m} E_i \beta_{(j|i)} \right] + \dots \tag{5.22b}$$

For sake of brevity, we did not write the entire list of contributions in (5.22), which can be easily derived from (5.20) by generalizing the weighting factors g_i/g_n to $g_i e^{-\Delta E_i/T_n}/\mathcal{Z}_n$, and similarly for other groups. By solving for total number and total energy of each group, according to equations (5.22a-5.22b), we can guarantee direct conservation of both mass (total number of levels $\mathcal{N}_n$) and energy ($\mathcal{E}_n$). However this approach presents some problems in determining the internal Boltzmann temperature, as will now be shown. First, let us define a total group/bin energy measured from the lower bound, i.e. $\Delta\mathcal{E}_n = \sum_{i\in n}(E_i - E_{n_0})N_i$; the rate of change of this shifted energy is still given by the right-hand-side of equation (5.22b). We can then write:

$$\Delta\mathcal{E}_n = \frac{N_{n_0}}{g_{n_0}} \sum_{i\in n} g_i \, \Delta E_i \, e^{-\Delta E_i/T_n} = \mathcal{N}_n \langle \Delta E \rangle_n \tag{5.23}$$

where

$$\langle \Delta E \rangle_n = \frac{1}{\mathcal{Z}_n} \sum_{i\in n} g_i \, \Delta E_i \, e^{-\Delta E_i/T_n} = T_n^2 \frac{d}{dT_n} \ln(\mathcal{Z}_n) \tag{5.24}$$

is the average group energy measured from the first internal level. Similarly, a specific heat at constant-volume can be determined, i.e.:

$$\begin{aligned} C_v(T_n) = \frac{d}{dT_n} \langle \Delta E \rangle_n &= T_n^{-2} \left[\frac{\sum_{i\in n} g_i (\Delta E_i)^2 e^{-\Delta E_i/T_n}}{\mathcal{Z}_n} - \langle \Delta E \rangle_n^2 \right] \\ &= T_n^{-2} \left[\langle \Delta E^2 \rangle_n - \langle \Delta E \rangle_n^2 \right] \end{aligned} \tag{5.25}$$

Since $\mathcal{N}_n$ and $\mathcal{E}_n$ are conserved variables, we obtain new values at each time level (k) and in order to compute the Boltzmann temperature T_n, we need to iterate the equation

$$\langle \Delta E \rangle_n (T_n^*) + C_v(T_n^*) \delta T_n^* = \frac{\Delta \mathcal{E}_n^{(k)}}{\mathcal{N}_n^{(k)}} \tag{5.26}$$

where T_n^* is the running iterated value, until convergence ($\delta T_n^* \simeq 0$). However, the slope of the curve $\langle \Delta E \rangle_n (T_n)$ is extremely flat at low temperature, i.e. $C_v \to 0$. In fact, when $T_n \to 0$, to the leading order we have: $\mathcal{N}_n \simeq N_{n_0}\, o(1+\epsilon)$, $\langle \Delta E \rangle_n \simeq o(\epsilon)$ and $C_v(T_n) \simeq o(\epsilon)$, where $\epsilon = e^{-\Delta E_1 / T_n}$ is a small parameter. Therefore during the iterations $\delta T_n^* = o(\epsilon)/o(\epsilon)$ and arbitrary temperature solutions can be obtained. Our studies showed that indeed, numerical instabilities prevent us from obtaining satisfactory solutions in many test cases. While it is possible to introduce limiters to prevent unphysical or improbable values and stop the iteration counters, this is not a satisfactory solution to the problem. We should also emphasize that the problem occurs when T_n is small, which does *not* imply that electronic levels are unpopulated, since we may very well have small *internal* group temperatures as a result of initial conditions or running iterations, but non-negligible overall electronic excitation ($\mathcal{N}_n \neq 0$)[6].

5.3.3 Boltzmann grouping - partitioning

In the approach above, we are dealing with two reduced values $\mathcal{N}_n$ and $\mathcal{E}_n$ (or $\Delta \mathcal{E}_n$) which are both summations over the internal levels. An alternative may consist of keeping one of the level populations as a variable. Therefore we could instead choose for each group n to conserve the population of the lowest level in that group N_{n_0} and $\mathcal{N}_n$, whose evolution is given by a form similar to equation (5.22a). To evaluate the Boltzmann temperature of the group, we now have at

[6]Note that this problem is particularly relevant to ASDF kinetics because of the geometric progression of the energy levels. By performing tests on a pseudo-atom with equidistant energy levels, stability of the iterations was much improved, although not entirely eliminated for some conditions.

time step (k), from (5.17):

$$\mathcal{N}_n^{(k)} = \frac{N_{n_0}^{(k)}}{g_{n_0}} \sum_{i \in n} g_i e^{-\Delta E_i / T_n} = \frac{N_{n_0}^{(k)}}{g_{n_0}} \mathcal{Z}_n(T_n^{(k)})$$

so that in order to evaluate the new bin temperature $T_n^{(k)}$ we need to solve

$$\mathcal{Z}_n(T_n^*) + \left(\frac{d\mathcal{Z}_n}{dT_n}\right) \delta T_n^* = \frac{\mathcal{N}_n^{(k)}}{N_{n_0}^{(k)}} g_{n_0} \tag{5.27}$$

until convergence. Using (5.24), this leads to:

$$\delta T_n^* \simeq \frac{T_n^{*2}}{\mathcal{Z}_n(T_n^*)\langle \Delta E \rangle_n(T_n^*)} \left[\frac{\mathcal{N}_n^{(k)}}{N_{n_0}^{(k)}} g_{n_0} - \mathcal{Z}_n(T_n^*)\right] \tag{5.28}$$

where, again, the dependencies on temperature have been explicitly written. At low T_n, the denominator is $o(\epsilon)(1+\epsilon)$ and the numerator is a difference between two terms of $o(1+\epsilon)$. Therefore, the iterative procedure is again numerically unstable.

To attempt to alleviate this problem, we have examined yet another approach: for each group n we conserve the population of the lowest level in that group N_{n_0} and $\mathcal{N}'_n$, the total population of the *remaining* upper states n' of that group, such that $n = n_0 \cup n'$. This is an effective partitioning *within* the group, which allows us to separate the variables, one of $o(1)$ and the other of $o(\epsilon)$. Clearly, we have now:

$$\mathcal{N}'_n = \frac{N_{n_0}}{g_{n_0}} \underbrace{\sum_{i \in n'} g_i e^{-\Delta E_i / T_n}}_{\mathcal{Z}'_n} \qquad \text{using} \qquad N_i = \frac{\mathcal{N}'_n}{\mathcal{Z}'_n} g_i e^{-\Delta E_i / T_n} \tag{5.29}$$

In order to evaluate the new temperature from the two conserved variables, we iterate on δT_n^* using a form similar to equation (5.27):

$$\mathcal{Z}'_n(T_n^*) + \left(\frac{d\mathcal{Z}'_n}{dT_n}\right) \delta T_n^* = \frac{\mathcal{N}'^{(k)}_n}{N_{n_0}^{(k)}} g_{n_0} \tag{5.30}$$

However, it is easy to see that since $\frac{d}{dT}\mathcal{Z}' \equiv \frac{d}{dT}\mathcal{Z}$, we obtain a similar equation to (5.28):

$$\delta T_n^* \simeq \frac{T_n^{*2}}{\mathcal{Z}'_n(T_n^*)\langle \Delta E \rangle_n(T_n^*)} \left[\frac{\mathcal{N}'^{(k)}_n}{N_{n_0}^{(k)}} g_{n_0} - \mathcal{Z}'_n(T_n^*)\right]$$

In the same limit $T_n \to 0$, both numerators and denominators are of $o(\epsilon)$ and the temperature iterations are again unstable; this was verified through extensive tests under a variety of conditions and configurations. To avoid this systematic numerical problem, we must consider another way to evaluate the Boltzmann temperature inside each group.

Consider instead the following expansion of the partition function near the mean relative energy value $\overline{\Delta E}_n = \frac{1}{g_n}\sum_{i\in n} g_i \Delta E_i$. Defining $\delta_i \equiv \Delta E_i - \overline{\Delta E}_n$ as the shifted energy gap, we have:

$$\begin{aligned}
\mathcal{Z}_n(T_n) = \sum_{i\in n} g_i e^{-\Delta E_i/T_n} &= e^{-\overline{\Delta E}_n/T_n} \sum_{i\in n} g_i e^{-\delta_i/T_n} \\
&= e^{-\overline{\Delta E}_n/T_n} \sum_{i\in n} g_i \left[1 - \frac{\delta_i}{T_n} + \frac{1}{2}\frac{\delta_i^2}{T_n^2} + \ldots\right] \qquad (5.31) \\
&\simeq g_n e^{-\overline{\Delta E}_n/T_n} \left[1 + o(\langle\delta^2\rangle/T_n^2)\right]
\end{aligned}$$

where g_n is the total degeneracy - see equation (5.18). Therefore, up to second -order in the approximate ratio of the bin width to the temperature, the partition function can be approximated by a single exponential function and the relation (5.31) can be inverted. If we use the $(N_{n_0}, \mathcal{N})$ pair of conserved variables, we have:

$$\frac{\mathcal{N}_n^{(k)}}{N_{n_0}^{(k)}} g_0 = \mathcal{Z}_n(T_n^{(k)}) \simeq g_n e^{-\overline{\Delta E}_n/T_n^{(k)}} \qquad (5.32)$$

However, the left-hand-side of (5.32) is $o(1+\epsilon)$, and the right-hand-side should be as well. To see that this is the case, consider the first terms in the expansion of (5.31)[7]:

$$\mathcal{Z}_n(T_n) \simeq e^{-\overline{\Delta E}_n/T_n}\left[g_0 e^{-(\Delta E_0 - \overline{\Delta E}_n)/T_n} + g_1 e^{-(\Delta E_1 - \overline{\Delta E}_n)/T_n} + \ldots\right]$$

Since $\overline{\Delta E} \simeq \Delta E_1$ and $\Delta E_0 \equiv 0$, the right-hand-side is $o(\epsilon)[o(1/\epsilon) + 1 + \ldots] \simeq o(1+\epsilon)$. Again, this is not a desirable situation, since the evaluation of the group

[7] We have here temporarily simplified the notation $(g_0 \equiv g_{n_0}, g_1 \equiv g_{n_0+1}, \ldots)$.

temperature T_n is of the form $1/\ln(1+\epsilon)$, and is subject to significant errors. Furthermore, by computing the average gap $\overline{\Delta E}$ from the lower-bound of the energy bin, the requirement $\langle\delta\rangle \ll T_n$ may be hard to justify at low group temperature.

Instead, we can take advantage of the self-similar structure of the atomic spectrum (exact for Hydrogen, approximate for other atoms) and the fact that the energy gaps become narrower as the level index increases. Thus, let us define the average energy counting from the first level *above* the lowest level, as obtained from $\mathcal{Z}'_n$, defined in equation (5.29):

$$\mathcal{Z}'_n = \sum_{i\in n'} g_i e^{-\Delta E_i/T_n} = e^{-\overline{\Delta E'}_n/T_n} \sum_{i>n_0} g_i e^{-\delta'_i/T_n} \tag{5.33}$$

By definition of the mean, the first-order term in the expansion of the exponential on the right-hand-side should be: $\sum_{i\in n'} g_i\delta'_i = 0$, where now $\delta'_i \equiv \Delta E_i - \overline{\Delta E'}$. This yields:

$$\overline{\Delta E'} = \frac{1}{g'_n}\sum_{i\in n'} g_i \Delta E_i \qquad \text{with} \qquad g'_n = \sum_{i>n_0} g_i \tag{5.34}$$

Therefore $\overline{\Delta E'}$ differs from $\overline{\Delta E}$ only by a normalization factor, since $\Delta E_0 \equiv 0$. Note that $\overline{\Delta E'} > \Delta E_1$ and to *lowest*-order, $\mathcal{Z}'(T_n) \simeq g'_n e^{-\overline{\Delta E'}_n/T_n} \simeq o(\epsilon)$. Using the conserved pair $(N_{n_0}, \mathcal{N}')$, the group temperature is now estimated by:

$$\frac{\mathcal{N}'^{(k)}_n}{N^{(k)}_{n_0}} g_{n_0} = \mathcal{Z}'_n(T_n) \quad \rightarrow \quad T^{(k)}_n \simeq -\frac{\overline{\Delta E'}_n}{\ln\left[\frac{\mathcal{N}'_n}{g'_n}\frac{g_{n_0}}{N_{n_0}}\right]} \simeq -\frac{1}{\ln(\epsilon)} \tag{5.35}$$

This is now a stable computation when $\epsilon \rightarrow 0$. Furthermore, the approximation $\langle\delta\rangle \ll T_n$ is more justifiable since the largest value ($\delta_0 = E_{n_0} - \overline{\Delta E}$) is removed from the average.

We see that we now have the means to compute the internal group temperature from conserved variables without risking fatal numerical errors; this is possible *only* by separating the lowest and upper levels within the group, i.e. by performing a sub-scale, internal partitioning of the group[8]. This is the approach used here

[8]This approach is a reflection of the self-similar structure of the atomic levels.

for the last Boltzmann (hereafter denoted as B5) group we investigated, for which the appropriate pair of conserved variables to use is therefore $(N_{n_0}, \mathcal{N}'_n)$. Note that it is also possible to improve on the temperature evaluation by incorporating all higher-order terms into the definition of the total degeneracy, i.e.:

$$\mathcal{Z}'_n(T_n) = \tilde{g}'_n(T_n) e^{-\overline{\Delta E'}_n / T_n} \quad \rightarrow \quad \frac{d\mathcal{Z}'_n}{dT_n} = \mathcal{Z}'_n(T_n) \cdot \left[\frac{\overline{\Delta E'}_n}{T_n^2} + \frac{d}{dT_n} \ln \tilde{g}'_n \right] \tag{5.36}$$

If T_n^* is the running iteration, first evaluated by (5.35), successive estimates of $T_n^{(k)}$ are obtained, using (5.36), from:

$$T_n^{(k)} - T_n^* = \frac{\ln \mathcal{Z}'_n(T_n^{(k)}) - \ln \mathcal{Z}'_n(T_n^*)}{\frac{d \ln \mathcal{Z}'_n}{dT_n}(T_n^*)} \quad \text{where} \quad \mathcal{Z}'_n(T_n^{(k)}) = g_{n_0} \frac{\mathcal{N}'^{(k)}_n}{N^{(k)}_{n_0}} \tag{5.37}$$

This iterative procedure can rapidly converge (as demonstrated in our tests) because we have an excellent approximation of the initial temperature from the lowest-order direct evaluation (5.35), and the $o(\epsilon)$ term has been factored as the leading term in the expansion. In other words, $\tilde{g}'_n(T_n)$ is a smooth function of temperature with a non-vanishing gradient, allowing gradient-descent iterations.

5.3.4 Boltzmann grouping - effective rates

As before, the master equations are used to derive the conservation equations for the two new variables $(N_{n_0}, \mathcal{N}'_n)$, by setting $i = n_0$ for the first one, and summing

over all levels $j \in n'$ in the second case. The latter yields the following:

$$\begin{aligned}
\frac{d\mathcal{N}'_n}{dt} = &- N_e \mathcal{N}'_n \left[\sum_{m>n} \sum_{i \in n'} \frac{g_i e^{-\Delta E_i/T_n}}{\mathcal{Z}'_n} \sum_{j \in m} \alpha_{(j|i)} + \sum_{m<n} \sum_{i \in n'} \frac{g_i e^{-\Delta E_i/T_n}}{\mathcal{Z}'_n} \sum_{j \in m} \beta_{(j|i)} \right] \\
&+ N_e \mathcal{N}_m \left[\sum_{m<n} \sum_{i \in n'} \sum_{j \in m} \frac{g_j e^{-\Delta E_j/T_m}}{\mathcal{Z}_m} \alpha_{(i|j)} + \sum_{m>n} \sum_{i \in n'} \sum_{j \in m} \frac{g_j e^{-\Delta E_j/T_m}}{\mathcal{Z}_m} \beta_{(i|j)} \right] \\
&- \mathcal{N}'_n \left[\sum_{m<n} \sum_{i \in n'} \frac{g_i e^{-\Delta E_i/T_n}}{\mathcal{Z}'_n} \sum_{j \in m} A_{(j|i)} \right] + \mathcal{N}_m \left[\sum_{m>n} \sum_{i \in n'} \sum_{j \in m} \frac{g_j e^{-\Delta E_j/T_m}}{\mathcal{Z}_m} A_{(i|j)} \right] \\
&- N_e \mathcal{N}'_n \left[\sum_{i \in n'} \frac{g_i e^{-\Delta E_i/T_n}}{\mathcal{Z}'_n} \beta_{(n_0|i)} + \sum_{i \in n'} \frac{g_i e^{-\Delta E_i/T_n}}{\mathcal{Z}'_n} A_{(n_0|i)} \right] \\
&- N_e \mathcal{N}'_n \left[\sum_{i \in n'} \frac{g_i e^{-\Delta E_i/T_n}}{\mathcal{Z}'_n} \alpha_{(+|i)} \right] + N_e^2 N_+ \left[\sum_{i \in n'} \beta_{(i|+)} \right]
\end{aligned} \tag{5.38}$$

Note that we have used the total number $\mathcal{N}_m = N_{m_0} + \mathcal{N}'_m$ and the group total partition function $\mathcal{Z}_m = g_{m_0} + \mathcal{Z}'_m$ in the expressions on the right hand side, only as a way to group terms and lead to simpler expressions; the conserved variables remain N_{m_0} and $\mathcal{N}'_m$. Equation (5.38) takes in account all the interactions between the groups, assuming the Boltzmann distribution approximation within each group. The effective rates for group transitions can be expressed (and tabulated) as a function of two temperatures: the kinetic temperature T_e and the group excitation temperature T_n. Notice also that because of the bin-averaging, the effective radiative transition rates have also become temperature-dependent (T_n).

Similarly, the rate of change of the number density of the ground state of each

group is:

$$\begin{aligned}\frac{dN_{n_0}}{dt} =& - N_e N_{n_0}\left[\sum_{m>n}\sum_{j\in m}\alpha_{(j|n_0)} + \sum_{m<n}\sum_{j\in m}\beta_{(j|n_0)}\right] \\ &+ N_e\,\mathcal{N}_m\left[\sum_{m<n}\sum_{j\in m}\frac{g_j e^{-\Delta E_j/T_m}}{\mathcal{Z}_m}\alpha_{(n_0|j)} + \sum_{m>n}\sum_{j\in m}\frac{g_j e^{-\Delta E_j/T_m}}{\mathcal{Z}_m}\beta_{(n_0|j)}\right] \\ &- N_{n_0}\left[\sum_{m<n}\sum_{j\in m}A_{(j|n_0)}\right] + \mathcal{N}_m\left[\sum_{m>n}\sum_{j\in m}\frac{g_j e^{-\Delta E_j/T_m}}{\mathcal{Z}_m}A_{(n_0|j)}\right] \\ &+ N_e\,\mathcal{N}'_n\left[\sum_{i\in n'}\frac{g_i e^{-\Delta E_i/T_n}}{\mathcal{Z}'_n}\beta_{(n_0|i)} + \sum_{i\in n'}\frac{g_i e^{-\Delta E_i/T_n}}{\mathcal{Z}'_n}A_{(n_0|i)}\right] \\ &- N_e N_{n_0}\left[\alpha_{(+|n_0)}\right] + N_e^2 N_+\left[\beta_{(n_0|+)}\right]\end{aligned} \tag{5.39}$$

Again, using the total number of levels $\mathcal{N}_m = N_{m_0} + \mathcal{N}'_m$ on the right-hand-side allows us to consider together transitions between lowest states at the boundaries of different groups ($N_{n_0} - N_{m_0}$), as well as the transitions with the excited sub-partitions ($N_{n_0} - \mathcal{N}'_m$) and simply the expressions. Since the ion is conserved here as an individual state, the rate of change of its number density remains the same but can be rewritten in terms of the group number densities:

$$\frac{dN_+}{dt} = N_e\sum_n \mathcal{N}_n\left[\sum_{i\in n}\frac{g_i e^{-\Delta E_i/T_n}}{\mathcal{Z}_n}\alpha_{(+|i)}\right] - N_e^2 N_+\left[\sum_n\sum_{i\in n}\beta_{(i|+)}\right] \tag{5.40}$$

Each term in brackets in equations (5.38-5.40) is an effective rate for transfer between the group variables $(N_{n_0}, \mathcal{N}'_n), \forall n$. As mentioned in 5.3.1, both individual levels and groups (Uniform or Boltzmann) are considered when solving the ASDF. The few individual states are the lowest in the energy scale, with the largest successive gaps, while the multitude of upper levels is distributed into a variable number of groups. This is justified on the basis of the kinetic rates, and as justification of the expansion (5.31).

Model	Variables	Equations	T_n evaluation
U	$\mathcal{N}_n$	(5.20-5.21)	none
B1	$(\mathcal{N}_n, \mathcal{E}_n)$	(5.22a-5.22b, 5.40)	C_v – unstable
B2	$(N_{n_0}, \mathcal{N}_n)$	(5.39,5.22a)	C_v – unstable
B3	$(N_{n_0}, \mathcal{N}'_n)$	(5.39,5.38)	C_v – unstable
B4	$(N_{n_0}, \mathcal{N}_n)$	(5.39,5.22a)	equation (5.31) – unstable
B5	$(N_{n_0}, \mathcal{N}'_n)$	(5.39,5.38)	equation (5.33) – stable

Table 5.1: Summary of level-grouping models investigated.

5.4 Accuracy of uniform and Boltzmann methods

5.4.1 Isothermal ionization test case

In the previous section, we have discussed several approaches to the level grouping strategy; these are summarized in Table 5.1. This sequence of models was developed as a result of preliminary tests and the failure to obtain converged solutions for the group Boltzmann temperature T_n in many instances. Thus, we found that the *only* model which was able to provide stable and satisfactory solutions for all test cases was model B5, using a sub-partition of the group into the ground level n_0 and the remainder, and the use of the form (5.33) for the partition function, which allowed us to factorize out the vanishingly small terms at low T_n. Therefore, considerations of the "equation of state" of the Boltzmann group dictated the correct approach to use here, and while all the models explored are listed in table 5.1, only the zeroth-order uniform binning described in 5.3.1 and the B5 models are shown here and compared to the reference solution obtained from solving the full master equations; these are indicated as (U) and (B) models respectively.

We conducted a large number of additional tests but for the sake of brevity, we are showing here the results of three representative cases: the initial conditions

Case	T_e	$x_e = N_+/N_H$	N_n
1	3 eV - isothermal	10^{-9}	$(1-x_e)N_H$ for n=1 $10^{-20}N_H$ otherwise
2	1 eV - isothermal	Saha (3 eV)	Boltzmann (3 eV)
3	3 eV - isochoric	10^{-9}	$(1-x_e)N_H$ for n=1 $10^{-20}N_H$ otherwise

Table 5.2: Initial conditions of test cases. For all cases, the total atomic density N_H is 10^{21} m^{-3}.

are summarized in Table 5.2. For all the results shown in this section, a constant time step of 10^{-7} second had been used for the test cases in the ionization regime (cases 1 and 3), and a time step of 10^{-5} second was used for the recombination regime (case 2); the same backward-Euler scheme of 3.2 was used throughout.

As indicated in 5.3, the reference solution is based on the detailed kinetics for 20 atomic levels, while the group-based solutions will be based on a few low energy levels individually monitored, and with partitioning of the remaining upper states into a variable number of groups. The first test case is the iso-thermal relaxation in the excitation and ionization regime, i.e. the initial population of excited states and electron density is well below equilibrium[9]. This test case is the same as the one shown in Figure 5.1 for a variable number of electronic levels, solving for the full master equations (5.14-5.15). As the plasma relaxes towards equilibrium, an increasing number of electronic levels become populated and the electron number density grows exponentially, until an ionization cascade occurs. The rates increase very rapidly just before equilibrium, and the system becomes very stiff.

Figure 5.2 shows a comparison of the number densities of all the atomic states

[9]Since we are considering electron collisions only, all test cases must start with an initial degree of ionization $x_e \neq 0$.

Method	Error
3 levels + 1 U-group	2618%
3 levels + 1 B-group	89.2%
4 levels + 1 U-group	165.8%
4 levels + 1 B-group	23.7%
6 levels + 1 U-group	20.9%
6 levels + 1 B-group	0.9%

Table 5.3: Relative error on electron density at peak rate of growth (approx. 33 μsec).

for the iso-thermal test case (#1). In this simulation, the ground state and the first 4 excited states $(1, \ldots, 5)$ are conserved as discrete levels while the remaining upper states $(6, \ldots, 20)$ are partitioned into two groups, each of which has either a uniform or Boltzmann distribution. There are both significant and subtle differences in the traces of the upper states. First, comparison of the uniform (Figure 5.2-b) and Boltzmann (Figure 5.2-c) grouping shows the influence of the assumed internal distribution, as the reconstructed levels of the groups are clearly separated in the uniform case. Second, comparison with the reference solution of Figure 5.2-a shows that the Boltzmann groups are clearly more accurate. Slight differences remain in the very early stages of evolution[10] below 1 μsec for example and around 10 μsec.

The combined effect of the number of resolved lower levels and grouping strategy is shown in Figure 5.3. Generally speaking, one can clearly observe a dramatic improvement, for the same number of resolved levels, by switching from a uniform to Boltzmann group[11]. By selecting the time of maximum rate of growth of the

[10]This understandably so, since the ladder-climbing process of the early evolution would be difficult to describe with grouping methods, even by 1^{st}-order approximation of the internal distribution within the groups.

[11]By coincidence, the results of uniform binning for 6 resolved levels is right on top of the

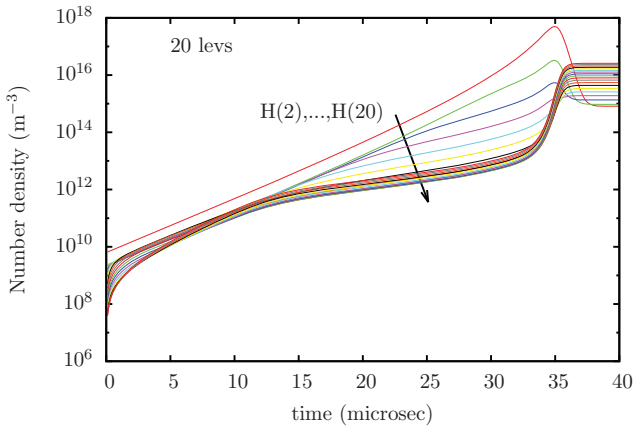

(a) Full solution with 20 levels.

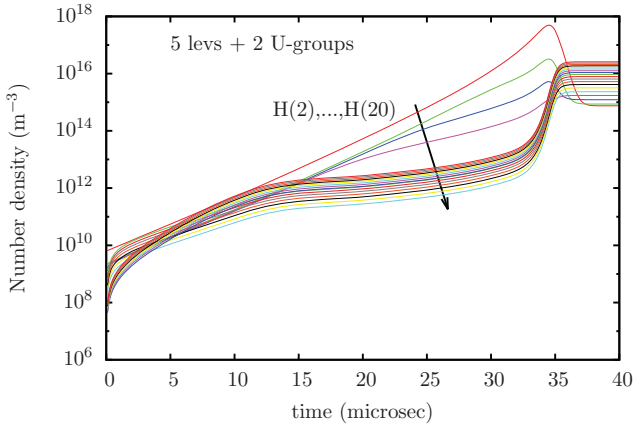

(b) Solution with 5 levels and 2 Uniform groups

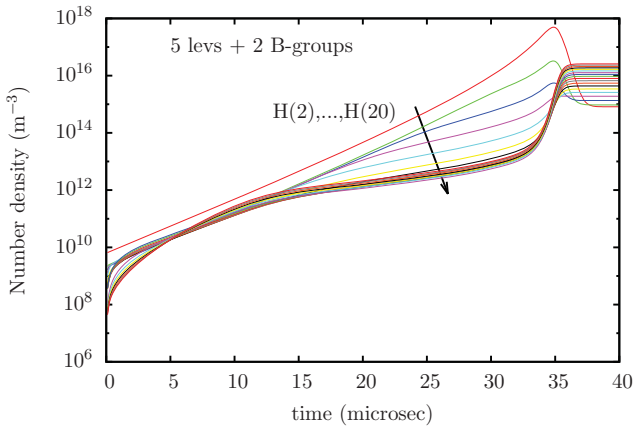

(c) Solution with 5 levels and 2 Boltzmann groups.

Figure 5.2: Comparison of the time evolution of the excited states during the isothermal heating test case ($T_e = 3$ eV). From top to bottom: (a) full solution with 20 levels; (b) solution with 5 levels and 2 Uniform groups; (c) solution with 5 levels and 2 Boltzmann groups. The first excited state - H(2) - is the top curve, followed by the next higher level, etc.

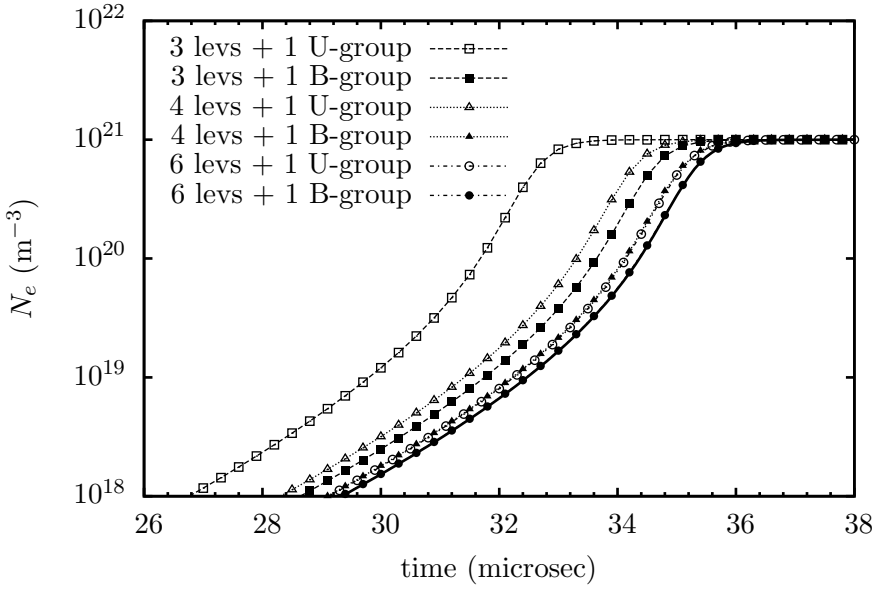

Figure 5.3: Comparison between the solution obtained using both level grouping approaches. The solid line represents the full solution.

electron density as the approximate location of the avalanche ionization, we can measure the relative error in density. As shown in Table 5.3, the error can be very substantial unless there is sufficient resolution of the ASDF kinetics, through the number of resolved lower levels and a higher-order (B) description of the groups. This is important when comparing, for example, with time-gated experimental results.

By conserving more discrete states and reducing the size of the upper state groups, the results are of course significantly improved. This is to be expected for ASDF kinetics, since the energy gaps are larger for the first levels, and grouping together these states would be less accurate, first by yielding excessive bin energy widths compared to mean energy and temperature scale – violating the validity condition for the expansion (5.31) – and also by disallowing potential deviations from Boltzmann equilibrium in the most populated range of excited states.

solution for a Boltzmann group with 4 lower levels.

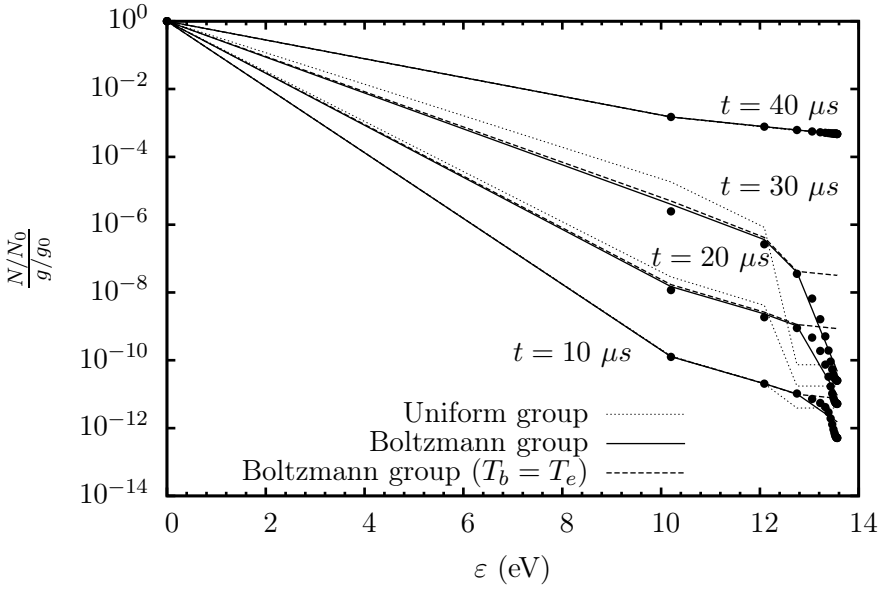

Figure 5.4: The internal states population during the heating process at various times. The solid symbols are the full solution; the solid lines are the level grouping with Boltzmann distribution; the doted lines are for level grouping with uniform distribution; dashed lines are for a simplified model with $T_b \equiv T_e$.

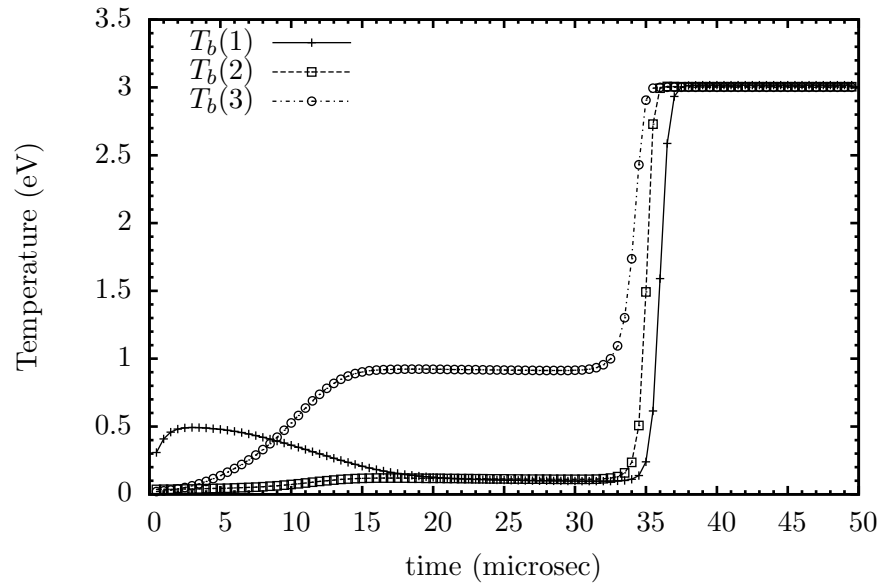

Figure 5.5: Boltzmann temperature of the upper states

There can of course be variations in the grouping strategy, but in all cases the general guidelines of keeping the *widths* of the groups small and the levels with the largest energy gaps as individual states are perfectly consistent with the objective of computational cost reduction, since the discrete lower energy states evolve more slowly and the upper states are numerous and have similar energy[12].

The relative accuracy of the grouping approaches can also be seen in Figure 5.4 where the ASDF is plotted at four different instances of time corresponding to $t =$ 10, 20, 30 and 40 μsec. Both solutions with level grouping are obtained from using 3 atomic levels and 1 group of upper states. It is clearly seen that the Boltzmann group gives a more accurate representation of the upper states distribution during the heating process. We also showed in Figure 5.4 the results of a simplified model where it is assumed (see section 5.3.2) that all groups have the same internal temperature, equal to the kinetic temperature, i.e. $T_b(i) \equiv T_e, \forall i$ (dashed line). This assumption is clearly violated, as shown in Figure 5.5, although the difference remains mostly confined to the upper states distribution. We should point out again that significant differences would be expected in a two-temperature kinetic system, i.e. including heavy-particle collisions.

We note also that the ASDF from the full solution indicates that the high lying states, starting from the third excited state, behave like a continuum state, although there appears to be two distinct sub-groups among the upper states, as can be seen most clearly at $t = 10$ μs. This suggests that the upper states are most effectively resolved by two groups or more, again confirming that relatively small widths of the groups are preferable, albeit at an increased computational expense. Figure 5.5 further illustrates this point by showing the evolution of the Boltzmann temperatures of the upper states, using here 4 discrete atomic states and partitioning the upper states into 3 groups. While the Boltzmann

[12] Although the grouping techniques are formulated here for a general set of kinetics, the effectiveness of the grouping approach is problem specific. For other situations, e.g. ro-vibrational states, a different strategy may be required than the one discussed here for atomic states.

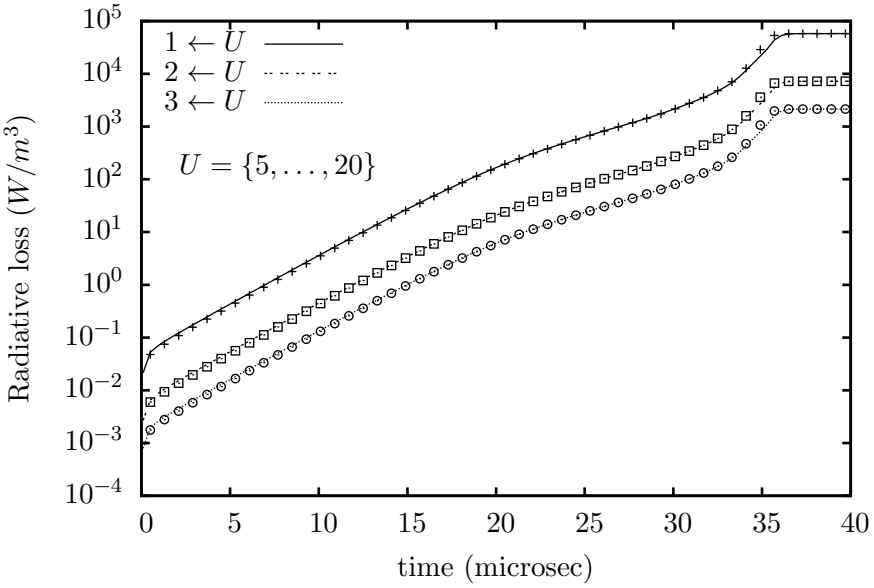

Figure 5.6: Radiative loss due to bound-bound radiation from the upper states to the first 3 atomic states. The lines indicate the solution obtained from the full CR kinetics. The dots represent solution obtained with level grouping (5 levels + 1 group).

temperatures of the first two groups are close to each other, the temperature of the third group is slightly higher. This again confirms that the upper states needs to be resolved by at least 2 groups. When the system is near equilibrium, both approaches give similar results.

In these simulations, we have assumed that the plasma is optically thin to all the radiation from the line transitions. Spectral signatures being a major diagnostic tool for determining plasma conditions, it is important to know the CR kinetics in detail in order to match experimental data. Usually, this is accomplished by post-processing the numerical solution with a highly resolved spectral code – including radiation transport (RT) if necessary – with detailed computation of line shapes. This approach is accurate if the key parameters of such a spectral model, in particular N_e and T_e, are also very accurate. As discussed above and shown in Table 5.3, our Boltzmann grouping procedure provides a significant improvement

over conventional approaches, leading to a potentially much more accurate spectral signature prediction in transient and non-equilibrium plasma conditions. In addition, the ASDF solution is much closer to the true physical state, which may also lead to faster integration of the detailed CR kinetics with RT. These will be investigated in the future.

Accurate evaluation of the radiative emission is also important during the computation of flow dynamics, from simple reasons of power coupling, e.g. radiative cooling. Figure 5.6 shows the radiative losses due to bound-bound radiation from the upper states $(5, \ldots, 20)$ to the first three atomic states $(1, 2, 3)$ computed by grouping all the upper states together as a single group with a Boltzmann distribution. Although this is a somewhat coarse approximation to the ASDF, it is clear that the grouping scheme provides an excellent approximation to the radiative power. An accurate reproduction of the radiative spectrum depends inevitably on the reconstructed population of the atomic levels and, as can be seen by comparing the profiles in Figure 5.2, the agreement can be excellent.

5.4.2 Isothermal recombination test case

In this case, we performed a cooling test where the plasma is suddenly brought down from 3 eV to 1 eV. Thus, the simulation was run at a constant temperature ($T_e = 1$ eV), while the initial conditions are the Boltzmann and Saha equilibrium values at 3 eV; these are exactly the conditions which would be obtained at the end of the first test case in the absence of radiative losses. For all the simulations shown in this case, a constant time step of 10^{-5} sec has been used.

In this case, the cooling process occurs very rapidly and the plasma is in a deexcitation and recombination regime; the ground state and the electron number densities are quickly adjusted to their new equilibrium values, as can be seen in Figure 5.7. Strictly speaking, since bound-bound radiation is assumed to be

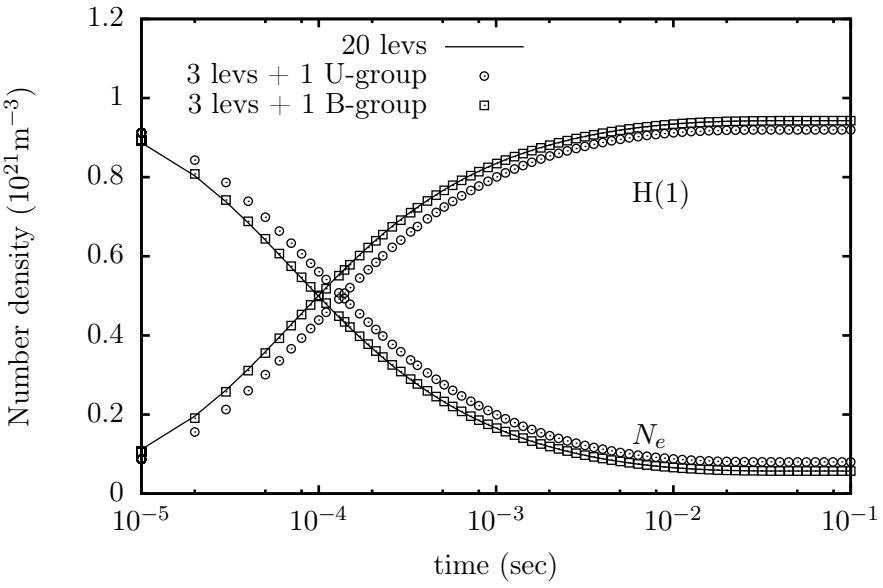

Figure 5.7: Comparison of the time evolution of the ground state and the free electrons during the isothermal cooling process (3 eV $\rightarrow$ 1 eV) using level grouping with Uniform and Boltzmann distribution (3 levels + 1 group).

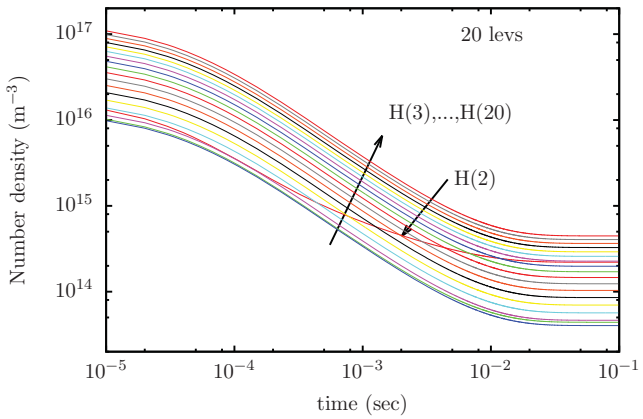

(a) Full solution with 20 levels.

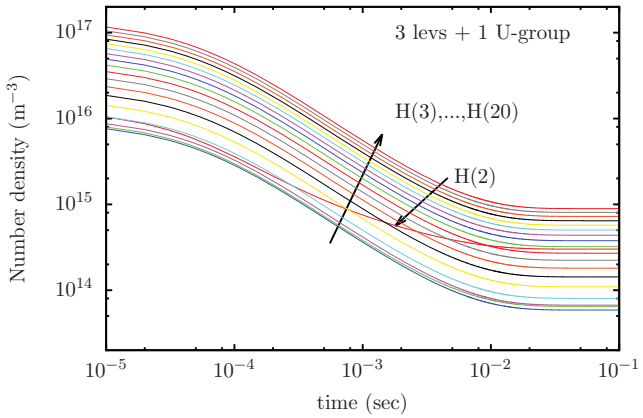

(b) Solution with 3 levels and 1 Uniform group

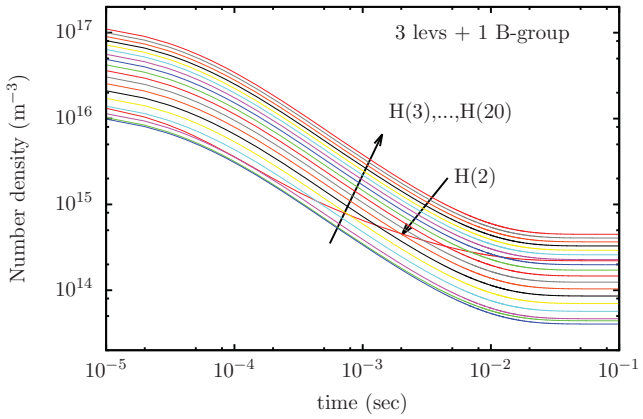

(c) Solution with 3 levels and 1 Boltzmann group.

Figure 5.8: Comparison of the time evolution of the excited states during the isothermal cooling test case ($T_e = 1$ eV). From top to bottom: (a) full solution with 20 levels; (b) solution with 3 levels and 1 Uniform group; (c) solution with 3 levels and 1 Boltzmann group. H(3) - is the bottom curve, followed by the next higher level, etc.; the non-conforming red curve is H(2).

optically thin, the system cannot reach equilibrium. However, a quasi-equilibrium state is achieved at approximately 1 msec, after which the bound-bound radiation is the dominant *net* rate of change and the system continues to cool down at the radiative time scales. Note also that the uniform grouping is significantly less time-accurate than the Boltzmann method, as was already the case in the ionization regime – see Figure 5.3.

Figure 5.8 shows the evolution of the excited states as function of time for reference, uniform groups and Boltzmann groups. Once again, there is a noticeable discrepancy between the reference solution and the uniform bin model, especially concerning the red curve which crosses other levels during the relaxation process. This curve is the density of H(2), the first excited state, and is an effect of the strong radiative decay of this state. Notice that the plot starts at $t = 10^{-5}$ sec, i.e. the first implicit time step, but already the solution is far from the Boltzmann equilibrium which is the initial condition at $t = 0$, such that there is a population inversion with respect to H(2) for many upper states. Notice also that the time scale is logarithmic, and the processes considerably slow down as the electron density drops significantly. Because we are considering only electron impact collisions, the ASDF essentially becomes "frozen" in a quasi-static but non-equilibrium state. If collisions by heavy particles were also considered, these would rapidly become the dominant process, leading to faster relaxation towards equilibrium. However, in some case of rapid plasma expansion, similar "frozen-in" non-equilibrium distribution functions of the ASDF could be obtained.

To better appreciate the accuracy of the Boltzmann grouping procedure, Figure 5.9 shows the evolution of several excited states compared to the exact solution and similarly to the "heating" (ionization) case, excellent agreement was obtained. In this simulation, the first 3 atomic states $(0, 1, 2)$ are conserved as discrete levels and the upper states $(3, \ldots, 19)$ are lumped into 1 Boltzmann group.

Finally, we show in Figure 5.10 the snapshots of the ASDF during the recom-

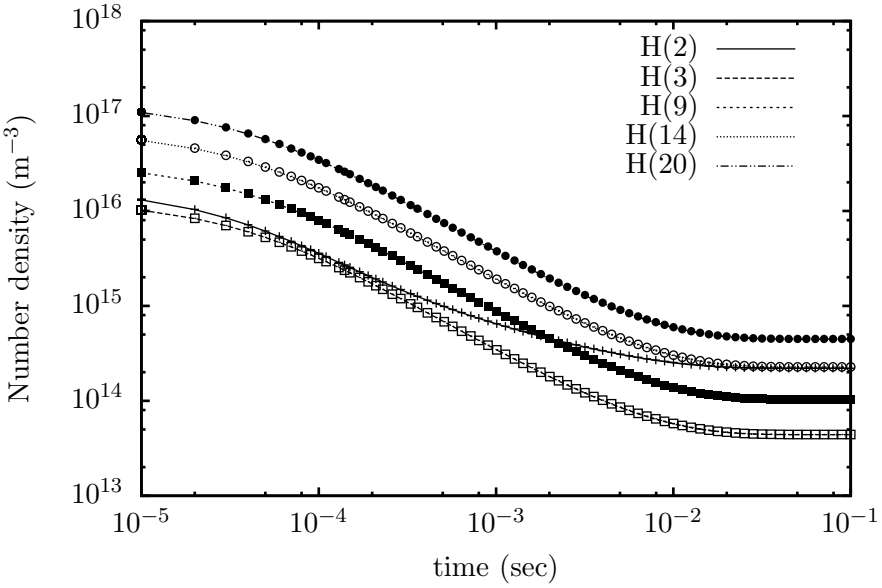

Figure 5.9: Comparison of the time evolution of the excited states number densities during the isothermal cooling process (3 levels + 1 B group).

bination. Contrary to the case of ionization, the upper states are not depleted but enhanced instead – as expected, since the recombination proceeds preferentially onto the upper states. As a reflection of the observation made for Figure 5.9, the agreement is excellent for all atomic states.

5.5 Energy conservation

The systems of equations (5.18-5.21) and (5.38-5.40) describe the complete evolution of the ASDF but for an iso-thermal plasma. In the more general case, the ASDF kinetics are coupled to the energy of the system; here, this includes only the total energy of the free electrons E_e. Thus for constant-volume or constant-pressure conditions, there must be an evolution equation for the energy or enthalpy (only constant-volume kinetics are considered here). We must then exert care that the formulation exactly conserves energy, i.e. that $E_e^{(k)}+\sum_n \mathcal{E}_n^{(k)}$ at any time level

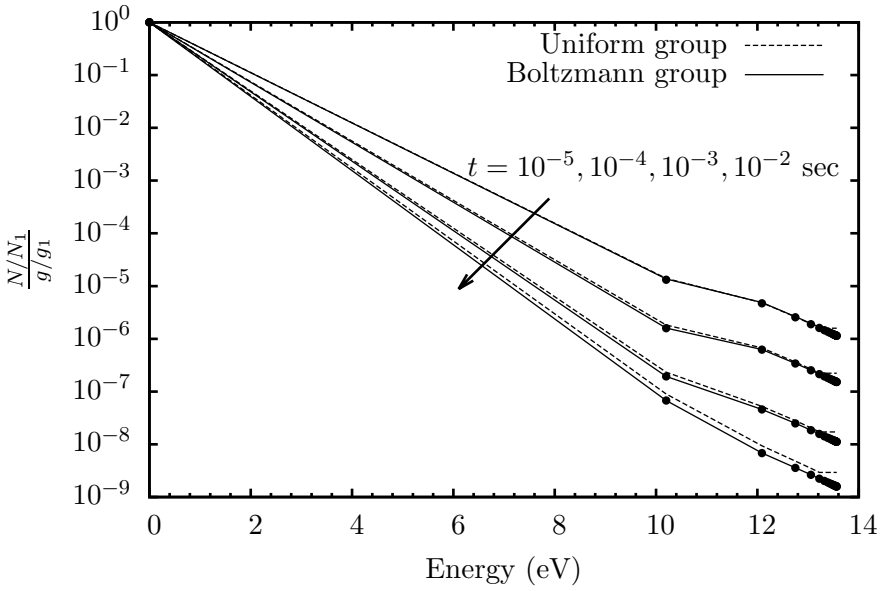

Figure 5.10: Snapshots of the ASDF at several times during the cooling process. The dots represent the full solution. The solid lines are the solution obtained using the level grouping with Boltzmann distribution. The broken lines are the solution obtained using the level grouping with uniform distribution.

(k) remains the same within numerical round-off errors. If we were dealing with only electron-impact collisions, it would be sufficient to sum the energies of all levels using the new population densities at the end of the time step, compute the difference and assign the change to E_e. However, there are two obvious problems with this scenario: a) when other collision partners must be accounted for, or when the electrons themselves are partitioned (e.g. for non-Maxwellian kinetics), one must be able to correctly apportion the changes in energy, e.g. to E_e and E_h (for heavy particles); and b) for large time steps, there is no guarantee that the subsequent change in E_e is physically acceptable, i.e. $E_e^{(k)} = E_e^{(k-1)} + \delta E_e > 0$. We must therefore include an evolution equation for E_e (and another for E_h if heavy particle collisions are included), which must then be fully coupled, so that the Jacobian of the system includes derivatives of the rates with respect to E_e, through the variation of T_e.

Energy conservation can be satisfied if the the construction of the source term on the right-hand-side of the master equations also satisfies it. Thus we must explicitly construct the energy source term from the master equations, as was already described briefly in equation (5.22). The same procedure is used, with the understanding that

$$\frac{dE_e}{dt} = -\sum_n \frac{d\mathcal{E}_n}{dt}$$

Thus we can combine contributions as follows:

$$\frac{dE_e}{dt} = -N_e \mathcal{N}_n \left[\sum_{\substack{m>n \\ i\in n}} \frac{g_i e^{-\Delta E_i/T_n}}{\mathcal{Z}_n} \sum_{j\in m} \Delta E_{ji} \alpha_{(j|i)} + \sum_{\substack{m<n \\ i\in n}} \frac{g_i e^{-\Delta E_i/T_n}}{\mathcal{Z}_n} \sum_{j\in m} \Delta E_{ji} \beta_{(j|i)} \right] \ldots \tag{5.41}$$

where $\Delta E_{ji} = E_j - E_i$. Note that in the case of excitation from level $|i)$, i.e. the first summation in equation (5.41), $\Delta E_{ji} > 0$, while $\Delta E_{ji} < 0$ in the second term for de-excitations from that level. We can then construct another set of effective rates, this time for the energy equation. Using the sub-partitioning of model B5,

the rates derived from the first term on the right of (5.38) are:

$$\tilde{\alpha}^{E}_{(m'|n')} = \left[\sum_{i\in n'} \frac{g_i e^{-\Delta E_i/T_n}}{\mathcal{Z}'_n} \sum_{j\in m'} \Delta E_{ji}\alpha_{(j|i)}\right] \tag{5.42a}$$

$$\tilde{\beta}^{E}_{(m'|n')} = \left[\sum_{i\in n'} \frac{g_i e^{-\Delta E_i/T_n}}{\mathcal{Z}'_n} \sum_{j\in m'} \Delta E_{ji}\beta_{(j|i)}\right] \tag{5.42b}$$

These rates enter the evolution equation for E_e as:

$$\frac{dE_e}{dt} = -N_e\mathcal{N}'_n \sum_{m>n} \tilde{\alpha}^{E}_{(m'|n')} - N_e\mathcal{N}'_n \sum_{m<n} \tilde{\beta}^{E}_{(m'|n')} + \ldots \tag{5.43}$$

Note that the same formulation applies for uniform groups by taking the limit $T_n \to \infty$, and summing over the complete set $n = \{n_0, n'\}$. The rate of energy change can also be expressed as:

$$\tilde{\alpha}^{E}_{(m'|n')} = \tilde{\alpha}_{(m'|n')} \cdot \overline{\varepsilon}_{(m'|n')} \tag{5.44}$$

where $\alpha_{(m'|n')}$ is of course given by the effective rate for the conserved number densities:

$$\tilde{\alpha}_{(m'|n')} = \sum_{j\in m'} \sum_{i\in n'} \frac{g_i e^{-\Delta E_i/T_n}}{\mathcal{Z}'_n} \alpha_{(j|i)}$$

Equation (5.44) defines an average energy $\overline{\varepsilon}_{(m'|n')}$, transferred during excitation of levels of group n' to levels of group m', which can be tabulated as function of the initial T_n and collisional (T_e) temperatures. This approach was successfully used, for example, for vibrational non-equilibrium [123].

5.5.1 Isochoric ionization test case

The third test case of Table 5.2 was designed to test for energy conservation. In this case, the energy loss and gain due to collisional processes are taken into account in the conservation equation for the electron energy. The evolution now proceeds at constant volume, and the electron temperature changes rapidly, as seen in Figure 5.11. The initial conditions are the same as those of the first

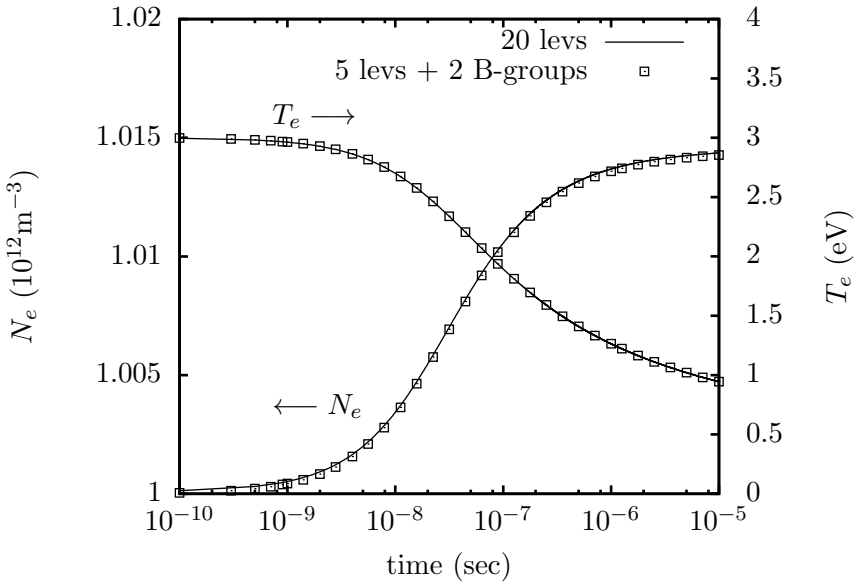

Figure 5.11: N_e, T_e evolution in constant-volume case.

test case, and the system is initially far below Boltzmann and Saha equilibrium However, contrary to the isothermal case, the initial excitation and ionization processes deplete the electron energy and the system "freezes" rapidly, and the excited states remain at a low population density. If an external heating source was applied (e.g. Ohmic heating), the system would more closely resemble the isothermal test case, and the system would become stiff again. Here, we are mostly concerned with testing energy conservation and to simplify the analysis, the radiative rates were removed from the kinetics, so that no radiative energy losses were present.

We can monitor the error by comparing the values of E_e at the end of each time step with the total potential energy contained in the electronic states, by reconstruction of the level populations. Figure 5.12 shows both the accumulated error (symbols) and the one at each time step (blue line); this test was conducted with 5 resolved levels and 2 Boltzmann bins, and all computations were were performed with a constant time step of 10^{-10} sec, using the same backward-Euler

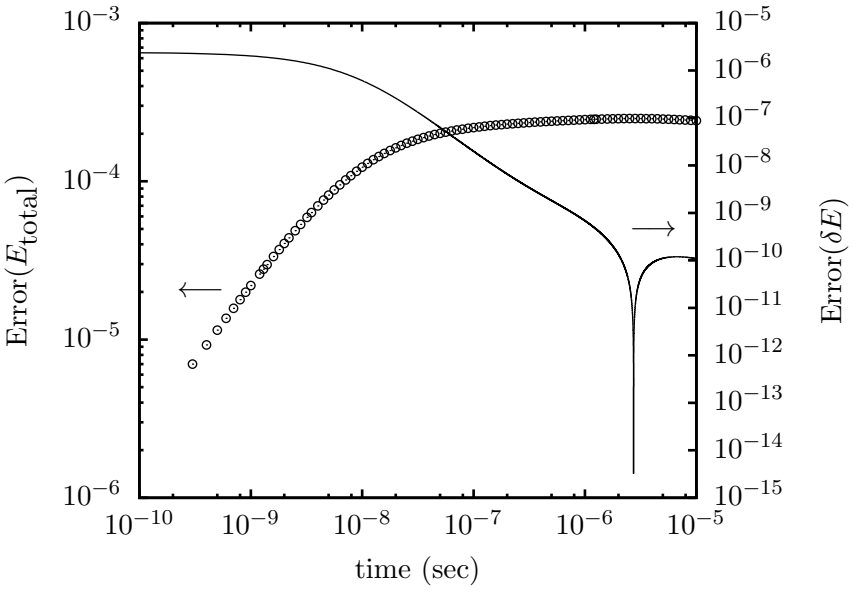

Figure 5.12: Cumulative and instantaneous relative errors in energy conservation - test case 3.

integration scheme [13].

The error is certainly acceptable, but it is not commensurate with numerical round-off, which we would have expected if the scheme was exactly energy-conserving. By comparison, the cumulative error in energy was below 10^{-13} when solving the full master equations without level grouping.

While the exact solution consists of summing-up the contributions from each individual level, leading to the rate of change expressed by equation (5.22). However, we are not using here the internal energy $\mathcal{E}_n$ as a conserved variable, and we must be careful that the procedure be consistent with our definition, or *reconstruction* of the internal energy. The corrected procedure is described next.

[13]Note that the scheme includes numerical errors resulting from the forward and backward sweeps of the Gaussian elimination procedure. However, this is negligible here, since we have used double-precision.

5.5.2 Corrected energy rates

Consider for example the change in electron energy due to excitations and de-excitations, and let us examine first the case of uniform grouping.

$$\frac{dE_e}{dt} = -\sum_{m>n}\sum_{n} \tilde{\alpha}^{E}_{(m|n)} \mathcal{N}_n N_e + \sum_{m>n}\sum_{n} \tilde{\beta}^{E}_{(n|m)} \mathcal{N}_m N_e \tag{5.45}$$

There are two formulations of the effective rates of energy transfer:

Formulation 1

$$\tilde{\alpha}^{E}_{(m|n)} = \sum_{j\in m}\sum_{i\in n} \frac{g_i}{g_n}(E_j - E_i)\alpha_{(j|i)} \tag{5.46a}$$

$$\tilde{\beta}^{E}_{(m|n)} = \sum_{j\in m}\sum_{i\in n} \frac{g_j}{g_m}(E_j - E_i)\beta_{(i|j)} \tag{5.46b}$$

Formulation 2

$$\tilde{\alpha}^{E}_{(m|n)} = (\tilde{E}_m - \tilde{E}_n)\sum_{j\in m}\sum_{i\in n} \frac{g_i}{g_n}\alpha_{(j|i)} \tag{5.47a}$$

$$\tilde{\beta}^{E}_{(m|n)} = (\tilde{E}_m - \tilde{E}_n)\sum_{j\in m}\sum_{i\in n} \frac{g_j}{g_m}\beta_{(i|j)} \tag{5.47b}$$

where $\tilde{E}_n = \sum_{i\in n} \frac{g_i}{g_n} E_i$ and similarly for $\tilde{E}_m$.

Only the second formulation is exactly energy-conserving. This is quite clear because in that case, the term on the right side of (5.47) is the product of the change in number density of the groups ($d\mathcal{N}_n/dt$) and the difference in average group energy ($\tilde{E}$). Energy conservation follows from the definition of the total group energy $\mathcal{E}_n = \tilde{E}_n \mathcal{N}_n$. Thus, the model assumptions *constrain* us to choose the appropriate formulation of the effective rates for energy change that is consistent with the definition of group energy.

Let us now examine the case of the Boltzmann grouping (B5), using the pair of conserved variables $(N_{n_0}, \mathcal{N}'_n)$; the rates of energy exchange must therefore be

consistent with the electronic energy defined from these two variables, and with the equation of state used to describe the internal partition (i.e. T_n). We start with the conservation of the group energy:

$$\frac{d\mathcal{E}_n}{dt} = \frac{d}{dt}\left(N_{n_0}E_{n_0} + \mathcal{N}'_n\langle E\rangle_{n'}\right) = E_{n_0}\frac{dN_{n_0}}{dt} + \langle E\rangle_{n'}\frac{d\mathcal{N}'_n}{dt} + \mathcal{N}'_n\frac{d\langle E\rangle_{n'}}{dt} \tag{5.48}$$

Note that the averaging $\langle\rangle_{n'}$ is done for the remaining levels above the ground level n_0 of that group. We can write a similar equation for the total energy measured from the ground state of that group, i.e.:

$$\frac{d\Delta\mathcal{E}_n}{dt} \equiv \sum_{i\in n}\Delta E_i\frac{dN_i}{dt} = \frac{d}{dt}\left(\mathcal{N}'_n\langle\Delta E\rangle_{n'}\right) = \langle\Delta E\rangle_{n'}\frac{d\mathcal{N}'_n}{dt} + \mathcal{N}'_n\frac{d\langle\Delta E\rangle_{n'}}{dt} \tag{5.49}$$

The first term in equation (5.49) describes the change in group energy from the global change in population of the group, i.e. $\langle E\rangle_n d\mathcal{N}_n/dt$. The last term describes the change of the internal structure of the group as a result of the collisional transitions, since

$$\frac{d\langle\Delta E\rangle_{n'}}{dt} = \frac{1}{T_n^2}\left[\langle\Delta E^2\rangle_{n'} - \langle\Delta E\rangle_{n'}^2\right]\frac{dT_n}{dt} = C_{v,n'}\frac{dT_n}{dt} \tag{5.50}$$

From (5.33),

$$\frac{d\mathcal{Z}'_n}{dt} = \frac{g_{n_0}}{N_{n_0}}\left[\frac{d\mathcal{N}'_n}{dt} - \frac{\mathcal{N}'_n}{N_{n_0}}\frac{dN_{n_0}}{dt}\right] = \mathcal{Z}'_n\left[\frac{\overline{\Delta E'}_n}{T_n^2} + \frac{d\ln\tilde{g}'_n}{dT_n}\right]\frac{dT_n}{dt} \tag{5.51}$$

Inserting into (5.49),

$$\mathcal{N}'_n\frac{d\langle\Delta E\rangle_{n'}}{dt} = \frac{C_{v,n'}T_n^2}{\left(\overline{\Delta E'}_n + T_n^2\frac{d\ln\tilde{g}'_n}{dT_n}\right)}\left[\frac{d\mathcal{N}'_n}{dt} - \frac{\mathcal{N}'_n}{N_{n_0}}\frac{dN_{n_0}}{dt}\right] \tag{5.52}$$

We can now combine with the other terms of (5.49) to obtain an expression which only depends on the rates of change of the conserved variables $(N_{n0}, \mathcal{N}'_n)$. Defining

$$\xi_{n'} = \frac{C_{v,n'}T_n^2}{\left(\overline{\Delta E'}_n + T_n^2\frac{d\ln\tilde{g}'_n}{dT_n}\right)} \quad \text{and} \quad \omega_{n'} = \xi_{n'}\frac{\mathcal{N}_{n'}}{N_{n_0}} \tag{5.53}$$

and adding the contribution from the ground state of the group, we obtain:

$$\frac{d\mathcal{E}_n}{dt} = \left[E_{n_0} - \omega_{n'}\right]\frac{dN_{n_0}}{dt} + \left[E_{n_0} + \langle\Delta E\rangle_{n'} + \xi_{n'}\right]\frac{d\mathcal{N}'_n}{dt} \tag{5.54}$$

One can then identify the rates of change of the population density with the effective rates. Considering transitions between groups n and $m > n$, and using a similar expression for $d\mathcal{E}_m/dt$, we have:

$$\tilde{\alpha}^E_{(m_0|n_0)} = [E_{m_0} - \omega_{m'} - E_{n_0} + \omega_{n'}] \cdot \tilde{\alpha}_{(m_0|n_0)} \qquad \equiv \overline{\varepsilon}_{(m_0|n_0)} \cdot \tilde{\alpha}_{(m_0|n_0)} \tag{5.55a}$$

$$\tilde{\alpha}^E_{(m'|n_0)} = [E_{m_0} + \langle \Delta E \rangle_{m'} + \xi_{m'} - E_{n_0} + \omega_{n'}] \cdot \tilde{\alpha}_{(m'|n_0)} \qquad \equiv \overline{\varepsilon}_{(m'|n_0)} \cdot \tilde{\alpha}_{(m'|n_0)} \tag{5.55b}$$

$$\tilde{\alpha}^E_{(m_0|n')} = [E_{m_0} - \omega_{m'} - E_{n_0} - \langle \Delta E \rangle_{n'} - \xi_{n'}] \cdot \tilde{\alpha}_{(m_0|n')} \qquad \equiv \overline{\varepsilon}_{(m_0|n')} \cdot \tilde{\alpha}_{(m_0|n')} \tag{5.55c}$$

$$\tilde{\alpha}^E_{(m'|n')} = [E_{m_0} + \langle \Delta E \rangle_{m'} + \xi_{m'} - E_{n_0} - \langle \Delta E \rangle_{n'} - \xi_{n'}] \cdot \tilde{\alpha}_{(m'|n')} \equiv \overline{\varepsilon}_{(m'|n')} \cdot \tilde{\alpha}_{(m'|n')} \tag{5.55d}$$

It is instructive to examine the limit of infinite Boltzmann temperatures; in this case,

$$\mathcal{Z}_{n'} \to g'_n, \quad C_{v,n'}, \xi_{n'}, \omega_{n'} \to 0 \quad \text{and} \quad \langle \Delta E \rangle_{n'} \to \overline{\Delta E'}_n$$

and similarly for m'. Equation (5.54) becomes:

$$\begin{aligned} \frac{d\mathcal{E}_n}{dt} &= E_{n_0} \frac{dN_{n_0}}{dt} + \frac{\sum_{i \in n'} g_i E_i}{g'_n} \frac{\mathcal{N}_{n'}}{dt} = E_{n_0} \frac{dN_{n_0}}{dt} + \frac{\sum_{i \in n'} g_i E_i}{g_{n_0}} \frac{dN_{n_0}}{dt} \\ &= \frac{\sum_{i \in n} g_i E_i}{g_{n_0}} \frac{dN_{n_0}}{dt} = \tilde{E}_n \frac{d\mathcal{N}_n}{dt} \end{aligned} \tag{5.56}$$

where we have also used the fact that in that limit, $N_{n_0}/g_{n_0} = \mathcal{N}_n/g_n$, and used the definition of the average group energy – see equation (5.47). Since a similar equation is found for $d\mathcal{E}_m/dt$, the combination exactly yields (5.47). Thus, we have verified that by taking the limit $T_n, T_m \to 0$, we recover the uniform group model.

For ionizations and recombinations, a similar procedure can be found. Considering the change in electron energy due to ionization and recombination from

and to the group n, we have:

$$\left.\frac{dE_e}{dt}\right)_n = -\sum_{i\in n}\frac{dN_i}{dt}I_i = -\frac{d}{dt}\left[\langle I\rangle_n \mathcal{N}_n\right] = -I_{n_0}\frac{dN_{n_0}}{dt} - \langle I\rangle_{n'}\frac{d\mathcal{N}_{n'}}{dt} - \mathcal{N}_{n'}\frac{d\langle I\rangle_{n'}}{dt} \tag{5.57}$$

where I_i is the ionization potential for level i and $\langle I\rangle_{n'}$ is the group ionization potential averaged over the sub-partition n'. Using $I_i = I_H - E_i = I_{n_0} - \Delta E_i$, it is easy to see that:

$$\langle I\rangle_{n'} = I_{n_0} - \langle \Delta E\rangle_{n'} \quad \text{and} \quad \frac{d\langle I\rangle_{n'}}{dt} = -C_{v,n'} \tag{5.58}$$

Equations (5.51,5.52) are still valid, and using again the definitions (5.53), we obtain the final form:

$$\left.\frac{dE_e}{dt}\right)_n = -\left[I_{n_0} + \omega_{n'}\right]\frac{dN_{n_0}}{dt} - \left[I_{n_0} - \langle \Delta E\rangle_{n'} - \xi_{n'}\right]\frac{d\mathcal{N}_{n'}}{dt} \tag{5.59}$$

Note the similarity with (5.54). The effective rates are therefore:

$$\tilde{\alpha}^E_{(+|n_0)} = \left[I_{n_0} + \omega_{n'}\right]\cdot\tilde{\alpha}_{(+|n_0)} \qquad \equiv \overline{\varepsilon}_{(+|n_0)}\cdot\tilde{\alpha}_{(+|n_0)} \tag{5.60a}$$

$$\tilde{\alpha}^E_{(+|n')} = \left[I_{n_0} - \langle \Delta E\rangle_{n'} - \xi_{n'}\right]\cdot\tilde{\alpha}_{(+|n')} \equiv \overline{\varepsilon}_{(+|n')}\cdot\tilde{\alpha}_{(+|n')} \tag{5.60b}$$

Examination of equations (5.55) and (5.60) reveals that the overall procedure consists of replacing the energy of the group's ground state n_0 and sub-partition n' by *effective energies* for the energy exchange:

$$\tilde{E}_{n_0} = E_{n_0} - \omega_{n'} \quad \text{and} \quad \tilde{E}_{n'} = E_{n_0} + \langle \Delta E\rangle_{n'} + \xi_{n'} \tag{5.61}$$

Thus, the effective rates of energy transfer become:

$$\tilde{\alpha}^E_{(m_0|n_0)} = \left(\tilde{E}_{m_0} - \tilde{E}_{n_0}\right)\cdot\tilde{\alpha}_{(m_0|n_0)} \tag{5.62a}$$

$$\tilde{\alpha}^E_{(m'|n_0)} = \left(\tilde{E}_{m'} - \tilde{E}_{n_0}\right)\cdot\tilde{\alpha}_{(m'|n_0)} \tag{5.62b}$$

$$\tilde{\alpha}^E_{(m_0|n')} = \left(\tilde{E}_{m_0} - \tilde{E}_{n'}\right)\cdot\tilde{\alpha}_{(m_0|n')} \tag{5.62c}$$

$$\tilde{\alpha}^E_{(m'|n')} = \left(\tilde{E}_{m'} - \tilde{E}_{n'}\right)\cdot\tilde{\alpha}_{(m'|n')} \tag{5.62d}$$

and for ionization:

$$\tilde{\alpha}^{E}_{(+|n_0)} = \left(I_H - \tilde{E}_{n_0}\right) \cdot \tilde{\alpha}_{(+|n_0)} \tag{5.63a}$$

$$\tilde{\alpha}^{E}_{(+|n')} = \left(I_H - \tilde{E}_{n'}\right) \cdot \tilde{\alpha}_{(+|n')} \tag{5.63b}$$

The use of effective group energies[14] provides a straightforward approach, and the effective rates of energy transfer for *all* transitions (including de-excitations, recombination and radiative transitions) can now be expressed in a simple form. Note that (5.63) is similar to the case of uniform grouping (5.47) and since we have already demonstrated that we can recover the uniform grouping case in the limit of infinite temperatures, we have achieved here a fully consistent model.

We are now left with the task of verifying energy conservation with this revised approach. Using the same test case (#3), we now find a much smaller level of error, as can be seen from Figure 5.13 – compare with Figure 5.12 – that is characteristic of the level of numerical round-off. Note that the cumulative error sums the absolute values of the stepwise error (L_1 norm), and is therefore a maximum bound. Figure 5.14 shows the effect of bin size on the relative error; this observation is similar to the one made regarding the accuracy of the ASDF – see Figure 5.4, i.e. smaller group widths are preferred. However, it is clear that even for one or two bins, the error on energy conservation remains very small.

[14]Contrary to the uniform grouping case, we need to use two values, one for n_0 and one for n', which reflects the additional degrees of freedom in the Boltzmann model.

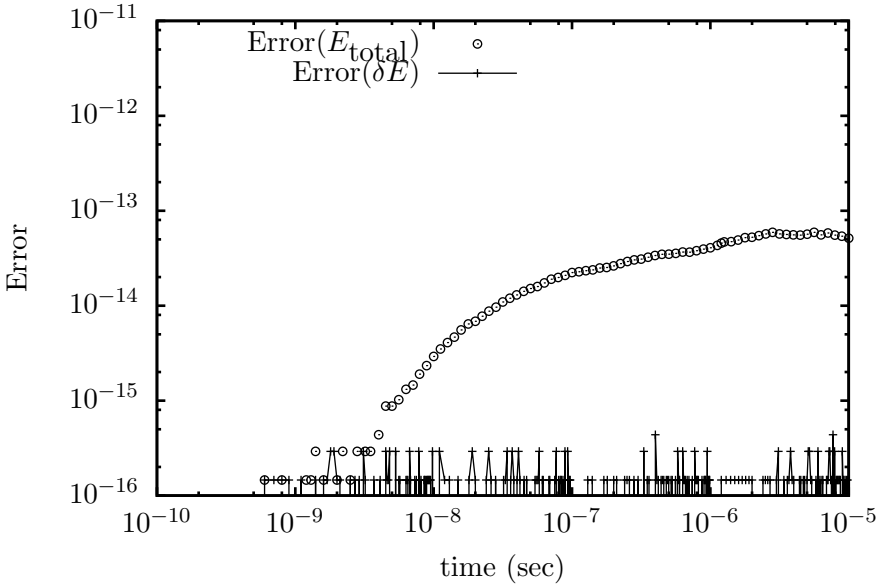

Figure 5.13: Cumulative and instantaneous relative errors in energy conservation - test case 3 - with revised formulation

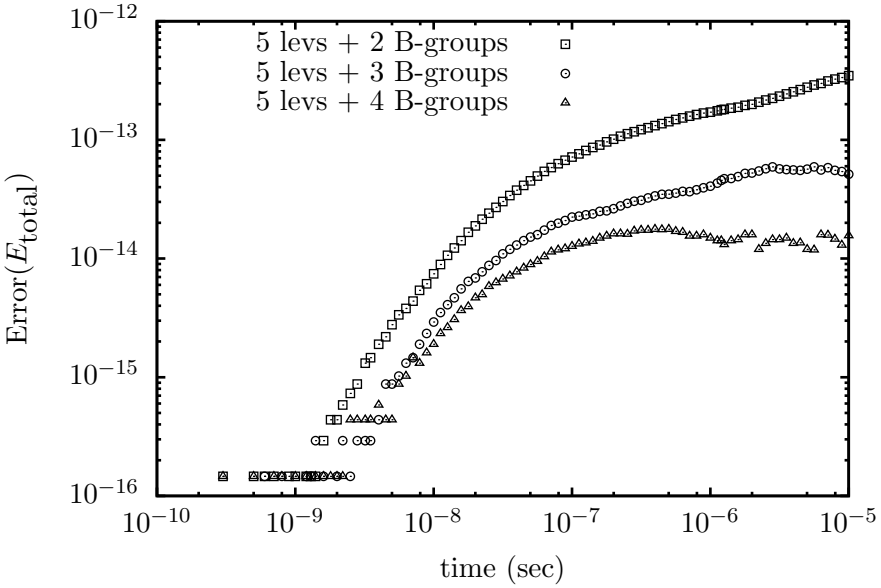

Figure 5.14: Cumulative relative errors in energy conservation as function of group sizes; revised formulation.

CHAPTER 6

Modeling of Collisions in Multifluid Plasmas

6.1 Introduction

Modeling of elastic collisions in neutral gases and plasmas is a classical topic widely studied in the kinetic theory of transport phenomena [52, 44, 84, 53]. The derivation starts from the kinetic equation with a Boltzmann collision operator for neutral collision, and/or Landau-Fokker-Planck collision operator for charged particle collision. The transport terms appearing in the hydrodynamic equations, e.g., viscous shear stress and heat flux, are obtained by computing the collision integral with a perturbative expansion of the velocity distribution function (VDF) about a local Maxwellian one, i.e., $f = f^M + \epsilon\delta f + O(\epsilon^2)$, where ϵ is a small parameter. The Chapman-Enskog expansion [44] and Grad's method [47] are the two well-known moment closure schemes, from which the Euler/Navier-Stokes and the Grad-moment equations are derived, respectively.

The treatment of elastic collisions, within a *multi-fluid* framework, can be found from the works of Braginskii [46] and Burgers [43]. In 1965, Braginskii derived a two-fluid system of equations for a fully ionized plasma with a Chapman-Enskog closure for the transport fluxes taking into account the effect of the magnetic field; these equations are now commonly referred to as the Braginskii's equations. Burgers, on the other hand, presented a rather general framework for the modeling of elastic collisions, which is applicable for a general system of moment equations beyond the standard five-moment model.

In this chapter, we present a derivation of the exchange terms for number, momentum, and total energy densities due to *inelastic* collisions. These terms are relevant for the construction of a collisional-radiative (CR) model within the framework of the multi-fluid equations. We restrict ourselves to the case where the VDF of each fluid is a Maxwellian distribution function. Current work focuses on excitation and deexcitation collisions, but the method can be generalized to other collision types, e.g., ionization/recombination, charge exchange collision, etc.

6.2 Transfer integral

Let us consider an inelastic collision between two particles s and t, such that the particle t changes its internal state. The particles s and t are respectively the scattered and target in the laboratory frame of reference (LAB), the former being identified here as the electron and the target being the atom, but we will keep the s, t notation until explicit assumptions and approximations are made, such as neglecting terms of order m_s/m_t for final expressions.

$$s(\mathbf{v}_s) + t(\mathbf{v}_t) \Leftrightarrow s'(\mathbf{v}'_s) + t'(\mathbf{v}'_t) \tag{6.1}$$

The initial velocities are $\mathbf{v}_s, \mathbf{v}_t$, where $\mathbf{v} = \mathbf{u}+\mathbf{c}$ and $\mathbf{u}$ is the fluid mean velocity in the LAB frame, and post-collision values are indicated by a prime. Thus, $\mathbf{c}$ is the thermal velocity and if $\langle \ldots \rangle$ denotes a statistical average over the corresponding distribution function, we have $\langle \mathbf{v} \rangle \equiv \mathbf{u}$ and $\langle \mathbf{c} \rangle \equiv 0$. It is more convenient to treat the collision in the center of mass (COM) reference frame, moving with velocity $\mathbf{V}$ with respect to the LAB frame. Similarly, we can also define a mean velocity of this COM frame as $\mathbf{U}$. The subsequent Galilean transformations yield the following definitions:

$$\mathbf{V} = \frac{m_s\mathbf{v}_s + m_t\mathbf{v}_t}{M} \qquad \mathbf{g} = \mathbf{v}_s - \mathbf{v}_t \tag{6.2a}$$

$$\mathbf{U} = \frac{m_s\mathbf{u}_s + m_t\mathbf{u}_t}{M} \qquad \mathbf{w} = \mathbf{u}_s - \mathbf{u}_t \tag{6.2b}$$

where $M = m_s + m_t$. The inverse transformation yields:

$$\mathbf{v}_s = \mathbf{V} + \frac{m_t}{M}\mathbf{g} \qquad \mathbf{u}_s = \mathbf{U} + \frac{m_t}{M}\mathbf{w} \tag{6.3a}$$

$$\mathbf{v}_t = \mathbf{V} - \frac{m_s}{M}\mathbf{g} \qquad \mathbf{u}_t = \mathbf{U} - \frac{m_s}{M}\mathbf{w} \tag{6.3b}$$

One can also define a similar transformation for the post-collision variables. Expressed in the COM frame and for any inelastic collision with an energy transfer $\Delta\varepsilon$, momentum and energy conservation yield:

$$M\mathbf{V} \equiv M\mathbf{V}' \tag{6.4a}$$

$$\frac{1}{2}M\mathbf{V}^2 + \frac{1}{2}\mu\mathbf{g}^2 \equiv \frac{1}{2}M\mathbf{V}'^2 + \frac{1}{2}\mu\mathbf{g}'^2 + \Delta\varepsilon \tag{6.4b}$$

where $\mathbf{V}'$ and $\mathbf{g}'$ are defined similarly to (6.2), and $\mu = m_s m_t/M$ is the reduced mass. Note that we have also implicitly assumed that the collision produces only two particles, as evidenced by the expression for the kinetic energy – this assumption must be revisited when dealing with ionization and recombination, along with the assumption of equal masses of individual particles before and after the collision, e.g. $m_s' \equiv m_s$, such that mass conservation is automatically obtained. Therefore, we have the following constraints:

$$\mathbf{V} \equiv \mathbf{V}' \qquad \text{and} \quad \mathbf{g}^2 = \mathbf{g}'^2 + \frac{2\Delta\varepsilon}{\mu} \tag{6.5}$$

For an excitation between two atomic levels, the transferred energy is a fixed value $\Delta\varepsilon \equiv \varepsilon^*$, the energy gap between levels, while for ionization the energy is a continuum of values: $\Delta\varepsilon \in [\varepsilon^*, \varepsilon]$, where $\varepsilon = \frac{1}{2}\mu\mathbf{g}^2$ is the available kinetic energy (in the COM frame). In the limit $\Delta\varepsilon \to 0$, the collision is elastic.

We can then define a transfer integral of the collision operator between the two species s and t [43].

$$\Psi_{st} = n_s n_t \int d^3\mathbf{v}_s d^3\mathbf{v}_t \, f_s f_t \, g \int \psi \, d\omega(\mathbf{v}_s, \mathbf{v}_t; \mathbf{v}'_s, \mathbf{v}'_t) \tag{6.6}$$

where g is the magnitude of the relative velocity ($g = |\mathbf{g}|$), $d\omega$ is the differential cross section, and ψ is any moment variable exchanged during the collision. Let

us now utilize the transformation defined in appendix C:

$$\mathbf{V}^* = \mathbf{V} - \mathbf{U} + \gamma\tilde{\mathbf{g}} \qquad T^* = \frac{MT_sT_t}{m_sT_t+m_tT_s} \qquad a^2 = \frac{2kT^*}{M} \tag{6.7a}$$

$$\tilde{\mathbf{g}} = \mathbf{g} - \mathbf{w} \qquad \tilde{T} = \frac{m_sT_t+m_tT_s}{M} \qquad \alpha^2 = \frac{2k\tilde{T}}{\mu} \tag{6.7b}$$

$$\gamma = \frac{\mu(T_t - T_s)}{m_sT_t+m_tT_s} \tag{6.7c}$$

One can easily show that the Jacobian of the transformations is unity, i.e.

$$d^3\mathbf{v}_s d^3\mathbf{v}_t \equiv d^3\mathbf{V} d^3\mathbf{g} \equiv d^3\mathbf{V}^* d^3\mathbf{g} \equiv d^3\mathbf{V}^* d^3\tilde{\mathbf{g}} \tag{6.8}$$

Using the transformed variables, the product of two Maxwellian VDFs in equation (6.6) becomes:

$$f_s \cdot f_t = \left(\frac{M}{2\pi kT^*}\right)^{\frac{3}{2}} \exp\left[-\frac{M\mathbf{V}^{*2}}{2kT^*}\right] \cdot \left(\frac{\mu}{2\pi k\tilde{T}}\right)^{\frac{3}{2}} \exp\left[-\frac{\mu\tilde{\mathbf{g}}^2}{2k\tilde{T}}\right] \equiv f_{V^*} \cdot f_g \tag{6.9}$$

Substituting the result of equation (6.9) into (6.6), the transfer integral can be written as follows:

$$\begin{aligned}\Psi_{st} =& n_s n_t \left(\frac{M}{2\pi kT^*}\right)^{\frac{3}{2}} \int d^3\mathbf{V}^* \exp\left[-\frac{M\mathbf{V}^{*2}}{2kT^*}\right] \cdot \\ & \left(\frac{\mu}{2\pi k\tilde{T}}\right)^{\frac{3}{2}} \int d^3\mathbf{g} \exp\left[-\frac{\mu(\mathbf{g}-\mathbf{w})^2}{2k\tilde{T}}\right] g \int \psi d\omega(\mathbf{g};\mathbf{g}')\end{aligned} \tag{6.10}$$

In the COM reference frame, the differential cross section only depends on the relative velocities, i.e., $d\omega(\mathbf{v}_s, \mathbf{v}_t; \mathbf{v'}_s, \mathbf{v'}_t) \equiv d\omega(\mathbf{g};\mathbf{g}')$, and can be expressed as:

$$d\omega(\mathbf{g};\mathbf{g}') = \sigma_{st}(g,\Omega')d\Omega' \tag{6.11}$$

where Ω' is the solid angle between the initial and final relative velocities, i.e., $d\Omega' = d\rho\, d\cos\chi$ with $\mathbf{g}\cdot\mathbf{g}' = gg'\cos\chi$. Without loss of generality, we can now choose a reference frame (LAB) such that the relative *mean* velocity $\mathbf{w}$ is aligned with the z axis, as shown in figure 6.1. Thus, the unit vectors $\hat{\mathbf{g}}$, $\hat{\mathbf{g}}'$ are obtained by subsequent rotations of the (x, y, z) frame. Using the abbreviated notation

$c_\varphi \equiv \cos\varphi$, $s_\varphi \equiv \sin\varphi$, etc, we define this rotation operator by the matrix:

$$R(\varphi,\theta) = \begin{pmatrix} c_\varphi s_\theta & -s_\varphi & c_\varphi s_\theta \\ s_\varphi c_\theta & c_\varphi & s_\varphi s_\theta \\ -s_\theta & 0 & c_\theta \end{pmatrix} \quad \text{and} \qquad \hat{\mathbf{g}} = \frac{\mathbf{g}}{g} = R(\varphi,\theta)\cdot\hat{\mathbf{z}} = \begin{pmatrix} c_\varphi s_\theta \\ s_\varphi s_\theta \\ c_\theta \end{pmatrix} \tag{6.12}$$

Similarly, the post-collision relative velocity is rotated by the angles (ρ,χ), such that $\hat{\mathbf{g}}' = R(\rho,\chi)\cdot\hat{\mathbf{g}}$.

Using $d^3\mathbf{g} = g^2 dg d\varphi dc_\theta = 2\pi g^2 dg dc_\theta$ and equation (6.11), the transfer integral can be written as:

$$\begin{aligned}\Psi_{st} = \frac{4n_s n_t}{\pi^{\frac{1}{2}}\alpha^3} e^{-w^2/\alpha^2} \cdot \int d^3\mathbf{V}^* f_{V^*} \cdot \int dg\, g^3\, e^{-g^2/\alpha^2} \cdot \\ \frac{1}{2}\int dc_\theta\, e^{2gwc_\theta/\alpha^2} \int d\rho dc_\chi\, \psi\sigma_{st}(g,\Omega')\end{aligned} \tag{6.13}$$

Note that if ψ is independent of $\mathbf{V}^*$, the first integral on the RHS is simply the normalization of a Maxwellian VDF ($= 1$). For clarity, let us now consider the case where ψ is not a function of $\mathbf{V}^*$, so the integral $\int d^3\mathbf{V}^* f_{V^*}$ can be omitted. By symmetry, the differential cross-section σ_{st} does not depend on ρ, and we can write:

$$\sigma_{st}(g,\Omega') \equiv \overline{\sigma}_{st}(g)\cdot\mathcal{G}(g,\chi) \quad \text{s.t.} \quad \int d\rho\; d\cos\chi\, \mathcal{G}(g,\chi) \equiv 1 \tag{6.14}$$

More generally, we will define the averaging of any function ψ over the scattering angles as:

$$\langle\psi\rangle_{\Omega'} = 2\pi\int_{-1}^{+1} dc_\chi \psi\; \mathcal{G}(g,\chi) \tag{6.15}$$

We now define the following, normalized energy variables:

$$\varepsilon = \frac{1}{2}\mu g^2 \qquad \overline{e} = \frac{1}{2}\mu w^2 \tag{6.16a}$$

$$x = \frac{\varepsilon}{k\tilde{T}} \qquad \lambda = \frac{\overline{e}}{k\tilde{T}} \tag{6.16b}$$

$$x^* = \frac{\Delta\varepsilon}{k\tilde{T}} \qquad x' = \frac{\varepsilon'}{k\tilde{T}} = x - x^* \tag{6.16c}$$

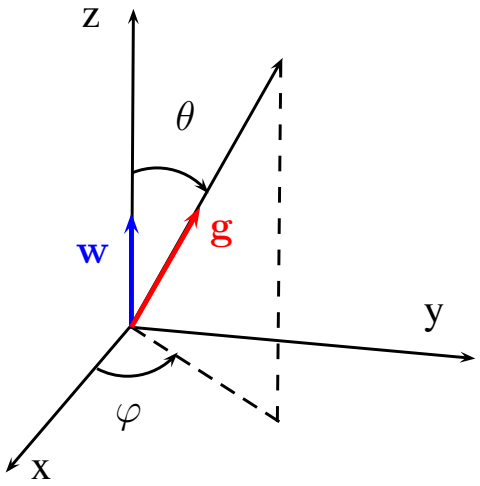

(a)

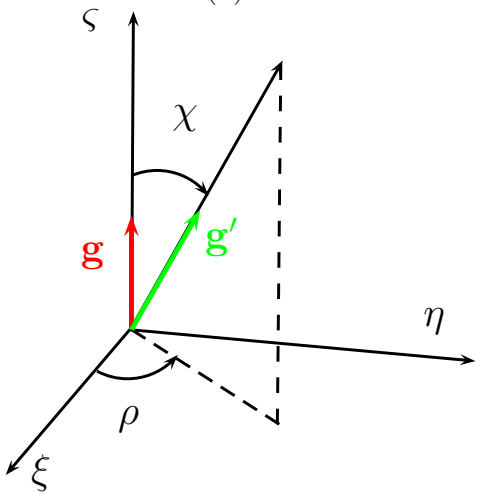

(b)

Figure 6.1: Frame rotation and relative orientation of (a) $\mathbf{w}$ and $\mathbf{g}$ and (b) $\mathbf{g}$ and $\mathbf{g}'$. The rotation operator matrix $R(\varphi, \theta)$ (or $R(\rho, \chi)$) is defined such that $\hat{\mathbf{g}} = R(\varphi, \theta) \cdot \hat{\mathbf{w}}$ and $\hat{\mathbf{g}}' = R(\rho, \chi) \cdot \hat{\mathbf{g}}$.

Using $g^3 dg \equiv 2\varepsilon d\varepsilon/\mu^2$ and a trivial integration[1] over φ, we obtain:

$$\Psi_{st} = n_s n_t \underbrace{\left(\frac{8k\tilde{T}}{\pi\mu}\right)^{\frac{1}{2}}}_{\overline{g}_{\tilde{T}}} \frac{e^{-\overline{\varepsilon}/k\tilde{T}}}{(k\tilde{T})^2} \int_{\varepsilon^*}^{\infty} d\varepsilon\, \varepsilon\, e^{-\varepsilon/k\tilde{T}}\, \overline{\sigma}_{st}(\varepsilon) \cdot \frac{1}{2} \int_{-1}^{+1} dc_\theta e^{2\sqrt{\overline{\varepsilon}\varepsilon} c_\theta/k\tilde{T}} \cdot \langle \psi \rangle_{\Omega'} \tag{6.17}$$

where $\overline{g}_{\tilde{T}}$ is a thermal velocity based on the average temperature $\tilde{T}$. Equation (6.17) can be written in terms of the normalized variables as follows:

$$\Psi_{st} = n_s n_t \overline{g}_{\tilde{T}} e^{-\lambda} \int_{x^*}^{\infty} dx\, x\, e^{-x}\, \overline{\sigma}_{st}(x) \cdot \frac{1}{2} \int_{-1}^{+1} dc_\theta e^{2\sqrt{\lambda x} c_\theta} \cdot \langle \psi \rangle_{\Omega'} \tag{6.18}$$

Note that we have left the variable ψ undetermined, and since it could potentially depend on all integration variables (x, χ, θ), it must be kept inside all integrals. We will see next what simplifications can be made, depending on which moment variables we are integrating. Note also that the lower limit of integration, x^*, is zero for elastic collisions.

6.3 Excitation/Deexcitation collisions

In this section, we consider an excitation collision and its reverse process:

$$s(\mathbf{v}_s) + t(E_\ell, \mathbf{v}_t) \Leftrightarrow s(\mathbf{v'}_s) + t(E_u, \mathbf{v'}_t) \tag{6.19}$$

where the particle indices (s, t) are kept the same to indicate that both internal states (ℓ, u) belong to the same fluid t. For the case of an excitation collision, particle t changes its internal states from ℓ to u $(\ell \rightarrow u)$, where ℓ and u denote the lower and upper energy states, respectively. For a deexcitation collision, we have the reverse $(u \rightarrow \ell)$. Conservation of momentum and energy are the same as those expressed in equation (6.4) with $\Delta\varepsilon = E_u - E_\ell$ and $\Delta\varepsilon > 0$.

In the CR model, each internal state is treated as a pseudo-species, so the rate of change in number density for each state (n_ℓ, n_u) is taken into account separately.

[1] Using symmetry principles.

However, since both states (ℓ, u) belong to the same fluid, we only need to keep track of the net change of momentum and energy of each fluid due to the collision.

6.3.1 Zeroth-order moment: number density

The rate of change of the number density due to an excitation collision of type (6.19) can be obtained by setting $\psi \equiv 1$ in (6.18), so the average over all the scattering angle is trivially removed. We can express the rate of change of number density as:

$$\Gamma^{\uparrow}_{s\ell} = n_s n_\ell \overline{g}_{\tilde{T}} e^{-\lambda} \int_{x^*}^{\infty} dx\, x\, e^{-x}\, \overline{\sigma}^{\uparrow}_{s\ell}(x) \cdot \frac{1}{2} \int_{-1}^{+1} dc_\theta e^{2\sqrt{\lambda x} c_\theta} \tag{6.20}$$

where superscript $\uparrow$ denotes the forward process ($\ell \to u$), and (n_ℓ, n_u) are the number densities of the lower and upper states.

To perform the integral over dc_θ, we define:

$$\zeta^{(0)}(\xi) = \frac{1}{2} \int_{-1}^{+1} dy\, e^{2\xi y} = \frac{\sinh(2\xi)}{2\xi} \qquad \text{s.t.:} \quad \lim_{\xi \to 0} \zeta^{(0)} = 1 \tag{6.21}$$

Combining all, we arrive at the following expression for the rate of change of the number density:

$$\Gamma^{\uparrow}_{s\ell} = n_s n_\ell \overline{g}_{\tilde{T}} e^{-\lambda} \int_{x^*}^{\infty} dx\, x\, e^{-x}\, \zeta^{(0)}(\sqrt{\lambda x}) \overline{\sigma}^{\uparrow}_{s\ell}(x) \tag{6.22}$$

Note that

$$\frac{dn_\ell}{dt} = -\Gamma^{\uparrow}_{s\ell} = -\frac{dn_u}{dt}$$

In the case of electron-impact excitation ($s \equiv e$), we can neglect terms of order m_e/M, and for an atomic transition between levels $\ell \to u$, we obtain:

$$\Gamma^{\uparrow}_{e\ell} = n_e n_\ell \overline{v}_e\, e^{-\lambda} \int_{x^*}^{\infty} dx\, x\, e^{-x}\, \zeta^{(0)}(\sqrt{\lambda x}) \overline{\sigma}^{\uparrow}_{e\ell}(x) \tag{6.23}$$

where $\overline{v}_e = \sqrt{\frac{8kT_e}{\pi m_e}}$. In the limit of thermal plasma when multi-fluid effects are weak, i.e. $\lambda \to 0$, we obtain:

$$\Gamma^{\uparrow}_{e\ell} = n_e n_\ell \overline{v}_e \int_{x^*}^{\infty} dx\, x\, e^{-x}\, \overline{\sigma}^{\uparrow}_{e\ell}(x) \tag{6.24}$$

which is *exactly* the expected result for a single-fluid plasma.

The reverse process of deexcitation ($u \to \ell$) can be computed in a similar fashion by considering $\mathbf{g}', \mathbf{g}$ as the initial and final relative velocities respectively. The transfer integral becomes:

$$\Psi^{\downarrow}_{su} = n_s n_u \overline{g}_{\tilde{T}} e^{-\lambda} \int d^3\mathbf{V}'^{*} f_{V'^{*}} \cdot \int_0^{\infty} dx'\, x'\, e^{-x'}\, \overline{\sigma}^{\downarrow}_{su}(x') \cdot \frac{1}{2} \int_{-1}^{+1} dc_\theta e^{2\sqrt{\lambda x'} c_\theta} \cdot \langle \psi \rangle_{\Omega'} \tag{6.25}$$

where superscript $\downarrow$ indicates the reverse process ($u \to \ell$), and now $\cos\theta = \hat{\mathbf{g}}' \cdot \hat{\mathbf{w}}$. Setting $\psi = 1$, it is straightforward to obtain:

$$\Gamma^{\downarrow}_{su} = n_s n_u \overline{g}_{\tilde{T}}\; e^{-\lambda} \int_0^{\infty} dx'\, x'\, e^{-x'}\, \zeta^{(0)}(\sqrt{\lambda x'})\, \overline{\sigma}^{\downarrow}_{su}(x') \tag{6.26}$$

Note that the lower limit of integration has changed, since deexcitation does not have an energy threshold (recall that $x' = x - x^*$). Using the Klein-Rosseland relation for detailed balance [87],

$$\overline{\sigma}^{\uparrow}_{s\ell}(x) x \mathcal{g}_\ell = \overline{\sigma}^{\downarrow}_{su}(x') x' \mathcal{g}_u \tag{6.27}$$

where $\mathcal{g}_\ell, \mathcal{g}_u$ are the degeneracies of the lower and upper atomic levels respectively. The principle of detailed balance for various processes are discussed in detail in appendix D. We can write the excitation rate as follows:

$$\Gamma^{\uparrow}_{s\ell} = n_s n_\ell \overline{g}_{\tilde{T}}\; e^{-\lambda} \frac{\mathcal{g}_u}{\mathcal{g}_\ell} e^{-x^*} \int_0^{\infty} dx'\, x'\, e^{-x'}\, \zeta^{(0)}(\sqrt{\lambda(x^* + x')})\, \overline{\sigma}^{\downarrow}_{su}(x') \tag{6.28}$$

One can then easily extract reaction rates, for example:

$$\Gamma^{\uparrow}_{s\ell} = \varpi^{\uparrow}_{s\ell} \cdot n_s n_\ell$$

It is instructive to consider the ratio of these rates:

$$\frac{\varpi^{\uparrow}_{s\ell}}{\varpi^{\downarrow}_{su}} = \left[\frac{\mathcal{g}_u}{\mathcal{g}_\ell} e^{-x^*} \right] \cdot \frac{\int_0^{\infty} dx'\, x'\, e^{-x'} \zeta^{(0)}(\sqrt{\lambda(x' + x^*)}) \overline{\sigma}^{\downarrow}_{su}(x')}{\int_0^{\infty} dx'\, x'\, e^{-x'} \zeta^{(0)}(\sqrt{\lambda x'}) \overline{\sigma}^{\downarrow}_{su}(x')} \tag{6.29}$$

The first term in brackets is the traditional Boltzmann equilibrium relation; the second term contains the correction due to the multi-fluid effects, and is apparent

only through the presence of the $\zeta^{(0)}$ function. A Taylor expansion near $\lambda = 0$ yields (with an obvious definition of the Boltzmann function $\mathcal{B}$):

$$\frac{\varpi_{s\ell}^{\uparrow}}{\varpi_{su}^{\downarrow}} = \left[\frac{\mathcal{J}_u}{\mathcal{J}_\ell} e^{-x^*}\right] \cdot \frac{\int_0^\infty dx'\, x'\, e^{-x'} \left[1 + \frac{2\lambda(x^*+x')}{3}\right] \overline{\sigma}_{su}^{\downarrow}(x')}{\int_0^\infty dx'\, x'\, e^{-x'} \left[1 + \frac{2\lambda x'}{3}\right] \overline{\sigma}_{su}^{\downarrow}(x')}$$
$$\simeq \left[\mathcal{B}_{\ell u}(\tilde{T})\right] \cdot \left(1 + \frac{2\lambda x^*}{3}\right) \tag{6.30}$$

Thus, we recover the expression for Boltzmann equilibrium in the single-fluid limit ($\lambda \to 0$). Note that the correction term is larger for large energy thresholds, i.e. transitions between high levels ($x^* \to 0$) will not be affected very much by the multi-fluid effects, while the impact will be stronger for excitation from low energy levels, with high energy gaps.

6.3.2 First-order moment: momentum density

Consider the forward reaction and the corresponding loss of momentum to the particles with velocity $\mathbf{v}_s$. The transfer variable in this case is $\psi = m_s \mathbf{v}_s$, and starting from equation (6.13), this leads to the following contribution to the momentum equation:

$$\mathbf{R}_s^- = -\frac{4 n_s n_\ell}{\pi^{\frac{1}{2}} \alpha^3} \cdot \int d^3\mathbf{V}^* f_{V^*} \cdot \int dg\, g^3\, e^{-g^2/\alpha^2}\, \overline{\sigma}_{s\ell}^{\uparrow}(g) \cdot \frac{1}{2} \int dc_\theta\, e^{2gwc_\theta/\alpha^2}\, \langle m_s \mathbf{v}_s \rangle_{\Omega'} \tag{6.31}$$

Similarly, the gain in momentum is given by the production of new particles with velocity $\mathbf{v'}_s$:

$$\mathbf{R}_s^+ = +\frac{4 n_s n_\ell}{\pi^{\frac{1}{2}} \alpha^3} \cdot \int d^3\mathbf{V}^* f_{V^*} \cdot \int dg\, g^3\, e^{-g^2/\alpha^2}\, \overline{\sigma}_{s\ell}^{\uparrow}(g) \cdot \frac{1}{2} \int dc_\theta\, e^{2gwc_\theta/\alpha^2}\, \langle m_s \mathbf{v'}_s \rangle_{\Omega'} \tag{6.32}$$

The *net* rate of change to the momentum density of species s is:

$$\mathbf{R}_s^{\uparrow} = -\frac{4 \mu n_s n_\ell}{\pi^{\frac{1}{2}} \alpha^3} \cdot \int dg\, g^3\, e^{-g^2/\alpha^2}\, \overline{\sigma}_{s\ell}^{\uparrow}(g) \cdot \frac{1}{2} \int dc_\theta\, e^{2gwc_\theta/\alpha^2}\, \langle \mathbf{g} - \mathbf{g}' \rangle_{\Omega'} \tag{6.33}$$

where we have used the relation:

$$m_s(\mathbf{v}_s - \mathbf{v'}_s) = \mu(\mathbf{g} - \mathbf{g}') \tag{6.34}$$

Note that in equation (6.33), the integral over $\mathbf{V}^*$-space is omitted since ψ does not depend on $\mathbf{V}^*$. Let us consider the last integral over the scattering angle. From figure 6.1, the vectors $\mathbf{g}, \mathbf{g}'$ in the rotated frame (ξ, η, ς) are:

$$\mathbf{g} = g\ \hat{\mathbf{g}} = g \cdot \begin{pmatrix} 0 \\ 0 \\ 1 \end{pmatrix} \qquad \mathbf{g}' = g \cdot\ \hat{\mathbf{g}}' = g' \begin{pmatrix} c_\rho s_\chi \\ s_\rho s_\chi \\ c_\chi \end{pmatrix} \tag{6.35}$$

Therefore the integral yields, using (6.15):

$$\begin{aligned} \int d\Omega'(\mathbf{g}'-\mathbf{g})\mathcal{G}(g,\Omega') &= 2\pi g' \int dc_\chi c_\chi \mathcal{G}(g,\chi)\hat{\mathbf{g}} - 2\pi g \int dc_\chi \mathcal{G}(g,\chi)\hat{\mathbf{g}} \\ &= \left[g'\langle \cos\chi \rangle_{\Omega'} - g\right]\ \hat{\mathbf{g}} \end{aligned} \tag{6.36}$$

We must now express the vector $\hat{\mathbf{g}}$ in the initial (x, y, z) frame, which is given by (6.12). Let us also utilize the normalized variables as defined in (6.16). This leads to the following expression:

$$\begin{aligned} \mathbf{R}_s^{\uparrow} = -\hat{\mathbf{w}}\mu\alpha n_s n_\ell \overline{g}_{\tilde{T}} e^{-\lambda} \int_{x^*}^{\infty} dx\, x\, e^{-x}\, \overline{\sigma}_{s\ell}^{\uparrow}(x)\ \left[\sqrt{x} - \sqrt{x'}\langle \cos\chi \rangle_{\Omega'}\right] \\ \cdot \frac{1}{2} \int_{-1}^{+1} dc_\theta c_\theta e^{2\sqrt{\lambda x} c_\theta} \end{aligned} \tag{6.37}$$

As before, we can define another function as follows:

$$\zeta^{(1)}(\xi) = \frac{3}{4\xi} \int_{-1}^{+1} dy\, y\, e^{2\xi y} = \frac{3}{4\xi^2}\left[\cosh(2\xi) - \frac{\sinh(2\xi)}{2\xi}\right] \qquad \text{s.t.:} \quad \lim_{\xi \to 0} \zeta^{(1)} = 1 \tag{6.38}$$

The last integration in (6.37) then yields:

$$\mathbf{R}_s^{\uparrow} = -\frac{2}{3}\mu \mathbf{w} n_s n_\ell \overline{g}_{\tilde{T}} e^{-\lambda} \int_{x^*}^{\infty} dx\, x^{\frac{3}{2}}\, e^{-x}\, \overline{\sigma}_{s\ell}^{\uparrow}(x)\, \zeta^{(1)}(\sqrt{\lambda x}) \left[\sqrt{x} - \sqrt{x'}\langle \cos\chi \rangle_{\Omega'}\right] \tag{6.39}$$

We can also define average cross-sections as follows:

$$\begin{aligned} \sigma_{s\ell}^{\uparrow(\ell)}(x) &= 2\pi \left(\frac{x'}{x}\right)^{\ell/2} \int_{-1}^{1} (c_\chi)^\ell \sigma_{s\ell}^{\uparrow}(x, c_\chi) dc_\chi \\ &= \left(\frac{x'}{x}\right)^{\ell/2} \overline{\sigma}_{s\ell}^{\uparrow}(x) \langle (\cos\chi)^\ell \rangle_{\Omega'} \end{aligned} \tag{6.40}$$

Note that $\sigma_{st}^{\uparrow(0)} = \overline{\sigma}_{st}^{\uparrow}$ and $x = x' + x^*$. Using the average cross-sections in equation (6.40), equation (6.39) becomes:

$$\mathbf{R}_s^{\uparrow} = -\frac{2}{3}\mu \mathbf{w} n_s n_\ell \overline{g}_{\tilde{T}} e^{-\lambda} \int_{x^*}^{\infty} dx\, x^2\, e^{-x}\, \zeta^{(1)}(\sqrt{\lambda x}) \left[\sigma_{st}^{\uparrow(0)}(x) - \sigma_{st}^{\uparrow(1)}(x)\right] \tag{6.41}$$

A similar (but of opposite sign) expression can be obtained for the species of type t. Note that the expression (6.41) is obtained in a frame where $\mathbf{w}$ is aligned with the z direction, and corresponds to the change in momentum density along that direction. Thus, it is the component of a force *parallel* to $\mathbf{w}$, while all components in the transverse directions are zero, by reason of symmetry[2]. The components in an arbitrary rest-frame must be obtained by projecting $\mathbf{w}$. Since the force density is approximately proportional to $\mathbf{w}$, we can group all the other terms into the definition of a coefficient, such that

$$\mathbf{R}_s^{\uparrow} = -K_{s\ell}^{\uparrow}(\mathbf{u}_s - \mathbf{u}_t) \tag{6.42}$$

where $K_{s\ell}^{\uparrow}$ is known as the resistance coefficient:

$$K_{s\ell}^{\uparrow} = \frac{2}{3}\mu n_s n_\ell \overline{g}_{\tilde{T}} e^{-\lambda} \int_{x^*}^{\infty} dx\, x^2\, e^{-x}\, \zeta^{(1)}(\sqrt{\lambda x}) \left[\sigma_{st}^{\uparrow(0)}(x) - \sigma_{st}^{\uparrow(1)}(x)\right] \tag{6.43}$$

In the limit of weak divergence of mean fluid velocities ($\lambda \to 0$) and isotropic scattering ($\mathcal{G}(\chi) = 1/4\pi$), we have:

$$K_{s\ell}^{\uparrow} \simeq \frac{2}{3}\mu n_s n_\ell \overline{g}_{\tilde{T}} \int_{x^*}^{\infty} dx x^2 \overline{\sigma}_{s\ell}^{\uparrow}(x) e^{-x} \tag{6.44}$$

Consider now the reverse process ($u \to \ell$) and the transfer integral (6.25), the rate of change of momentum density of species s can be written as:

$$\mathbf{R}_s^{\downarrow} = -\mu n_s n_u \overline{g}_{\tilde{T}} e^{-\lambda} \int_0^{\infty} dx'\, x'\, e^{-x'}\, \overline{\sigma}_{su}^{\downarrow}(x') \cdot \frac{1}{2} \int_{-1}^{+1} dc_\theta e^{2\sqrt{\lambda x'} c_\theta} \cdot \langle \mathbf{g}' - \mathbf{g} \rangle_{\Omega'} \tag{6.45}$$

Following the same procedure described above for the excitation process, we obtain:

$$\mathbf{R}_s^{\downarrow} = -\frac{2}{3}\mu n_s n_u \mathbf{w} \overline{g}_{\tilde{T}} e^{-\lambda} \int_0^{\infty} dx'\, x'^2\, e^{-x'}\, \zeta^{(1)}(\sqrt{\lambda x'}) \left[\overline{\sigma}_{su}^{\downarrow(0)}(x') - \overline{\sigma}_{su}^{\downarrow(1)}(x')\right] \tag{6.46}$$

[2]This is obtain by integrating over the φ angular variable.

where

$$\sigma_{su}^{\downarrow(\ell)}(x') = \left(\frac{x}{x'}\right)^{\ell/2} \overline{\sigma}_{su}^{\downarrow}(x') \langle (\cos\chi)^{\ell} \rangle_{\Omega'} \tag{6.47}$$

Since $\overline{\sigma}_{s\ell}^{\uparrow}(x)$ and $\overline{\sigma}_{su}^{\downarrow}(x')$ are related by the Klein-Rosseland relation (6.27), $\sigma_{su}^{\downarrow(\ell)}(x')$ can be computed as a function of x. We can also define a resistance coefficient similar to the case of excitation:

$$K_{su}^{\downarrow} = \frac{2}{3}\mu n_s n_u \overline{g}_{\tilde{T}} e^{-\lambda} \int_0^{\infty} dx'\, x'^2\, e^{-x'}\, \zeta^{(1)}(\sqrt{\lambda x'}) \left[\sigma_{st}^{\downarrow(0)}(x') - \sigma_{st}^{\downarrow(1)}(x')\right] \tag{6.48}$$

such that

$$\mathbf{R}_s^{\downarrow} = -K_{su}^{\downarrow}(\mathbf{u}_s - \mathbf{u}_t) \tag{6.49}$$

Let us examine the ratio of the resistance coefficients for the forward and backward processes in the case of weak divergence of mean fluid velocities and isotropic scattering:

$$\frac{K_{s\ell}^{\uparrow}}{K_{su}^{\downarrow}} \simeq \left[\mathcal{B}_{\ell u}(\tilde{T})\right] \cdot \frac{\int_0^{\infty} dx' e^{-x'} x'(x'+x^*)\left[1+\frac{2}{5}\lambda(x'+x^*)\right]\overline{\sigma}_{su}^{\downarrow}(x')}{\int_0^{\infty} dx' e^{-x'} x'^2\left[1+\frac{2}{5}\lambda x'\right]\overline{\sigma}_{su}^{\downarrow}(x')} \tag{6.50}$$

Note that there is an additional contribution from high-order moment from the expansion. Therefore, there is no equivalence between the resistance coefficients of the forward and backward processes in the limit $\lambda \to 0$. Detailed balance is enforced through relation (6.27) at the microscopic level.

6.3.3 Second-order moment: total energy density

The rate of change of total energy of species s can be obtained by setting $\psi = \frac{1}{2}m_s\left(\mathbf{v}'^2_s - \mathbf{v}_s^2\right)$ into equation (6.13):

$$Q_s^{\uparrow} = \frac{4n_s n_\ell}{\pi^{\frac{1}{2}}\alpha^3} \cdot \int d^3\mathbf{V}^* f_{V^*} \cdot \int dg\, g^3\, e^{-g^2/\alpha^2}\, \overline{\sigma}_{s\ell}^{\uparrow}(g) \cdot \frac{1}{2} \int dc_\theta\, e^{2gwc_\theta/\alpha^2}\, \langle \frac{1}{2} m_s (\mathbf{v}'^2_s - \mathbf{v}_s^2) \rangle_{\Omega'} \tag{6.51}$$

Using the transformation defined in (6.7), we can obtain:

$$\frac{1}{2}m_s\left(\mathbf{v}'^2_s - \mathbf{v}_s^2\right) = \mu\left(\mathbf{g}' - \mathbf{g}\right) \cdot \left[\mathbf{V}^* + \mathbf{U} + \gamma\mathbf{w} - \gamma\mathbf{g}\right] - \frac{m_t}{m_s + m_t}\Delta\varepsilon \tag{6.52}$$

Note that equation (6.51) must include f_{V^*} since the change in total energy depends on $\mathbf{V}^*$. The integration of the first term in the bracket is zero since $\int d^3\mathbf{V}^*\,\mathbf{V}^*\,f_{V^*} = 0$. The results for the second and the third terms are simply $\mathbf{R}_s^{\uparrow}\cdot\mathbf{U}$ and $\gamma\mathbf{R}_s^{\uparrow}\cdot\mathbf{w}$, respectively. The fourth integral can be expressed in terms of normalized variables as:

$$\begin{aligned}&\gamma\mu\alpha^2 n_s n_\ell \overline{g}_{\tilde{T}} e^{-\lambda}\int_{x^*}^{\infty} dx\, x^{\frac{3}{2}}\, e^{-x}\,\overline{\sigma}_{s\ell}^{\uparrow}(x)\zeta^{(0)}(\sqrt{\lambda x})\left[\sqrt{x}-\sqrt{x'}\langle\cos\chi\rangle_{\Omega'}\right]\\ =&\gamma\mu\alpha^2 n_s n_\ell \overline{g}_{\tilde{T}} e^{-\lambda}\int_{x^*}^{\infty} dx\, x^{2}\, e^{-x}\,\zeta^{(0)}(\sqrt{\lambda x})\left[\sigma_{s\ell}^{\uparrow(0)}-\sigma_{s\ell}^{\uparrow(1)}\right]\end{aligned} \tag{6.53}$$

The integral with the last term on the RHS of equation (6.52) is simply $-\frac{m_t}{m_s+m_t}\Gamma_{s\ell}^{\uparrow}\Delta\varepsilon$. By summing all the contributions, the expression for $Q_s^{\uparrow}$ becomes:

$$\begin{aligned}Q_s^{\uparrow} = \mathbf{R}_s^{\uparrow}\cdot\mathbf{U} + \gamma\mathbf{R}_s^{\uparrow}\cdot\mathbf{w} - \frac{m_t}{m_s+m_t}\Gamma_{s\ell}^{\uparrow}\Delta\varepsilon +\\ \gamma\mu\alpha^2 n_s n_\ell \overline{g}_{\tilde{T}} e^{-\lambda}\int_{x^*}^{\infty} dx\, x^{2}\, e^{-x}\,\zeta^{(0)}(\sqrt{\lambda x})\left[\sigma_{s\ell}^{\uparrow(0)}-\sigma_{s\ell}^{\uparrow(1)}\right]\end{aligned} \tag{6.54}$$

Let us now define a thermal relaxation coefficient $K_{s\ell}^{\varepsilon\uparrow}$ as follows:

$$K_{s\ell}^{\varepsilon\uparrow} = \frac{2}{3}\mu n_s n_\ell \overline{g}_{\tilde{T}} e^{-\lambda}\int_{x^*}^{\infty} dx\, x^{2}\, e^{-x}\,\left[\zeta^{(0)}(\sqrt{\lambda x}) - \frac{2}{3}\lambda\zeta^{(1)}(\sqrt{\lambda x})\right]\left(\sigma_{s\ell}^{\uparrow(0)}-\sigma_{s\ell}^{\uparrow(1)}\right) \tag{6.55}$$

The expression for $Q_s^{\uparrow}$ reduces to:

$$Q_s^{\uparrow} = \frac{3k(T_t-T_s)}{m_s+m_t}K_{s\ell}^{\varepsilon\uparrow} + \mathbf{R}_s^{\uparrow}\cdot\mathbf{U} - \frac{m_t}{m_s+m_t}\Gamma_{s\ell}^{\uparrow}\Delta\varepsilon \tag{6.56}$$

where we have used the relation $\gamma\alpha^2 = \frac{2k(T_t-T_s)}{m_s+m_t}$. Note that due to the definition of the thermal relaxation coefficient, the contributions from the second and last terms of equation (6.54) to $Q_s^{\uparrow}$ are grouped together. It must be pointed out that the rate of change of thermal energy of species s, $H_s \equiv \frac{d\varepsilon_s}{dt}$, can always be related to $Q_s^{\uparrow}$ by the following expression:

$$H_s^{\uparrow} = Q_s^{\uparrow} - \mathbf{R}_s^{\uparrow}\cdot\mathbf{u}_s \tag{6.57}$$

The rate of change of total energy of species t can be found similarly by setting $\psi = \frac{1}{2}m_t(\mathbf{v}'^2_t - \mathbf{v}^2_t)$. Following the same procedure, we arrive at the following result:

$$Q_t^{\uparrow} = -\frac{3k(T_t - T_s)}{m_s + m_t} K_{s\ell}^{\varepsilon\uparrow} - \mathbf{R}_s^{\uparrow} \cdot \mathbf{U} - \frac{m_s}{m_s + m_t} \Gamma_{s\ell}^{\uparrow} \Delta\varepsilon \tag{6.58}$$

In the limit of $\lambda \to 0$ and isotropic scattering, the resistant and thermal relaxation coefficients reduce to:

$$K_{s\ell}^{\varepsilon\uparrow} \simeq K_{s\ell}^{\uparrow} \simeq \frac{2}{3}\mu n_s n_\ell \overline{g}_{\tilde{T}} \int_{x^*}^{\infty} dx\, x^2\, e^{-x}\, \overline{\sigma}_{s\ell}^{\uparrow}(x) \tag{6.59}$$

Let us now consider the reverse process ($u \to \ell$). Similarly, we set $\mathbf{v}'$, $\mathbf{v}$ to be the initial and final velocities, respectively. The energy transfer rate for species s becomes:

$$\begin{aligned} Q_s^{\downarrow} = \frac{4n_s n_u}{\pi^{\frac{1}{2}}\alpha^3} \cdot \int d^3\mathbf{V}'^* f_{V'^*} \cdot \int dg'\, g'^3\, e^{-g'^2/\alpha^2}\, \overline{\sigma}_{su}^{\downarrow}(g') \cdot \\ \frac{1}{2}\int dc_\theta\, e^{2g'wc_\theta/\alpha^2}\, \langle \frac{1}{2} m_s(\mathbf{v}_s^2 - \mathbf{v}'^2_s) \rangle_{\Omega'} \end{aligned} \tag{6.60}$$

One can easily show that:

$$Q_s^{\downarrow} = \frac{3k(T_t - T_s)}{m_s + m_t} K_{su}^{\varepsilon\downarrow} + \mathbf{R}_s^{\downarrow} \cdot \mathbf{U} + \frac{m_t}{m_s + m_t} \Gamma_{su}^{\downarrow} \Delta\varepsilon \tag{6.61}$$

$$Q_t^{\downarrow} = -\frac{3k(T_t - T_s)}{m_s + m_t} K_{su}^{\varepsilon\downarrow} - \mathbf{R}_s^{\downarrow} \cdot \mathbf{U} + \frac{m_s}{m_s + m_t} \Gamma_{su}^{\downarrow} \Delta\varepsilon \tag{6.62}$$

where

$$K_{s\ell}^{\varepsilon\downarrow} = \frac{2}{3}\mu n_s n_u \overline{g}_{\tilde{T}} e^{-\lambda} \int_0^{\infty} dx'\, x'^2\, e^{-x'} \left[\zeta^{(0)}(\sqrt{\lambda x'}) - \frac{2}{3}\lambda\zeta^{(1)}(\sqrt{\lambda x'})\right] \left(\sigma_{su}^{\downarrow(0)} - \sigma_{su}^{\downarrow(1)}\right) \tag{6.63}$$

6.4 Summary of results

All exchange terms the number density, momentum and total energy due to an excitation and deexcitation collisions of type (6.19) can be summarized as follows:

$$\frac{dn_s}{dt} = 0 \tag{6.64}$$

$$\frac{dn_\ell}{dt} = -\Gamma^{\uparrow}_{s\ell} + \Gamma^{\downarrow}_{su} \tag{6.65}$$

$$\frac{dn_u}{dt} = +\Gamma^{\uparrow}_{s\ell} - \Gamma^{\downarrow}_{su} \tag{6.66}$$

$$\frac{d(\rho_s \mathbf{u}_s)}{dt} = K^{\uparrow}_{s\ell}(\mathbf{u}_t - \mathbf{u}_s) + K^{\downarrow}_{su}(\mathbf{u}_t - \mathbf{u}_s) \tag{6.67}$$

$$\frac{d(\rho_t \mathbf{u}_t)}{dt} = -K^{\uparrow}_{s\ell}(\mathbf{u}_t - \mathbf{u}_s) - K^{\downarrow}_{su}(\mathbf{u}_t - \mathbf{u}_s) \tag{6.68}$$

$$\begin{aligned}\frac{dE_s}{dt} &= K^{\uparrow}_{s\ell}(\mathbf{u}_t - \mathbf{u}_s)\cdot\mathbf{U} + \frac{3k(T_t - T_s)}{m_s + m_t}K^{\varepsilon\uparrow}_{s\ell} - \frac{m_t}{m_s + m_t}\Gamma^{\uparrow}_{s\ell}\Delta\varepsilon \\ &\quad + K^{\downarrow}_{su}(\mathbf{u}_t - \mathbf{u}_s)\cdot\mathbf{U} + \frac{3k(T_t - T_s)}{m_s + m_t}K^{\varepsilon\downarrow}_{su} + \frac{m_t}{m_s + m_t}\Gamma^{\downarrow}_{su}\Delta\varepsilon\end{aligned} \tag{6.69}$$

$$\begin{aligned}\frac{dE_t}{dt} &= -K^{\uparrow}_{s\ell}(\mathbf{u}_t - \mathbf{u}_s)\cdot\mathbf{U} - \frac{3k(T_t - T_s)}{m_s + m_t}K^{\varepsilon\uparrow}_{s\ell} - \frac{m_s}{m_s + m_t}\Gamma^{\uparrow}_{s\ell}\Delta\varepsilon \\ &\quad - K^{\downarrow}_{su}(\mathbf{u}_t - \mathbf{u}_s)\cdot\mathbf{U} - \frac{3k(T_t - T_s)}{m_s + m_t}K^{\varepsilon\downarrow}_{su} + \frac{m_s}{m_s + m_t}\Gamma^{\downarrow}_{su}\Delta\varepsilon\end{aligned} \tag{6.70}$$

For the purpose of numerical calculation, one can precompute and tabulate all the reaction rate and resistance coefficients[3] as a function of two parameters $\tilde{T}$ and λ. It must be pointed out that the coefficients for the forward and the backward processes must be tabulated separately, since there is no correspondence between the two. The principle of detailed balance is enforced at the microscopic level.

[3]Note that all the product of number densities, e.g., $n_s n_t$, can be factored out.

CHAPTER 7

Simulations of Laser-Plasma Interactions

7.1 Introduction

Laser-plasma interactions (LPI) present a physically rich research topic with a wide range of applications. The dynamics of the interactions can span several physical regimes, and encompasses a great deal of physical phenomena, e.g., plasma instabilities, resonant absorption, X-ray generation, multi-phase ablation, particle acceleration [41, 38, 124, 125]. Due to the highly transient nature of the interaction, computational models for LPI are often designed to work only on a specific physical domain. For example, in ultra-short and ultra-high intensity LPI, the laser absorption occurs at very fast time scales requiring a kinetic treatment, i.e., PIC or Vlasov solver. On the contrary, once the plasma is formed and thermalized, the expansion of the plasma bulk[1] mostly occur at the hydrodynamic time scales and is often modeled by fluid codes.

In this chapter, a computational model for LPI is introduced based on the multi-fluid description of a plasma described in section 2.2. The multi-fluid model has several advantages over the traditional single-fluid model, often used in inertial fusion calculation [40]. The first advantage is that it permits a self-consistent coupling of the plasma with the electromagnetic field, which is relevant in the study of laser-induced electric and magnetic fields and their effects on hydrodynamic instabilities and charged particle acceleration [38]. The second advantage

[1] with the exception of superthermal or relativistic electrons.

of the multi-fluid model is that it can be used to hybridize with a kinetic method. For instance, in the fast ignition concept proposed by Tabak *et al.* [126], the fuel is first compressed by a low intensity laser, and then quickly ignited with a petawatt laser. The incidence of the petawatt laser creates a channel into the compressed core from which the superthermal electron beam generated from the interaction of the laser can penetrate deep into the capsule and heat the compressed fuel. In this scenario, the electrons can be decomposed into two populations: cold and hot (superthermal) electrons. The interaction of the cold electrons with the ions can be described by a multi-fluid model, and the hot electrons can be treated by a kinetic method.

7.2 Electromagnetic wave propagation in plasmas

7.2.1 Electrodynamic equations

The physics of electromagnetic wave propagating in a plasma is first reviewed, leading to the physical model for the laser and corresponding exchange terms with the plasma. Let us now consider Maxwell's equations, which governs the evolution of the electric and magnetic field in a plasma [127, 128]:

$$\nabla \times \mathbf{E} = -\partial_t \mathbf{B} \tag{7.1}$$

$$\epsilon_0 c^2 \nabla \times \mathbf{B} = \mathbf{j} + \epsilon_0 \partial_t \mathbf{E} \tag{7.2}$$

The plasma current, $\mathbf{j}$, appearing on the RHS of equation (7.2) describes the plasma response and its modification to the electromagnetic wave. By taking the curl of (7.1) and utilizing the relation $\nabla \times \nabla \times \mathbf{A} = \nabla(\nabla \cdot \mathbf{A}) - \nabla^2 \mathbf{A}$, we get:

$$\partial_{tt}\mathbf{E} - c^2 \nabla^2 \mathbf{E} + c^2 \nabla(\nabla \cdot \mathbf{E}) + \frac{1}{\epsilon_0} \partial_t \mathbf{j} = 0 \tag{7.3}$$

Equation (7.3) is the wave equation governing the evolution of the electric field in the plasma. Similarly, by taking the curl of (7.2), we obtain the wave equation

governing the evolution of the magnetic field:

$$\partial_{tt}\mathbf{B} - c^2\nabla^2\mathbf{B} - \frac{1}{\epsilon_0}\nabla\times\mathbf{j} = 0 \tag{7.4}$$

For a high frequency oscillation of the electromagnetic field, the plasma current can be modeled by Ohm's law, i.e., equation (2.25). Here we only include the resistive term, so Ohm's law can be written as:

$$\partial_t\mathbf{j} + \nu\mathbf{j} = \epsilon_0\omega_p^2\mathbf{E} \tag{7.5}$$

where ν is the plasma collision frequency. Let us now consider a monochromatic oscillation with radian frequency ω for the quantities $\mathbf{E}$, $\mathbf{B}$ and $\mathbf{j}$:

$$\mathbf{E}(\mathbf{x},t) = \hat{\mathbf{E}}(\mathbf{x})e^{-i\omega t} + c.c. \tag{7.6}$$

$$\mathbf{B}(\mathbf{x},t) = \hat{\mathbf{B}}(\mathbf{x})e^{-i\omega t} + c.c. \tag{7.7}$$

$$\mathbf{j}(\mathbf{x},t) = \hat{\mathbf{j}}(\mathbf{x})e^{-i\omega t} + c.c. \tag{7.8}$$

Ohm's law immediately yields:

$$\hat{\mathbf{j}} = \sigma\hat{\mathbf{E}} \tag{7.9}$$

$$\sigma = \frac{i\epsilon_0\omega_p^2}{\omega(1+i\nu/\omega)} \tag{7.10}$$

where σ is the complex conductivity of the plasma. Substituting (7.9) into the wave equation for the electric field (7.3), we obtain:

$$\nabla^2\hat{\mathbf{E}} + k_0^2\varepsilon\hat{\mathbf{E}} - \nabla(\nabla\cdot\hat{\mathbf{E}}) = 0 \tag{7.11}$$

where $k_0 = \omega/c$ and ε is the dielectric function of the plasma:

$$\varepsilon = \eta^2 = 1 - \frac{\omega_p^2}{\omega^2(1+i\nu/\omega)} \tag{7.12}$$

and η is the refractive index. Similarly for the magnetic field $\mathbf{B}$, equation (7.4) becomes:

$$\nabla^2\hat{\mathbf{B}} + k_0^2\varepsilon\hat{\mathbf{B}} + \nabla(\ln\varepsilon)\times\left(\nabla\times\hat{\mathbf{B}}\right) = 0 \tag{7.13}$$

Equations (7.11) and (7.13) are the governing equations for a monochromatic wave propagating in a plasma. In practice, one only needs to solve for either $\hat{\mathbf{E}}$ or $\hat{\mathbf{B}}$; the remaining quantity can be determined from Faraday's or Ampere's law:

$$i\omega\hat{\mathbf{B}} = \nabla \times \hat{\mathbf{E}} \tag{7.14}$$

$$c\nabla \times \hat{\mathbf{B}} = -ik_0\varepsilon\hat{\mathbf{E}} \tag{7.15}$$

Note that here we assume that the refractive index is time independent. This is certainly a good approximation for long interaction times of laser-plasma system characterized by fluid equations ($\omega/k \gg v_T$)[2]. For short interaction times, a kinetic description must be utilized, and the time dependent solution of the electromagnetic fields must be solved.

For a homogeneous medium with no charge separation, the wave equations for both $\hat{\mathbf{E}}$ and $\hat{\mathbf{B}}$ become identical, since $\nabla \cdot \hat{\mathbf{E}} = 0$ and $\nabla \ln \varepsilon = 0$. For simplicity, let us consider a simple case of a linearly polarized electromagnetic wave normally incident onto a homogeneous plasma medium. Let us define x to be the propagating direction and y and z are the directions of the oscillating electric and magnetic fields, respectively (see figure 7.1). The solution the wave equations can be written as:

$$\mathbf{E}(x,t) = \hat{\mathbf{e}}_y E_0 e^{i(kx-\omega t)} \tag{7.16}$$

$$\mathbf{B}(x,t) = \hat{\mathbf{e}}_z B_0 e^{i(kx-\omega t)} \tag{7.17}$$

where E_0 and B_0 are determined from boundary conditions, and the wave number k is given from the dispersion relation:

$$k^2 = k_0^2\left(1 - \frac{\omega_p^2}{\omega^2(1+i\nu/\omega)}\right) \tag{7.18}$$

It is interesting to note that in the absence of collision, i.e., $\nu = 0$, k is imaginary for $\omega < \omega_p$. In this case, the wave is evanescent with a skin depth of $\delta \approx \frac{c}{\omega_p}$. This indicates that the laser cannot propagate past the critical surface, i.e., $\omega = \omega_p$.

[2]We also assume that $\frac{\omega}{k} \gg \nu_{\text{ion}} \sim \frac{1}{n_e}\frac{dn_e}{dt}$ such that no ionization occurs during the interaction.

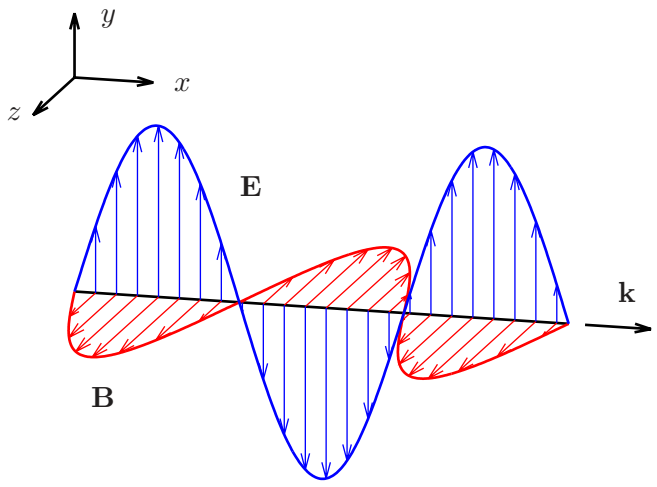

Figure 7.1: Coordinate system of a one dimensional electromagnetic wave propagation where x is the direction of propagation: $\mathbf{E} = E(x)\hat{\mathbf{e}}_y$, $\mathbf{B} = B(x)\hat{\mathbf{e}}_z$, and $\mathbf{k} = k\hat{\mathbf{e}}_x$.

7.2.2 WKB approximation

In this section, the Wentzel-Kramers-Brillouin (WKB) approximation for solving the wave equations is described. Let us now consider a one dimensional propagation of a monochromatic wave in an inhomogeneous medium. Using the same coordinate system as defined previously (see figure 7.1), the electric and magnetic fields can be written as:

$$\mathbf{E} = \hat{\mathbf{e}}_y \left[\hat{E}(x) e^{-i\omega t} + c.c. \right] \tag{7.19}$$

$$\mathbf{B} = \hat{\mathbf{e}}_z \left[\hat{B}(x) e^{-i\omega t} + c.c. \right] \tag{7.20}$$

The wave equations for the electric and magnetic fields, equation (7.11) and (7.13), reduce to second order ODEs:

$$\partial_{xx}\hat{E} + k_0^2 \varepsilon(x) \hat{E} = 0 \tag{7.21}$$

$$\partial_{xx}\hat{B} + k_0^2 \varepsilon(x) \hat{B} = 0 \tag{7.22}$$

where the dielectric function ε is defined in equation (7.12). The WKB approximation looks for a solution of the form:

$$\hat{E} = \hat{E}_0(x) e^{ik_0 \int_x \psi(\zeta) d\zeta} \tag{7.23}$$

For simplicity, we assume that there is no collision, hence ψ is real. If we substitute expression (7.23) to equation (7.21) and to the lowest and first order, we obtain the following:

$$\psi = \sqrt{\varepsilon} = \eta \tag{7.24}$$

$$\hat{E}_0(x) = \frac{E_V}{\eta^{1/2}} \tag{7.25}$$

where E_V is the electric field in free space.

$$E_V = \sqrt{\frac{2I}{\epsilon_0 c}} \tag{7.26}$$

The validation of the WKB approximation requires a smooth variation of the plasma density or the refractive index. This assumption breaks down in the region near the critical density where $\varepsilon \to 0$. Mathematically, the following relations needs to be satisfied for the WKB approximation to be valid [129]:

$$\frac{\sqrt{3}}{2}\frac{|\partial_x \eta|}{k_0|\eta|^2} \ll 1 \tag{7.27}$$

$$\frac{1}{2}\frac{|\partial_{xx} \eta|}{k_0^2|\eta|^3} \ll 1 \tag{7.28}$$

The WKB solution for the electric field reads:

$$\hat{E}(x) = \frac{E_V}{\eta^{1/2}} e^{ik_0 \int_x \eta d\zeta} \tag{7.29}$$

The solution for the magnetic field can be determined from Faraday's law:

$$\hat{B}(x) = \frac{1}{c}\eta^{1/2} E_V e^{ik_0 \int_x \eta d\zeta} + \frac{i}{2k_0 c}\frac{E_V}{\eta^{3/2}}\partial_x \eta e^{ik_0 \int_x \eta d\zeta} \tag{7.30}$$

One can see that the amplitude of the electric and magnetic fields can undergo increase or swelling when propagating in a medium with a spatially varying refractive index. The second term in (7.30) is referred to as a phase term [130]; this term is essential in the generation of non-linear forces, which will be described later in this chapter. In addition, we have not discussed collisional absorption yet, but one can see that since η can be complex, its imaginary component is related to the absorption of the electromagnetic energy.

7.2.3 Collisional absorption

When collision is included, the wave can be collisionally damped as it passes through the medium. Considering an electromagnetic wave propagating through a homogeneous medium and utilizing the WKB solution of the electric field, i.e., equations (7.29) and (7.30), one can compute the intensity of the wave as follows

[125]:

$$\begin{aligned} I(x) &= \epsilon_0 c^2 |\langle \mathbf{E} \times \mathbf{B} \rangle| \\ &= \frac{1}{2} \epsilon_0 c E_V^2 e^{-2k_0 \int_x \eta_I d\zeta} \\ &= I(x_0) e^{-\int_{x_0}^{x} \kappa d\zeta} \end{aligned} \tag{7.31}$$

where $I(x_0)$ is the intensity of the incident wave, $\langle \bullet \rangle$ denotes a time-average operator, and η_I is the imaginary part of the refractive index, i.e., $\eta = \eta_R + i\eta_I$. Equation (7.31) is a form of Beer's law [125]. The spatial damping rate κ, also known as the absorption coefficient, is related to the plasma refractive index as follows:

$$\kappa = 2k_0 \eta_I \tag{7.32}$$

Using the dielectric function as defined in equation (7.12), the real and the imaginary parts of the refractive index for a plasma read:

$$\eta_R = \frac{1}{\sqrt{2}} \left[\sqrt{\left(1 - \frac{\omega_p^2}{\omega^2 + \nu^2}\right)^2 + \left(\frac{\nu}{\omega} \frac{\omega_p^2}{\omega^2 + \nu^2}\right)^2} + \left(1 - \frac{\omega_p^2}{\omega^2 + \nu^2}\right) \right]^{1/2} \tag{7.33}$$

$$\eta_I = \frac{1}{\sqrt{2}} \left[\sqrt{\left(1 - \frac{\omega_p^2}{\omega^2 + \nu^2}\right)^2 + \left(\frac{\nu}{\omega} \frac{\omega_p^2}{\omega^2 + \nu^2}\right)^2} - \left(1 - \frac{\omega_p^2}{\omega^2 + \nu^2}\right) \right]^{1/2} \tag{7.34}$$

For $\nu/\omega \ll 1$, one can do a series expansion and obtain an expression for the absorption constant:

$$\kappa = \frac{\nu}{c} \frac{\omega_p^2}{\omega^2} \left(1 - \frac{\omega_p^2}{\omega^2}\right)^{-1/2} \tag{7.35}$$

It must be noted that the absorption constant as described in equation (7.35) depends only on the plasma properties. In the so-called linear regime ($I \lesssim 10^{15}$ W/cm^2), this is certainly a good approximation. However, if the laser intensity is high enough that the oscillation energy exceeds the electron thermal energy, i.e., the quivering motion of the electrons is comparable to or larger than their

thermal motion, the absorption becomes dependent on the laser and one has to add correction to the collision frequency and the absorption constant. This is typically referred to as non-linear collisional absorption [130]; the treatment of non-linear absorption in hydrodynamic codes will be described later in this chapter. If the laser intensity is much higher, relativistic particle beam can be generated; all the relativistic effects are neglected in the current framework.

In the general case, laser absorption can be computed directly from the conservation of electromagnetic energy, which is expressed by the Poynting theorem:

$$\frac{1}{2}\epsilon_0 \partial_t \left(\mathbf{E} \cdot \mathbf{E} + c^2 \mathbf{B} \cdot \mathbf{B} \right) + \nabla \cdot \mathbf{S} = -\mathbf{j} \cdot \mathbf{E} \tag{7.36}$$

where $\mathbf{S} = \frac{1}{\mu_0} \mathbf{E} \times \mathbf{B}$ is the Poynting vector. Since transient effects of the electromagnetic fields are neglected, the first term in equation (7.36) is negligible. The heating rate due to laser absorption, denoted by W_L, is obtained by time averaging the Joule heating term, i.e., the work done on the plasma by the electromagnetic wave:

$$W_L = \langle \mathbf{j} \cdot \mathbf{E} \rangle = -\nabla \cdot \langle \mathbf{S} \rangle \tag{7.37}$$

where $\mathbf{E}$ and $\mathbf{B}$ are obtained from the wave equations.

7.2.4 Ponderomotive forces

When a high-frequency electromagnetic wave propagates through a plasma, it induces a slow time scale pressure force on the plasma as a result of conservation of momentum. This force is known as the ponderomotive force or light pressure, which plays an important roles in many physical phenomena occurring in laser produced plasma, such as momentum transfer, density modification, magnetic field generation, and parametric instabilities [38].

The derivation of the ponderomotive force, sometimes referred to as the non-linear force[3] in the general case can get complicated. The most general expression

[3]The terms non-linear and pondermotive forces are often used interchangeably in the lit-

found in literature for the non-linear force caused by a transient monochromatic radiation in a plasma is as follows:

$$\mathbf{f}_{nl} = \mathbf{j} \times \mathbf{B} + \epsilon_0 \mathbf{E} \nabla \cdot \mathbf{E} + \epsilon_0 \left(1 + \omega^{-1} \partial_t\right) \nabla \cdot (\eta^2 - 1) \mathbf{E}\mathbf{E} \tag{7.38}$$

The complete derivation of equation (7.38) is given in appendix C of Hora [129], Zeidler *et al.* [131] and Hora [132]. The non-linear force in equation (7.38) can be rewritten in terms of the electromagnetic energy tensor. Conservation of momentum of the electromagnetic field gives:

$$\partial_t \mathbf{S} + \nabla \cdot \mathbb{T} = -\epsilon_0 \mathbf{E} \nabla \cdot \mathbf{E} - \mathbf{j} \times \mathbf{B} \tag{7.39}$$

where $\mathbb{T}$ is the Maxwell tensor, written in index notation as follows:

$$\mathbb{T}_{ij} = -\epsilon_0 E_i E_j - \frac{1}{\mu_0} B_i B_j + \frac{1}{2} \delta_{ij} \left(\epsilon_0 E^2 + \frac{1}{\mu_0} B^2 \right) \tag{7.40}$$

Utilizing equations (7.38) and (7.39), we obtained the following expression for the non-linear force:

$$\mathbf{f}_{nl} = -\nabla \cdot \left[\mathbb{T} - \epsilon_0 \left(1 + \omega^{-1} \partial_t\right) \left(\eta^2 - 1\right) \mathbf{E}\mathbf{E} \right] - \frac{1}{c^2} \partial_t \mathbf{S} \tag{7.41}$$

The slow time-scale ponderomotive force is obtained by time averaging the non-linear force $\mathbf{f}_{nl}$ over many oscillation cycles. In the current work, transient effects are neglected, so the expression for the ponderomotive force reduces to:

$$\mathbf{f}_p = \langle \mathbf{f}_{nl} \rangle = -\nabla \cdot \left[\langle \mathbb{T} \rangle - \epsilon_0 \left(\eta^2 - 1\right) \langle \mathbf{E}\mathbf{E} \rangle \right] \tag{7.42}$$

For a one-dimensional perpendicular incidence along x direction (see figure 7.1), the expression for the ponderomotive force is simplified to:

$$\begin{aligned} \mathbf{f}_p &= -\frac{\epsilon_0}{4} \partial_x \left(\hat{\mathbf{E}} \hat{\mathbf{E}}^\star + \frac{1}{c^2} \hat{\mathbf{B}} \hat{\mathbf{B}}^\star \right) \\ &= -\frac{\epsilon_0}{4} \partial_x \left(\hat{\mathbf{E}} \hat{\mathbf{E}}^\star + \frac{1}{k_0^2} \partial_x \hat{\mathbf{E}} \partial_x \hat{\mathbf{E}}^\star \right) \\ &= -\frac{\epsilon_0 \omega_p^2}{4\omega^2} \partial_x \left(\hat{\mathbf{E}} \hat{\mathbf{E}}^\star \right) \end{aligned} \tag{7.43}$$

erature to indicate the radiation pressure force. Here we use the term pondermotive force to indicate the slow time scale force, appearing on the hydrodynamic equations; the ponderomotive dorce is obtained simply by time averaging the non-linear force, i.e., $\mathbf{f}_p = \langle \mathbf{f}_{nl} \rangle$.

The last step is performed with the help of the wave equation (7.21). Although less general, equation (7.42) is commonly used to express the ponderomotive force [38]. An alternative derivation of the ponderomotive force, by considering a single particle motion, is given in appendix E, the result of which, leads to the same expression as (7.42). If the WKB approximation, i.e., equation (7.23) is used, the ponderomotive force can be simplified much further [129]:

$$\mathbf{f}_p = \hat{\mathbf{e}}_x \frac{\epsilon_0 E_V^2}{2\eta^2} \frac{\omega_p^2}{\omega^2} \partial_x \eta \tag{7.44}$$

where E_V is the electric field in vacuum, given by equation (7.26). As will be shown later, the solution of the ponderomotive force using WKB equations can develop a singularity near the critical layer, and do not take in account local reflection of the wave. The latter is responsible for the density modification due to ponderomotive bunching.

7.3 Multi-fluid model for laser plasma interactions

In this section, a self-consistent hydrodynamic model is introduced for simulations of laser plasma interactions. This model is based on the multi-fluid equations described in section 2.2 with additional coupling terms due to the interaction with the laser. In high intensity laser plasma interaction, the strong coupling with the laser can drive the electrons out of equilibrium with the ions, which gives rise to charge separation, sheath formation, magnetic field generation, etc. Furthermore, the electrons themselves can possibly be non-Maxwellian, in which the VDF must be resolved. A kinetic treatment of the electrons is beyond the scope of the current study. Here we assumed that the electron VDF is close to a Maxwellian distribution such that it can be characterized by fluid equations.

Considering a fully ionized plasma and assuming that inelastic collisions are

negligible, the continuity equations for the electrons (e) and ions (i) read:

$$\partial_t \rho_e + \nabla \cdot (\rho_e \mathbf{u}_e) = 0 \tag{7.45}$$

$$\partial_t \rho_i + \nabla \cdot (\rho_i \mathbf{u}_i) = 0 \tag{7.46}$$

In the multi-fluid model, the momentum of ions and electrons are conserved separately, leading to different averaged velocity for each species, and thus allowing charge separation. In the current work, we neglect the effect of the magnetic field and only consider electrostatic fields; the resultant equations are referred to as the Euler-Poisson system. When the magnetic field is included, the full Maxwell's equations need to be solved self-consistently.

The momentum equations for the ions and electrons are as follows:

$$\partial_t(\rho_e \mathbf{u}_e) + \nabla \cdot (\rho_e \mathbf{u}_e \mathbf{u}_e + p_e \mathbb{I}) = -e n_e \mathbf{E} + \rho_e \nu_{ei} \mathbf{w}_{ei} + \mathbf{f}_p \tag{7.47}$$

$$\partial_t(\rho_i \mathbf{u}_i) + \nabla \cdot (\rho_i \mathbf{u}_i \mathbf{u}_i + p_i \mathbb{I}) = Z_i e n_i \mathbf{E} - \rho_e \nu_{ei} \mathbf{w}_{ei} \tag{7.48}$$

where $\mathbf{w}_{ei} = \mathbf{u}_i - \mathbf{u}_e$ is the mean drift velocity, ν_{ei} is the Coulomb collision frequency between ions and electrons, and $\mathbb{I}$ is an identity tensor. The first terms on the RHS of equations (7.47) and (7.48) correspond to the Coulomb force and the second terms correspond to the momentum relaxation term [46]. One can check that momentum conservation are satisfied. The third term, which only acts on the electron fluid, is due to the ponderomotive force, discussed in section 7.2.4. The ponderomotive force $\mathbf{f}_p$ in the general case can be expressed by equation (7.42); for one dimensional problems studied here, we use the expression given by (7.43). For the ions, this force scales as m_e/m_i and can be neglected.

The collision frequency for Coulomb interaction is:

$$\nu_{ei} = \frac{4}{3}(2\pi)^{1/2} \left(\frac{Ze^2}{4\pi\epsilon_0 m_e} \right)^2 \left(\frac{m}{kT_e} \right)^{3/2} n_i \ln \Lambda \tag{7.49}$$

where $\Lambda = \lambda_D / b_{\min}$ and $b_{\min}$ is the minimum impact parameter. In addition to collisional friction, the collision frequency ν_{ei} is also used to describe the dielectric

function of the medium. As pointed out earlier in this chapter, for high intensity lasers ($I > 10^{15}$ W/cm^{-2}), the electron quiver velocity is comparable to the thermal velocity, so the absorption process becomes dependent of the laser intensity (non-linear absorption). In hydrodynamic codes, this effect is taken into account by introducing an effective collision frequency $\nu^{\star}_{ei}$ [129]:

$$\nu^{\star}_{ei} \approx \nu_{ei} \frac{(kT_e)^{3/2}}{(kT_e + \mathcal{E})^{3/2}} \tag{7.50}$$

and $\mathcal{E} = I/cn_{cr}$ is the oscillation energy of the electrons due to the laser.

The conservation equations for the thermal energy of each species, denoted as ε_s, can we written as:

$$\begin{aligned} \partial_t \varepsilon_e + \nabla \cdot (\varepsilon_e \mathbf{u}_e) + p_e \nabla \cdot \mathbf{u}_e = &- \nabla \cdot \mathbf{q}_e + 3\tilde{m}_e n_e \nu_{ei} k (T_i - T_e) \\ &+ \tilde{m}_i \rho_e \nu_{ei} \mathbf{w}_{ei} \cdot \mathbf{w}_{ei} + W_L \end{aligned} \tag{7.51}$$

$$\begin{aligned} \partial_t \varepsilon_i + \nabla \cdot (\varepsilon_i \mathbf{u}_i) + p_i \nabla \cdot \mathbf{u}_i = &- 3\tilde{m}_e n_e \nu_{ei} k (T_i - T_e) \\ &+ \tilde{m}_e \rho_e \nu_{ei} \mathbf{w}_{ei} \cdot \mathbf{w}_{ei} \end{aligned} \tag{7.52}$$

where $\tilde{m}_s = \frac{m_s}{m_e + m_i}$. Here we include electron thermal conduction, which is the main heat transport mechanism in LPI. It must be pointed out that the thermal energy exchange process, i.e., RHS of equations (7.51) and (7.52), is due to both thermal relaxation effects (temperature difference) and frictional heating (velocity difference). The frictional heating term scales as $|\mathbf{w}_{ei}|/v_{Te}$, and can be neglected in the limit of small relative drift velocity. Laser absorption is taken into account by the heating term W_L, which represents the energy transfer from the laser to the plasma. W_L can be computed directly from the Poynting theorem via equation (7.37).

The thermal energy equations (7.51) and (7.52) can be combined with the momentum equations (7.47) and (7.48) to yield the conservation equations for the total energy of each species:

$$\begin{aligned} \partial_t E_e + \nabla \cdot [(E_e + p_e)\mathbf{u}_e] = &- \nabla \cdot \mathbf{q}_e + \mathbf{j}_e \cdot \mathbf{E} + \rho_e \nu_{ei} \mathbf{w}_{ei} \cdot \overline{\mathbf{u}}_{ei} \\ &+ 3 n_e \nu_{ei} k (T_i - T_e) + \mathbf{f}_p \cdot \mathbf{u}_e + W_L \end{aligned} \tag{7.53}$$

$$\partial_t E_i + \nabla \cdot [(E_i + p_i)\mathbf{u}_i] = \mathbf{j}_i \cdot \mathbf{E} - \rho_e \nu_{ei} \mathbf{w}_{ei} \cdot \overline{\mathbf{u}}_{ei} - 3 n_e \nu_{ei} k (T_i - T_e) \tag{7.54}$$

where

$$\mathbf{j}_s = Z_s e n_s \mathbf{u}_s \tag{7.55}$$

$$E_s = \varepsilon_s + \frac{1}{2} \rho_s \mathbf{u}_s \cdot \mathbf{u}_s \tag{7.56}$$

$$\overline{\mathbf{u}}_{ei} = \frac{m_i \mathbf{u}_i + m_e \mathbf{u}_e}{m_i + m_e} \tag{7.57}$$

To close the system, an ideal gas equation of state is used, i.e., $p_s = n_s k T_s$ and $\varepsilon_s = p_s/(\gamma_s - 1)$. One can easily check that energy conservation is satisfied for the collision terms; this is only possible with the inclusion of the frictional heating terms in equations (7.51) and (7.52). The electrostatic field $\mathbf{E}$ is determined from Gauss's law[4]:

$$\nabla \cdot \mathbf{E} = \frac{e}{\epsilon_0} (Z_i n_i - n_e) \tag{7.58}$$

It is often convenient to express the electric field in terms of the electrostatic potential, i.e., $\mathbf{E} = -\nabla \phi$, which leads to the Poisson equation:

$$\nabla^2 \phi = -\frac{e}{\epsilon_0} (Z_i n_i - n_e) \tag{7.59}$$

The electron heat flux takes the classical form of Spitzer-Harm (SH) [54]:

$$\mathbf{q}_{SH} = -\kappa_e \nabla T_e \tag{7.60}$$

where κ_e is the electron thermal conductivity:

$$\kappa_e = \frac{\gamma_Z n_e k^2 T_e}{m_e \nu_{ei}} \tag{7.61}$$

$$\gamma_Z \approx \frac{3.22554 (Z_i + 0.24)}{1 + 0.24 Z_i} \tag{7.62}$$

It must be noted that since $\nu_{ei} \sim T_e^{-3/2}$, $\kappa_e \sim T_e^{5/2}$. SH formula is valid for $\lambda_{ei} \ll T_e/|\nabla T_e|$ where λ_{ei} is the collisional mean free path between ions and

[4]This is the low frequency field induced by the plasma, which is different from the electric field of the laser.

electrons. Beyond this limit, non-local effects in heat transport becomes important, requiring a kinetic treatment. In most hydrodynamic codes, the heat flux from SH theory is limited such that it can never exceed the free-stream limit, $q_{FS} = \left(\frac{2}{\pi}\right)^{1/2} kT_e v_{Te}$, where v_{Te} is the thermal velocity of the electrons. The same approach was employed here, leading to the following modification for the heat flux:

$$\mathbf{q}_e = \min(f\frac{q_{FS}}{|\mathbf{q}_{SH}|}\mathbf{q}_{SH}, \mathbf{q}_{SH}) \tag{7.63}$$

where f is a flux limit value. Here we set $f = 0.15$.

7.4 Numerical solutions of the wave equations

7.4.1 Finite difference method

In this section, the numerical methods for solving the wave equations (7.21) and (7.22) for $\hat{\mathbf{E}}$ and $\hat{\mathbf{B}}$ are briefly described. Instead of solving both equations, it is more convenient to solve for $\hat{\mathbf{E}}$ from equation (7.21), and $\hat{\mathbf{B}}$ can be determined from Faraday's law. Equation (7.21) can be solved easily by a finite difference (FD) discretization; detail of such a discretization can be found in LeVeque[133] and will not be repeated here.

One can see that the general solution of equation (7.21) is of the form:

$$\hat{E}(x) = E_+ e^{ikx} + E_- e^{-ikx} \tag{7.64}$$

where the first term represents the wave coming from the left and the second term is due to the wave coming from the right. For a problem with laser incidence from the left, the boundary conditions are defined as follows:

$$E_+(x = 0) = E_V \tag{7.65}$$

$$E_-(x = L) = 0 \tag{7.66}$$

where E_V given by equation (7.26). Note that here we assume that the phase of the incident wave is zero at $x = 0$, and there is no light coming in from $x = L$. The two conditions on E_+ and E_- lead to two mixed boundary conditions (Neumann and Dirichlet) on the two sides of the domain. The discretized version of the wave equation is a tridiagonal system of equations, which can be solved easily by the Thomas algorithm.

7.4.2 Transfer-matrix method

The second approach of solving the wave equations is the transfer-matrix method (TMM) [134, 135]. Instead of solving the second order wave equation, we look for the solution of a system of two first order ODEs:

$$\partial_x \hat{E} = i\omega \hat{B} \tag{7.67}$$

$$c\partial_x \hat{B} = ik_0 \eta^2 \hat{E} \tag{7.68}$$

One can rewrite the system above into the form:

$$\frac{dU}{dx} = i\frac{\beta}{p} V \tag{7.69}$$

$$\frac{dV}{dx} = ip\beta U \tag{7.70}$$

where $p = \eta$, $\beta = \frac{\omega p}{c}$, $U \equiv \hat{E}$ and $V \equiv c\hat{B}$. The solution for the equation above in the region where η^2 is uniform reads:

$$U = E_+ e^{i\beta x} + E_- e^{-i\beta x} \tag{7.71}$$

$$V = p(E_+ e^{i\beta x} + E_- e^{-i\beta x}) \tag{7.72}$$

where $E_\pm = \frac{1}{2}(U \pm V/p)$. Assuming an uniform value of the complex refractive index within a computational cell, the field values at two faces next to each other can be related by the following analytical expression:

$$\begin{bmatrix} U_{j-1/2} \\ V_{j-1/2} \end{bmatrix} = \begin{bmatrix} \cos(\beta_j \Delta x) & -\frac{i}{p_j}\sin(\beta_j \Delta x) \\ -ip_j \sin(\beta_j \Delta x) & \cos(\beta_j \Delta x) \end{bmatrix} \begin{bmatrix} U_{j+1/2} \\ V_{j+1/2} \end{bmatrix} \tag{7.73}$$

Taking of the product of all the matrices for all the cells, one obtains a relation for the first and last faces:

$$\begin{bmatrix} U_{-1/2} \\ V_{-1/2} \end{bmatrix} = \begin{bmatrix} m_{11} & m_{12} \\ m_{21} & m_{22} \end{bmatrix} \begin{bmatrix} U_{N+1/2} \\ V_{N+1/2} \end{bmatrix} \tag{7.74}$$

Assuming the phase of the incident electric field is zero and there is no light incident from the right, the boundary conditions at the laser incident side (left) read:

$$E_{+,-1/2} = E_V = \frac{1}{2}(U_{-1/2} + V_{-1/2}) \tag{7.75}$$

$$E_{-,N+1/2} = 0 = \frac{1}{2}(U_{N+1/2} - V_{N+1/2}) \tag{7.76}$$

Utilizing equations (7.74), (7.75) and (7.76), we obtain the following relations:

$$U_{N+1/2} = \frac{2E_V}{m_{11} + m_{12} + m_{21} + m_{22}} \tag{7.77}$$

$$V_{N+1/2} = U_{N+1/2} \tag{7.78}$$

Once the solution at $N + 1/2$ is computed, one can recursively utilize relation (7.73) to find U and V at other faces.

7.4.3 Benchmark problems

In this section, the wave solver for the laser fields is validated with an analytical problem. For a linearly increasing plasma density profile $n \sim x$, the wave equation (7.21) can be solved exactly [124]. The dielectric function also follows the same linear relation:

$$\varepsilon(x) = \eta^2(x) = (x - x_c)/L \tag{7.79}$$

where x_c is the location of the critical surface, i.e., $n(x_c) = n_{cr}$. By using the transformation $\xi = (k_0^2/L)^{1/3}(x - x_c)$, equation (7.21) is reduced to the homogeneous Stokes equation:

$$\partial_{\xi\xi}\hat{E} + \xi\hat{E} = 0 \tag{7.80}$$

Assuming the wave is evanescent to the right halfspace ($\xi > 0$), the exact solution of the electric field is the Airy function, denoted as $\mathrm{Ai}(\xi)$:

$$\hat{E}(\xi) = 2\sqrt{\pi}(k_0 L)^{1/6} E_V e^{i\varphi} \mathrm{Ai}(\xi) \tag{7.81}$$

where φ is a phase factor which does not affect $|\hat{E}|$. The solution of the magnetic field is determined from Faraday's law, i.e., equation (7.14):

$$\hat{B}(\xi) = -\frac{i}{c} 2\sqrt{\pi}(k_0 L)^{-1/6} E_V e^{i\varphi} \mathrm{Ai}'(\xi) \tag{7.82}$$

where $\mathrm{Ai}'(\xi)$ is the derivative of the Airy function.

We tested the two numerical approaches finite difference and transfer matrix methods in solving the wave equations for the electromagnetic fields using the linear density profile defined in equation (7.79). In the first test case, collision is neglected, resulting in a real value of the refractive index, and hence there is no absorption of the electromagnetic energy. The numerical solutions of the electric field along with the exact solution are shown in figure 7.2. The results show excellent agreement between the numerical and the exact solutions. It can be seen that the solution obtained with the transfer-matrix method is slightly more accurate. However, the finite difference method can be easily generalized to multiple dimensions.

The ponderomotive force is computed for the same test case using equation (7.43) and plotted in figure 7.3. The same quantity was computed by Lindl and Kaw [136] using the analytical solution of the field. A discrepancy between the current numerical solution and Lindl and Kaw's result was found; the numerical result suggests that the term due to the magnetic field in the Maxwell tensor, i.e., second term on the RHS of equation (7.43), was missing from their calculation. It can be seen that at approximately $\xi = -1$, the ponderomotive force is pushing the cold plasma inward on the right side, and pushing the left side further away. On the left of $\xi = -2$, there exits a standing wave due to local reflection of the

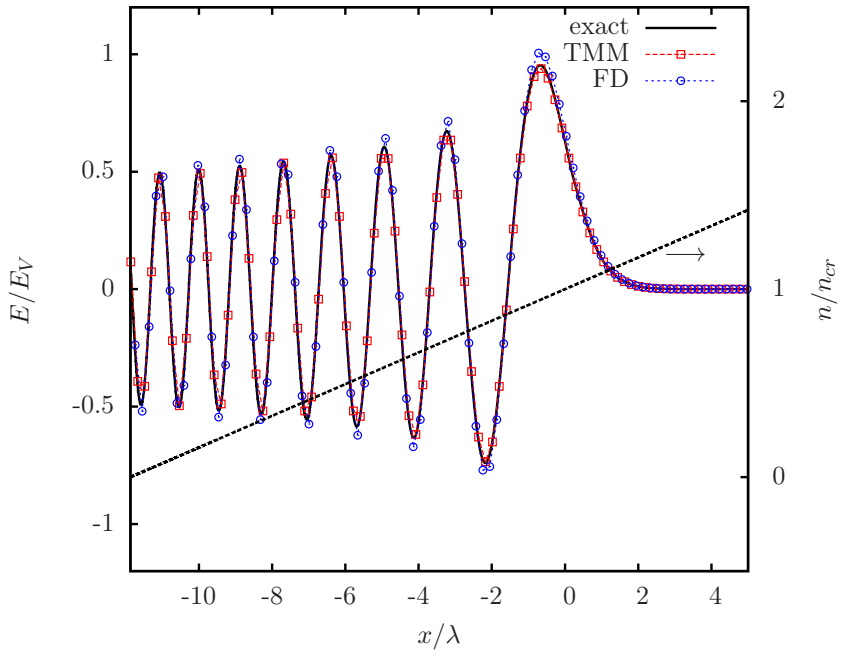

Figure 7.2: Solution of the electric field for a linear density profile (shown by the black dotted line) computed using both TMM and FD methods. The solid black line is the exact solution given by the Airy function. The length is normalized by the laser wavelength

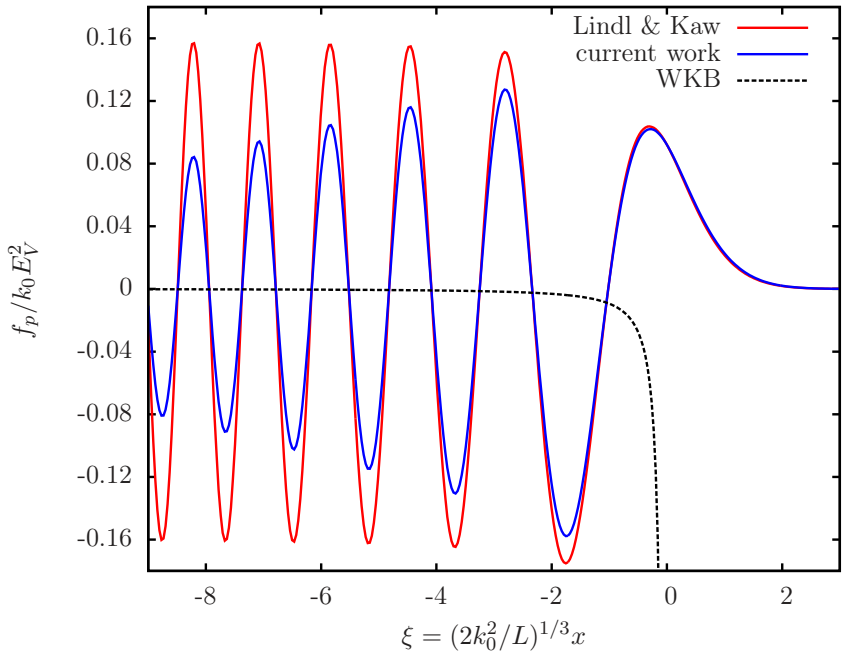

Figure 7.3: Ponderomotive force for a linear density profile. The numerical solution is obtained using the electric field computed in figure 7.2. The solution of Lindl and Kaw [136] is reproduced by omitting the term containing the magnetic field in the expression of the Maxwell stress tensor. The broken line is the solution obtained from the WKB approximation, i.e., equation (7.44).

electromagnetic wave, which gives rise to the ponderomotive bunching effects. The solution of the poderomotive force computed using the equation (7.44) is also shown in the figure 7.3 with a singularity near $\xi = 0$ due to the breakdown of the WKB approximation.

In the second test case, collision is included in the expression of the refractive index, which allows the wave to be collisionally damped. The spatial profile of the intensity of the electromagnetic wave is shown in figure 7.4 using the field values obtained from solving the wave equations and the WKB approximation. The numerical solutions from both approaches (wave equations and WKB approximation) agree very well with unnoticeable difference near the critical layer. The

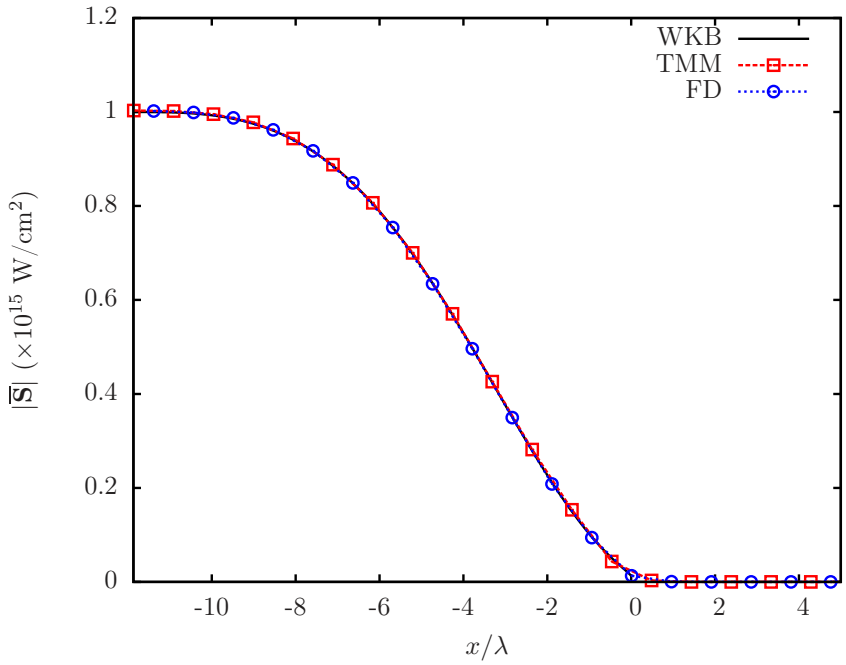

Figure 7.4: Spatial profile of the electromagnetic wave intensity as it propagates into the plasma. The wave energy is completely absorbed near the critical surface.

WKB solution is obtained by solving a radiation transport equation:

$$\partial_x I = -\kappa(x) I \tag{7.83}$$

where κ is given by equation (7.35).

7.5 Ion acceleration via Ponderomotive forces

In this section, we utilize the multi-fluid model described in the previous section to simulate ion acceleration by the ponderomotive force, commonly referred to as radiation pressure acceleration (RPA) mechanism [137]. Similar to another mechanism such as the target normal sheath acceleration (TNSA) [138, 139], ion acceleration is achieved as a direct consequence of an intense electric field, generated due to a large charge separation. The basics of the RPA process rely on the action of the laser ponderomotive force, accelerating electrons near the critical

surface and consequently creating a charge displacement. The TNSA process, on the other hand, refers to the direct conversion of the laser energy to kinetic energy of the electrons through various absorption mechanisms, leading to generation of relativistic electrons. These electrons are expanded to vacuum, thus creating an extremely large electric field, which accelerates the ions.

The RPA mechanism is reproduced by simulating the interaction of a high intensity laser pulse with a plasma density gradient using the multi-fluid equations. The effect of the laser ponderomotive force (appearing in the electron momentum equation) in modifying the plasma density and accelerating charged particles is examined. A similar problem was studied by Hora *et al.* in 1984 [140] albeit with a more compact domain size. Hora *et al.*'s work focuses on examining the generation of a double layer near the critical surface. In this work, we extended the domain to model the entire profile starting from the overdense plasma to near vacuum[5].

The plasma is initialized using an Epstein transition layer profile [141] with a thickness $\delta = 4$ μm. The initial profile assumes a fully ionized hydrogen plasma at rest, and the computational domain is $x \in [0, L]$ where $L = 25$ μm. The initial density profile is as follows:

$$b = 1 - \frac{\exp\left[4(x - L/2)/\delta\right]}{1 + \exp\left[4(x - L/2)/\delta\right]} \tag{7.84}$$

$$n_i = n_e = a\, n_{cr}\, (1 - b) \tag{7.85}$$

where $a = 1.02$ and n_{cr} is the laser critical density. The initial temperatures of the ions and electrons are 1 keV. The laser wavelength is chosen to be 1.053 μm. The laser pulse is simulated as a Gaussian pulse with a peak intensity of 10^{16} W/cm^2, a pulse duration of 1 ps, and a FWHM of 0.2 ps (see figure 7.5). At $t = 0^+$, the laser

[5]Due to the use of an Eulerian code, one can not have zero number density, so a minimum value ($0.01 n_{cr}$) for the number density is imposed in the "vacuum" region. This far field region does interact with the laser but does not affect the overall dynamics near the plasma density gradient.

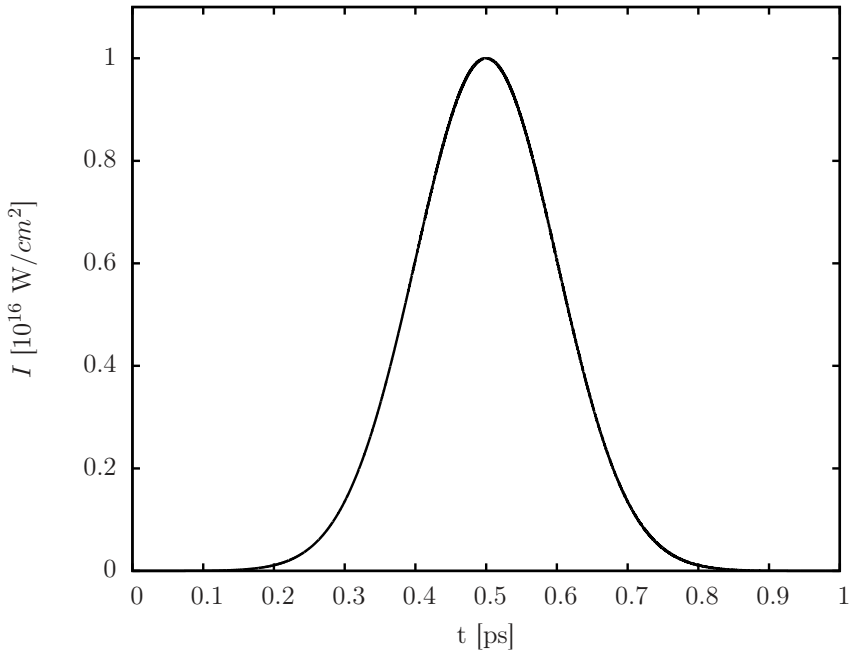

Figure 7.5: Gaussian laser pulse with a maximum intensity of 10^{16} W/cm^2

is incident from the left side of the domain. Although the calculation also includes absorption, its effect is negligible due to high temperature and laser intensity. Simulation results show little difference whether or not absorption is included. The reason for choosing a weak absorption condition is to enhance the effect of the ponderomotive force on the plasma acceleration and density modification. The initial conditions and the laser properties are chosen similarly to Hora's test case but with a longer computational domain and a slightly different density profile. This allows us to validate the code by comparing with Hora's result near the critical density layer, and also look at at the evolution of the plasma density in the corona region.

Figure 7.6 shows the ion number density profile and the laser ponderomotive potential at various times during the laser pulse. At $t = 0.3$ ps, the profile still looks very much similar to the initial one as the laser intensity begins to rise. One can see the formation of a large potential hill near the critical layer. The resultant

ponderomotive force due to this potential rapidly pushes the electrons down the hill, thus creating a charge displacement and an electrostatic field, which drags the ions along. At $t = 0.5$ ps, the laser is at its peak intensity, and we begin to see the formation of a caviton at $x \approx 16$ μm, as a direct consequence of the charge particle being rolled down the potential hill. This effects was also shown in the simulation of Hora *et al.* [140] with a more compact domain size. It must be pointed out that nonlinear force produced caviton was observed in the case of a plasma density gradient being imposed with an external rf field, and had been studied extensively by a number of researchers [142, 143]. In addition, the current simulation also shows an oscillatory structure of the density profile for $x < 16$ μm, which persists even after the laser is gone. The density ripples effectively make the plasma less transparent to the laser field; this can be seen from the density profile during the second half of the laser cycle where most of the laser is being reflected.

The appearance of the ripple in the density profile was not revealed in the previous simulation of Hora *et al.* [140] due to the limit on their computational domain size. This effect is due to local reflection of the laser electromagnetic wave as it propagates through the plasma medium, forming a standing wave pattern as can be seen in the ponderomotive potential profile. The standing wave nature of the potential results in an oscillatory (in space) acceleration of the electrons. The dynamics of the ions is mainly an electrostatic response to the charge separation as illustrated in figure 7.7. The magnitude of the electrostatic field induced in plasma can be significantly large during the laser period (up to 10^7 V/cm). Since plasma temperature is relatively high, collisional relaxation plays a minor role.

Figure 7.8 shows the ion velocity profile at different instances of time. Highly oscillatory velocity profile can be observed in the plasma corona region, and most importantly one can see that the ions are accelerated inward with an velocity of approximately 10^7 cm/sec. It must be clarified that the acceleration of the bulk

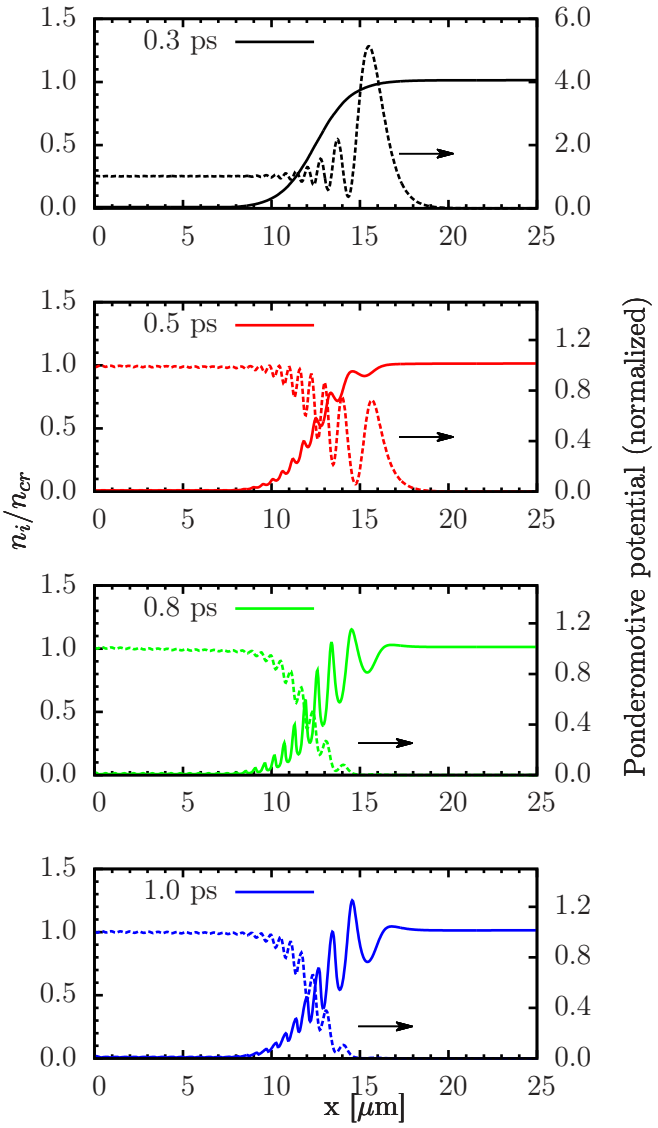

Figure 7.6: Ion number density (solid line) and the ponderomotive potential (dashed line) at four different times during the laser pulse. The ponderomotive potential is defined as $\epsilon_0(E^2 + c^2B^2)$. The ion number density is normalized by the laser critical number density, and the potential is normalized by its value at the vacuum region.

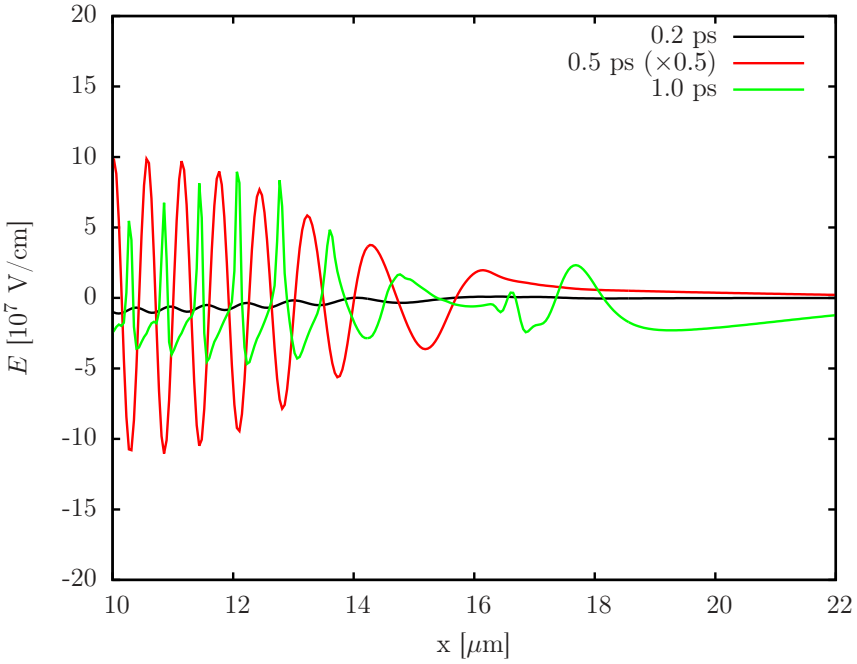

Figure 7.7: Electrostatic field generated in the plasmas due to charge separation.

of the plasma is merely due to the acoustic wave launched into the plasma. The ion acceleration, however, is a result of the intense electric field induced inside the plasma. This E-field consequently generates bursts of high energy ions in a transient fashion, which is the essence of RPA mechanism. The result in this simulation indicates that in the regime of weak collision and low absorption, non-linear force can dominate thermal action and plays an important role in charge acceleration. This is sometimes referred to as the laser piston regime. The same acceleration mechanism can be observed at kinetic time scale with ultra-high intensity laser-matter interaction, by which the ions can be accelerated to relativistic speed [144].

Let us now look at the evolution of the plasma after the laser pulse and the dependences on the laser parameters. In particular, we examine numerically the density modification effects due to a negatively chirped laser pulse. The effect of chirped lasers in LPI was examined in the context of charge acceleration both

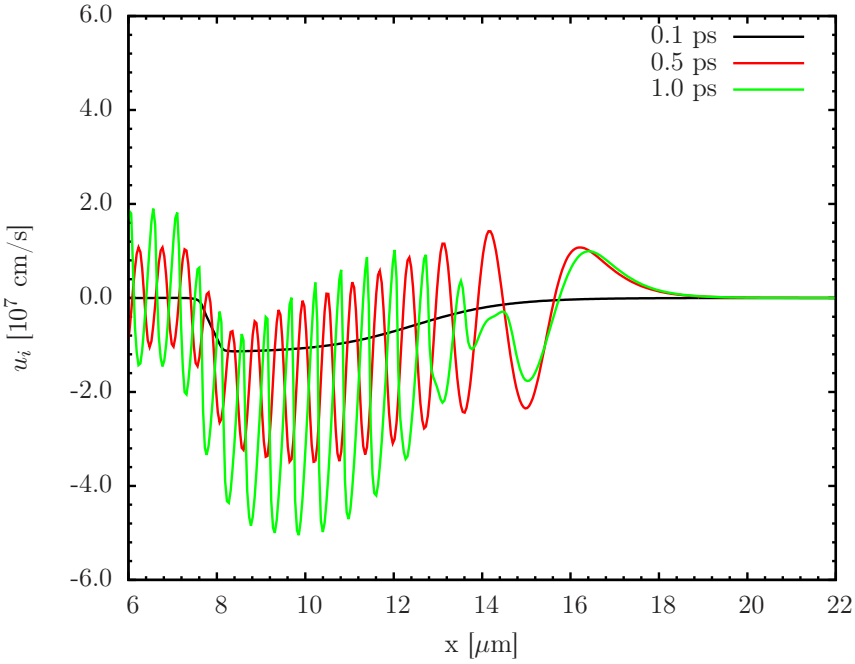

Figure 7.8: Ion velocity at various times after the laser pulse initiation.

from theoretical and application aspects [145, 146, 147, 148]. We focus here on characterizing the density steepening effect due to the action of ponderomotive force and variation of the laser frequency. Since the laser period is much shorter than the pulse duration ($2\pi\omega^{-1} \simeq 3.5$ fs), the effect of a chirped laser can be incorporated by imposing a time variation of the laser frequency ω in the wave equations. In this study, the laser frequency is modeled by a linear relation:

$$\omega(\tau) = \omega_0(1 - b\tau) \tag{7.86}$$

where b is the chirp parameter and τ is the time normalized by the laser pulse duration. In this study, we choose $b = 0.25$.

Figure 7.9 shows the ion densities for both cases of negatively chirped and unchirped lasers at several times. It can be seen that the formation of the density bump is delayed and the peak density value is higher when the laser is chirped. This can be explained by examining the dynamics of the laser ponderomotive forces during the laser pulse. Figure 7.10 shows the ponderomotive potential for

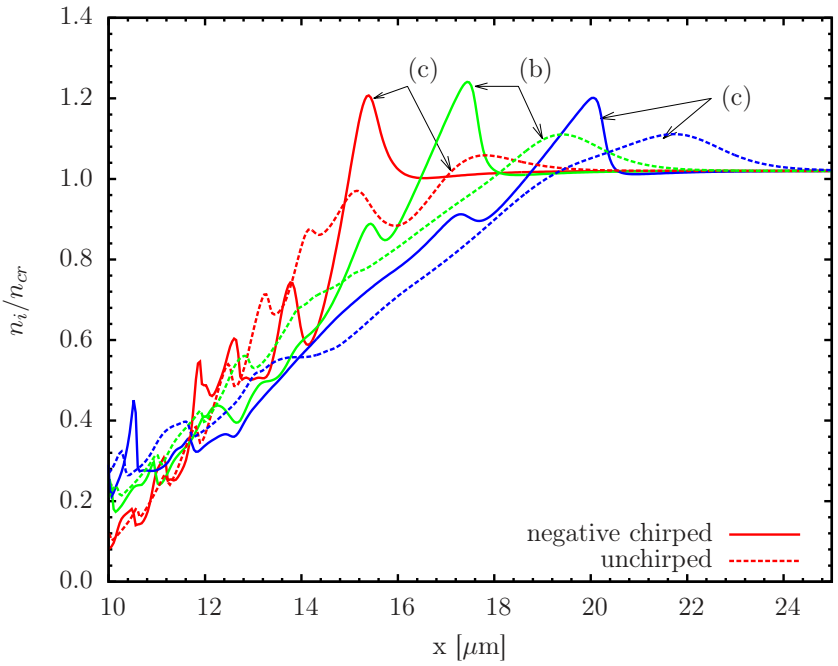

Figure 7.9: Ion number density at (a) 20 ps, (b) 50 ps, and (c) 90 ps for both cases of negatively chirped and unchirped laser pulse. For the negatively chirped laser, the frequency is linearly decreased 25 % over the entire pulse duration.

the first half the pulse. As expected, one can see a shift in the location of the potential hill when the laser is chirped as a indication of a change in the laser critical frequency. Consequently, as time progresses, the pressure force from the chirped laser starts pushing lower density plasma in the corona region inward, resulting a more compressed density bump. This suggests that the negatively chirped laser can enhance compression and steepen the plasma density near the critical layer. The existence of profile steepening is advantageous for energy transport process, i.e., excessive heating in the corona region can be minimized and resonance absorption is more efficient.

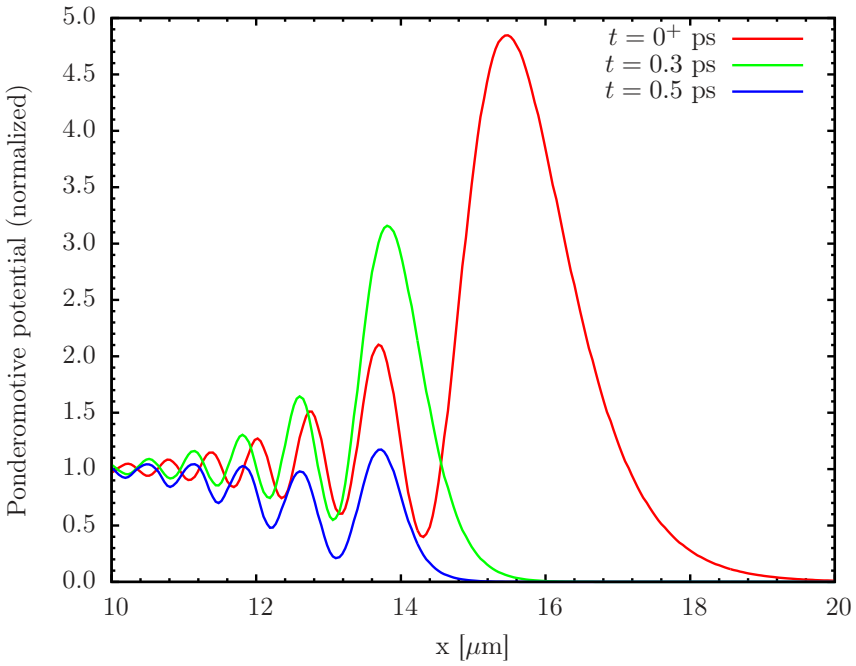

(a)

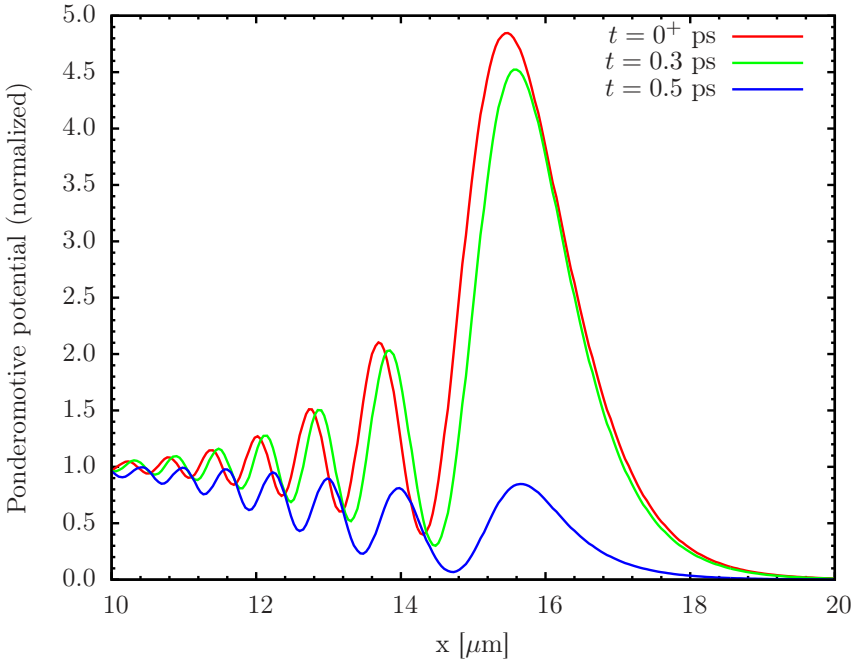

(b)

Figure 7.10: Comparison of the ponderomotive pontential for (a) negatively chirped and (b) unchirped laser. The ponderomotive potential is defined as $\epsilon_0(E^2 + c^2B^2)$. The values of the potential are normalized by its value in the vacuum region.

CHAPTER 8

Conclusions and Future Directions

8.1 Achievements and contributions

In this dissertation, a hydrodynamic framework was developed to simulate multi-component plasmas including both elastic and inelastic interactions by means of a collisional-radiative (CR) model. The hydrodynamic equations can be derived by taking moments of the plasma kinetic equation with an appropriate closure of the transport fluxes. The CR model takes in account nonequilibrium distribution of the internal energy degrees of freedom. These energy states are convected as pseudo-species and their evolution due to CR kinetics are determined by solving a system of rate equations.

Two families of fluid models were considered in this work. The first one is the multi-fluid equations which characterize the plasma species in terms of their own set of conservation laws, which are coupled through collisional and electromagnetic interaction. The electromagnetic fields, governed by Maxwell's equations, are solved self-consistently with the plasmadynamics. In the limit of small electron inertia, the electron momentum reduces to the generalized Ohm's law, which relates the plasma current and the electromagnetic field. Various magnetohydrodynamic models can be derived from Ohm's law. Furthermore, in the limit of fast momentum exchange rate between the plasma components, the plasmadynamics can be characterized by the bulk fluid instead of individual components; this leads to the second family referred to as single-fluid models. Thermal nonequilib-

rium among different plasma components can be captured by multi-temperature equations, i.e., the thermal energy of each component is convected separately.

These hydrodynamic equations could be casted in system of conservation laws, which may be solved by a variety of numerical methods. In the current work, a finite volume discretization was utilized to solve for the fluid transport. The numerical fluxes were computed by solving an approximated Riemann solver at each interface. In order to achieve high-order accuracy, a high-order reconstruction procedure along with multi-stage Runge-Kutta method were employed for the flux integration and time marching, respectively. The coupling source terms were treated with an operator splitting approach. Stiff source terms were computed with a backward Euler method for stability reasons. An extensive set of benchmark problems for both single-fluid and multi-fluid equations were presented to validate the numerical methods and various physical modules implemented in the code.

Detailed CR models for Argon, Krypton and Xenon were constructed, taking into account excitation and ionization mechanisms both from collisional and radiative interaction, and thermal relaxation via elastic collision. The macroscopic rates were obtained directly from the cross section assuming a Maxwellian energy distribution function. A majority of the cross sections are based on ab initio calculations, and semi-empirical formula are used for missing data. Using both steady and unsteady 1D simulations, these CR models were calibrated against available experimental shock tube data with satisfactory agreement over a wide range of flow conditions. The source of remaining discrepancy discovered through these simulations calls for future multi-dimensional simulations with viscous phenomena.

In order to lower the complexity and computational requirement in solving the CR kinetics, a model reduction mechanism for atomic plasma was developed, by grouping electronic states into groups and deriving the corresponding macroscopic

rates to take in account all the transitions. In contrast to the common level-grouping approach, a higher-order description of the internal structure of the groups was developed here by assuming a Boltzmann distribution of the levels within the group, with different temperatures for each group. This approach provides substantial accuracy at minimal computational cost, making it suitable for multidimensional flow calculations.

The modeling of inelastic collisions is extended to the multi-fluid regime, with much emphasis on excitation collision and its reverse process. The exchange source terms due to collision are derived by taking moment of the collision transfer integral. It is shown that the macroscopic rates for multi-fluid equations can deviate significantly from the single-fluid limit due to the difference in the mean flow velocities. In addition, inelastic collisions impose momentum and energy exchange analogously to elastic collisions. The derivation also shows that common expressions of detailed balance for excitation and deexcitation collision does not hold at the macroscopic level when the relative mean drift velocity between the two components is apparent.

The multi-fluid equations were used to simulate laser-plasma interaction phenomena. In particular, the ion acceleration mechanism due to radiation pressure is modeled, showing a strong coupling between the laser, the plasma, and the induced electromagnetic field at high intensity ($I \geq 10^{15}$ W/cm^2). These simulations highlighted the advantage of the multi-fluid model over the single-fluid model to capture charge separation and electromagnetic effects in plasma, which play an essential role in the dynamics of charged particle acceleration, magnetic field generation, and instabilities.

8.2 Future directions

The hydrodynamic models developed in this dissertation can be utilized to study a wide range of problems. In particular, the CR model is directly applicable for the study of plasma formation and radiation, which is relevant, for example, in field-reversed configuration (FRC) plasma formation [42] and aerothermodynamics [20]. The FRC modeling can be accomplished by solving the magnetohydrodynamic (MHD) equations or the multi-fluid equations with a detailed CR model. The validity of the MHD approximation in this plasma regime can be revealed via comparison with the multi-fluid solutions. The same set of equations can be used to study shock and instabilities, occurring in hypersonic reentry [20], inertial confinement devices [149], and astrophysical plasmas [150]. The aspect of excitation and ionization kinetics is of most interests in these simulations since it is often neglected (assuming a fully ionized plasma) or over-simplified (one-step kinetics, quasi steady-state model).

The CR model itself can be improved in several ways. The empiricism of the collision cross section (heavy-particle impact collision) can be removed by using ab initio cross sections. In addition, the simplified treatment of the radiative term can be improved with a radiation transport (RT) model, which takes into account the distribution of the radiation field [95]. Although the solution of the RT equation can be computationally very expensive, various approximations can be used to reduce the cost, e.g., tangent-slab method, multi-group diffusion approximation, etc. By combining the level-grouping method developed in this work with a simplified RT model, a time-dependent flow solution with detailed CR kinetics coupled with the radiation field can be made feasible, allowing us to extract the synthetic radiation spectra for comparison with experiments. In fact, this coupling approach was attempted by Cambier [113] albeit with the use of a simplified model for the CR kinetics. Cambier's work shows that precursor effects can be

of importance for very high shock Mach number; these phenomena are highly non-local and cannot be captured without a RT model.

Extension of the CR model to the multi-fluid regime requires a full description of all the macroscopic rates (density, momentum, and energy) for each transition. The rates must be consistent with kinetic theory, and obey the principle of detailed balance. The same derivation carried out for the excitation and deexcitation collisions can be extended to model ionization and recombination. The contribution of the radiative terms can be derived in a similar fashion with some simplification. Since the mean momentum of the photon is usually much smaller than the thermal momentum of the particle, momentum transfer can be neglected for the radiative transitions. The fully developed multi-fluid CR model can complement the existing work on multi-fluid transport to construct a self-consistent plasmadynamic model. This model is a generalization of the traditional MHD model, therefore having a wider range of applicability, and can potentially provide a robust coupling with hybrid fluid-kinetic methods.

APPENDIX A

Eigensystems

A.1 2T Model

The expressions for the pressure and energy derivatives, which enter the flux Jacobian matrix, are given here. From the equation of state (2.54), the total pressure derivatives can be determined as:

$$p_E \equiv \frac{\partial p}{\partial E} = \gamma_h - 1 \tag{A.1}$$

$$p_{S_e} \equiv \frac{\partial p}{\partial S_e} = \rho^{\gamma_e - 1}\left(1 - \frac{\gamma_h - 1}{\gamma_e - 1}\right) \tag{A.2}$$

$$p_{\rho\mathbf{u}} \equiv \frac{\partial p}{\partial(\rho\mathbf{u})} = -(\gamma - 1)\mathbf{u} \tag{A.3}$$

$$p_{\rho_e} \equiv \frac{\partial p}{\partial \rho_e} = (\gamma_e - \gamma_h)\frac{p_e}{\rho} + (\gamma_h - 1)\frac{\mathbf{u}\cdot\mathbf{u}}{2} \tag{A.4}$$

$$p_{\rho_{s\neq e}} \equiv \frac{\partial p}{\partial \rho_{s\neq e}} = p_{\rho_e} - (\gamma_h - 1)\varepsilon_s + \frac{p_s}{\rho_s} \tag{A.5}$$

$$p_\rho \equiv \frac{\partial p}{\partial \rho} = p_{\rho_e} - (\gamma_h - 1)\sum_{s\neq e} y_s\varepsilon_s + \frac{p - p_e}{\rho} \tag{A.6}$$

The energy derivatives can also be obtained in a similar manner from equation (2.55):

$$E_{\rho_e} \equiv \frac{\partial E}{\partial \rho_e} = -\frac{1}{2}\mathbf{u}\cdot\mathbf{u} \tag{A.7}$$

$$E_{\rho_{s\neq e}} \equiv \frac{\partial E}{\partial \rho_{s\neq e}} = \varepsilon_s + E_{\rho_e} - \frac{p_s}{(\gamma - 1)\rho_s} \tag{A.8}$$

$$E_{\mathbf{u}} \equiv \frac{\partial E}{\partial \mathbf{u}} = \rho\mathbf{u} \tag{A.9}$$

$$E_p \equiv \frac{\partial E}{\partial p} = \frac{1}{\gamma_h - 1} \tag{A.10}$$

$$E_{p_e} \equiv \frac{\partial E}{\partial p_e} = \frac{1}{\gamma_e - 1} - \frac{1}{\gamma_h - 1} \tag{A.11}$$

where y_s is the species mass fraction.

The vector of conservative variables and the inviscid flux vector in the two-temperature model within the context of a finite-volume approximation is as follows:

$$\mathbf{Q} = \begin{bmatrix} \rho_s \\ \rho u_x \\ \rho u_y \\ \rho u_z \\ E \\ S_e \end{bmatrix}, \qquad \mathbf{F}_n = \begin{bmatrix} \rho_s u_n \\ \rho u_n u_x + p n_x \\ \rho u_n u_y + p n_y \\ \rho u_n u_z + p n_z \\ u_n H \\ u_n S_e \end{bmatrix} \tag{A.12}$$

where $\mathbf{F}_n$ is the numerical flux normal to the interface. The three components of the unit vector normal to the face are defined as n_x, n_y and n_z, and u_n is the normal component of the velocity:

$$u_n = u_x n_x + u_y n_y + u_z n_z \tag{A.13}$$

We also define the two tangential velocities to the face

$$u_t = u_x t_x + u_y t_y + u_z t_z \tag{A.14}$$

$$u_s = u_x s_x + u_y s_y + u_z s_z \tag{A.15}$$

The flux Jacobian for the Euler equations for the 2T model is given as:

$$\mathbf{A} = \begin{bmatrix} u_n(\delta_{sr} - y_s) & y_s n_x & y_s n_y & y_s n_z & 0 & 0 \\ p_{\rho_r} n_x - u_n u_x & \mathcal{A}_{m_x,m_x} & \mathcal{A}_{m_y,m_x} & \mathcal{A}_{m_z,m_x} & p_E n_x & p_{S_e} n_x \\ p_{\rho_r} n_y - u_n u_y & \mathcal{A}_{m_x,m_y} & \mathcal{A}_{m_y,m_y} & \mathcal{A}_{m_z,m_y} & p_E n_y & p_{S_e} n_y \\ p_{\rho_r} n_z - u_n u_z & \mathcal{A}_{m_x,m_z} & \mathcal{A}_{m_y,m_z} & \mathcal{A}_{m_z,m_z} & p_E n_z & p_{S_e} n_z \\ u_n\,(p_{\rho_r} - h) & u_n p_{m_x} + h n_x & u_n p_{m_y} + h n_y & u_n p_{m_z} + h n_z & u_n\,(1 + p_E) & u_n p_{S_e} \\ -u_n \hat{s}_e & \hat{s}_e n_x & \hat{s}_e n_y & \hat{s}_e n_z & 0 & u_n \end{bmatrix} \tag{A.16}$$

where $y_s = \rho_s/\rho$ is the species mass fraction, and $\mathcal{A}_{m_\alpha,m_\beta} = p_{m_\alpha} n_\beta + u_\beta n_\alpha + \delta_{\alpha\beta} u_n$. The speed of sound can be extracted from the determinant of the flux Jacobian:

$$a^2 = \sum y_s \frac{\partial p}{\partial \rho_s} + \left(\varepsilon_h + \varepsilon_e + \frac{p}{\rho} - \frac{\mathbf{u}\cdot\mathbf{u}}{2}\right)\frac{\partial p}{\partial E} + \hat{s}_e \frac{\partial p}{\partial S_e} \tag{A.17}$$

The similarity transformation matrices $\mathbf{R}$ and $\mathbf{L}$ are defined as:

$$\mathbf{R} = \begin{bmatrix} \delta_{sr} & y_s & 0 & 0 & y_s & 0 \\ u_x & u_x - n_x a & t_x\rho & s_x\rho & u_x + n_x a & 0 \\ u_y & u_y - n_y a & t_y\rho & s_y\rho & u_y + n_y a & 0 \\ u_z & u_z - n_z a & t_z\rho & s_z\rho & u_z + n_z a & 0 \\ E_{\rho_r} & h - a u_n & E_{u_t} & E_{u_s} & h + a u_n & E_{p_e} \\ (1-\gamma_e)\hat{s}_e & \hat{s}_e & 0 & 0 & \hat{s}_e & \rho^{1-\gamma_e} \end{bmatrix} \tag{A.18}$$

$$\mathbf{L} = \begin{bmatrix} \delta_{sr} - y_s\frac{p_{\rho_s}}{a^2} & -y_s\frac{p_{m_x}}{a^2} & -y_s\frac{p_{m_y}}{a^2} & -y_s\frac{p_{m_z}}{a^2} & -y_s\frac{p_E}{a^2} & -y_s\frac{p_{S_e}}{a^2} \\ \frac{p_{\rho_r}+cu_n}{2a^2} & \frac{p_{m_x}-cn_x}{2a^2} & \frac{p_{m_y}-cn_y}{2a^2} & \frac{p_{m_z}-cn_z}{2a^2} & \frac{p_E}{2a^2} & \frac{p_{S_e}}{2a^2} \\ -\frac{u_t}{\rho} & \frac{t_x}{\rho} & \frac{t_y}{\rho} & \frac{t_z}{\rho} & 0 & 0 \\ -\frac{u_s}{\rho} & \frac{s_x}{\rho} & \frac{s_y}{\rho} & \frac{s_z}{\rho} & 0 & 0 \\ \frac{p_{\rho_r}-cu_n}{2a^2} & \frac{p_{m_x}+cn_x}{2a^2} & \frac{p_{m_y}+cn_y}{2a^2} & \frac{p_{m_z}+cn_z}{2a^2} & \frac{p_E}{2a^2} & \frac{p_{S_e}}{2a^2} \\ \frac{(\gamma_e-1)p_e}{\rho} - \frac{\gamma_e p_e p_{\rho_r}}{\rho a^2} & -\frac{\gamma_e p_e p_{m_x}}{\rho a^2} & -\frac{\gamma_e p_e p_{m_y}}{\rho a^2} & -\frac{\gamma_e p_e p_{m_z}}{\rho a^2} & -\frac{\gamma_e p_e p_E}{\rho a^2} & \frac{p_e}{S_e} - \frac{\gamma_e p_e p_{S_e}}{\rho a^2} \end{bmatrix} \tag{A.19}$$

The diagonal matrix of eigenvalues of $\mathbf{\Lambda}$ is defined by

$$\mathbf{\Lambda} = \begin{bmatrix} u_n & \dots & 0 & 0 & 0 & 0 & 0 & 0 \\ \vdots & \ddots & \vdots & \vdots & \vdots & \vdots & \vdots & \vdots \\ 0 & \dots & u_n & 0 & 0 & 0 & 0 & 0 \\ 0 & \dots & 0 & u_n - a & 0 & 0 & 0 & 0 \\ 0 & \dots & 0 & 0 & u_n & 0 & 0 & 0 \\ 0 & \dots & 0 & 0 & 0 & u_n & 0 & 0 \\ 0 & \dots & 0 & 0 & 0 & 0 & u_n + a & 0 \\ 0 & \dots & 0 & 0 & 0 & 0 & 0 & u_n \end{bmatrix} \tag{A.20}$$

A.2 Maxwell's equations

The vector of conservative variables and the inviscid flux vector in Maxwell's equations within the context of a finite-volume approximation is as follows:

$$\mathbf{Q} = \begin{bmatrix} B_x \\ B_y \\ B_z \\ E_x \\ E_y \\ E_z \end{bmatrix}, \qquad \mathbf{F}_n = \begin{bmatrix} E_z n_y - E_y n_z \\ -E_z n_x + E_x n_z \\ E_y n_x - E_x n_y \\ c^2(-B_z n_y + B_y n_z) \\ c^2(B_z n_x - B_x n_z) \\ c^2(-B_y n_x + B_x n_y) \end{bmatrix} \tag{A.21}$$

where n_x, n_y and n_z are the three component of a unit vector normal to a computational cell. The flux Jacobian for the Maxwell's equations is given as:

$$\mathbf{A} = \begin{bmatrix} 0 & 0 & 0 & 0 & -n_z & n_y \\ 0 & 0 & 0 & n_z & 0 & -n_x \\ 0 & 0 & 0 & -n_y & n_x & 0 \\ 0 & c^2 n_z & -c^2 n_y & 0 & 0 & 0 \\ -c^2 n_z & 0 & c^2 n_x & 0 & 0 & 0 \\ c^2 n_y & -c^2 n_x & 0 & 0 & 0 & 0 \end{bmatrix} \tag{A.22}$$

The transformation matrices $\mathbf{R}$ and $\mathbf{L}$ are defined as:

$$\mathbf{R} = \begin{bmatrix} 0 & n_x & -\frac{n_x n_y}{c} & \frac{n_x n_z}{c} & \frac{n_x n_y}{c} & -\frac{n_x n_z}{c} \\ 0 & n_y & \frac{n_x^2+n_z^2}{c} & \frac{n_y n_z}{c} & -\frac{n_x^2+n_z^2}{c} & -\frac{n_y n_z}{c} \\ 0 & n_z & -\frac{n_y n_z}{c} & -\frac{n_x^2+n_y^2}{c} & \frac{n_y n_z}{c} & \frac{n_x^2+n_y^2}{c} \\ n_x & 0 & -n_z & -n_y & -n_z & -n_y \\ n_y & 0 & 0 & n_x & 0 & n_x \\ n_z & 0 & n_x & 0 & n_x & 0 \end{bmatrix} \tag{A.23}$$

$$\mathbf{L} = \begin{bmatrix} 0 & 0 & 0 & n_x & n_y & n_z \\ n_x & n_y & n_z & 0 & 0 & 0 \\ -\frac{cn_y}{2n_x} & c/2 & 0 & -n_z/2 & -\frac{n_y n_z}{2n_x} & \frac{n_x^2+n_y^2}{2n_x} \\ \frac{cn_z}{2n_x} & 0 & -c/2 & -n_y/2 & \frac{n_x^2+n_z^2}{2n_x} & -\frac{n_y n_z}{2n_x} \\ \frac{cn_y}{2n_x} & -c/2 & 0 & -n_z/2 & -\frac{n_y n_z}{2n_x} & \frac{n_x^2+n_y^2}{2n_x} \\ -\frac{cn_z}{2n_x} & 0 & c/2 & -n_y/2 & \frac{n_x^2+n_z^2}{2n_x} & -\frac{n_y n_z}{2n_x} \end{bmatrix} \tag{A.24}$$

The diagonal matrix of eigenvalues of $\mathbf{\Lambda}$ is defined by

$$\mathbf{\Lambda} = \begin{bmatrix} 0 & 0 & 0 & 0 & 0 & 0 \\ 0 & 0 & 0 & 0 & 0 & 0 \\ 0 & 0 & -c & 0 & 0 & 0 \\ 0 & 0 & 0 & -c & 0 & 0 \\ 0 & 0 & 0 & 0 & c & 0 \\ 0 & 0 & 0 & 0 & 0 & c \end{bmatrix} \tag{A.25}$$

where $c = 3 \times 10^8$ m/s is the speed of light.

APPENDIX B

Steady-state Flow Equations

This appendix describes the steady-state 1D flow approximation used to compute an ionizing shock profile. Utilizing the two temperature model described in section 2.4 and dropping the unsteady terms, the governing equations for steady-state flow are reduced to a system of ODEs:

$$\frac{d}{dx}\left(\rho_s u\right) = m_s \dot{\omega}_s \tag{B.1}$$

$$\frac{d}{dx}\left(p + \rho u^2\right) = 0 \tag{B.2}$$

$$\frac{d}{dx}\left(uH\right) = \dot{\omega}_{\varepsilon_h} + \dot{\omega}_{\varepsilon_e} \tag{B.3}$$

$$\frac{d}{dx}\left(uS_e\right) = \frac{\gamma_e - 1}{\rho^{\gamma_e - 1}} \dot{\omega}_{\varepsilon_e} \tag{B.4}$$

$$\tag{B.5}$$

where $H = E + p$. Using the Jacobian defined in appendix A, one can write the system as:

$$\mathbf{A}\frac{d\mathbf{Q}}{dx} = \dot{\mathbf{\Omega}} \tag{B.6}$$

where $\mathbf{Q}$ is the typical vector of hydrodynamic variables. Here we consider a semi-implicit approximation in which only the RHS is treated implicitly. The linearization follows from a Taylor series expansion:

$$\mathbf{A}\frac{d\mathbf{Q}^n}{dx} = \dot{\mathbf{\Omega}}^n + \frac{\partial \dot{\mathbf{\Omega}}}{\partial x}\Delta x \tag{B.7}$$

$$\mathbf{A}\frac{d\mathbf{Q}^n}{dx} = \dot{\mathbf{\Omega}}^n + \mathbf{J}\frac{d\mathbf{Q}^n}{dx}\Delta x \tag{B.8}$$

where $\mathbf{J} = \frac{\partial \dot{\mathbf{\Omega}}}{\partial \mathbf{Q}}$. Note that the inviscid flux Jacobian $\mathbf{A}$ is assumed constant in the expansion which makes the scheme not fully implicit. However, the main concern of the stiffness due to kinetics can be avoided. The final expression for the change in the conservative variables reads:

$$\Delta \mathbf{Q^n} = \Delta x \left(\mathbf{A} - \Delta x \mathbf{J} \right)^{-1} \dot{\mathbf{\Omega}}^n \tag{B.9}$$

For the steady-state shock flow, we seek for a solution of an initial value problem with the initial conditions being the post-shock flow properties determined from the Rankine-Hugoniot conditions with frozen chemistry. The flow variables are then marched forward in space using the approximation given by equation (B.9). The size of Δx is selected such that sharp flow features such as the electron avalanche can be well resolved.

APPENDIX C

Collision kinematics

C.1 Two-body processes

Let us consider an inelastic collision[1] between two particles s and t, such that the post-collision particles can have modified internal states. The process is formally described as the relation

$$s(\mathbf{v}_s) + t(\mathbf{v}_t) \Leftrightarrow s'(\mathbf{v'}_s) + t'(\mathbf{v'}_t) \tag{C.1}$$

Note that only two particles are produced by the collision, and that the reverse process is indicated by the left arrow in (C.1). The initial velocities are $\mathbf{v}_s, \mathbf{v}_t$. One can define a fluid velocity $\mathbf{u}$ such that $\mathbf{u} \equiv \langle \mathbf{v} \rangle \equiv \int d^3\mathbf{v}\mathbf{v} f(\mathbf{v})$ and a thermal velocity $\mathbf{c} = \mathbf{v} - \mathbf{u}$. By definition, we also have $\langle \mathbf{c} \rangle \equiv 0$

The collision can be transformed to the center of mass (COM) reference frame, moving with velocity $\mathbf{V}$ with respect to the LAB frame. Similarly, we can also define a mean velocity of this COM frame as $\mathbf{U}$. The subsequent Galilean transformations yield the following definitions:

$$\mathbf{V} = \frac{m_s\mathbf{v}_s + m_t\mathbf{v}_t}{M} \qquad \mathbf{g} = \mathbf{v}_s - \mathbf{v}_t \tag{C.2a}$$

$$\mathbf{U} = \frac{m_s\mathbf{u}_s + m_t\mathbf{u}_t}{M} \qquad \mathbf{w} = \mathbf{u}_s - \mathbf{u}_t \tag{C.2b}$$

[1] The particles s and t are respectively the scattered and target in the laboratory frame of reference (LAB)

where $M = m_s + m_t$. The inverse transformation yields:

$$\mathbf{v}_s = \mathbf{V} + \frac{m_t}{M}\mathbf{g} \qquad \mathbf{u}_s = \mathbf{U} + \frac{m_t}{M}\mathbf{w} \tag{C.3a}$$

$$\mathbf{v}_t = \mathbf{V} - \frac{m_s}{M}\mathbf{g} \qquad \mathbf{u}_t = \mathbf{U} - \frac{m_s}{M}\mathbf{w} \tag{C.3b}$$

Mass conservation imposes the relation $m_s + m_t = M = m'_s + m'_t$. For the case of two-body processes such as excitation of internal states, the masses are individually conserved, i.e. $m'_s = m_s, m'_t = m_t$. Expressed in the COM frame, momentum and energy conservation yield, respectively:

$$M\mathbf{V} = M\mathbf{V}' \tag{C.4a}$$

$$\frac{1}{2}M\mathbf{V}^2 + \frac{1}{2}\mu\mathbf{g}^2 = \frac{1}{2}M\mathbf{V}'^2 + \frac{1}{2}\mu\mathbf{g}'^2 + \Delta\varepsilon \tag{C.4b}$$

where $\mu = m_s m_t / M$. Therefore, we have the following constraints:

$$\mathbf{V} = \mathbf{V}' \qquad \text{and} \quad \mathbf{g}^2 = \mathbf{g}'^2 + \frac{2\Delta\varepsilon}{\mu} \tag{C.5}$$

For an excitation between two atomic levels, the transferred energy is a fixed value $\Delta\varepsilon \equiv \varepsilon^*$, the energy gap between levels. In the limit $\Delta\varepsilon \to 0$, the collision is elastic.

Consider now the Maxwellian velocity distribution functions (VDF) of each particle type, normalized to unity, e.g. (recall that $\mathbf{c} = \mathbf{v} - \mathbf{u}$):

$$f_s(\mathbf{v}_s) = \left(\frac{m_s}{2\pi k T_s}\right)^{\frac{3}{2}} \exp\left[-\frac{m_s \mathbf{c}_s^2}{2kT_s}\right] \tag{C.6}$$

and similarly for f_t. The averaging over initial states will yield a product of these two distributions:

$$f_s(\mathbf{v}_s) f_t(\mathbf{v}_t) = \left(\frac{m_s}{2\pi k T_s}\right)^{\frac{3}{2}} \left(\frac{m_t}{2\pi k T_t}\right)^{\frac{3}{2}} \exp[\mathcal{A}] \tag{C.7}$$

where the argument of the exponential function is, from inverting (C.2):

$$\mathcal{A} = \frac{m_s}{2kT_s}\left[\mathbf{V} - \mathbf{U} + \frac{m_t}{M}(\mathbf{g} - \mathbf{w})\right]^2 + \frac{m_t}{2kT_t}\left[\mathbf{V} - \mathbf{U} - \frac{m_s}{M}(\mathbf{g} - \mathbf{w})\right]^2 \tag{C.8}$$

Following Burgers [43], this expression can be simplified with an appropriate transformation of variables; since the basic procedure will be used elsewhere, we describe it below. First, we define the following variables

$$\beta_p = \frac{m_p}{2kT_p}, \qquad \tilde{\mathbf{g}} = \mathbf{g} - \mathbf{w} \tag{C.9}$$

such that

$$\begin{aligned}\mathcal{A} &= \beta_s \left[(\mathbf{V}-\mathbf{U}) + \frac{m_t}{M}\tilde{\mathbf{g}}\right]^2 + \beta_t \left[(\mathbf{V}-\mathbf{U}) - \frac{m_s}{M}\tilde{\mathbf{g}}\right]^2 \\ &= (\beta_s+\beta_t)(\mathbf{V}-\mathbf{U})^2 + \left[\beta_s\frac{m_t^2}{M^2} + \beta_t\frac{m_s^2}{M^2}\right]\tilde{\mathbf{g}}^2 + 2\left[\beta_s\frac{m_t}{M} - \beta_t\frac{m_s}{M}\right](\mathbf{V}-\mathbf{U})\cdot\tilde{\mathbf{g}}\end{aligned} \tag{C.10}$$

Define now

$$\mathbf{V}^* = \mathbf{V}-\mathbf{U}+\gamma\tilde{\mathbf{g}} \tag{C.11}$$

and comparing the expression

$$(\beta_s+\beta_t)\mathbf{V}^{*2} = (\beta_s+\beta_t)(\mathbf{V}-\mathbf{U})^2 + (\beta_s+\beta_t)\gamma^2\tilde{\mathbf{g}}^2 + 2\gamma(\beta_s+\beta_t)(\mathbf{V}-\mathbf{U})\cdot\tilde{\mathbf{g}} \tag{C.12}$$

with (C.10), we see that we can choose the appropriate value of the coefficient γ to eliminate the dot product from $\mathcal{A}$:

$$\gamma = \frac{1}{\beta_s+\beta_t}\left(\beta_s\frac{m_t}{M} - \beta_t\frac{m_s}{M}\right) \tag{C.13}$$

We then obtain complete separation of variables:

$$\mathcal{A} = (\beta_s+\beta_t)\mathbf{V}^{*2} + \left[\beta_s\frac{m_t^2}{M^2} + \beta_t\frac{m_s^2}{M^2} - \frac{1}{\beta_s+\beta_t}\left(\beta_s\frac{m_t}{M} - \beta_t\frac{m_s}{M}\right)^2\right]\tilde{\mathbf{g}}^2 \tag{C.14}$$

The term in brackets is easily simplified:

$$[\ldots] = \frac{\beta_s\beta_t}{\beta_s+\beta_t} \tag{C.15}$$

We can now define effective, average temperatures:

$$\beta_s+\beta_t = \frac{m_s}{2kT_s} + \frac{m_t}{2kT_t} = \frac{M}{2k}\frac{m_sT_t + mtT_s}{MT_sT_t} \equiv \frac{M}{2kT^*} \tag{C.16a}$$

$$\frac{\beta_s\beta_t}{\beta_s+\beta_t} = \frac{\mu}{2k}\frac{M}{T_sT_t}\frac{T_sT_t}{m_sT_t+m_tT_s} \equiv \frac{\mu}{2k\tilde{T}} \tag{C.16b}$$

and γ becomes:

$$\gamma = \frac{\mu}{M}\frac{T_t - T_s}{\tilde{T}} = \mu\frac{T_t - T_s}{m_s T_t + m_t T_s} \tag{C.17}$$

To summarize, we have performed the following change of variables:

$$\mathbf{V}^* = \mathbf{V} - \mathbf{U} + \mu\frac{T_t - T_s}{m_s T_t + m_t T_s}\tilde{\mathbf{g}} \qquad \tilde{\mathbf{g}} = \mathbf{g} - \mathbf{w} \tag{C.18a}$$

$$T^* = M\frac{T_s T_t}{m_s T_t + m_t T_s} \qquad \tilde{T} = \frac{m_s T_t + m_t T_s}{M} \tag{C.18b}$$

These are the same expressions found in [43, pp. 45-46] (with an occasional change of naming convention) for which it is easy to verify that the Jacobian of the transformations is unity, i.e.

$$d^3\mathbf{v}_s d^3\mathbf{v}_t \equiv d^3\mathbf{V} d^3\mathbf{g} \equiv d^3\mathbf{V}^* d^3\tilde{\mathbf{g}} \tag{C.19}$$

Furthermore, we note that:

$$\left(\frac{m_s}{2kT_s}\right)^{\frac{3}{2}}\left(\frac{m_t}{2kT_t}\right)^{\frac{3}{2}} \equiv (\beta_s\beta_t) = (\beta_s+\beta_t)^{\frac{3}{2}}\left(\frac{\beta_s\beta_t}{\beta_s+\beta_t}\right)^{\frac{3}{2}} \equiv \left(\frac{M}{2kT^*}\right)^{\frac{3}{2}}\left(\frac{\mu}{2k\tilde{T}}\right)^{\frac{3}{2}} \tag{C.20}$$

The product of distributions can now be written as:

$$f_s \cdot f_t = \left(\frac{M}{2\pi kT^*}\right)^{\frac{3}{2}}\exp\left[-\frac{M\mathbf{V}^{*2}}{2kT^*}\right]\cdot\left(\frac{\mu}{2\pi k\tilde{T}}\right)^{\frac{3}{2}}\exp\left[-\frac{\mu\tilde{\mathbf{g}}^2}{2k\tilde{T}}\right] \equiv f^*(\mathbf{V}^*)\cdot\tilde{f}(\tilde{\mathbf{g}}) \tag{C.21}$$

All subsequent expressions can now be simplified with this separation of variables, since for any operator $\mathscr{O}$ that depends on variables expressed in the COM frame, we have:

$$\int d^3\mathbf{v}_s d^3\mathbf{v}_t f_s f_t \mathscr{O}(\mathbf{g}) = \underbrace{\int d^3\mathbf{V}^* f^*(\mathbf{V}^*)}_{\equiv 1}\cdot\int d^3\tilde{\mathbf{g}}\tilde{f}(\tilde{\mathbf{g}})\mathscr{O}(\mathbf{g}) \tag{C.22}$$

The elimination of the variable $\mathbf{V}^*$ is simply a consequence of the Galilean invariance of the collision process.

The procedure above can be also used for the reverse process, where the initial

variables are now the prime quantities. Thus, similarly to (C.2,C.3), we have

$$\mathbf{V} = \frac{m_s \mathbf{v'}_s + m_t \mathbf{v'}_t}{M} \qquad \mathbf{v'}_s = \mathbf{V} + \frac{m_t}{M}\mathbf{g'} \tag{C.23a}$$

$$\mathbf{g'} = \mathbf{v'}_s - \mathbf{v'}_t \qquad \mathbf{v'}_t = \mathbf{V} - \frac{m_s}{M}\mathbf{g'} \tag{C.23b}$$

while the mean flow velocity relations are unchanged, since the s', t' particles belong to the same fluids as s, t. One can therefore use the exact same procedure described above to re-cast the product of the distribution functions of the initial variables into separated variables:

$$\begin{aligned} f_s(\mathbf{v'}_s) \cdot f_t(\mathbf{v'}_t) &\equiv \left(\frac{M}{2\pi k T^*}\right)^{\frac{3}{2}} \exp\left[-\frac{M\mathbf{V'}^{*2}}{2kT^*}\right] \cdot \left(\frac{\mu}{2\pi k \tilde{T}}\right)^{\frac{3}{2}} \exp\left[-\frac{\mu \tilde{\mathbf{g'}}^2}{2k\tilde{T}}\right] \\ &\equiv f^*(\mathbf{V'}^*) \cdot \tilde{f}(\tilde{\mathbf{g}'}) \end{aligned} \tag{C.24}$$

C.2 Three-body processes

Similarly to excitation, the ionization process has two particles in the initial state, but the final state includes a third particle, since an electron extracted from the target to yield an ion state ($t \to i + e$). The process is therefore:

$$s(\mathbf{v}_s) + t(\mathbf{v}_t) \Leftrightarrow s'(\mathbf{v}'_s) + i(\mathbf{v}''_i) + e(\mathbf{v}''_e) \tag{C.25}$$

We have used double-prime variables for the ion and electron, for reasons which will soon become clear. In the case of ionization, one must integrate over the distribution functions of the initial variables, which remain s, t, and the procedure of section C.1 remains valid. However, for recombination, we have a triple product of VDFs:

$$\begin{aligned} f_s(\mathbf{v}'_s)\, f_i(\mathbf{v}''_i)\, f_e(\mathbf{v}''_e) = &\left(\frac{m_s}{2\pi k T_s}\right)^{\frac{3}{2}} e^{-\beta_s(\mathbf{v}'_s - \mathbf{u}_s)^2} \\ &\left(\frac{m_i}{2\pi k T_i}\right)^{\frac{3}{2}} e^{-\beta_i(\mathbf{v}''_i - \mathbf{u}_i)^2} \left(\frac{m_e}{2\pi k T_e}\right)^{\frac{3}{2}} e^{-\beta_e(\mathbf{v}''_e - \mathbf{u}_e)^2} \end{aligned} \tag{C.26}$$

In order to perform the separation of variables, it is necessary to proceed in two steps. Thus, we can consider the ionization process as follows:

a) the formation of an excited state t' via scattering: $s(\mathbf{v}_s) + t(\mathbf{v}_t) \Rightarrow s'(\mathbf{v}'_s) + t'(\mathbf{v}'_t)$

b) the spontaneous ionization of the t' state into ion and electron: $t'(\mathbf{v}'_t) \Rightarrow e(\mathbf{v}''_e) + i(\mathbf{v}''_i)$

The reverse process, recombination, would similarly follow two steps:

a) the formation of an excited state t' via recombination: $e(\mathbf{v}''_e) + i(\mathbf{v}''_i) \Rightarrow t'(\mathbf{v}'_t)$

b) the spontaneous deexcitation of the t' state via scattering: $s'(\mathbf{v}'_s) + t'(\mathbf{v}'_t) \Rightarrow s(\mathbf{v}_s) + t(\mathbf{v}_t)$

Consider now the following change of variables

$$\mathbf{g}' = \mathbf{v}'_s - \mathbf{v}'_t \tag{C.27a}$$

$$\mathbf{g}'' = \mathbf{v}''_e - \mathbf{v}''_i \tag{C.27b}$$

along with the COM velocity definition ($m_t = m_e + m_i$):

$$\mathbf{V} = \frac{m_s\mathbf{v}_s + m_t\mathbf{v}_t}{M} = \frac{m_s\mathbf{v}'_s + m_t\mathbf{v}'_t}{M} = \frac{m_s\mathbf{v}'_s + m_e\mathbf{v}''_e + m_i\mathbf{v}''_i}{M} \tag{C.28}$$

Thus,

$$\begin{pmatrix} \mathbf{V} \\ \mathbf{g}' \\ \mathbf{g}'' \end{pmatrix} = \begin{pmatrix} m_s/M & m_e/M & m_i/M \\ 1 & -m_e/m_t & -m_i/m_t \\ 0 & 1 & -1 \end{pmatrix} \cdot \begin{pmatrix} \mathbf{v}'_s \\ \mathbf{v}''_e \\ \mathbf{v}''_i \end{pmatrix} \tag{C.29}$$

One can easily verify that this transformation is unitary, i.e. $d\mathbf{V}d\mathbf{g}'d\mathbf{g}'' \equiv d\mathbf{v_s}'d\mathbf{v}''_e d\mathbf{v}''_i$.

Consider now the first part of this two-step recombination process, which involves the product of the two VDFs for electron and ion: $f_e(\mathbf{v}''_e)f_i(\mathbf{v}''_i)$. Therefore, the argument of the exponential function resulting from this product is:

$$\mathcal{A}_{ei} = \frac{m_e}{2kT_e}(\mathbf{v}''_e - \mathbf{u}_e)^2 + \frac{m_i}{2kT_i}(\mathbf{v}''_i - \mathbf{u}_i)^2 \tag{C.30}$$

From (C.29) and $\mathbf{v}_t' = (m_e\mathbf{v}_e'' + m_i\mathbf{v}_i'')/m_t$, we have:

$$\mathbf{v}_e'' = \mathbf{v}_t' + \frac{m_i}{m_t}\mathbf{g}'' \tag{C.31a}$$

$$\mathbf{v}_i'' = \mathbf{v}_t' - \frac{m_e}{m_t}\mathbf{g}'' \tag{C.31b}$$

Similarly, we can define mean fluid variables

$$\begin{aligned} \mathbf{u}_t' &= \tfrac{m_e\mathbf{u}_e + m_i\mathbf{u}_i}{m_t} \\ \mathbf{w}'' &= \mathbf{u}_e - \mathbf{u}_i \end{aligned} \quad \Rightarrow \quad \begin{aligned} \mathbf{u}_e &= \mathbf{u}_t' + \tfrac{m_i}{m_t}\mathbf{w}'' \\ \mathbf{u}_i &= \mathbf{u}_t' - \tfrac{m_e}{m_t}\mathbf{w}'' \end{aligned} \tag{C.32}$$

With the usual definition $\tilde{\mathbf{g}}'' = \mathbf{g}'' - \mathbf{w}''$, The argument (C.30) becomes

$$\begin{aligned} \mathcal{A}_{ei} &= \beta_e\left(\mathbf{v}_t' - \mathbf{u}_t' + \frac{m_i}{m_t}(\tilde{\mathbf{g}}'')\right)^2 + \beta_i\left(\mathbf{v}_t' - \mathbf{u}_t' - \frac{m_e}{m_t}(\tilde{\mathbf{g}}'')\right)^2 \\ &= (\beta_e+\beta_i)(\mathbf{v}_t' - \mathbf{u}_t')^2 + \left(\beta_e\frac{m_i^2}{m_t^2} + \beta_i\frac{m_e^2}{m_t^2}\right)(\tilde{\mathbf{g}}'')^2 + 2\left(\beta_e\frac{m_i}{m_t} - \beta_i\frac{m_e}{m_t}\right)(\mathbf{v}_t' - \mathbf{u}_t')\cdot\tilde{\mathbf{g}}'' \end{aligned} \tag{C.33}$$

We recognize the same form as (C.10); we can thus apply the same procedure, and define

$$\mathbf{C}_t = \mathbf{v}_t' - \mathbf{u}_t' + \gamma(\tilde{\mathbf{g}}'') \tag{C.34}$$

where now

$$\gamma = \frac{1}{\beta_e+\beta_i}\left(\beta_e\frac{m_i}{m_t} - \beta_i\frac{m_e}{m_t}\right) \tag{C.35}$$

such that the argument now becomes:

$$\mathcal{A}_{ei} = (\beta_e+\beta_i)\mathbf{C_t}^2 + \frac{\beta_e\beta_i}{\beta_e+\beta_i}(\tilde{\mathbf{g}}'')^2 \tag{C.36}$$

We can now multiply by the VDF for the scattering particle for the second step of the recombination process. This leads to the total argument:

$$\mathcal{A} = (\beta_e+\beta_i)\mathbf{C_t}^2 + \frac{\beta_e\beta_i}{\beta_e+\beta_i}(\tilde{\mathbf{g}}'')^2 + \beta_s(\mathbf{v}_s' - \mathbf{u}_s)^2 \tag{C.37}$$

Similarly to (C.32), we have

$$\begin{aligned} \mathbf{U} &= \tfrac{m_s\mathbf{u}_s + m_t\mathbf{u}_t'}{M} \\ \mathbf{w}' &= \mathbf{u}_s - \mathbf{u}_t' \end{aligned} \quad \Rightarrow \quad \begin{aligned} \mathbf{u}_s &= \mathbf{U} + \tfrac{m_t}{M}\mathbf{w}' \\ \mathbf{u}_t' &= \mathbf{U} - \tfrac{m_s}{M}\mathbf{w}' \end{aligned} \tag{C.38}$$

Let us also define

$$\mathbf{V}^* = \mathbf{V} - \mathbf{U} - \frac{m_s}{M}\tilde{\mathbf{g}}' \qquad \text{with} \quad \tilde{\mathbf{g}}' = \mathbf{g}' - \mathbf{w}' \tag{C.39}$$

This yields:

$$\mathbf{v}_s' - \mathbf{u}_s = \mathbf{V} - \mathbf{U} + \frac{m_t}{M}\tilde{\mathbf{g}}' = \mathbf{V}^* + \tilde{\mathbf{g}}' \tag{C.40}$$

and, from (C.34)

$$\mathbf{C}_t = \mathbf{V}^* + \gamma\,\tilde{\mathbf{g}}'' \tag{C.41}$$

Inserting into (C.37):

$$\begin{aligned}\mathcal{A} = (\beta_s + \beta_e + \beta_i)\mathbf{V}^{*2} + \beta_s(\tilde{\mathbf{g}}')^2 \\ + \left[(\beta_e + \beta_i)\gamma^2 + \frac{\beta_e\beta_i}{\beta_e + \beta_i}\right](\tilde{\mathbf{g}}'')^2 \\ + 2\gamma(\beta_e + \beta_i)\mathbf{V}^* \cdot \tilde{\mathbf{g}}'' + 2\beta_s\mathbf{V}^* \cdot \tilde{\mathbf{g}}'\end{aligned} \tag{C.42}$$

Let us now try the following variable substitution

$$\mathbf{V}^{**} = \mathbf{V}^* + \tilde{\gamma}\tilde{\mathbf{g}}'' + \tilde{\delta}\tilde{\mathbf{g}}' \tag{C.43}$$

Thus,

$$\begin{aligned}\mathbf{V}^{**2} = \mathbf{V}^{*2} + \tilde{\gamma}^2(\tilde{\mathbf{g}}'')^2 + \tilde{\delta}^2(\tilde{\mathbf{g}}')^2 \\ + 2\tilde{\gamma}\mathbf{V}^* \cdot \tilde{\mathbf{g}}'' + 2\tilde{\delta}\mathbf{V}^* \cdot \tilde{\mathbf{g}}' + 2\tilde{\gamma}\tilde{\delta}\tilde{\mathbf{g}}' \cdot \tilde{\mathbf{g}}''\end{aligned}$$

Defining $\Sigma_\beta = \beta_s + \beta_s + \beta_i$ and choosing

$$\tilde{\delta} = \frac{\beta_s}{\Sigma_\beta}, \qquad \tilde{\gamma} = \frac{\beta_e + \beta_i}{\Sigma_\beta}\gamma \tag{C.44}$$

we obtain

$$\begin{aligned}\Sigma_\beta\mathbf{V}^{**2} = \Sigma_\beta\mathbf{V}^{*2} + \frac{\beta_s^2}{\Sigma_\beta}(\tilde{\mathbf{g}}')^2 + \frac{(\beta_e + \beta_i)^2}{\Sigma_\beta}\gamma^2(\tilde{\mathbf{g}}'')^2 \\ + 2\gamma(\beta_e + \beta_i)\mathbf{V}^* \cdot \tilde{\mathbf{g}}'' + 2\beta_s\mathbf{V}^* \cdot \tilde{\mathbf{g}}' + 2\gamma\frac{\beta_s(\beta_e + \beta_i)}{\Sigma_\beta}\tilde{\mathbf{g}}' \cdot \tilde{\mathbf{g}}''\end{aligned}$$

Comparing with (C.42), we can simplify the argument as:

$$\begin{aligned}\mathcal{A} =&\Sigma_\beta \mathbf{V}^{**2} + \left[\frac{\beta_s(\beta_e+\beta_i)}{\Sigma_\beta}\gamma^2 + \frac{\beta_e\beta_i}{\beta_e+\beta_i}\right](\tilde{\mathbf{g}}'')^2 \\ &+ \frac{\beta_s(\beta_e+\beta_i)}{\Sigma_\beta}]\left[(\tilde{\mathbf{g}}')^2 - 2\gamma\tilde{\mathbf{g}}'\cdot\tilde{\mathbf{g}}''\right]\end{aligned} \tag{C.45}$$

Define now

$$\mathbf{j} = (\mathbf{g}'-\mathbf{w}') - \gamma(\mathbf{g}''-\mathbf{w}'') \tag{C.46}$$

We can now eliminate the last dot product, since $(\tilde{\mathbf{g}}')^2-2\gamma\tilde{\mathbf{g}}'\cdot\tilde{\mathbf{g}}''=\mathbf{j}^2-\gamma^2(\tilde{\mathbf{g}}'')^2$. Inserting into (C.45), we finally obtain:

$$\mathcal{A} = (\beta_s+\beta_e+\beta_i)\mathbf{V}^{**2} + \frac{\beta_e\beta_i}{\beta_e+\beta_i}(\mathbf{g}''-\mathbf{w}'')^2 + \frac{\beta_s(\beta_e+\beta_i)}{\beta_s+\beta_e+\beta_i}\mathbf{j}^2 \tag{C.47}$$

We have achieved variable separation, i.e. all dot products have been removed with the proper change of variables. One can also show that:

$$\beta_s+\beta_e+\beta_i = \frac{M}{2k}\frac{m_sT_eT_i+m_eT_sT_i+m_iT_sT_e}{MT_sT_eT_i} \equiv \frac{M}{2kT^*} \tag{C.48}$$

$$\frac{\beta_e\beta_i}{\beta_e+\beta_i} = \frac{m_em_i}{2k(m_e+m_i)}\frac{m_e+m_i}{m_eT_i+m_iT_e} \equiv \frac{\mu_t}{2k\tilde{T}_t} \tag{C.49}$$

$$\frac{\beta_s(\beta_e+\beta_i)}{\beta_s+\beta_e+\beta_i} = \frac{m_s(m_e+m_i)}{2kM}\frac{M\tilde{T}_t}{m_sT_eT_i+m_eT_sT_i+m_iT_sT_e} \equiv \frac{\mu}{2k\tilde{T}} \tag{C.50}$$

where

$$T^* = \frac{MT_sT_eT_i}{m_sT_eT_i+m_eT_sT_i+m_iT_sT_e} \tag{C.51}$$

$$\tilde{T}_t = \frac{m_eT_i+m_iT_e}{m_e+m_i} \tag{C.52}$$

$$\tilde{T} = \frac{m_sT_eT_i+m_eT_sT_i+m_iT_sT_e}{M\tilde{T}_t} \tag{C.53}$$

$$\mu_t = \frac{m_em_i}{m_e+m_i} \tag{C.54}$$

$$\mu = \frac{m_s(m_e+m_i)}{M} \tag{C.55}$$

The product of the three Maxwellian VDF becomes:

$$f_s(\mathbf{v}'_s)\cdot f_e(\mathbf{v}''_e)\cdot f_i(\mathbf{v}''_i)=\left(\frac{M}{2\pi kT^*}\right)^{\frac{3}{2}}\exp\left[-\frac{M\mathbf{V}'^{**2}}{2kT^*}\right]\cdot\left(\frac{\mu_t}{2\pi k\tilde{T}_t}\right)^{\frac{3}{2}}\exp\left[-\frac{\mu_t\tilde{\mathbf{g}''}^2}{2k\tilde{T}_t}\right]\cdot\left(\frac{\mu}{2\pi k\tilde{T}}\right)^{\frac{3}{2}}\exp\left[-\frac{\mu\mathbf{j}^{*2}}{2k\tilde{T}}\right]\equiv f^{**}(\mathbf{V}^{**})\cdot\tilde{f}_t(\tilde{\mathbf{g}''})\cdot\tilde{f}(\mathbf{j}^*) \tag{C.56}$$

Since $m_e/m_i \ll 1$, $\tilde{T}_t \simeq T_e + o(m_e/m_i)$. For a heavy particle induced recombination, $m_e/m_s \ll 1$ and $\tilde{T} \simeq \frac{m_sT_i+m_iT_s}{m_s+m_i} + o(m_e/M)$. If $m_s \simeq m_i$, $\tilde{T} \to \frac{T_s+T_i}{2}$. For an electron induced recombination, $\tilde{T} \to T_e$.

APPENDIX D

Microscopic Detailed Balance

In this appendix, the principle of detailed balance (DB) are described for various inelastic processes occurring in an atomic plasma. These are essentially explicit forms of the reciprocal relations introduced in section 4.2. The notation of differential and total cross section for various processes are introduced and the reciprocal relation is derived by considering microscopy reaction balance.

D.1 Collisional excitation and deexcitation

Consider now a collisional excitation between particles s and t and its reverse process similar to section C.1:

$$s(\mathbf{v}_s) + t(\mathbf{v}_t, E_\ell) \Leftrightarrow s'(\mathbf{v}'_s) + t'(\mathbf{v}'_t, E_u) \tag{D.1}$$

where E_ℓ and E_u are the energy of the lower and upper states of particle t, respectively. Conservation of momentum and energy lead to:

$$m_s\mathbf{v}_s + m_t\mathbf{v}_t = m_s\mathbf{v}'_s + m_t\mathbf{v}'_t \tag{D.2}$$

$$\frac{1}{2}m_s\mathbf{v}_s^2 + \frac{1}{2}m_t\mathbf{v}_t^2 = \frac{1}{2}m_s\mathbf{v}_s'^2 + \frac{1}{2}m_t\mathbf{v}_t'^2 + \Delta\varepsilon \tag{D.3}$$

It can be shown that in the COM frame, momentum conservation indicates that the COM velocity is unchanged after collision.

$$\mathbf{V}' = \mathbf{V} = \frac{m_s\mathbf{v}_s + m_t\mathbf{v}_t}{m_s + m_t} = \frac{m_s\mathbf{v}'_s + m_t\mathbf{v}'_t}{m_s + m_t} \tag{D.4}$$

Energy conservation gives the change in the magnitude of the relative velocity:

$$g' = \left(g^2 - \frac{2\Delta\varepsilon}{\mu} \right)^{1/2} \tag{D.5}$$

where

$$\mathbf{g} = \mathbf{v}_s - \mathbf{v}_t \tag{D.6}$$

$$\mathbf{g}' = \mathbf{v}'_s - \mathbf{v}'_t \tag{D.7}$$

$$\mu = \frac{m_s m_t}{m_s + m_t} \tag{D.8}$$

One can also show that:

$$\left| \frac{\partial(\mathbf{V}, \mathbf{g})}{\partial(\mathbf{v}_s, \mathbf{v}_t)} \right| = \left| \frac{\partial(\mathbf{V}', \mathbf{g}')}{\partial(\mathbf{v}'_s, \mathbf{v}'_t)} \right| = 1 \tag{D.9}$$

such that

$$d^3\mathbf{v}_t d^3\mathbf{v}_s = d^3\mathbf{V} d^3\mathbf{g} \tag{D.10}$$

$$d^3\mathbf{v}'_t d^3\mathbf{v}'_s = d^3\mathbf{V}' d^3\mathbf{g}' \tag{D.11}$$

$$d^3\mathbf{V} = d^3\mathbf{V}' \tag{D.12}$$

$$g dg = g' dg' \tag{D.13}$$

$$\frac{d^3\mathbf{g}}{d^3\mathbf{g}'} = \frac{g'}{g} \tag{D.14}$$

Equation (D.14) is a direct result of the collision dynamics where the relative orientation of $\mathbf{g}$ and $\mathbf{g}'$ is always fixed. We can then write a rate equation for this process as follows:

$$\begin{aligned} &n_s f_s(\mathbf{v}_s) d^3\mathbf{v}_s \cdot n_\ell f_t(\mathbf{v}_t) d^3\mathbf{v}_t \cdot g \cdot \sigma_{s\ell}(g, \Omega) d\Omega \\ &= n_s f_s(\mathbf{v}'_s) d^3\mathbf{v}'_s \cdot n_u f_t(\mathbf{v}'_t) d^3\mathbf{v}'_t \cdot g' \cdot \sigma_{su}(g', \Omega) d\Omega \end{aligned} \tag{D.15}$$

where n_ℓ, n_u are the number densities of the lower and upper states, and $\sigma_{s\ell}, \sigma_{su}$ are the differential cross sections for excitation and deexcitation. By utilizing equation (4.14) for n_ℓ, n_u, equation (4.11) for f_s, conservation of momentum and energy, and change of variables, we arrive at the following expression:

$$\mathcal{g}_\ell g^2 \sigma_{s\ell}(g, \Omega) = \mathcal{g}_u g'^2 \sigma_{su}(g', \Omega) \tag{D.16}$$

where $\mathcal{g}$ is the state degeneracy factor. A special case of zero net energy, $\Delta\varepsilon = 0$, corresponds to elastic collision. This relation can also be expressed in term of total energetic cross sections by integrating over all scattering solid angle, i.e., $\overline{\sigma}(\varepsilon) = \int \sigma \, d\Omega$:

$$\mathcal{g}_\ell \varepsilon \overline{\sigma}_{s\ell}(\varepsilon) = \mathcal{g}_u \varepsilon' \overline{\sigma}_{su}(\varepsilon') \tag{D.17}$$

where $\varepsilon = \frac{1}{2}\mu g^2$. This expression is known as the *Klein-Rosseland* relation which describes DB of collisional excitation and deexcitation at the microscopic level[1].

D.2 Collisional ionization and recombination

We consider now a collisional ionization and a three body recombination process similar to (C.25):

$$s(\mathbf{v}_s) + t(\mathbf{v}_t) \Leftrightarrow s'(\mathbf{v}'_s) + i(\mathbf{v}''_i) + e(\mathbf{v}''_e) \tag{D.18}$$

Again, momentum and energy are conserved which leads to:

$$m_s\mathbf{v}_s + m_t\mathbf{v}_t = m_s\mathbf{v}'_s + \underbrace{m_i\mathbf{v}''_i + m_e\mathbf{v}''_e}_{m_t\mathbf{v}'_t} \tag{D.19}$$

$$\frac{1}{2}m_s\mathbf{v}_s^2 + \frac{1}{2}m_t\mathbf{v}_t^2 = \frac{1}{2}m_s\mathbf{v}_s'^2 + \frac{1}{2}m_i\mathbf{v}_i''^2 + \frac{1}{2}m_e\mathbf{v}_e''^2 + \Delta\varepsilon \tag{D.20}$$

where $\Delta\varepsilon$ is now the ionization potential of t. The rate equations for the both processes are:

$$\begin{aligned} &n_s f_s(\mathbf{v}_s)d^3\mathbf{v}_s \cdot n_t f_t(\mathbf{v}_t)d^3\mathbf{v}_t \cdot g \cdot \sigma_{ion}(\mathbf{g};\mathbf{g}',\mathbf{g}'')d^3\mathbf{g}'d^3\mathbf{g}'' \\ &= n_s f_s(\mathbf{v}'_s)d^3\mathbf{v}'_s \cdot n_i f_i(\mathbf{v}''_i)d^3\mathbf{v}''_i \cdot n_e f_e(\mathbf{v}''_e)d^3\mathbf{v}''_e \cdot g'g'' \cdot \sigma_{rec}(\mathbf{g}',\mathbf{g}'';\mathbf{g})d^3\mathbf{g} \end{aligned} \tag{D.21}$$

where we have previously defined $\mathbf{g} = \mathbf{v}_s - \mathbf{v}_t$, $\mathbf{g}' = \mathbf{v}'_s - \mathbf{v}'_t$ and $\mathbf{g}'' = \mathbf{v}''_e - \mathbf{v}''_i$ (see section C.2). Note that in the COM reference frame, σ_{ion} is a triply differential cross section.

[1] which is, independent of the form of the distribution function.

By utilizing the transformation defined in section C.2, one can obtain the following relations:

$$d^3\mathbf{v}_s d^3\mathbf{v}_t = d^3\mathbf{V} d^3\mathbf{g} \tag{D.22}$$

$$d^3\mathbf{v}_s' d^3\mathbf{v}_i'' d^3\mathbf{v}_e'' = d^3\mathbf{V} d^3\mathbf{g}' d^3\mathbf{g}'' \tag{D.23}$$

We can proceed similarly by introducing the Maxwell distribution for f_s, f_t, f_i and f_e, and Saha distribution for $n_i n_e/n_t$ in equation (D.21). This leads to the following expression:

$$\mathscr{g}_t g \sigma_{ion}(\mathbf{g}; \mathbf{g}', \mathbf{g}'') = 2\mathscr{g}_i \frac{\mu_t^3}{h^3} g' g'' \sigma_{rec}(\mathbf{g}', \mathbf{g}''; \mathbf{g}) \tag{D.24}$$

For an electron impact ionization process, this expression reduces to the Fowler's relation:

$$\mathscr{g}_t v \sigma_{ion}(\mathbf{v}; \mathbf{v}', \mathbf{v}'') = 2\mathscr{g}_i \frac{m_e^3}{h^3} v' v'' \sigma_{rec}(\mathbf{v}', \mathbf{v}''; \mathbf{v}) \tag{D.25}$$

where $\mathbf{v}$, $\mathbf{v}'$, and $\mathbf{v}''$ are the velocities of the incident, reflected, and ejected electrons, respectively. The cross section can be averaged over all angular variables to yield the following:

$$\mathscr{g}_t \varepsilon \overline{\sigma}_{ion}(\varepsilon; \varepsilon', \varepsilon'') = \frac{16\pi m_e}{h^3} \mathscr{g}_i \varepsilon' \varepsilon'' \overline{\sigma}_{rec}(\varepsilon', \varepsilon''; \varepsilon) \tag{D.26}$$

It must be noted that $\overline{\sigma}_{ion}$ is now a singly differential ionization cross section; one can define total ionization cross section by integrating over all the possible energy transfer values, i.e., $\Sigma_{ion} = \int_{\Delta\varepsilon}^{\infty} \overline{\sigma}_{ion} dW$ where $W = \varepsilon - \varepsilon'$. It is, however, not possible to obtain a total recombination cross section in a similar fashion; integrating over the final states of the recombination process is not possible without also partially summing over the initial states. Due to energy conservation, once the initial state is determined by the pair $(\varepsilon', \varepsilon'')$, the final state ε is also fully determined; there is only one final state possible, and $\overline{\sigma}_{rec}$ from equation (D.26) is the total cross section of recombination for the given initial state.

D.3 Line emission and absorption

Consider now a bound bound emission and absorption process, written as:

$$t(E_u) \Leftrightarrow t(E_\ell) + h\nu \tag{D.27}$$

where $h\nu = \Delta\varepsilon = E_u - E_\ell$ for energy conservation. In this transition, we assume that the momentum transfer between particle t and the photon is negligible. One can construct a rate equation for this process by taking in account absorption, stimulated and spontaneous emission processes:

$$n_u(A_{u\ell} + B_{u\ell}I_\nu) = n_\ell B_{\ell u} I_\nu \tag{D.28}$$

where $A_{u\ell}$, $B_{\ell u}$ and $B_{u\ell}$ are Einstein coefficients. Comparing this with equation (4.22), it is easy to see that:

$$\frac{B_{u\ell}}{A_{u\ell}} = \frac{c^2}{2h\nu^3} \tag{D.29}$$

Combining the result above with equation (D.28), we obtain the relation of $B_{u\ell}$ and $B_{\ell u}$:

$$g_\ell B_{\ell u} = g_u B_{u\ell} \tag{D.30}$$

which is known as the Einstein relations.

D.4 Photoionization and radiative recombination

Consider now a balance of the photoionization and radiative recombination processes:

$$t(\varepsilon) + h\nu \Leftrightarrow i(\varepsilon_i) + e^-(\mathbf{v}) \tag{D.31}$$

For simplicity, we assume that the atom (t) and ion (i) are stationary and neglect their translational degree of freedom. The rate equation corresponding to this

reaction is:

$$\begin{aligned} & n_t \cdot \frac{I_\nu}{h\nu} d\nu d\Omega \cdot \sigma^\nu_{ion}(\nu;\chi) d\Omega_e \\ & = n_i \cdot n_e f_e(\mathbf{v}) \underbrace{v^2 dv d\Omega_e}_{d^3\mathbf{v}} \cdot v \cdot \sigma^\nu_{rec}(v;\chi) d\Omega \left(1 + \frac{c^2}{2h\nu^3} I_\nu\right) \end{aligned} \tag{D.32}$$

where χ is the angle between the photon beam and the electron. Inserting the Maxwell distribution for f_e, Saha distribution for $n_i n_e/n_t$ and Planck distribution for I_ν, one obtain:

$$\mathcal{g}_t (h\nu)^2 \sigma^\nu_{ion}(\nu;\chi) = \mathcal{g}_i m_e^2 c^2 v^2 \sigma^\nu_{rec}(v;\chi) \tag{D.33}$$

For isotropic distribution function, one can write the DB relation in terms of total cross sections $\overline{\sigma}^\nu_{ion} = \int \sigma^\nu_{ion} d\Omega_e$:

$$\mathcal{g}_t (h\nu)^2 \overline{\sigma}^\nu_{ion}(\nu) = 2\mathcal{g}_i m_e c^2 \varepsilon \overline{\sigma}^\nu_{rec}(\varepsilon) \tag{D.34}$$

APPENDIX E

Derivation of the Ponderomotive Force for a Single Particle

In this appendix, we derive the expression of the ponderomotive force for a single particle [38]. We start with the equation of motion for an electron moving in the laser fields:

$$m_e \frac{d\mathbf{v}}{dt} = -e\left(\mathbf{E} + \mathbf{v} \times \mathbf{B}\right) \tag{E.1}$$

Let us consider a monochromatic field of the form:

$$\mathbf{E} = \mathbf{E}_L(\mathbf{x}) \cos(\omega t) \tag{E.2}$$

$$\mathbf{B} = -\frac{1}{\omega} \sin(\omega t) \nabla \times \mathbf{E}_L(\mathbf{x}) \tag{E.3}$$

where the second relation came from Faraday's law. For nonrelativistic electrons, the second term in equation (E.1) due to the Lorentz force is small compared to the first. Let us perform an expansion of the position and velocity vectors:

$$\mathbf{x} = \mathbf{x}_0 + \mathbf{x}_1 + \mathbf{x}_2 + \ldots \tag{E.4}$$

$$\mathbf{v} = \mathbf{v}_0 + \mathbf{v}_1 + \mathbf{v}_2 + \ldots \tag{E.5}$$

where $\mathbf{v}_0 = 0, \mathbf{v}_1 = \frac{d\mathbf{x}_1}{dt}, \mathbf{v}_2 = \frac{d\mathbf{x}_2}{dt}, \ldots$ The fields can also be expressed via a Taylor series expansion:

$$\mathbf{E} = \mathbf{E}(\mathbf{x}_0) + (\mathbf{x}_1 \cdot \nabla)\mathbf{E}(\mathbf{x}_0) + \ldots \tag{E.6}$$

$$\mathbf{B} = \mathbf{B}(\mathbf{x}_0) + (\mathbf{x}_1 \cdot \nabla)\mathbf{B}(\mathbf{x}_0) + \ldots \tag{E.7}$$

The lowest order reads:

$$m_e \frac{d\mathbf{v}_1}{dt} = -e\mathbf{E}_L(\mathbf{x}_0)\cos(\omega t) \tag{E.8}$$

Integrating twice equation (E.8) yields the equations for $\mathbf{v}_1$ and $\mathbf{x}_1$:

$$\mathbf{v}_1 = -\frac{e}{m_e\omega}\mathbf{E}_L(\mathbf{x}_0)\sin(\omega t) \tag{E.9}$$

$$\mathbf{x}_1 = \frac{e}{m_e\omega^2}\mathbf{E}_L(\mathbf{x}_0)\cos(\omega t) \tag{E.10}$$

The next order reads:

$$m_e \frac{d\mathbf{v}_2}{dt} = -e\left[(\mathbf{x}_1 \cdot \nabla)\mathbf{E}_L(\mathbf{x}_0) + \mathbf{v}_1 \times \mathbf{B}_L(\mathbf{x}_0)\right] \tag{E.11}$$

Utilizing the relations above, we get:

$$m_e \frac{d\mathbf{v}_2}{dt} = -\frac{e^2}{m_e\omega^2}\left[\cos^2(\omega t)(\mathbf{E}_L \cdot \nabla)\mathbf{E}_L + \sin^2(\omega t)\mathbf{E}_L \times \nabla \times \mathbf{E}_L\right] \tag{E.12}$$

By averaging the force over a laser period, we get:

$$\tilde{\mathbf{f}}_p = -\frac{e^2}{2m_e\omega^2}\left[(\mathbf{E}_L \cdot \nabla)\mathbf{E}_L + \mathbf{E}_L \times \nabla \times \mathbf{E}_L\right] \tag{E.13}$$

where $\tilde{\mathbf{f}}_p$ is the ponderomotive force on a single electron. For the electron fluid, we simply multiply expression (E.13) by n_e:

$$\begin{aligned} \mathbf{f}_p &= -\frac{n_e e^2}{4m_e\omega^2}\nabla\mathbf{E}_L^2 \\ &= -\frac{\epsilon_0\omega_p^2}{4\omega^2}\nabla\mathbf{E}_L^2 \end{aligned} \tag{E.14}$$

Since $\mathbf{f}_p \sim 1/m$, one can see that the ponderomotive force acting on the ions is negligible compared to the electrons.

References

[1] F. F. Chen. *Introduction to plasma physics and controlled fusion*. Plenum Press, 2nd ed edition, 1984.

[2] P. A. Sturrock. *Plasma physics: an introduction to the theory of astrophysical, geophysical, and laboratory plasmas*. Cambridge University Press, 1994.

[3] T. E. Cravens. *Physics of Solar System Plasmas*. Cambridge University Press, 2004.

[4] R. G. Jahn. *Physics of electric propulsion*. Dover books on physics. Dover Publications, Inc, Mineola, N.Y, 2006.

[5] M. A. Lieberman. *Principles of plasma discharges and materials processing*. Wiley-Interscience, 2nd ed edition, 2005.

[6] N. A. Krall. *Principles of plasma physics*. McGraw-Hill, 1973.

[7] P. M. Bellan. *Fundamentals of plasma physics*. Cambridge University Press, 2008.

[8] T. ONeil and F. Coroniti. The collisionless nature of high-temperature plasmas. *Reviews of Modern Physics*, 71(2):S404–S410, March 1999.

[9] L. Landau. On the vibration of the electronic plasma. *J. Phys. USSR*, 10:25, 1946.

[10] F. R. Chang Diaz. The vasimr rocket. *Scientific American*, 283(5), 2000.

[11] M. Capitelli, C. M. Ferreira, B. F. Gordiets, and A. I. Osipov. *Plasma Kinetics in Atmospheric Gases*. Springer Berlin Heidelberg, 2000.

[12] I. V. Adamovich, W. R. Lempert, J. W. Rich, Y. G. Utkin, and M. Nishihara. Repetitively pulsed nonequilibrium plasmas for magnetohydrodynamic flow control and plasma-assisted combustion. *Journal of Propulsion and Power*, 24(6):1198–1215, 2008.

[13] I. V. Adamovich, I. Choi, N. Jiang, J.-H. Kim, S. Keshav, W. R. Lempert, E. Mintusov, M. Nishihara, M. Samimy, and M. Uddi. Plasma assisted ignition and high-speed flow control: non-thermal and thermal effects. *Plasma Sources Science and Technology*, 18(3):034018, August 2009.

[14] S. M. Starikovskaia. Plasma assisted ignition and combustion. *Journal of Physics D: Applied Physics*, 39(16):R265–R299, August 2006.

[15] G. Pilla, D. Galley, D. A. Lacoste, F. Lacas, D. Veynante, and C. O. Laux. Stabilization of a turbulent premixed flame using a nanosecond repetitively pulsed plasma. *IEEE Transactions on Plasma Science*, 34(6):2471–2477, 2006.

[16] L. S. Jacobsen, C. D. Carter, R. A. Baurle, T. A. Jackson, S. Williams, D. Bivolaru, S. Kuo, J. Barnett, and C.-J. Tam. Plasma-assisted ignition in scramjets. *Journal of Propulsion and Power*, 24(4):641–654, July 2008.

[17] S. Serbin, A. Mostipanenko, I. Matveev, and A. Topina. Improvement of the gas turbine plasma assisted combustor characteristics. Paper AIAA-2011-61, January 2011.

[18] J.-L. Cambier, T. Roth, C. Zeineh, and A. R. Karagozian. The pulse detonation rocket induced MHD ejector (PDRIME) concept. Paper AIAA-2008-4688, 44th AIAA/ASME/SAE/ASEE Joint Propulsion Conference and Exhibit, July 2008.

[19] C. F. Zeineh, L. K. Cole, T. Roth, A. R. Karagozian, and J.-L. Cambier. Magnetohydrodynamic augmentation of pulse detonation rocket engines. *Journal of Propulsion and Power*, 28(1):146–159, January 2012.

[20] P. A. Gnoffo. Planetary-entry gas dynamics. *Annual Review of Fluid Mechanics*, 31(1):459–494, January 1999.

[21] C. Park. *Nonequilibrium hypersonic aerothermodynamics*. Wiley, 1990.

[22] B. A. Cruden. Recent progress in entry radiation measurements in the NASA ames electric ARC shock tube facility. Barcelona, Spain, 2012.

[23] J. H. Grinstead, M. J. Wright, D. W. Bogdanoff, and G. A. Allen. Shock radiation measurements for mars aerocapture radiative heating analysis. *Journal of Thermophysics and Heat Transfer*, 23(2):249–255, April 2009.

[24] B. A. Cruden, R. Martinez, J. Grinstead, and J. Olejniczak. Simultaneous vacuum-ultraviolet through near-IR absolute radiation measurement with spatiotemporal resolution in an electric arc shock tube. Paper AIAA-2009-4240, 2009.

[25] A. M. Brandis, R. Morgan, T. McIntyre, and P. A. Jacobs. Nonequilibrium radiation intensity measurements in simulated titan atmospheres. *Journal of Thermophysics and Heat Transfer*, 24(2):291–300, April 2010.

[26] B. Cruden, D. Prabhu, R. Martinez, H. P. Le, J. Grinstead, and D. Bose. Absolute radiation measurement in high mass venus and mars entry conditions. Paper AIAA-2010-4508, June 2010.

[27] C. O. Johnston. *Nonequilibrium Shock-Layer Radiative Heating for Earth and Titan Entry*. Ph.d. thesis, Virginia Tech, 2006.

[28] C. Johnston. A comparison of EAST shock-tube radiation measurements with a new air radiation model. Paper AIAA-2008-1245, January 2008.

[29] M. Panesi, Y. Babou, and O. Chazot. Predictions of nonequilibrium radiation: analysis and comparison with EAST experiments. Paper AIAA-2008-3812, June 2008.

[30] R. Jaffe, D. Schwenke, G. Chaban, and W. Huo. Vibrational and rotational excitation and relaxation of nitrogen from accurate theoretical calculations. Paper AIAA-2008-1208, January 2008.

[31] F. Esposito and M. Capitelli. Quasiclassical molecular dynamic calculations of vibrationally and rotationally state selected dissociation cross-sections: N+n2(v,j)3n. *Chemical Physics Letters*, 302(12):49–54, March 1999.

[32] M. G. Kapper. *A High-Order Transport Scheme for Collisional-Radiative and Nonequilibrium Plasma*. Ph.d. thesis, Ohio State University, 2009.

[33] W. Wang, H. C. Yee, B. Sjgreen, T. E. Magin, and C.-W. Shu. Construction of low dissipative high-order well-balanced filter schemes for non-equilibrium flows. *Journal of Computational Physics*, 230(11):4316–4335, May 2011.

[34] W. Wang, C.-W. Shu, H. C. Yee, and B. Sjgreen. High order finite difference methods with subcell resolution for advection equations with stiff source terms. *Journal of Computational Physics*, 231(1):190–214, January 2012.

[35] D. V. Kotov, H. C. Yee, M. Panesi, D. Prabhu, and A. A. Wray. Computational challenges for simulations related to the NASA electric arc shock tube (EAST) experiments. *Journal of Computational Physics*, 269:215–233, July 2014.

[36] T. E. Magin, M. Panesi, A. Bourdon, R. L. Jaffe, and D. Schwenke. Coarse-grain model for internal energy excitation and dissociation of molecular nitrogen. *Chemical Physics*, 398:90–95, April 2012.

[37] A. Guy, A. Bourdon, and M.-Y. Perrin. Consistent multi-internal-temperatures models for nonequilibrium nozzle flows. *Chemical Physics*, 420:15–24, July 2013.

[38] S. Eliezer. *The Interaction of High-Power Lasers with Plasmas*. CRC Press, 2002.

[39] S. Eliezer and K. Mima, editors. *Applications of laser-plasma interactions*. Series in plasma physics. CRC Press/Taylor & Francis, Boca Raton, 2009.

[40] S. Atzeni and J. Meyer-teh Vehn. *The Physics of Inertial Fusion*. Number 125 in International Series of Monographs on Physics. Oxford University Press, 2009.

[41] P. Gibbon and E. Forster. Short-pulse laser-plasma interactions. *Plasma Physics and Controlled Fusion*, 38(6):769–793, June 1996.

[42] L. C. Steinhauer. Review of field-reversed configurations. *Physics of Plasmas*, 18(7):070501, 2011.

[43] J. M. Burgers. *Flow equations for composite gases*. Academic Press, 1969.

[44] S. Chapman and T. G. Cowling. *The mathematical theory of non-uniform gases*. Cambridge mathematical library. Cambridge University Press, 3rd edition, 1990.

[45] D. Burnett. The distribution of velocities in a slightly non-uniform gas. *Proceedings of the London Mathematical Society*, s2-39(1):385–430, 1935.

[46] S. I. Braginskii. Transport processes in a plasma. In *Review of plasma physics*, volume 1, pages 205–311. Consultants Bureau, New York, 1965.

[47] H. Grad. On the kinetic theory of rarefied gases. *Communications on Pure and Applied Mathematics*, 2(4):331–407, December 1949.

[48] B. Alexeev, A. Chikhaoui, and I. Grushin. Application of the generalized chapman-enskog method to the transport-coefficient calculation in a reacting gas mixture. *Physical Review E*, 49(4):2809–2825, 1994.

[49] E. V. Kustova and D. Giordano. Cross-coupling effects in chemically non-equilibrium viscous compressible flows. *Chemical Physics*, 379(1-3):83–91, 2011.

[50] C. K. Birdsall and A. B. Langdon. *Plasma physics via computer simulation*. Taylor & Francis, 2005.

[51] G. Lapenta. Particle simulations of space weather. *Journal of Computational Physics*, 231(3):795–821, February 2012.

[52] J. O. Hirschfelder, C. F. Curtiss, and R. B. Bird. *The Molecular Theory of Gases and Liquids*. Wiley-Interscience, 1964.

[53] V. Giovangigli. *Multicomponent flow modeling*. Birkhauser, 1999.

[54] L. Spitzer. *Physics of fully ionized gases*. Dover Publications, 2006.

[55] A. Decoster. *Modeling of collisions*. Gauthier-Villars, 1998.

[56] L. Landau, L. P. Pitaevskii, and E. M. Lifshitz. *Electrodynamics of Continuous Media*, volume 8 of *Course of Theoretical Physics*. 2nd edition, 1979.

[57] R. J. Rosa. *Magnetohydrodynamic Energy Conversion*. McGraw-Hill, 1968.

[58] M. Panesi, R. L. Jaffe, D. W. Schwenke, and T. E. Magin. Rovibrational internal energy transfer and dissociation of n2-n system in hypersonic flows. *The Journal of Chemical Physics*, 138(4):044312, 2013.

[59] H. S. Reksoprodjo and R. Agarwal. A kinetic scheme for numerical solution of ideal magnetohydrodynamics equations with a bi-temperature model. Paper AIAA-2000-0448, 2000.

[60] J.-L. Cambier, M. Carroll, and M. G. Kapper. Development of a hybrid model for non-equilibrium high-energy plasmas. Paper AIAA 2004-2166, 2004.

[61] J.-L. Cambier. *Unpublished*.

[62] G. Strang. On the construction and comparison of difference schemes. *SIAM Journal on Numerical Analysis*, 5(3):506–517, 1968.

[63] M. Duarte, M. Massot, S. Descombes, C. Tenaud, T. Dumont, V. Louvet, and F. Laurent. New resolution strategy for multiscale reaction waves using time operator splitting, space adaptive multiresolution, and dedicated high order implicit/explicit time integrators. *SIAM Journal on Scientific Computing*, 34(1):A76–A104, 2012.

[64] H. Lomax. *Fundamentals of computational fluid dynamics*. Scientific computation. Springer, 2001.

[65] B. Einfeldt, C.D Munz, P.L Roe, and B Sjogreen. On godunov-type methods near low densities. *Journal of Computational Physics*, 92(2):273–295, 1991.

[66] A. Suresh and H.T. Huynh. Accurate monotonicity-preserving schemes with rungekutta time stepping. *Journal of Computational Physics*, 136(1):83–99, September 1997.

[67] X.-D. Liu, S. Osher, and T. Chan. Weighted essentially non-oscillatory schemes. *Journal of Computational Physics*, 115(1):200–212, 1994.

[68] G.-S. Jiang and C.-W. Shu. Efficient implementation of weighted ENO schemes. *Journal of Computational Physics*, 126(1):202–228, 1996.

[69] A. Harten, B. Engquist, S. Osher, and S. R. Chakravarthy. Uniformly high order accurate essentially non-oscillatory schemes, III. *Journal of Computational Physics*, 71(2):231–303, 1987.

[70] E. S. Oran and J. P. Boris. *Numerical Simulation of Reactive Flow*. Cambridge University Press, 2nd edition, 2005.

[71] P. Colella and P. R. Woodward. The piecewise parabolic method (PPM) for gas-dynamical simulations. *Journal of Computational Physics*, 54(1):174–201, 1984.

[72] P. Woodward and P. Colella. The numerical simulation of two-dimensional fluid flow with strong shocks. *Journal of Computational Physics*, 54(1):115–173, 1984.

[73] M. Van Dyke. *An Album of Fluid Motion*. Parabolic Press, Inc., 1982.

[74] C. L. Gardner, J. Glimm, O. McBryan, R. Menikoff, D. H. Sharp, and Q. Zhang. The dynamics of bubble growth for rayleigh-taylor unstable interfaces. *Physics of Fluids*, 31(3):447, 1988.

[75] L. K. Cole, A. R. Karagozian, and J.-L. Cambier. Stability of flame-shock coupling in detonation waves: 1d dynamics. *Combustion Science and Technology*, 184(10-11):1502–1525, 2012.

[76] C. J. Jachimowski. An analysis of combustion studies in shock expansion tunnels and reflected shock tunnels. Technical report, NASA-TP-3224, 1992.

[77] G. J. Sharpe and M. I. Radulescu. Statistical analysis of cellular detonation dynamics from numerical simulations: one-step chemistry. *Combustion Theory and Modelling*, 15(5):691–723, 2011.

[78] M. A. Lieberman. Model of plasma immersion ion implantation. *Journal of Applied Physics*, 66(7):2926, 1989.

[79] J. Freidberg. Ideal magnetohydrodynamic theory of magnetic fusion systems. *Reviews of Modern Physics*, 54(3):801–902, 1982.

[80] R. J. Thompson, A. Wilson, R. Moeller, and C. L. Merkle. A strong conservative riemann solver for the solution of the coupled maxwell and navier-stokes equations. *Journal of Computational Physics*, 258:431–450, February 2014.

[81] U. Shumlak and J. Loverich. Approximate riemann solver for the two-fluid plasma model. *Journal of Computational Physics*, 187(2):620–638, 2003.

[82] O. V. Batishchev, V. Yu. Bychenkov, F. Detering, W. Rozmus, R. Sydora, C. E. Capjack, and V. N. Novikov. Heat transport and electron distribution function in laser produced plasmas with hot spots. *Physics of Plasmas*, 9(5):2302, 2002.

[83] Y. B. Zeldovich and Y. B. Raizer. *Physics of shock waves and high-temperature hydrodynamic phenomena*. Dover Publications, 2002.

[84] V. M. Zhdanov. *Transport processes in multicomponent plasma*. Taylor & Francis, 2002.

[85] A. R. Bell. Non-spitzer heat flow in a steadily ablating laser-produced plasma. *Physics of Fluids*, 28(6):2007, 1985.

[86] M. Mitchner. *Partially ionized gases*. Wiley, 1973.

[87] J. Oxenius. *Kinetic theory of particles and photons*, volume 20 of *Springer Series in Electronics and Photonics*. Springer, 1986.

[88] J.A.M. van der Mullen. Excitation equilibria in plasmas; a classification. *Physics Reports*, 191(2-3):109–220, 1990.

[89] L. M. Biberman, V. S. Vorobev, and I. T. Yakubov. *Kinetics of Nonequilibrium Low-temperature Plasmas.* Springer Verlag, 2012.

[90] M. G. Kapper and J.-L. Cambier. Ionizing shocks in argon. part i: Collisional-radiative model and steady-state structure. *Journal of Applied Physics*, 109(11):113308, 2011.

[91] J. Vlcek. A collisional-radiative model applicable to argon discharges over a wide range of conditions. i. formulation and basic data. *Journal of Physics D: Applied Physics*, 22(5):623–631, 1989.

[92] A. Bultel, B. van Ootegem, A. Bourdon, and P. Vervisch. Influence of ar2+ in an argon collisional-radiative model. *Physical Review E*, 65(4), March 2002.

[93] T. E. Magin and M. G. Kapper. Advanced physical models and numerical methods for high enthalpy and plasma flows applied to hypersonics. Technical report AFRL-AFOSR-UK-TR-2011-0023, 2011.

[94] J.-L. Cambier. Numerical methods for TVD transport and coupled relaxing processes in gases and plasmas. Paper AlAA-90-1574, 1990.

[95] W. M. Huo, M. Panesi, and T. E. Magin. Ionization phenomena behind shock waves. In *High Temperature Phenomena in Shock Waves*. Springer, 2012.

[96] M. A. Liberman and A. L. Velikovich. *Physics of shock waves in gases and plasmas*, volume 19 of *Springer series in electrophysics*. Springer-Verlag, 1986.

[97] M. G. Kapper and J.-L. Cambier. Ionizing shocks in argon. part II: Transient and multi-dimensional effects. *Journal of Applied Physics*, 109(11):113309, 2011.

[98] A. Kramida, Y. Ralchenko, J. Reader, and NIST ASD Team. *NIST Atomic Spectra Database*. 2013.

[99] H. W. Drawin. *Z. Physik*, 225(470), 1969.

[100] H. W. Drawin. Report EUR-CEA-FC-510, 1969.

[101] P. O. Haugsjaa and R. C. Amme. Ionization and metastable excitation in low-energy collisions of ground-state argon atoms. *The Journal of Chemical Physics*, 52(9):4874, 1970.

[102] O. Zatsarinny and K. Bartschat. B-spline breit-pauli r -matrix calculations for electron collisions with argon atoms. *Journal of Physics B: Atomic, Molecular and Optical Physics*, 37(23):4693–4706, 2004.

[103] H. Deutsch, K. Becker, S. Matt, and T. D. Mark. Calculated cross sections for the electron-impact ionization of metastable atoms. *Journal of Physics B: Atomic, Molecular and Optical Physics*, 32(17):4249–4259, 1999.

[104] R. P. McEachran and A. D. Stauffer. Relativistic effects in low-energy electron - argon scattering. *Australian Journal of Physics*, 50(3):511, 1997.

[105] O. Zatsarinny and K. Bartschat. Benchmark calculations for near-threshold electron-impact excitation of krypton and xenon atoms. *Journal of Physics B: Atomic, Molecular and Optical Physics*, 43(7):074031, 2010.

[106] J. Mitroy. The momentum transfer cross section for krypton. *Australian Journal of Physics*, 43(1):19–25, 1990.

[107] R. P. McEachran and A. D. Stauffer. Elastic scattering of electrons from krypton. *Journal of Physics B: Atomic, Molecular and Optical Physics*, 36(19):3977–3984, October 2003.

[108] D. Erwin and J. Kunc. Ionization of excited xenon atoms by electrons. *Physical Review A*, 70(2), 2004.

[109] O. Zatsarinny, K. Bartschat, and M. Allan. High-resolution experiments and b-spline r-matrix calculations for elastic electron scattering from krypton. *Physical Review A*, 83(3), 2011.

[110] I. I. Glass and W. S. Liu. Effects of hydrogen impurities on shock structure and stability in ionizing monatomic gases. part 1. argon. *Journal of Fluid Mechanics*, 84(01):55, 1978.

[111] I. I. Glass, W. S. Liu, and F. C. Tang. Effects of hydrogen impurities on shock structure and stability in ionizing monatomic gases: 2. krypton. *Canadian Journal of Physics*, 55(14):1269–1279, 1977.

[112] H. Ezumi, M. Kawamura, and N. Gohda. Shock-tube measurements of the excitational cross-section in xenon-hydrogen mixture. *Journal of the Physical Society of Japan*, 53(2):592–600, 1984.

[113] J.-L. Cambier. Numerical simulations of a nonequilibrium argon plasma in a shock-tube experiment. Paper AIAA-91-1464, 1991.

[114] H. P. Le, A. R. Karagozian, and J.-L. Cambier. Complexity reduction of collisional-radiative kinetics for atomic plasma. *Physics of Plasmas*, 20(12):123304, 2013.

[115] E. Josyula and W. F. Bailey. Vibration-dissociation coupling using master equations in nonequilibrium hypersonic blunt-body flow. *Journal of Thermophysics and Heat Transfer*, 15(2):157–167, 2001.

[116] D. Giordano, V. Bellucci, G. Colonna, M. Capitelli, I. Armenise, and C. Bruno. Vibrationally relaxing flow of n past an infinite cylinder. *Journal of Thermophysics and Heat Transfer*, 11(1):27–35, 1997.

[117] G. Colonna, L. D. Pietanza, and M. Capitelli. Recombination-assisted nitrogen dissociation rates under nonequilibrium conditions. *Journal of Thermophysics and Heat Transfer*, 22(3):399–406, 2008.

[118] Y. Liu, M. Vinokur, M. Panesi, and T. E. Magin. A multi-group maximum entropy model for thermo-chemical non-equilibrium. Paper AIAA-2010-4332, 2010.

[119] C. O. Laux, L. Pierrot, and R. J. Gessman. State-to-state modeling of a recombining nitrogen plasma experiment. *Chemical Physics*, 398:46–55, 2012.

[120] A. Bultel, B. G. Cheron, A. Bourdon, O. Motapon, and I. F. Schneider. Collisional-radiative model in air for earth re-entry problems. *Physics of Plasmas*, 13(4):043502, 2006.

[121] M. Panesi, T. E. Magin, A. Bourdon, A. Bultel, and O. Chazot. Electronic excitation of atoms and molecules for the FIRE II flight experiment. *Journal of Thermophysics and Heat Transfer*, 25(3):361–374, 2011.

[122] A. Munafo, M. Panesi, and T. E. Magin. Boltzmann rovibrational collisional coarse-grained model for internal energy excitation and dissociation in hypersonic flows. *Physical Review E*, 89(2), 2014.

[123] J.-L. Cambier and S. Moreau. Simulations of a molecular plasma in collisional-radiative nonequilibrium. Paper AIAA-93-3196, 1993.

[124] W. Kruer. *The Physics Of Laser Plasma Interactions*. Frontiers in Physics, 2003.

[125] P. Mulser and D. Bauer. *High power laser-matter interaction*. Number 238 in Springer tracts in modern physics. Springer, Heidelberg ; New York, 2010.

[126] M. Tabak, J. Hammer, M. E. Glinsky, W. L. Kruer, S. C. Wilks, J. Woodworth, E. M. Campbell, M. D. Perry, and R. J. Mason. Ignition and high gain with ultrapowerful lasers. *Physics of Plasmas*, 1(5):1626, 1994.

[127] V. L. Ginzburg. *Propagation of Electromagnetic Waves in Plasma*. Gordon & Science, 1961.

[128] J. D. Jackson. *Classical electrodynamics*. Wiley, New York, 2nd edition, 1975.

[129] H. Hora. *Plasmas at high temperature and density: applications and implications of laser-plasma interaction*. Number m1 in Lecture notes in physics. Springer-Verlag, 1991.

[130] H. Hora. *Laser plasma physics: forces and the nonlinearity principle*. SPIE Optical Engineering Press, 2000.

[131] A. Zeidler, H. Schnabl, and P. Mulser. Light pressure of timedependent fields in plasmas. *Physics of Fluids*, 28(1):372–376, 1985.

[132] H. Hora. The transient electrodynamic forces at laserplasma interaction. *Physics of Fluids*, 28(12):3705, 1985.

[133] R. J. LeVeque. *Finite difference methods for ordinary and partial differential equations: steady-state and time-dependent problems*. Society for Industrial and Applied Mathematics, 2007.

[134] R. Ramis, K. Eidmann, J. Meyer-ter Vehn, and S. Hller. MULTI-fs a computer code for laserplasma interaction in the femtosecond regime. *Computer Physics Communications*, 183(3):637–655, 2012.

[135] M. Born and E. Wolf. *Principles of Optics*. Pergamon Press, 1980.

[136] J. D. Lindl and P. Kaw. Ponderomotive force on laser-produced plasmas. *Physics of Fluids*, 14(2):371, 1971.

[137] A. Macchi, F. Cattani, T. Liseykina, and F. Cornolti. Laser acceleration of ion bunches at the front surface of overdense plasmas. *Physical Review Letters*, 94(16), April 2005.

[138] S. C. Wilks, A. B. Langdon, T. E. Cowan, M. Roth, M. Singh, S. Hatchett, M. H. Key, D. Pennington, A. MacKinnon, and R. A. Snavely. Energetic proton generation in ultra-intense lasersolid interactions. *Physics of Plasmas*, 8(2):542, 2001.

[139] M. Passoni, L. Bertagna, and A. Zani. Target normal sheath acceleration: theory, comparison with experiments and future perspectives. *New Journal of Physics*, 12(4):045012, 2010.

[140] H. Hora, P. Lalousis, and S. Eliezer. Analysis of the inverted double layers produced by nonlinear forces in a laser-produced plasma. *Physical Review Letters*, 53(17):1650–1652, October 1984.

[141] K. Rawer. *Ann. Phys.*, 35(385), 1939.

[142] H. Kim, R. Stenzel, and A. Wong. Development of "caviton" and trapping of rf field. *Physical Review Letters*, 33(15):886–889, October 1974.

[143] G. Morales and Y. Lee. Ponderomotive-force effects in a nonuniform plasma. *Physical Review Letters*, 33(17):1016–1019, October 1974.

[144] T. Esirkepov, M. Borghesi, S. Bulanov, G. Mourou, and T. Tajima. Highly efficient relativistic-ion generation in the laser-piston regime. *Physical Review Letters*, 92(17), 2004.

[145] F. V. Hartemann, E. C. Landahl, A. L. Troha, J. R. Van Meter, H. A. Baldis, R. R. Freeman, N. C. Luhmann, L. Song, A. K. Kerman, and D. U. L. Yu. The chirped-pulse inverse free-electron laser: A high-gradient vacuum laser accelerator. *Physics of Plasmas*, 6(10):4104, 1999.

[146] A. G. Khachatryan, F. A. van Goor, J. W. J. Verschuur, and K.-J. Boller. Effect of frequency variation on electromagnetic pulse interaction with charges and plasma. *Physics of Plasmas*, 12(6):062116, 2005.

[147] D. N. Gupta and H. Suk. Frequency chirping for resonance-enhanced electron energy during laser acceleration. *Physics of Plasmas*, 13(4):044507, 2006.

[148] F. Sohbatzadeh, S. Mirzanejhad, and M. Ghasemi. Electron acceleration by a chirped gaussian laser pulse in vacuum. *Physics of Plasmas*, 13(12):123108, 2006.

[149] B. Srinivasan, G. Dimonte, and X.-Z. Tang. Magnetic field generation in rayleigh-taylor unstable inertial confinement fusion plasmas. *Physical Review Letters*, 108(16), 2012.

[150] J. F. Hansen, M. J. Edwards, D. H. Froula, G. Gregori, A. D. Edens, and T. Ditmire. Laboratory observation of secondary shock formation ahead of a strongly radiative blast wave. *Physics of Plasmas*, 13(2):022105, 2006.